Improved Turbulence Models for Computational Wind Engineering

by Gary Easom B.Eng., M.Res.

Thesis submitted to the University of Nottingham for the degree of Doctor of Philosophy, January 2000.

Supervisor
Dr N.G. Wright – School of Civil Engineering, The University of Nottingham.

Associate Supervisor
Dr R.P. Hoxey – Bio-engineering Division, Silsoe Research Institute.

Table of contents.

Abstract.

The fundamental errors in the numerical modelling of the turbulent component of fluid flow are one of the main reasons why computational fluid dynamics techniques have not yet been fully accepted by the wind engineering community.

This thesis is the result of extensive research that was undertaken to assess the various methods available for numerical simulation of turbulent fluid flow. The research was undertaken with a view to developing improved turbulence models for computational wind engineering. Investigations have concentrated on analysing the accuracy and numerical stability of a number of different turbulence models including both the widely available models and state of the art techniques.

These investigations suggest that a turbulence model, suitable for wind engineering applications, should be able to model the anisotropy of turbulent flow as in the differential stress model whilst maintaining the ease of use and computational stability of the two equation *k-e* models. Therefore, non-linear expansions of the Boussinesq hypotheses, the quadratic and cubic non-linear *k-e* models, have been tested in an attempt to account for anisotropic turbulence and curvature related strain effects.

Furthermore, large eddy simulations using the standard Smagorinsky sub-grid scale model have been completed, in order to account for the four dimensional nature of turbulent flow. This technique, which relies less heavily on the need to model turbulence by utilising advances in computer technology and processing power to directly resolve more of the flow field, is now becoming increasingly popular in the engineering community.

The author has detailed and tested all of the above mentioned techniques and given recommendations for both the short and longer term future of turbulence modelling in computational wind engineering.

Improved turbulence models that will more accurately predict bluff body flow fields and that are numerically stable for complex geometries are of paramount importance if the use of CFD techniques are to gain wide acceptance by the wind engineering community.

List of figures.

List of tables.

Acknowledgements.

Profound thanks to the following people:

Dr N.G. Wright, for his full support, help and encouragement throughout this study and his contribution to the making the Ph.D. such a rewarding experience.

Professor Baker, for his continuing help and encouragement.

Dr. Andrew Quinn, a source of great help throughout the Ph.D, and someone whom, in the early days, had a good deal of CFD knowledge when I had none!.

Dr D. Hargreaves, a very helpful and extremely clever chap.

Dr R. Hoxey, definitely the man to speak to when it comes to experimental fluid mechanics (and CFD too).

Dr I.P. Jones and N. Wilkes of CFX-International, without whom this Ph.D. would possibly have been much shorter and not particularly interesting!.

Matt Straw, for many hours of discussion putting (CFD and) the world to rights.

My wife Samantha, for putting up with me, an eternal student, for all these years while she has gone out and put food on the table.

My family for their continued support and encouragement through the years.

List of publications.

Wright, N.G., Easom, G.J. and Hoxey, R. (1998). *'Improved computational models for wind engineering.'*, Proceedings of the 4th UK Conference on Wind Engineering, Bristol University, Bristol, England.

Wright, N.G., Easom, G.J. and Hoxey, R. (1999). *'Improved computational models for wind engineering.'*, Proceedings of the 10th ICWE, Copenhagen, Denmark.

Wright, N.G. and Easom, G.J. (1999). *'Comparison of several computational turbulence models with full-scale measurements of flows around buildings.'*, Paper accepted for publication in the Journal of Wind and Structures.

Wright, N.G. and Easom, G.J. (1999). *'Improved computational models for wind engineering.'*, Paper accepted for publication in the Journal of Wind and Structures.

1. Introduction.

> ‘Generally Computational Fluid Dynamics can be defined as the analysis of systems involving fluid flow, heat transfer and associated phenomena such as chemical reactions by computer based simulation.’ (Versteeg and Malalasekera 1995, p1)

The majority of practical fluid flows are turbulent and consist of many complex flow features which may contain, among other features, recirculation zones and flow stagnation points. The types of flows encountered in the field of wind engineering are no exception.

Traditionally, due to the complexity of this subject, all the research and design work undertaken in this field has concentrated on the use of full-scale and wind tunnel analysis. This has involved the use of expensive wind tunnel and data recording facilities and has required significant time and effort to obtain the desired results. However during the 1970’s and 1980’s there was a great deal of interest among the engineering community into a relatively new technique known as computational fluid dynamics (CFD). The advances made in high speed digital computer technology had enabled the solution of flow problems, which were described mathematically by a set of coupled nonlinear partial differential equations and the appropriate boundary conditions, in a relatively short space of time and for a low financial cost. Initially the wind engineering community largely ignored this technique due to the need for powerful computers and the errors in early modelling techniques. Nonetheless, the rapidly falling costs of computer hardware and further advances in technology in the late 1980’s and early 1990’s enabled CFD to be applied to the complex field of wind engineering.

In theory it is numerically possible to completely resolve all aspects of a fluid dynamics problem including the rapid spatial and temporal variations of turbulence in the flow using a CFD technique known as direct numerical simulation. This technique involves discretising the equations using the finite volume method at a mesh size below the smallest eddies in turbulent flow, the Kolmorogov length scale, and therefore resolving the flow down to the smallest spatial and temporal variations. Unfortunately the direct numerical simulation of practical turbulent fluid flows using the time dependent Navier-Stokes equations in their simplest form is well beyond the capabilities of present day computing power. This is due to the fact that the amount of

computer processing (CPU) time required is dependent on the degree of resolution of the small scale eddies. The smallest eddies in turbulent flow, the so-called 'Kolmogorov microscale', are very small at about 0.1 to 1mm for natural wind (Murakami 1997). Therefore the numerical discretisation of an entire wind engineering flow field with a complex geometry at high Reynolds numbers is at present well beyond the capabilities of even the most powerful supercomputers available.

The only economically feasible way to solve this problem is to employ statistically averaged equations which govern the mean flow equations. Turbulence models are then required to achieve closure of the averaged equations and represent the action of turbulent stresses on the mean flow. Unfortunately the mathematical models used in CFD are only able to perform as well as the physical assumptions and knowledge built into them will allow. In particular the assumptions made regarding the modelling of the turbulent component of engineering flows have proved to be a major source of error in wind engineering simulations.

Presently, the most popular and widely used models use equations to represent a single length and velocity scale and are based on Reynolds averaging and the isotropic eddy viscosity concept. Although many of these turbulence models have been used successfully in aeronautical applications, in which fluid flow without separation may be a regular occurrence the same is not true of wind engineering applications. Wind engineering flow fields are highly complex and are characterised by the presence of multiple recirculation zones embedded within a uni-directional flow. The addition of streamline curvature and favourable and adverse pressure gradients leads to flow fields possessing very different turbulence scales and structures. Consequently such turbulence models have great difficulty in simulating wind engineering flow fields which are essentially transient and highly anisotropic.

It is therefore apparent that one of the main obstacles to the use of CFD in wind engineering is that of turbulence modelling.

In view of these shortcomings the aim of this work has been to conduct research into the various turbulence modelling methods available with a view to developing improved turbulence models for computational wind engineering. This project has concentrated on a number of different turbulence models and analysed their effects on the accuracy of the results obtained for bluff body flow simulations from the CFD package CFX. A number of bluff body test cases have been used, all of which have

also been analysed experimentally at ‘full-scale’ to allow direct comparisons of the available data. As far as the author is aware these tests represent the first comparison of experimental data from a full-scale surface mounted cube, rather than model scale, to CFD derived results.

This thesis is structured as follows:

Chapter 2 introduces the reader to the subjects of wind engineering and computational wind engineering (CWE).

All the important numerical considerations regarding the computational analysis of fluid flow are reviewed in chapter 3. This chapter offers comprehensive detail on all the important aspects of numerical discretisation including methods of dealing with the convection terms in the transport equations.

Chapters 4 and 5 detail the main problem area for attaining accurate CFD simulations, that of turbulence modelling. Chapter 4 reviews both the more conventional models in wide spread use today and a number of more theoretical models and highlights their errors and potential inadequacies. Chapter 5 summarises the main problems with these ‘conventional’ models and offers a number of possible improvements.

Chapter 6 details the performance of many of the models described in chapters 4 and 5 for a number of different bluff body flow fields and compares the results obtained against full-scale data obtained from the Silsoe Research Institute. Full analysis and discussion of the results is offered based on the ability of the model to meet certain criteria, described later, in order to assess their applicability as a wind engineering turbulence model.

Chapter 7 highlights a completely different technique for modelling turbulent flow fields described as Large Eddy Simulation. This was separated from chapter 6 due to the fact that this technique is based on a different method of filtering the main fluid flow equations and different methods have been used to ascertain its accuracy. Due to the large computational overheads of this technique this chapter was mainly used to assess whether LES can be applied to flows with high Reynolds numbers and large flow domains, i.e. wind engineering applications and to assess the future work to be undertaken. Full analysis and discussion is offered.

Results obtained from these investigations have clearly shown the essential requirements for turbulence models to adequately predict bluff body flow fields as highlighted in chapter 8.

2. Wind Engineering.

2.1 Introduction

This chapter provides a general introduction into the field of wind engineering with a brief overview of this complex and diverse subject. The reader is offered a brief history of the subject with reference to past disasters and the more prominent figures who have contributed to this subject. The significant effects of the atmospheric boundary layer on the surface pressures around buildings are graphically demonstrated and a brief discussion of the available wind loading codes of practice for structural design is given. This chapter then introduces the reader to the following chapters through a brief discussion of computational wind engineering focusing on the relative benefits of applying this technique to wind engineering problems.

2.2 Wind Engineering - Bluff Body Aerodynamics

Wind engineering is a relatively young field, with the advent of computational wind engineering perhaps as little as ten or fifteen years ago. Nevertheless the development of both computational and experimental wind engineering has been fast, building on the knowledge gained during the explosive expansion of fluid dynamics at the beginning of the century, in the rush to perfect and exploit the aeroplane (Cook 1986a). The foundations of wind engineering and fluid mechanics can be traced back to the late seventeenth century with advances and discoveries by such prominent figures as Newton, Hook and Bernoulli. The discipline has progressed from these early years through a combination of advances made in other related disciplines such as aeronautics and through a series of high profile failures in the early 19^{th} and 20^{th} centuries. Such disasters include the collapse of the Tay and the Tacoma Narrows bridges in 1879 and 1940 respectively. These gave added impetus to the need to understand wind effects in the lower atmosphere and led to pioneering experiments being undertaken by Reynolds, Stokes and Jenson. Unfortunately until about 1960 it was still assumed that the general techniques applied to aeronautics could be successfully applied to ground based structures. As such wind forces on buildings were determined using relatively smooth inflow conditions in the various wind tunnel experiments undertaken. Experiments that compared wind tunnel results of models in smooth air to full-scale studies discovered major discrepancies that were quickly recognised and explained. These events and discoveries have led to a sound

understanding of wind effects in the lower atmosphere and have brought about the development of design codes that allow safer structures to be built.

2.2.1 Fundamental Aspects

Wind engineering is concerned with the accurate calculation of wind induced loading of a structure and the ability of the said structure to resist such forces without failure. Consequently there are three fundamental considerations as follows:

1. the wind climate comprising the weather
2. the atmospheric boundary layer
3. the structure.

The first point is important as various locations in the world experience vastly different extreme weather systems due to their respective climates i.e. polar, tropical and moderate. In the United Kingdom, the climate is dominated by prevailing westerly winds and by a band of low pressure between Scotland and Ireland. Atlantic depressions caused by the instability of the polar front track across the Atlantic and dominate the weather systems in the UK (Cook 1986a). Consequently as these depressions pass over the UK they influence different parts of the country in varying degrees of severity.

The Atmospheric Boundary Layer (ABL) is the result of the interaction of the wind and the Earth's surface. Between the Earth's surface and the top of the boundary layer, the gradient height, the wind is retarded due to roughness elements such as grass, trees, buildings and general relief or topography. These effects are transmitted upwards by Reynolds stresses resulting from the exchange of momentum between successive layers of the atmosphere. The ground level shear stresses increase with increasing ground roughness (Cook 1986a). The overall effect of the ABL on the incident wind at ground level is one of the main factors that makes the field of wind engineering so different from, for example, aeronautical engineering. The turbulence generated by the retarding effect of the ground results in a significant increase in the complexity of the incident wind and the effects on ground based structures. The ABL can be further divided into a number of sub-layers as follows:

Roughness Sub-layer – This layer extends from the surface to the average height of the roughness elements that may range from snow and grass to trees and buildings.

Inertial Sub-layer – This layer extends from the roughness layer to a height that is dependent on the degree of roughness of the surface retarding the flow. Both the roughness and inertial sub-layers are encompassed within the surface layer.

Ekman layer – extends from the top of the surface layer to a height where the wind is unaffected by the Earth's surface. This height is commonly referred to as the gradient height.

A general idea of the extent of these regions is given in Figure 1.

Further considerations that add to the complexity of the incident wind at any location are apparent due to the surrounding topography and fetch. Sites located near to hills and inclines may experience higher winds or be sheltered depending on the particular location and wind direction. The development of the boundary layer and roughness of the fetch has to be taken into consideration in determining the possible wind speeds, turbulence levels and therefore gust strengths that affect a structure at a given location. The affect of altitude and seasonal variations in weather also needs to be included.

The method of construction and shape of the structure define the way in which the atmospheric boundary layer interacts with a building. Considering the building as a whole, when a structure is small it will be loaded by small gusts and the full range of frequencies in the boundary layer will be significant. Conversely when the structure is large the smaller gusts will not act simultaneously on the structure and will tend to cancel each other out so that only the lower frequencies are significant. When a structure is stiff it will have a high natural frequency in each of its first few nodes and will tend to follow the fluctuations of load without significant amplification or attenuation (Cook 1986a). As the lowest modal frequencies are high there is little energy in the spectrum of the atmospheric turbulence available to excite resonance. Deflection of the structure is not significant and as such the structure is said to be static. This class of structure represents the majority of buildings in wind engineering analysis. The only design parameter of importance for a static structure is the maximum load likely to be experienced in its lifetime (Cook 1986a). The designer therefore ensures that the design strength of the structure exceeds this load by a suitable safety margin to account for variations of material strengths and uncertainties in the assessment. Other structures, which are susceptible to deflection, may come under the heading of dynamic or even aero-elastic structures. These can be excited by

loading at frequencies at the natural frequency of the structure, which may result in excessive deflections. Therefore the excessive deflection and the consequent increase in stresses will become important in designing the structure.

The majority of the damage that occurs with static structures in the UK follows major windstorms such as the 1987 storm that affected the south of England. Damage is usually concentrated on the cladding or roofs of buildings in localised areas of high negative (suction) pressures, as detailed in the following section. In addition, depending on the direction of the incident wind to the structure, delta wing vortices may occur resulting in very high negative pressures. Fatigue loading of cladding may also occur as a consequence of repeated or fluctuating loading on a surface which can result in the general weakening of structural ties and connections. Further details can be found in Cook (1986b).

2.2.2 Bluff Body Flow Fields

Wind engineering flow fields are complicated firstly by virtue of the turbulent atmospheric boundary layer, as briefly detailed, and secondly due to the fact that we are mainly dealing with non-aerodynamic or bluff bodies, defined as follows:

> ‘A body is aerodynamically bluff when the flow streamlines do not follow the surface of the body, but detach from it leaving regions of separated flow and a wide trailing wake.’ (Cook 1986a, p27)

The flow fields around a classical bluff body, a surface mounted cube will now be briefly described in order to highlight both the effects of the ABL and the complex flow fields produced. It is worth noting that the descriptions to follow are simplistic and that there are complex interactions between the different flow effects. Castro and Robbins (1977) give a full and detailed description of the following.

For the windward face in a uniform wind the maximum pressure is located on the centreline of the face next to the ground as all kinetic energy of the flow is transferred to dynamic pressure as the flow velocity reduces to zero (see Figure 2).

The revised incident wind gradient, best represented by a logarithmic law profile (see Figure 3) allows the flow to move down the face in addition to the tendency to move around the sides and over the top of the cube. Above the front stagnation point the

flow rises over the top of the building resulting in a lower mass of air flowing over the roof. Below this point the flow travels down the front face of the cube until it reaches the ground level. As the flow moving down the front of the cube has more kinetic energy than the incident wind at this level it is able to move upstream against the incident wind. Eventually all the kinetic energy of the flow is exhausted in working against the incident flow and the vortex is formed in front of the building as the air rolls up next to the ground. The existence of this vortex has a marked effect on the distribution of pressure on the windward face. This frontal vortex facilitates formation of the horseshoe vortex at the sides of the building (Cook 1986a).

The existence of the frontal vortex, due to the ABL incident flow, has the effect of bringing faster airflow to ground from higher up the front face of the cube (see Figure 4). Air entering this vortex escapes around the sides of the cube resulting in significantly faster air flow at near ground level than found in the incident wind at this level. This results in a vortex forming around the front and sides of the cube which has a horseshoe shape and is thus termed a horseshoe vortex. This in turn causes high suction pressures at the upwind edge of the side face and high values of lateral diffusion in the wake of the building (Castro and Robbins 1977).

For the roof of the building with a uniform incident wind the flow from the full height of the building rises over the roof and does not reattach (see Figure 5).

For the boundary layer incident wind case, only the flow from the upper third of the cube rises over the roof. This effect combined with the increased mixing effect of the higher levels of turbulence tends to make the flow reattach at some point along the roofline (see Figure 6).

For a cube skewed to the incident wind the flow separating at the upwind corner will tend to be displaced under the flow separating immediately downwind of the corner. The net effect is that the vorticity of the flow is increased until a strong conical vortex is formed (shown in Figure 7) resulting in very high negative pressures. If the cube is skewed to the flow by 45° then a symmetrical pair of vortices will occur. If this is not the case then the vortices will be of different strengths.

The flow in the wake of a surface mounted cube is defined by flow recirculation (see Figure 8) along with unsteady fluctuating pressures and Karman's vortex street.

2.2.3 Codes of Practice

The structural designer or wind engineer must be able to produce designs that will safely withstand the wind loads produced by the prevailing weather systems and by the effects of the ABL and surrounding topography. At present there are two wind loading codes of practice available in the UK, as will be briefly detailed in the following:

CP3 Chapter V part II 'Codes of Basic Data for the Design of Buildings 1972.'

This code is generally accepted as being one of the first wind loading codes of practice available and was completed prior to major advances in the understanding of the atmospheric wind. As such the loading model employed by this code is a simplified version of the earliest available model for the action of turbulent wind, the quasi-steady technique simplified to the equivalent steady gust model (see Cook (1986a) and (1986b) for details). Very briefly this model assumes that the crosswind and vertical turbulence terms can be disregarded. This leads to the modelling of the atmospheric turbulence as temporary variations of incident wind speed with no changes of azimuth or elevation angle (Cook 1986a). Therefore the code tends to mix conservatism in some sections of the wind speed estimation along with significant under estimation of the effects of topographical features. Furthermore, the code does not take account of the effects of upwind terrain changes or fetch which have marked effects on wind speeds. Finally Eaton and Newbury (1972) state that, due to the increasing complexity of structures, this code no longer covers the full range of building designs that are now available.

BS6399 part 2, 1997 'Code of Practice for Wind Loads.'

This code represents the most recent method of determining wind speeds for any given site in the UK. BS6399 is generally superior to the code it supersedes CP3 Chapter V part II, as it accounts for the upwind fetch and fetch changes, topographical features, directional wind speeds and a far greater range of building shapes and designs. Furthermore, the wind speed data used in this code was prepared by using the maximum wind speed during every period of windy weather as opposed to the analysis of a series of annual maximum wind speeds. Consequently the amount of

available data was greatly increased which in turn allowed directional and seasonal characteristics of the UK wind climate to be examined (BS6399 1997).

2.2.4 Wind Damage Costs

In order to highlight the importance and need for greater understanding of the subject of wind engineering it is worth briefly discussing the financial costs that can be incurred as the result of wind storms (see Table 1).

Windstorm event	***Country***	***Cost to insurers £ Million***
Winter Storm (1987)	Great Britain	1100
Hurricane 'Gilbert' (1988)	Jamaica	417
Hurricane 'Hugo' (1989)	USA	2617
Winter storms (1990)	Germany	1035
	Great Britain	2370
	Netherlands	600

Table 1: Wind damage costs (Windstorm 1990)

The fact that the 1990 winter storms in the UK were almost as costly as the damage caused by Hurricane Hugo in the USA gives an indication of the scale of the wind induced damage that may occur. More importantly consideration must be given to the injuries and deaths caused by the effects of the wind and structural damage which are not shown here. In addition, data accumulated over more than 30 years has shown that the incidence of high winds and wind storms in Britain and around the world has increased significantly in the last 10 years and is continuing to do so (Windstorm 1990). To a certain extent climatic fluctuations are responsible for this increase in the extremes in the weather, for example the El-Nino phenomenon. Nevertheless it is becoming evident that human intervention in the balance of nature is causing a general change of environmental conditions. This has resulted in climatic change and more extreme weather conditions and thus increased wind induced structural damage, injury and loss of life.

2.3 Computational Wind Engineering (CWE)

The preceding sections have briefly demonstrated the complexity of the atmospheric wind and the ensuing financial and human costs incurred from wind induced failures. These facts, therefore, highlight the need to be able to accurately assess the effects of

the atmospheric wind on ground based structures and the requirement for further research in this field.

In order to improve our understanding of how the ABL interacts with complex ground based shapes engineers and scientists have for many years studied the results of full-scale and wind tunnel tests, the results of which have increased our knowledge of wind engineering to its present level. Although much is known about the interaction of wind and surface based structures there is obviously still a good deal to learn. While it is apparent that the traditional methods will dominate for many years to come, it is also clear that new technology and techniques should be used whenever possible to aid the advancement of knowledge. Traditionally, as is the case in wind engineering, research in structural analysis and design has centered on experiments in the laboratory. The advent of the electric computer, arguably one of the most important discoveries of the 20^{th} century, has brought about a revolution in this field allowing quick, accurate and low cost analysis of structural elements. This new technique is well proven in structural analysis and has now become a major design tool comparable to, if not exceeding, the use of full-scale experimental apparatus.

Since the first application of CFD to wind engineering approximately 15 years ago the overall progress in CWE has been a good deal slower. This is mainly due to a combination of the need for large computing power and a poor understanding of the physics of fluid flow, namely the phenomena known as turbulence and how it can be modelled. These problems associated with the numerical solution of fluid flow are unfortunately further highlighted when we apply this technique to wind engineering flows due to the highly turbulent nature of the ABL, the non-aerodynamic 'bluff bodies', as discussed, and the need for large computational domains for external flow fields.

2.3.1 The Beginnings of CWE – 1980's and early 1990's

The very first use of CFD in wind engineering occurred in the mid to late 1980's by Summers et al (1986), Matthews (1987) and Murakami and Mochida (1988) with the application of the standard *k-e* model to flows around building shapes. Early attempts at large eddy simulation in wind engineering (see section 5.7 and chapter 7) were also undertaken as early as 1987 by Murakami et al (1987). These tests were in fact the first to fully analyse the results of a simulation that involved flow impingement and thus showed the fundamental flaws in the standard *k-e* model based on the isotropic

eddy viscosity model, as described in section 4.2.3. This ‘early’ discovery initiated one of the most attractive research targets since the start of CFD that of improved turbulence modelling. The main areas of interest included the following:

1. the improvement of the standard *k-e* model and the introduction of a more sophisticated Reynolds Averaged Navier-Stokes (RANS) models

2. the development of easier methods for applying LES to CWE problems (Murakami and Mochida 1999).

The results of this intense research effort to improve the application of CFD to wind engineering, or to engineering applications in general, have included a number of new turbulence models. These range from ad-hoc modifications to the *k-e* model to more advanced RANS models such as the differential stress model, many of which have been fully tested as part of this project. In addition new large eddy simulation techniques have allowed for significant improvements in the predictive accuracy of CFD when applied to wind engineering. Invaluable work over the past 15 years by researchers and academics such as Leschziner, Speziale, Launder, Rodi and Murakami, from many different engineering disciplines, have significantly contributed to improving the accuracy and applicability of CFD techniques.

Unfortunately, although CWE has progressed a long way from the ‘early days’ of the 1980’s, there is still a long way to go before the same confidence can be placed on CWE as with finite element analysis in structural engineering. There are still many problems in CWE, including errors in wall boundary conditions and near wall functions, and although much has been achieved the biggest problem is still that of turbulence modelling in the highly turbulent and complex flow fields encountered.

Nevertheless, even at the current stage of development, the theoretical advantages of ‘virtual’ computer based ‘full scale’ tests such as the ones undertaken in this project are significant. So much so that according to Murakami and Mochida (1999) CWE has evolved into a powerful tool for analysing wind engineering flow fields.

Generally the benefits brought about by the use of CFD in other engineering disciplines have proved a strong incentive to improve the performance of CFD in wind engineering. The eventual aim of all CFD wind engineering researchers it to be able to exactly match a computational solution to the real situation. While it is unclear at this time whether or not this goal will ever be achieved, it is apparent that continued

research is required to, at the very least, attain success in CWE comparable to that found in, say, aeronautical engineering where CFD is routinely used. As such the author is of the opinion that the work detailed in the following chapters is very useful to the wind engineering community in attempting to offer possible improvements to the problem of turbulence modelling and therefore advancing the use of CFD in wind engineering.

3. Solution Procedures and Numerical Methods.

3.1 Introduction

The aim of this chapter is to introduce the reader to the methods and concept of numerical analysis of fluid flow. Firstly, there is a brief introduction to the equations of fluid motion and the simplifications and techniques used to account for turbulence. This is followed by a description of the discretisation schemes whereby the governing differential equations are transformed into their corresponding numerical analogues. A number of common differencing schemes for the convection terms and the associated numerical problems are also reviewed.

3.2 The Navier-Stokes Equations

The numerical solution of any fluid flow problem requires the solution of the general equations of fluid motion, the Navier-Stokes and the continuity equations. Fluid flow problems are described mathematically by these equations which are a set of coupled non-linear partial differential equations with appropriate boundary conditions. These equations are derived from Newton's Second Law and describe the conservation of momentum in the flow.

The general form of the three dimensional incompressible instantaneous Navier-Stokes equations is as follows, in Cartesian tensor form:

$$\frac{\partial(\rho u_i)}{\partial t} = -\frac{\partial(\rho u_i u_j)}{\partial x_j} - \frac{\partial P}{\partial x_i} + \frac{\partial}{\partial x_j}\left[\mu\left(\frac{\partial u_i}{\partial x_j} + \frac{\partial u_j}{\partial x_i}\right)\right] + F \qquad (3.1)$$

acceleration term	convection term	pressure gradient	effects of viscosity	body force

and the continuity equation:

$$\frac{\partial \rho}{\partial t} + \frac{\partial \rho u_i}{\partial x_i} = 0 \qquad (3.2)$$

Refer to the nomenclature page for details of the individual terms.

For full details of the derivation of these equations the interested reader is referred to Young (1989).

For low speed laminar flows without heat transfer the equations detailed above can be used to describe the flow exactly. However, in turbulent flows the velocity components vary rapidly in both time and space and difficulties arise in the numerical discretisation of the flow field as briefly described in chapter 1. Furthermore, there is a major problem in simply representing or modelling turbulence. This is due to the fact that turbulence is an extremely complex and little understood phenomena which is defined by a number of highly complex mechanisms including irregularity, diffusivity, three dimensional vorticity fluctuations and dissipation. A brief introduction to turbulence theory follows; for a detailed description the interested reader is referred to Tennekes and Lumley (1972).

Experiments conducted on fluid flow have shown that for Reynolds numbers below a 'critical' value the flow is found to be smooth and ordered as adjacent layers of the fluid slide past each other, the flow is said to be laminar and the viscosity of the fluid dominates. Above the value of the critical Reynolds number the flow state changes to include more or less random fluctuations superimposed on the mean flow direction and the flow effectively becomes turbulent as the momentum of the fluid increases.

The length scales or eddy sizes in a turbulent flow are bounded by the dimensions of the flow field and by the diffusive action of molecular viscosity. Therefore turbulent flows are characterised by many different velocity and length scales. The largest eddies do most of the 'work' in the flow field by transferring momentum and contaminants at rates up to several orders of magnitude greater than that by molecular diffusion (Launder 1972). These large turbulent eddies interact with and extract energy from the mean flow by a process called vortex stretching. In turn eddies of a smaller size are stretched by larger eddies and less by the action of the mean flow. This process continues with smaller and smaller eddies until all the energy extracted from the mean flow by the largest eddies is handed down to the small scale dissipative eddies. This process, where the kinetic energy is effectively passed down from the largest to the smallest eddies, is termed the energy cascade.

The effect of viscosity dictates the scale of the smallest eddies as an equilibrium is reached whereby the ability of the eddy to perform work against the action of viscosity is matched by the dissipative action of the fluid viscosity. The energy of the rotational eddies is therefore dissipated into thermal energy. These small scale eddies

are of the Kolmogorov length. It is believed that the structure of the small scale eddies at high Reynolds numbers, away from the near wall region, is isotropic as the diffusive action of viscosity tends to smear out directionality. This is contrasted to the largest scale eddies which, due to the fact that they interact strongly with the mean flow, are believed to be highly anisotropic in nature (Tennekes and Lumley 1972).

The most accurate way to model fluid flow numerically is direct numerical simulation (Murakami 1997) (see section 5.6) which involves discretising the equations at a mesh size below the Kolmogorov length scale and applying Equation 3.1 along with suitable wall boundary conditions to the whole flow field. Unfortunately for practical wind engineering flows this is well beyond the capabilities of present day computers. Therefore to reduce the amount of computational effort the effect of turbulence has to be modelled. The starting point in this modelling process is to make the assumption that the velocity at a given point in space and time can be made up of the superposition of some mean velocity which varies slowly with time and a random component that varies rapidly (Shaw 1989).

Therefore the instantaneous velocity component u can be described as:

$$u = \overline{u} + u' \tag{3.3}$$

Refer to the nomenclature page for details of the individual terms.

To incorporate the effects of turbulence on the mean flow, Equation 3.3 is substituted into Equations 3.2 and 3.1 and integrated over time to obtain the mean flow equations. As the fluctuating components are random and do not show any preferential direction the integrals over time will be zero for the linear terms in the continuity and momentum equations. The convective terms in the momentum equation are in fact non-linear being the product of velocity and derivatives of the velocity component. As such the convective terms generate extra higher order terms for the products of fluctuating components. These terms are referred to as the Reynolds stresses.

3.3 The Reynolds Stresses

Proceeding with the averaging process results in the instantaneous values being replaced with the mean variables except for the case of the convection transport term.

Referring to the convection term, (in Equation 3.1) the substitution of the fluctuating component of velocity results in:

$$\begin{aligned}\overline{u_j u_i} &= \overline{(\bar{u}_j + u'_j)(\bar{u}_i + u'_i)} \\ &= \overline{\bar{u}_j \bar{u}_i} + \overline{\bar{u}_j u'_i} + \overline{u'_j \bar{u}_i} + \overline{u'_j u'_i} \\ &= \overline{\bar{u}_j \bar{u}_i} + \overline{u'_j u'_i}\end{aligned} \qquad (3.4)$$

(Launder 1994)

where the over-bar indicates mean values per unit time.

Thus the time averaged equation of fluid motion becomes:

$$\frac{\partial(\rho \bar{u}_i)}{\partial t} = -\frac{\partial(\rho \bar{u}_j \bar{u}_i)}{\partial x_j} - \frac{\partial \bar{P}}{\partial x_i} + \frac{\partial}{\partial x_j}\left[\mu\left(\frac{\partial \bar{u}_i}{\partial x_j} + \frac{\partial \bar{u}_j}{\partial x_i}\right) - \rho \overline{u'_i u'_j}\right] + F_i \qquad (3.5)$$

(Launder 1994)

Equation 3.5 is generally referred to as the Reynolds equation and differs from the equation describing a laminar flow only by the presence of the term containing averaged products of fluctuating velocity. The process it represents is the additional transfer of momentum due to turbulent fluctuations. The first term in the brackets is the viscous term and the second term $\rho \overline{u'_i u'_j}$ is the turbulent stress or the Reynolds stress tensor.

$$\overline{u_i u_j} = \begin{bmatrix} \overline{u'u'} & \overline{u'v'} & \overline{u'w'} \\ \overline{v'u'} & \overline{v'v'} & \overline{v'w'} \\ \overline{w'u'} & \overline{w'v'} & \overline{w'w'} \end{bmatrix}$$

where $\tau_{xx} = -\rho \overline{u'^2}$

$\tau_{yy} = -\rho \overline{v'^2}$)- Three normal stresses

$\tau_{zz} = -\rho \overline{w'^2}$

$\tau_{xy} = \tau_{yx} = -\rho \overline{u'v'}$

$\tau_{xz} = \tau_{zx} = -\rho \overline{u'w'}$)- Three shear stresses

$\tau_{yz} = \tau_{zy} = -\rho \overline{v'w'}$ (3 symmetrical pairs)

The convention used to describe the Reynolds stresses is detailed on Figure 9.

In turbulent flows the normal stresses are always non-zero because they contain squared velocity fluctuations. The shear stresses are associated with correlations between different velocity components.

It is therefore the main aim of the turbulence model to predict the effect of these Reynolds stresses on the mean flow. Consequently the next step in the turbulence modelling process is the formulation and application of a suitable model that can accurately represent these stresses over a range of flow fields, see chapter 4 for further details.

3.4 Common Discretisation Schemes

As digital computers are only able to process digital data the partial differential equations that describe fluid flow, detailed in the previous sections, need to be transformed into an appropriate form. This process of transforming a partial differential equation to a numerical analogue of the equation is called discretisation. There are a variety of techniques available to do this as follows:

1. the finite difference method
2. the finite element method
3. the finite volume method
4. spectral methods.

These methods are described in detail by Versteeg and Malalasekera (1996), Smith (1978), Zienkiewicz and Taylor (1989) and Patankar (1980). The first three of these methods are generally similar, modified for application to certain classifications of partial differential equations (see Smith 1985) used in different engineering fields.

The finite volume method is in fact the most popular discretisation technique used in CFD applications and is a mixture of the finite difference and finite element techniques. The basic theory behind these techniques is to build a tool kit of equations that describe the derivatives of a variable as the difference between successive values of the variable at various points, elements or volumes in space or time. For example, for the finite difference method:

Using a truncated Taylor series expansion, the value of U at the point $x + h$ and $x - h$ is equal to (see Figure 10):

$$U(x+h) = U(x) + h\frac{\partial u}{\partial x} + \frac{h^2}{2}\left(\frac{\partial^2 U}{\partial x^2}\right) + \frac{h^3}{6}\left(\frac{\partial^3 U}{\partial x^3}\right) + \ ..... \qquad (3.6)$$

$$U(x-h) = U(x) - h\frac{\partial u}{\partial x} + \frac{h^2}{2}\left(\frac{\partial^2 U}{\partial x^2}\right) - \frac{h^3}{6}\left(\frac{\partial^3 U}{\partial x^3}\right) + \ ..... \qquad (3.7)$$

where;

h = small displacement.

(Shaw 1989)

Obviously by manipulating these equations terms can be produced for the first and second derivatives of the function U purely in terms of the x and h as follows:

$$\frac{\partial^2 U}{\partial x^2} = \frac{U(x+h) - 2U(x) + U(x-h) + \ O(h^2)}{h^2} \qquad (3.8)$$

(Shaw 1989)

There are many techniques to obtaining the differencing formula. The method above would be classed as a central difference formula. Additionally, the differences can be assessed with reference to a known value prior to or after the value to be assessed, in terms of positive displacement h. These methods are thus termed backward and forward differencing.

The finite volume method was originally developed as a special finite difference formulation. Using this method the partial differential equation representing the conservation principle for a flow variable over an infinitesimal control volume is discretised to simply express the same principle over a finite control volume (Patankar 1980). As such the domain of interest is divided into a number of non-overlapping control volumes such that one control volume surrounds each nodal point. The boundaries of the control volumes are usually placed midway between adjacent nodes. Physical and control volume boundaries are also matched. The procedure that distinguishes the control volume method from the finite difference technique is the control volume integration. The differential equation expressing the variation of a flow variable is integrated over each control volume. The resulting discretised equation expresses the exact conservation of the relevant properties for each finite cell

size. For example the conservation of a general flow variable within a finite control volume can be expressed as a balance between the various processes tending to increase or decrease it:

Rate of change of flow variable in control volume w.r.t. time	=	net flux of variable due to convection into control volume	+	net flux of variable due to diffusion
	+	net rate of creation of variable inside the control volume.		

(Versteeg and Malalasekera 1996)

Values of the properties of flow variables are defined and evaluated at the nodal points. To calculate gradients and hence fluxes at the control volume faces an approximate distribution of properties between nodal points is used. Therefore interpolated values of the diffusion coefficient at the control volume faces as well as diffusive flux terms and source terms are substituted into the integral form of the partial differential equation expressing the flow field for each of the control volumes. This is repeated for all nodal points in the domain with modifications for control volumes adjacent to the domain boundaries. The result of this procedure is a system of linear algebraic equations which are solved through iterative solution procedures to obtain the distribution of the flow property at all nodal points (see section 3.6.1) (Versteeg and Malalasekera 1996).

Finally, spectral methods approximate the unknowns by means of truncated Fourier series. Unlike the above-mentioned approaches the approximations are not local but valid throughout the computational domain. As a consequence it is reported that this method is not used in CFD applications as there are difficulties in applying the technique to flows with complex geometries (Versteeg and Malalasekera 1996). The interested reader should refer to Gotlieb and Orszag (1977) if further information is required.

3.5 Common Differencing Schemes - Discretisation of the Convection Term

Disregarding the continuity equation, all of the equations solved by CFD packages have the same general form which includes fluid flow processes such as transient, convection, advection, diffusion and source terms.

$$\frac{\partial \rho f}{\partial t} + . \frac{\partial \rho u_i f}{\partial x_i} - \frac{\partial}{\partial x_i}\left(\Gamma \frac{\partial f}{\partial x_i} \right) = S \qquad (3.9)$$

Where Γ is the relevant effective diffusivity for a variable ϕ. If an integration of Equation 3.9 is performed using Gaus's law where a volume integral is transformed into a surface integral the following equation is obtained:

$$\int \frac{\partial \rho f}{\partial t} \partial V \quad + . \int \rho u_I f dA_i \quad - \int \Gamma \frac{\partial f}{\partial x_i} dA_i \quad = \int S dV \qquad (3.10)$$

Time dependant. *Convection.* *Diffusion.* *Source.*

The differencing scheme for each term can then be selected to match its physical characteristics. For example, the diffusion term, which affects the distribution of a transported quantity along its gradients in all directions, is usually dealt with by second order centered differencing (see section 3.5.1).

Conversely the convection term in the general equation spreads influence only in the flow direction as fluid properties are convected downstream. Therefore the size of the grid cells and the accuracy and properties of the differencing scheme becomes of rather more importance. As a consequence, differencing schemes which favour upstream values are preferred.

In theory the numerical results obtained using any differencing scheme should be indistinguishable from the exact solution for an infinite number of cells. This follows from the consideration that, as the grid points move closer together the change in the variables between neighbouring grid points becomes smaller and actual details of the profile assumption become unimportant. In practice only a finite number of cells are possible and the differencing schemes have their own unique properties as different interpolation techniques between neighbouring nodes are employed. Therefore to a large degree this term determines the accuracy of the solution to the solved equations.

In Computational Fluid Dynamics the differencing schemes should have certain fundamental properties for them to produce physically realistic results. These properties are known as conservation, boundedness, transportiveness and accuracy.

Conservation

This property ensures global conservation of the fluid properties for the entire domain. This is a very important property and is achieved by means of consistent expressions for fluxes through the cell faces of adjacent control volumes in the finite volume scheme (Versteeg and Malalasekera 1996). This is an important consideration when different schemes are used to discretise the diffusion and convection terms.

Boundedness

The boundedness property is akin to stability and requires that in a linear problem without sources the solution is bounded by the maximum and minimum boundary values of the flow variables (Versteeg and Malalasekera 1996). Very simply, if the boundary temperatures of a problem are 500 and 200 degrees then the interior values of temperature should be less than 500 and greater than 200 degrees.

Transportiveness

Flow processes contain effects due to convection and diffusion. In diffusion phenomena, such as heat conduction, a change in temperature at one location affects the temperature in more or less equal measure in all directions around it. Convective phenomena influences exclusively in the flow direction so that a point only experiences effects due to changes at upstream locations. The transportiveness property is a measure of the ability of the scheme to recognise the direction of flow. The measure of these relative strengths are defined by the local cell Peclet number (Versteeg and Malalasekera 1996). Differencing schemes dealing only with diffusion will not require this property.

Accuracy

Classically the accuracy to which convection and diffusion terms are approximated is judged via the truncation terms of the Taylor series expansion hence the ‘order’ of the scheme, although it should be noted that other features of the differencing schemes make the assessment of accuracy less straight forward (Patankar 1980). For example

equation 3.8 is termed second order accurate as terms higher than second order are truncated.

The following differencing schemes, which represent the most popular high and low order schemes, will be discussed in terms of their suitability in dealing with the convection terms.

In the control volume notation our attention is focused on a general node P with the neighbouring nodes identified by W and E with the control volume faces denoted by w and e. Further detail is given in Figure 11.

3.5.1 The Central Differencing Scheme

Many commercial CFD packages use this scheme for evaluation of the diffusive fluxes. Generally this scheme is not appropriate for use in dealing with the convection term in wind engineering simulations or indeed any high Reynolds number flow as it is only stable and accurate for local cell Reynolds numbers of less than 2. For a given viscosity the velocity must be very low or the grid size very small to achieve such a Reynolds number. In addition, this scheme does not possess the transportiveness property (Versteeg and Malalasekera 1996). The accuracy of the central differencing scheme in terms of the Taylor series truncation error is second order. For further information see Abbott and Basco (1989).

Referring to Figure 11, for a uniform grid we can write the west cell face property as:

$$f_w = (f_P + f_W)/2 \tag{3.11}$$

3.5.2 The Upwind Differencing Scheme

When the flow is in a positive direction, the west cell face is simply deduced from:

$$f_w = f_W \tag{3.12}$$

This scheme satisfies the requirements of conservativeness, boundedness and transportiveness. Accuracy is said to be first order in terms of the Taylor series truncation error. One particular drawback with upwind differencing is apparent when

the flow direction is not aligned with the grid lines. This resulting error is often termed false diffusion and is found to dominate the physical diffusion whenever the Peclet number exceeds two, refer to Patankar (1980) for full details. It has been found that when the leading term of the truncation error is an even order derivative the numerical solution will appear to have an extra viscosity. A very simple explanation of this effect can be given upon referring to the Navier-Stokes equations in section 3.2. These equations have terms such as $\frac{\partial^2 u}{\partial x^2}$ multiplied by the coefficient of viscosity, μ, which represents the dissipative effect of the physical viscosity on the flow. The even order derivatives in the finite difference formula also act as a dissipative term much like the viscous terms in the Navier-Stokes equations. However this is a consequence of numerical discretisation and as such is purely of numerical origin (Anderson 1995). This artificial viscosity has the effect of increasing the stability of a simulation by reducing high flow gradients due to the artificially high viscosity generated. Unfortunately this effect also makes the scheme inaccurate.

3.5.3 Hybrid Differencing Scheme (Spalding 1972)

This differencing scheme is a combination of the central and upwind differencing schemes reviewed earlier. Below local cell Reynolds numbers or Peclet numbers of 2 the central differencing scheme is used, above this value the upwind differencing scheme is utilised. For computationally economical numbers of grid nodes used in wind engineering applications the hybrid scheme defaults to the upwind scheme as the Peclet number is greater than 2. The same accuracy limitations as previously explained for the upwind scheme apply here although minor modifications and improvements have been made, refer to Patankar (1980) for further details.

3.5.4 QUICK -Quadratic Upstream Interpolation for Convective Kinetics (Leonard 1979)

In order to increase the accuracy of a differencing scheme it is necessary to involve more neighbouring points and effectively bring in a wider influence of the surrounding variables to deduce the next value of the dependent variable. In the example given in section 3.4 the value of U at the point x was determined from two neighbouring points. By increasing the number of neighbouring points it is possible to reduce the discretisation errors. Linear interpolation between points is therefore no

longer a possibility. The next higher order interpolation, quadratic, is employed to join the extra nodal points. Using the finite volume method the QUICK scheme approximates the face value by quadratic interpolation between the immediately adjacent nodal values and the next nearest upstream nodal value. This scheme has many benefits as it satisfies the requirements of conservativeness and transportiveness with third order accuracy in terms the Taylor series truncation error and it is not affected by numerical viscosity (Lau 1987). However the QUICK scheme can cause instabilities in a numerical simulation due to the fact that under and over shoots can occur, as this scheme does not posses the boundedness property discussed earlier. In complex turbulent flow fields such as those found in wind engineering the QUICK scheme can sometimes lead to negative turbulence which is unphysical.

For a uniform grid the west cell face property is as follows:

$$f_w = \frac{3}{8} f_P + \frac{6}{8} f_W - \frac{1}{8} f_{WW} \tag{3.13}$$

3.5.5 CCCT - Curvature Compensated Convective Transport Scheme (Gaskell and Lau 1988)

As a consequence of the quadratic profile the interpolation may overshoot the physical boundary of the solution domain (see Figure 12). This problem led to the development of the CCCT algorithm that maintains the beneficial features of the QUICK scheme whilst providing boundedness and hence computational stability. Rather than interpolating with a quadratic profile the scheme uses a monotonic profile as shown in Figure 13.

The CCCT scheme has:

$$f_w = \left(\frac{3}{8} - a\right) f_P + \left(\frac{3}{4} + 2a\right) f_W - \left(\frac{1}{8} + a\right) f_{WW} \tag{3.14}$$

Where α depends on the curvature of the variable ϕ. The scheme is then treated like the QUICK scheme, refer to Gaskell and Lau (1988) for further details.

3.6 Calculation of the Flow Field and Pressure Correction

The solution of the momentum transport equations presents us with a number of problems, further to those already highlighted, as follows:

1. The convection terms in the momentum equations that are derived from the acceleration of a patch of fluid, contain non-linear quantities.

2. All three-momentum equations are intricately coupled because every velocity component appears in each momentum equation and the continuity equation. The most complex issue to resolve is the role played by the pressure. It appears in all the momentum equations, but there is no equation for pressure.

Both these problems are associated with the non-linearities in the equation set. The pressure velocity linkage can be resolved by adopting an iterative solution strategy such as the SIMPLE algorithm (Patankar and Spalding 1972). In this algorithm the convective fluxes per unit mass through the cell faces are evaluated from so called guessed velocity components. Furthermore, a guessed pressure field is used to solve the momentum equations and a pressure correction, deduced from the continuity equation, is used to update the velocity and pressure fields. The iteration is started by the use of an initial guess and proceeds until the accuracy of the initial guess is improved sufficiently.

Full details of this method and the related problems which facilitate the need for staggered grids and the Rhie and Chow (1983) algorithm can be found in Patankar (1980).

3.6.1 Solving the Simultaneous Equations

In most cases, using commercial CFD codes, the discretised equations produced from the partial differential equations are given in implicit form (for a full discussion on implicit and explicit schemes see Shaw (1989)). When implicit schemes are used a set of simultaneous equations are generated consisting of many individual equations. The solution of these equations is very computationally intensive and as such a good deal of work in the CFD community has focused on finding efficient solution techniques. Techniques of solving the equations used in commercial CFD codes include Jacobi and Gauss-Seidel methods including point relaxation and line relaxation techniques.

Advanced methods include Stones Strongly Implicit Procedure and matrix manipulation method. All these schemes are detailed in full in Smith (1978), Hirsch (1990), Abbott and Basco (1989) and Patankar (1980). One advanced method of solving the simultaneous equations that is now very popular in the CFD community is the multi-grid method. The philosophy behind this method is that the early iterations are carried out on a fine grid and then progressively transferred to a series of coarser grids. Since the coarser grids have less grid points fewer calculations are needed for a given sweep (see section 3.6) of the flow field and the computational effort is reduced. The results on the coarser grid are then transferred back to the fine grid and the process is repeated a sufficient number of times until satisfactory convergence (see section 3.6) on the fine grid is obtained (Anderson 1995). In mathematical terms this method is able to more effectively damp the numerical errors as errors in a flow field of wavelength approximately equal to the size of a cell are reduced much more quickly. It is stated that by transferring the results from a fine grid to a series of coarser grids the errors are more readily damped and faster solution convergence is possible (Anderson 1995).

3.7 Summary

In this chapter the reader has been introduced to the basis of numerical fluid flow calculations, the Navier-Stokes equations and the method of simplifying the effects of turbulence resulting in the Reynolds stresses. Discussion has been presented on the methods of discretising the partial differential equations, with special attention paid to the treatment of the convection term. Finally, other important issues such as treatment of the pressure term and solution procedures for the simultaneous equations have been briefly discussed with suitable references offered for further reading.

4. Turbulence Modelling

4.1 Introduction

> ‘Engineering fluid mechanics is dominated by the fact that in most situations of interest the fluid motion exhibits a chaotic non repeating unsteadiness known as turbulent motion. At an engineering level the flows are too complex for the details of turbulence to be resolved. Instead the equations of motion are averaged over a time period producing what are known as Reynolds equations. The approximate representation of these Reynolds stresses in the Reynolds equations in terms of known or calculable quantities is known as turbulence modelling’ (Launder 1989, p2).

The reader has previously been introduced to the Navier-Stokes equations (see section 3.2) and the necessity to make assumptions regarding these equations to allow for calculations of turbulent flow. Nonetheless, the procedure of time averaging these equations results in an additional set of terms, the Reynolds stresses, that have to be accurately represented in some way. Whereas the original instantaneous Navier-Stokes equations for laminar flow can be closed when the appropriate initial and boundary conditions are prescribed, the time-averaged equations unfortunately cannot. This is defined as the closure problem whereby further equations are required to tie the Reynolds stress tensor to the mean flow equations. The level of closure adopted refers to the number of supplementary transport equations required to achieve closure of the Reynolds equations. This can include a number of turbulence modelling practices that account for the convective and diffusive transport parameters including, kinetic energy, turbulent vorticity and the Reynolds stresses themselves.

Accurate representation of the effects of the Reynolds stresses in the time averaged Navier-Stokes equations is one of the most important aspects of a successful and realistic CFD simulation. Therefore it is the aim of this chapter to cover the general theory behind the most popular and widely available turbulence models, used at the present time, and to undertake a critical analysis of each of the models using the available published information.

4.2 Reynolds Averaged Navier-Stokes Equations (RANS)

The ensemble or time averaged form of the Navier-Stokes equations are called the Reynolds Averaged Navier-Stokes equations (RANS). These models calculate a mean, steady state velocity and pressure field and account for the velocity and pressure fluctuations through additional modelled variables. These equations express only the movement of large scale eddies thus allowing the use of coarse grids and making the models relatively economical to use. A number of models are available under this general heading which range from closure models based on the eddy viscosity concept to full second moment closure models which represent the effect of each component of the Reynolds stress tensor on the mean flow.

4.2.1 The Eddy Viscosity Concept

There are many theories regarding turbulence attributed to a number of researchers in the 19th and 20th centuries. Early discoveries by Reynolds drew an analogy between momentum transfer and the transfer of heat and matter for turbulent motion. Taylor (1921) and (1938) provided the earliest theoretical and mathematical explanation for the highly diffusive nature of turbulence. The pioneering work of Kolmogorov (1941) led to a greater understanding of how turbulence interacts with the mean flow, the energy cascade and its dissipation. In terms of the turbulence modelling perhaps the most important research is attributed to the earliest worker in this field, Boussinesq (1877), who postulated that the Reynolds stresses should be proportional to the mean strain rate. This concept is based on the assumption that both the viscous stresses and the Reynolds stresses act on the mean flow in a similar manner. Referring to Equation 3.5, inserted below for clarity, it can be seen that both these stresses appear on the right hand side of the momentum equation.

$$\frac{\partial(\rho\bar{u}_i)}{\partial t} = -\frac{\partial(\rho\bar{u}_j\bar{u}_i)}{\partial x_j} - \frac{\partial \bar{P}}{\partial x_i} + \frac{\partial}{\partial x_j}\left[\mu\left(\frac{\partial \bar{u}_i}{\partial x_j} + \frac{\partial \bar{u}_j}{\partial x_i}\right) - \rho\overline{u_i' u_j'}\right] + F_i$$

Furthermore:

> 'In Newton's Law of Viscosity the viscous stresses are taken to be proportional to the rate of deformation of fluid elements' (Versteeg and Malalasekera 1996, p63)

For an incompressible fluid this relationship can be expressed in mathematical terms as:

$$t_{ij} = me_{ij} = m\left(\frac{\partial u_i}{\partial x_j} + \frac{\partial u_j}{\partial x_i}\right) \quad (4.1)$$

(Versteeg and Malalasekera 1996)

Also

> 'It is experimentally observed that turbulence decays unless there is a shear in isothermal incompressible flows. Furthermore turbulent stresses are found to increase as the mean rate of deformation increases.' (Versteeg and Malalasekera 1996, p63)

Therefore, these statements led Boussinesq to propose a linear relationship between Reynolds stresses and the rate of deformation of a fluid linked by a coefficient of proportionality m_t as follows:

$$t_{ij} = -\rho\overline{u_i'u_j'} = m_t\left(\frac{\partial \bar{u}_i}{\partial x_j} + \frac{\partial \bar{u}_j}{\partial x_i}\right) \quad (4.2)$$

(Versteeg and Malalasekera 1996)

Boussinesq's reasoning seems to be logical when one considers that the energy dissipation and transport of mass momentum normal to the flow in laminar flows are all mediated by viscosity. As the effect of turbulence is to greatly increase this process it seems a natural assumption to conclude that an extra viscosity can adequately represent the effects of turbulence (Versteeg and Malalasekera 1996).

The right hand sides of Equations 4.1 and 4.2 are the same except for the coefficient used linking the two sides of the equations. The main difference between these two coefficients is that m is a function of the fluid properties only while m_t is a function of the turbulence.

If Equation 4.2 is substituted into Equation 3.1 then the mean flow equation now has an enhanced additional viscosity m_t due to the turbulence of the flow. Using this approach the modelling process can be completed if the turbulent viscosity can be found from other variables. For a full derivation of the eddy viscosity concept see

Gatski et al (1996). There are a number of methods available of deriving the value of turbulent viscosity as will be briefly detailed in the following sections.

4.2.2 The Mixing Length Model

In the mixing length model it is argued that at a given point and time in the flow field turbulence can be characterised by a single representative velocity scale and length scale. Hence the turbulent viscosity is expressed in terms of these two scales as a function of position as follows:

$$m_t = rC_m l^2 \left(\frac{\P\overline{u}}{\P y} + \frac{\P\overline{v}}{\P \mathrm{x}} \right) \qquad (4.3)$$

(Launder 1972)

The mixing length model is of use if the convection and diffusion of turbulent properties can be neglected (Versteeg and Malalasekera 1996). In fact these properties are very important for wind engineering flow fields, which include recirculatory flows. Consequently more complex statements are required involving fluid transport equations which may express these effects in terms of the dynamics of the turbulence. Full details of the mixing length model can be found in Lectures in Mathematical Turbulence by Launder (1972).

4.2.3 The Standard *k*-*e* Turbulence Model

The standard *k*-*e* model (Launder and Spalding 1974) has two model transport equations, one for the turbulent kinetic energy of the flow, *k* and one for the dissipation rate of *k*, *e*. These values are used to define the velocity scale and the length scale, at any given point and time in the flow field, representative of large scale turbulence as follows:

$$\text{Velocity scale } J = k^{\frac{1}{2}} \qquad (4.4)$$

$$\text{Length scale } l = \frac{k^{3/2}}{e} \qquad (4.5)$$

where k = turbulent kinetic energy

e = the dissipation of turbulent kinetic energy

From this the eddy viscosity can be specified as follows:

$$m_t = C_m . l . J = r C_m \, k^2 / e \tag{4.6}$$

Inserting the Boussinesq hypothesis into the momentum equation yields

$$\frac{\partial r \bar{u}_i}{\partial t} = -\frac{\partial r \bar{u}_j \bar{u}_i}{\partial x_j} - \frac{\partial \bar{P}}{\partial x_i} + \frac{\partial}{\partial x_j}\left[m_{eff}\left(\frac{\partial \bar{u}_i}{\partial x_j} + \frac{\partial \bar{u}_j}{\partial x_i} \right)\right] \tag{4.7}$$

where;

$$m_{eff} = m + m_t. \tag{4.8}$$

The standard k model equation is obtained by multiplication of the instantaneous Navier-Stokes equations by the appropriate fluctuating velocity components (i.e. x-component equation multiplied by u' etc.) and addition of all the results. This is followed by a repeat of this process on the time averaged Reynolds equations, subtraction of the two resulting equations and substantial re-arrangement yielding the equation for the turbulent kinetic energy k (Tennekes and Lumley 1972). It is also possible to develop similar transport equations, from the Navier-Stokes equations, for other turbulence quantities including the rate of viscous dissipation e. Nonetheless it should be noted that the energy dissipation equation is far more empirical and the modelling of terms is so severe that it is best to regard the entire equation as a model.

The standard k-e model equations are (including Equation 4.7) as follows:

Turbulent kinetic energy

$$r \frac{\partial k}{\partial t} + r \bar{u}_j \frac{\partial k}{\partial x_j} = t_{ij} \frac{\partial \bar{u}_i}{\partial x_j} - re + \frac{\partial}{\partial x_j}\left[\left(m + m_t / s_k \right) \frac{\partial k}{\partial x_j} \right] \tag{4.9}$$

Dissipation rate

$$r \frac{\partial e}{\partial t} + r \bar{u}_j \frac{\partial e}{\partial x_j} = C_{e1} \frac{e}{k} t_{ij} \frac{\partial \bar{u}_i}{\partial x_j} - C_{e2} r \frac{e^2}{k} + \frac{\partial}{\partial x_i}\left[\left(m + m_t / s_e \right) \frac{\partial e}{\partial x_j} \right] \tag{4.10}$$

where $t_{ij} = 2m_t S_{ij} - \frac{2}{3} rkd_{ij}$ = Reynolds stress tensor.

and d_{ij} = the Kronecker delta (1 when $i = j$)

$$S_{ij} = \left(\frac{\partial \bar{u}_i}{\partial x_j} + \frac{\partial \bar{u}_j}{\partial x_i} \right)$$

The various constants in the above equations are necessary due to the numerous simplifications made to the models and are derived from comprehensive data fitting to a wide range of turbulent flow fields (usually wind tunnel data).

To calculate the Reynolds stress tensor in the *k-e* model a revised Boussinesq relationship is used from that shown in Equation 4.2.

$$- r\overline{u_i' u'}_j = m_t \left(\frac{\P \bar{u}_i}{\P x_j} + \frac{\P \bar{u}_j}{\P x_i} \right) - \frac{2}{3} rkd_{ij} \qquad (4.11)$$

(1) (2) (3)

The effect of this extra term (3) added to the Boussinesq relationship is to make the term applicable to the normal Reynolds stresses as the standard hypothesis deals only with shear stresses. This term effectively allocates an equal third of the sum of the normal Reynolds stresses to each normal stress.

The result of the assumptions and simplifications discussed in this section, which result in a isotropic, scalar, description of the eddy viscosity coefficient, m_t, are discussed below.

4.2.3.1 Discussion

Of all the available turbulence models, the *k-e* model is by far the most widely used and has been tested for a vast number of flow fields. It is favoured in industrial applications due to its relatively low computational costs and generally better numerical stability than more complex turbulence models such as the differential stress model (see section 4.2.7). This model has proved a success in many

applications, particularly in confined flows where the normal Reynolds stresses are relatively unimportant. Unfortunately the opposite is true of wind engineering flow fields and the *k*-ε model performs poorly.

It is explained in a number of research papers (Murakami 1997, Murakami et al 1991) that the *k-e* model incorrectly estimates the level of turbulent kinetic energy around a surface mounted cube, in particular at the leading top edge (see chapter 6). This fundamental error results in a poor representation of the flow field and pressure distribution around the cube. In addition, wind tunnel tests have deduced that the streamwise normal stress $u'u'$ dominates in the area of the roof and in the downstream free shear layer. Also the lateral normal stress $v'v'$ dominates $u'u'$, with $w'w'$ the smallest, in the wake recirculation zone, where a Karman vortex street occurs (Murakami 1990). Consequently the turbulent flow field in wind engineering applications is most definitely anisotropic. Therefore the assumption of a simple isotropic eddy viscosity term is insufficient to adequately describe the complexity of a highly anisotropic flow field and results in the *k-e* models failure to accurately predict many turbulent flow fields, not least in wind engineering applications. The main source of error in this model is therefore rooted in the linear Boussinesq approximation and the isotropic eddy viscosity concept.

Full testing of this model and comparison with full-scale data is available in chapter 6.

4.2.4 The Low Reynolds Number *k-e* Model

The equations for this model are only slightly modified from the standard *k-e* model, the main difference is apparent in the treatment of the near wall region. The high Reynolds number *k-e* model reduces the computational effort of a given flow simulation by making use of the universal behaviour of near wall flows (see section 4.3). The low Reynolds number model does not use this method and effectively integrates to the wall surface in the low Reynolds number region of the flow. The standard model therefore has to be revised to effectively force the correct near wall conditions whereby the viscous stresses in the near wall region take over from the Reynolds stresses which are dominant in the flow at a much greater distance from the wall. This is achieved by the use of wall damping functions that multiply the model constants C_m, C_{e1} etc.

For example:

$$m_t = rC_m f_m k^2/e \tag{4.12}$$

where

$$f_m = \exp\left(\frac{-3.4}{(1+\frac{R_T}{50})^2}\right) \tag{4.13}$$

and

$$R_T = \frac{rk^2}{me} \tag{4.14}$$

Further damping functions are applied to the turbulence transport equations. Similar functions can be applied to any of the other models detailed in this section to allow them to resolve the flow in the low Reynolds, near wall region, of the flow.

For further details see Patel et al (1985).

4.2.5 The *k* -*w* Equation Model

This turbulence model, first proposed by Kolmogorov (1941), was in fact the first model of turbulence. The variable *k* is, as usual, the turbulent kinetic energy and *w* is the dissipation per unit turbulent kinetic energy. In the usual manner these two terms are modelled using partial differential equations. The advantage of replacing the *e* equation with the *w* equation is that the second is easier to integrate (more robust) and that it can be integrated through the sub-layer without the need for additional damping functions (Menter and Grotjans 1999)

Eddy viscosity

$$m_t = r\,k/w \tag{4.15}$$

Turbulent kinetic energy

$$\rho \frac{\partial k}{\partial t} + \rho \bar{u}_j \frac{\partial k}{\partial x_j} = \tau_{ij} \frac{\partial \bar{u}_i}{\partial x_j} - \beta^* \rho k \omega + \frac{\partial}{\partial x_j}\left[\left(\mu + \sigma^* \mu_T \right) \frac{\partial k}{\partial x_j} \right] \qquad (4.16)$$

Specific dissipation rate

$$\rho \frac{\partial \omega}{\partial t} + \rho \bar{u}_j \frac{\partial \omega}{\partial x_j} = \alpha \frac{\omega}{k} \tau_{ij} \frac{\partial \bar{u}_i}{\partial x_j} - \beta \rho \omega^2 + \frac{\partial}{\partial x_i}\left[\left(\mu + \sigma \mu_T \right) \frac{\partial \omega}{\partial x_j} \right] \qquad (4.17)$$

(Wilcox 1993)

where

β, β^*, σ etc. are closure coefficients

Although experimental evidence of the performance of this model is relatively scarce, Wilcox (1994) showed that for a two dimensional backward facing step the reattachment length of the recirculation zone was within three percent of the experimentally measured location. This out performed the standard *k*-*e* model, which significantly underestimated the reattachment length. Disadvantages with this model include the fact that the solutions produced are very sensitive to the values specified for *w* at the inlet. Menter has proposed a model that combines the advantages of the *k*-*e* and *k*-*w* models, thereby removing this deficiency (CFX-International 1998).

At present there is little information available on this model and its application to wind engineering flow fields, consequently the author has included this model in tests in chapter 7.

4.2.6 The Renormalisation Group (RNG) *k* - *e* Turbulence Model

An alternative way to derive turbulence closure models was proposed by Yakhot and Orzag (1986). They applied Renormalisation Group theory to the Navier-Stokes equations and derived a two equation *k*-*e* model. Further details of the RNG technique can be found in McComb (1990).

Referring to Equation 4.10, detailing the e equation for the standard k-e model, it can be seen that the only revision to this equation for the RNG model is the inclusion of the extra term C_{1RNG} and the inclusion of revised model constants:

$$r\frac{\partial e}{\partial t}+r\overline{u}_j\frac{\partial e}{\partial x_j}=(C_{e1}-C_{1RNG})\frac{e}{k}t_{ij}\frac{\partial \overline{u}_i}{\partial x_j}-C_{e2}\,r\frac{e^2}{k}+\frac{\partial}{\partial x_i}\left[\left(m+m_t/s_e\right)\frac{\partial e}{\partial x_j}\right] \tag{4.18}$$

where

$$C_{1RNG}=\frac{h\left(1-\frac{h}{h_0}\right)}{(1+bh^3)} \tag{4.19}$$

and

$$h=\left(\frac{P}{m_T}\right)^{1/2}\frac{k}{e} \tag{4.20}$$

h_0 and b are additional model constants.

The remaining equations for this model are identical to the standard k-e model.

4.2.6.1 Discussion

Unfortunately it appears that there is scant information available regarding testing of this model in wind engineering flow fields. Therefore a full test has been conducted by the author to assess the performance of this model, see chapter 6 for further details. Furthermore, although this model has been given impressive reviews by many researchers (refer to Orzag 1994) it is important to remember that it is only a variant of the k-e model and as such is still based on the flawed isotropic eddy viscosity assumption and Boussinesq approximation. In a similar manner to many other models that are modified versions of the standard k-e model it may provide improved predictions for some applications while giving lower accuracy for others.

This basic feature of these models led to a review of a turbulence model that does not employ the eddy viscosity concept to describe the effects of the Reynolds stresses but provides expressions for all the individual components of the Reynolds stress tensor.

4.2.7 The Differential Stress Equation Model (DSM)

A more complex version of the RANS equations is the differential stress model of Launder, Reece and Rodi (1975).

Second moment closure is based on exact transport equations for the individual Reynolds stresses and fluxes derived from the Navier-Stokes equations. The derivation of the Reynolds stress equations, detailed in full by Leschziner (1990), results in a total of nine transport equations, six of which describe the Reynolds normal stresses and shear stresses and a further three which describe the Reynolds fluxes, which for an incompressible fluid gives:

$$\underbrace{\frac{\partial}{\partial x_k}\left(\rho \overline{u}_k \overline{u_i u_j}\right)}_{-\!-\!-\ \rho C_{ij}\ -\!-\!-} = \underbrace{-\rho\left(\overline{u_j u_k}\frac{\partial \overline{u}_i}{\partial x_k} + \overline{u_i u_k}\frac{\partial \overline{u}_j}{\partial x_k}\right)}_{-\!-\!-\!-\!-\ \rho P_{ij}\ -\!-\!-\!-\!-} + \underbrace{\left(\overline{u_i f_i} + \overline{u_i f_i}\right)}_{-\!-\!-\ \rho F_{ij}\ -\!-} + \underbrace{\overline{p\left(\frac{\partial u_i}{\partial x_j} + \frac{\partial u_j}{\partial x_i}\right)}}_{-\!-\ \rho \Phi_{ij}\ -\!-}$$

$$\underbrace{-2\mu\overline{\frac{\partial u_i}{\partial x_k}\frac{\partial u_j}{\partial x_k}}}_{-\!-\!-\ \rho \varepsilon_{ij}\ -\!-\!-} \underbrace{-\frac{\partial}{\partial x_k}\left(\rho\overline{u_i u_j u_k} + \overline{p u_i}\delta_{jk} + \overline{p u_j}\delta_{ik} - \mu\frac{\partial \overline{u_i u_j}}{\partial x_k}\right)}_{-\!-\!-\!-\!-\!-\!-\!-\!-\!-\!-\!-\ \rho d_{ij}\ -\!-\!-\!-\!-\!-\!-\!-\!-\!-\!-\!-}$$

(4.21)

This translates to

ρC_{ij} = ρP_{ij} + ρF_{ij} + $\rho \Phi_{ij}$

Transport of Reynolds stresses by convection — Production of R.S — Stress production or distruction by action of rotational body forces — Redistribution of R.S due to pressure - strain interaction

$-\ \rho\varepsilon_{ij}$ $-\ \rho d_{ij}$

Rate of dissipation by viscosity — Rate of diffusion.

Wilcox (1994) details the individual contents of the equations and lists some of the reasons for improvements over the eddy viscosity models as follows.

Firstly, since the equation automatically accounts for the convection and diffusion of the Reynolds stresses, a second order closure model will include effects of flow history. In turbulent shear flow large bodies of fluid migrate across the flow, carrying smaller scale disturbances. In addition to migrating across the flow, they have a lifetime so long that they persist for distances as much as 30 times the width of the flow (Bradshaw 1973). Thus the turbulent stresses at a given point depend upon upstream history and cannot be uniquely specified in terms of the local strain rate tensor, as is the case with the eddy viscosity formulation, and the linear Boussinesq relationship.

Secondly, Equation 4.21, being more complex than the eddy viscosity approximation, contains a greater number of terms enabling a greater number of flow effects to be accounted for. The extra terms such as convection, production and body force allow representation of flows involving streamline curvature, system rotation and stratification. Thirdly, there is no reason why this model should give equal values for the normal and shear stresses as the individual components are calculated separately.

In a similar fashion to the models described previously, there is now a significant closure problem with the Reynolds stress model. In order to close the Reynolds stress equations it is necessary to eliminate the third moment correlations that appear in Equation 4.21 of the form $u_k u_i u_j$. Furthermore, it is necessary to model the dissipation tensor e_{ij}, the turbulent transport tensor C_{ij} and the pressure strain correlation tensor Φ_{ij} in the Reynolds stress transport equation. As each of these forms is a tensor the approximation required for closure can assume much more elaborate forms compared to approximations used in the *k* equation (Wilcox 1994).

The diffusion term in the Reynolds stress transport equation is often modelled using Kolmogorov's (1941) hypothesis of local isotropy of small scales where directionality of the small scale eddies is damped due to the effects of viscosity. The model is formulated so that the normal Reynolds stresses only are affected (Versteeg and Malalasekera 1996).

$$e_{ij} = \frac{2}{3} e d_{ij} \qquad (i = j) \tag{4.22}$$

where $e = \nu \overline{\left(\frac{\partial u_i}{\partial x_k} \frac{\partial u_i}{\partial x_k} \right)}$ = dissipation rate of the turbulent kinetic energy

It should be noted that this assumption is not always true and the dissipation of turbulent kinetic energy may, in certain circumstances, be anisotropic. Rotta (1972) has attempted to account for this.

The turbulent transport term is often modelled by the analogy that the rate of transport of Reynolds stresses by diffusion is proportional to the gradients of the Reynolds stresses.

The pressure-strain correlation in the differential stress model has proven the most difficult term to account for and has received the greatest amount of attention from turbulence modellers. The physical processes that cause pressure fluctuations to occur are detailed and complex and include interaction between neighbouring eddies and the effects of different mean velocities on the turbulent eddies (Tennekes and Lumley 1972). The main effect of this term is to reduce the level of the Reynolds shear stresses and redistribute this energy amongst the normal stresses. This returns the normal stresses towards a state of isotropy. Unfortunately the presence of a solid boundary tends to increase the anisotropy of the turbulent eddies and decrease the magnitude of the Reynolds shear stresses in contrast to the role of the pressure strain term. Modifications to the pressure-strain term are thus required to enable the model to accurately predict the effect of the wall on the turbulent eddies. Further details are given in chapter 6.

4.2.7.1 Discussion

The differential stress model has a far greater universality than the models based on the eddy viscosity concept due to its more rigorous and detailed mathematical formulation. The inclusion of a greater number of equations allows for a far greater description of the physics of turbulent flow.

Despite the considerable abilities of this model it still has many inadequacies and there are many years of development work to be undertaken on the differential stress model and its closure forms before it will show its real potential. At present the main areas identified as causing inaccuracies in flow predictions include the following:

1. the modelled turbulence energy dissipation equation

2. the closure form of the pressure-strain tensor and the effect of wall reflection terms

3. numerical instability and difficulties in obtaining converged solutions for the modelled partial differential equations in complex flows.

The turbulence energy dissipation equation used in the differential stress model is the same as that used in the *k-e* model and is said to be a source of considerable error. There is presently a lack of understanding regarding the whole energy spectrum for the dissipative process. The exact energy dissipation equation is significantly more complicated than the equation used in the model and involves terms such as production of dissipation, dissipation of dissipation, the sum of molecular diffusion of diffusion and turbulent transport of dissipation (Wilcox 1994). It is explained that these correlations are essentially impossible to measure using conventional experimental techniques and that only direct numerical solution techniques will 'shed light' on these terms.

Point number two is detailed further in section 5.5.

The third issue is particularly important with regards to general application of this model. As the time scales associated with the turbulence are much shorter than those connected with the mean flow, the equations for both the *k-e* model and DSM are much stiffer than the laminar flow equations, therefore the solution method has to take account of this. An equation is said to be numerically stiff when there are two or more very different scales of the independent variable on which the dependant variables are changing. For this reason, in the numerical solution procedure, one first performs an outer iteration of the momentum and pressure correction equations in which the value of the eddy viscosity or Reynolds stresses are based on the solution to the turbulence transport equations from the preceding iteration. Then an inner iteration of the *k*, *e* or Reynolds stress equations is performed following linearisation of the model equations. The outer iteration with an updated stress or eddy viscosity is then repeated and so on. The stiffness of the equations is the reason why they are treated separately as described above, coupling the equations would make convergence very difficult to obtain. Too large a time step (or its equivalent in an iterative method) can lead to negative or unrealisable values for the turbulence model equations and thus instability. The number of equations and time scales involved in describing turbulence with the DSM has led to even greater numerical stiffness and the need for great care with this model in order to obtain accurate solutions.

4.2.8 The Algebraic Stress Model (ASM)

The algebraic stress model is an economical way of accounting for the anisotropy of the Reynolds stresses without going to the full length of solving the Reynolds stress transport equations. Removing or modelling the convective and diffusive transport terms effectively reduces the Reynolds stress terms from transport equations to a set of algebraic equations. The general method chosen to model these terms is to assume that the sum of the convection and diffusion terms of the Reynolds stresses is proportional to the sum of the convection and diffusion terms of the turbulent kinetic energy. The resulting algebraic approximation of the Reynolds stress takes the following form:

$$\overline{u_i' u_j'} = \tfrac{2}{3} k d_{ij} + \left(\frac{C_D}{C_1 - 1 + \frac{P}{e}} \right) \left(P_{ij} - \tfrac{2}{3} P d_{ij} \right) \frac{k}{e} \qquad (4.23)$$

where C_D is an adjustable constant dependant on the type of flow field encountered and C_1 = 2.2.

4.2.8.1 Discussion

Although this model is reported to allow for anisotropic predictions of turbulence and is only marginally more computationally expensive than the standard *k-e* model it does have significant problems which have led the author not to include the model in the tests in chapter 6. The ASM is subject to all the disadvantages as described for the DSM, including the numerical stability problems, and it is reported to be severely restricted in flows where the transport assumptions for the convective and diffusive effects do not apply. Murakami et al (1991) has reported that the modelling assumptions for these terms produce particular inaccuracies in wind engineering flows where the convection and diffusion of the flow are extremely important. Furthermore the model has to be tuned to different flow fields through the adjustable constant detailed above. For further information the interested reader is referred to Murakami (1993).

4.3 Turbulent Wall Boundary Conditions

As briefly explained in section 4.2.4, a fundamental part of a CFD simulation is the method used to represent the effects of the wall on a turbulent flow. The majority of the turbulence models discussed will be used in high Reynolds number flows. This requires an economical method of modelling the effects of the wall on the momentum and turbulence transport equations. This is particularly important in wind engineering applications as these are often high Reynolds number turbulent flows with complex wall bounded geometries.

Normally wall boundary conditions are specified using wall functions. This is necessary to avoid the need for very fine grids to resolve the large gradients of energy dissipation in the near wall region and thus reduce the computational overheads of a given wall bounded problem. Wall functions are based on the universal assumptions that a constant shear stress exists in the near wall region and that the length scale of a typical eddy in this region is proportional to the distance from the wall. These assumptions result in a logarithmic velocity profile near the wall

The wall law relates the shear stress t to the turbulent kinetic energy:

$$t = r.C_m^{1/2}.k \tag{4.24}$$

This is used to define a velocity scale:

$$u^+ = \frac{(r.t)^{1/2}}{t}.u \tag{4.25}$$

and the scaled wall distance:

$$y^+ = \frac{\Delta y_p}{n}\sqrt{\frac{t}{r}} \tag{4.26}$$

For any high Reynolds number turbulence model the implementation of wall boundary conditions starts with the evaluation of y^+ (from Equation 4.26) where Δy_p is the distance of the near wall node to the solid surface. A near wall flow is taken to be laminar if $y^+ \le 11.63$ and the wall shear stress is assumed to be entirely viscous in origin. If $y^+ > 11.63$ the flow is turbulent and the wall function approach is used and the finite volume node is considered to be in the log law region of the turbulent

boundary layer. In this region wall function formulae associated with the log law are used to calculate shear stress, heat flux and other variables. High Reynolds number turbulence models usually employ the assumption that if y is the co-ordinate direction normal to the wall, the mean velocity at a point y_p with $30<y^+<500$ satisfies the log-law. Measurements of turbulent kinetic energy budgets indicate that the rate of turbulent production equals the rate of dissipation. Using these assumptions and the eddy viscosity formula it is possible to develop the following wall functions (Versteeg and Malalasekera 1996):

$$u^+ = \begin{cases} y^+, & for\ y^+ < y_0^+ \\ \frac{1}{k}\log\left(E.y^+\right), & for\ y^+ > y_0^+ \end{cases} \tag{4.27}$$

$$k = \frac{u_*^2}{\sqrt{C_m}} \tag{4.28}$$

$$e = \frac{u_*^3}{ky} \tag{4.29}$$

where y_0^+ defines the cross over point between the laminar sub-layer and the logarithmic region. E is the log layer constant and k is the Karman constant, both of which are empirical values found from experiments. If the walls were not smooth, as discussed above, E should be adjusted accordingly and a new limiting value of y^+ would result. See section 6.3.7 for details.

The wall function approach is not completely satisfactory for several reasons. Most importantly, numerical solutions are sensitive to the point above the surface where the wall functions are used, i.e. the point where the matching occurs. In addition, the law of the wall does not always hold for the flow near solid boundaries, most notably for separated flows (Wilcox 1994). Further discussion of this point is given in chapter 7. More details on the individual layers of the near wall region are given below.

4.3.1 Linear (or laminar) sub-layer – the fluid layer in contact with the wall

At the solid surface the fluid is stationary and turbulent eddying motions also stop very close to the wall. In the absence of turbulent (Reynolds) shear stress effects the

fluid closest to the wall is dominated by viscous shear. This layer is in practice extremely thin (y^+ <5) and we may assume that the shear stress is approximately constant and equal to the wall shear stress t_w throughout the layer. As there is a linear relationship between u^+ and y^+ this region is referred to as the linear sub-layer.

4.3.2 Log-law layer – The turbulent region close to a smooth wall

Outside the laminar sub-layer a region exists ($30 < y^+ < 500$) where viscous and turbulent effects are both important. The shear stress varies slowly with distance from the wall and within this region it is assumed to be constant and equal to the wall shear stress.

$$u^+ = \frac{1}{k}\ln y^+ + B \quad = \frac{1}{k}\ln(Ey^+) \tag{4.30}$$

Numerical values for the constants are found from experiments. Wall roughness causes a decrease in the value of B as highlighted in section 6.3.7. As there is a logarithmic relationship between u^+ and y^+ this region is referred to as the log-law layer.

4.4 Alternatives to the Navier Stokes Equations

4.4.1 Chaos

The mathematical theory of Chaos has been the subject of much research work in recent years. Wilcox (1994) states that mathematicians have discovered that certain non-linear dynamical systems, sets of non-linear ordinary differential equations, possess an extremely complicated chaotic structure. Researchers in this field have successfully used these systems to describe very simple turbulent fluid flow processes such as convection between two horizontal plates of different temperatures, known as Rayleigh-Benard convection. For detailed theories on this subject see Gleick (1988), Deissler (1989) and Stewart (1989).

There are many problems in using this very complex and theoretical approach to model turbulence. Bradshaw (1992) has shown that solving turbulent flow problems

using these methods would require an amount of computing time equivalent to that required for LES. Furthermore, it has been deduced there is more to turbulence than randomness or chaos. As is explained later (see section 5.7.2) so called coherent structures exist to some degree in a majority of turbulent flows. If turbulence was simply random then perhaps statistical methods would be able solve the problem.

4.4.2 The Discrete Vortex method

This technique is a much more viable alternative to the Navier-Stokes equations than Chaos theory. Very generally, the method is to assume a form of vortex, for example a point vortex, and then to consider an assembly of a few hundred or thousand such vortices. In this way turbulent shear layers can be reproduced. However, there are problems in adequately representing boundary conditions in complex flows (Quinn 1999) as well as the fact that flows are represented as being purely invisid, which is generally not appropriate for widespread CWE application.

For further details see McComb (1990), Kawai (1990) and Leonard (1985).

4.5 Summary

This chapter has introduced the reader to the concept of turbulence modelling and the various methods used to represent the effects of the turbulence on the mean flow or Reynolds averaged Navier-Stokes equations. A number of schemes have been reviewed ranging from simple eddy viscosity approximations, such as the mixing length model, through to more complex models such as the differential stress model. All of the techniques discussed have been subjected to a critical appraisal to allow a focused discussion, in the following chapter, of a number of ‘new’ turbulence models that may offer possible solutions or improvements to the main problems areas.

5. Developments in Turbulence Modelling.

5.1 Introduction

In the review of turbulence models in chapter 4 it was found that the main problem areas were as follows:

1. the isotropic eddy viscosity assumption and linear Boussinesq hypothesis used in the standard two equation turbulence models

2. numerical instability of the DSM and errors in the pressure-strain term

3. errors in the dissipation equation.

Unfortunately at the present time there are few, if any, improvements available for point 3 that can be applied to the dissipation equation and used in a generic manner. In addition, there is generally little that can be done to improve the numerical instabilities in the DSM. As this project uses a commercially available CFD code it is apparent that the developers have attempted to make the use of this package as user friendly as possible and have in some cases favoured numerical stability over accuracy (Wilkes 1999).

Consequently, excluding points 2 and 3, this chapter will expand upon the modelling errors discussed in chapter 4 and highlight improvements and developments in turbulence models to account for these defects. Wherever possible a critical appraisal will be given. Further model improvements beyond those highlighted already will also be discussed.

5.2 The Murakami, Mochida, Kondo (MMK) *k-e* Turbulence Model (Tsuchiya et al 1996)

Many techniques have been applied by scientists and researchers to improve the results obtained by the standard *k-e* model due to the deficiencies of the eddy viscosity concept. The technique which is by far the most popular is to make flow specific ad-hoc modifications to the model closure constants to force it into agreement with experimentally derived flow fields. This technique, although popular, has the

effect of reducing the universality of the model. There are many published revisions and ad-hoc changes to the model that successfully represent improvements over the standard model for certain flow fields. The following section will describe one of the more successful and extensive revisions appropriate to wind engineering flow fields, the MMK *k-e* model of turbulence.

The paper detailing this model proposes a *k-e* model that is said to resolve the problems encountered with the standard model (explained in section 4.2.3) by modifying the expression for the eddy viscosity approximation. The main *k* and *e* model equations are unchanged. The revised *k-e* model is then applied to flow fields around bluff bodies including a surface mounted cube both normal and skewed to the flow.

5.2.1 Outline of the revised model

$$P_k = \nu_t . s^2 \quad \text{where} \quad m_t = C_m \frac{k^2}{e} \tag{5.1}$$

The turbulent kinetic energy production term and the calculation of the eddy viscosity for the standard *k-e* are listed in Equation 5.1

For the MMK model, P_k and m_t are as per Equation 5.1 except that:

$$C_m = C_m \frac{\Omega}{s} \text{ for values of } \frac{\Omega}{s} < 1 \tag{5.2}$$

$$C_m = C_m \text{ for } \frac{\Omega}{s} \geq 1. \tag{5.3}$$

(Tsuchiya et al 1996)

In the standard *k*-ε model, *k* is overestimated near the front edge of a surface mounted cube which gives rise to a large eddy viscosity. This discrepancy is caused by overestimation of the turbulence production term P_k which is caused by the eddy viscosity concept as described by Murakami et al (1992) as follows.

The full term (2-dimensional) for P_k:

$$P_k = -\overline{u'u'}\frac{\partial \bar{u}}{\partial x} - \overline{w'w'}\frac{\partial \bar{w}}{\partial z} - \overline{u'w'}\frac{\partial \bar{u}}{\partial z} - \overline{w'u'}\frac{\partial \bar{w}}{\partial x} \qquad (5.4)$$

This term equates P_k to the difference between the turbulence production from diagonal elements of the strain rate tensor and production from off diagonal elements. The production term for the normal component of the Reynolds stress is as follows:

$$P_{kn} = (\overline{u'u'} - \overline{w'w'})\frac{\partial \bar{u}}{\partial x} \qquad (5.5)$$

Using the continuity equation and then the eddy viscosity concept this equation becomes:

$$P_{kn} = 4\nu_t\left(\frac{\partial \bar{u}}{\partial x}\right)^2 \qquad (5.6)$$

When an anisotropic model is used such as the differential stress model, P_{kn} is calculated using the form as described in Equation 5.5 which involves two velocity components. When using the eddy viscosity concept these two normal stresses cannot be incorporated so they are simply expressed as Equation 5.6 by adding the two components of turbulence production (Murakami et al 1992). Hence the value of turbulent production is always large and positive. Although the MMK model is still constrained by the eddy viscosity concept it attempts an 'ad-hoc' correction to the over production of P_{kn}. The standard model constant C_m becomes a variable that can reduce in magnitude dependent on the ratio of vorticity to shear. At flow impingement areas where there are high shear stresses the ratio is less than one and a reduced value of C_m is calculated thus reducing the eddy viscosity returned.

Tsuchiya et al (1996) conducted tests using the MMK and the standard *k-e* model for flows over a two dimensional square rib and a three dimensional cube. It has been reported that the MMK model out performs the standard model for wind engineering flow fields in all aspects, including a better distribution of surface pressures.

Although this model has had encouraging reports it should be borne in mind that it is still based on the fundamentally flawed assumption of isotropic eddy viscosity as used by the linear, standard, *k-e* model. This model could be described as an ad-hoc

modification to force the standard *k-e* model into agreement with wind engineering flows as the additions to the equations are not derived in any way from the Navier-Stokes equations.

Although it is clear that this model has been previously tested in wind engineering flow fields the author has conducted full tests in chapter 6 to obtain a full appreciation of this technique.

5.3 Two Layer Turbulence Models

Low Reynolds number turbulence models, so called because they are able to integrate into the near wall low Reynolds number region of the flow, are reported to require high degrees of numerical resolution in the sub-layer. This is due to the need to account for the steep gradients of the energy dissipation term, *e* (Patel et al 1985). As such the computational requirements of this model in complex three-dimensional wall bounded flows can become excessive, as previously discussed.

Due to these constraints, and in an attempt to improve the performance of turbulence models by taking a greater account of the effects of the viscous sub-layer, two layer turbulence models have been formulated. These models make use of either a standard *k-e* or full Reynolds stress model to describe the flow field in the outer region and a simpler model to describe the near wall region. The advantages of this method are twofold. Firstly a more accurate description of the sub-layer is given than with the use of wall functions and secondly a lower degree of numerical resolution is needed than with the low Reynolds model. In order to avoid the resolution problems encountered with the low Reynolds number model the sub-layer turbulence model usually avoids the use of the transport equation to determine *e* in favour of determination from a prescribed length scale.

The sub-layer models tested and documented at this time consist of either a mixing length model, which is applicable for both the inner and outer flow regions, or more usually a one-equation model (Malecki et al 1993). For the one equation model a value of the eddy viscosity in the near wall region is calculated from:

$$v_t = C_m k^{1/2} l_m \qquad (5.7)$$

Only one partial differential equation is solved in this model as the dissipation rate, e is determined from a prescribed length scale distribution:

$$e = \frac{k^{1/2}}{l_e} \tag{5.8}$$

The length scales l_m and l_e are described by exponential functions that express a linear variation in the log law region until very near the wall where deviations occur (Rodi 1990). The length scale l_m reduces rapidly in the region very close to the wall thus reducing the value of eddy viscosity determined in Equation 5.7.

The use of two layer turbulence models with the one equation model as described means that there are now two descriptions of the turbulent kinetic energy k. Consequently the natural matching point of the two models appears to be at the outer edge of the log law sub-layer. Exact methods of matching the two models range from the specification of exact grid points away from the wall to the fulfillment of certain specific criteria. These can include such factors as ratios of eddy viscosity to molecular viscosity and the value of l_m, damping function relation close to unity, i.e. very small viscous effects (Rodi 1990).

5.3.1 Discussion.

Experimental evidence suggests that the sub-layer velocity distribution deviates from the logarithmic assumption for certain flow fields such as those including strong secondary flows and separated regions, which may extend into the sub-layer (Rodi 1990). Therefore it could be argued that a more rigorous determination of the sub-layer is required than that provided by simple wall functions.

Rodi (1990) has undertaken testing of *k-e* and Reynolds stress two layer models for a number of flow problems including those of interest in the field of wind engineering. The flow over a 2D backward facing step was analysed with the aid of a two layer *k-e* model and compared with the standard *k-e* model and experimental results. The standard model was found to drastically under predict the reattachment length of the separation and recirculation zone. The two-layer model was found to improve the predictions with better predictions of velocity and shear stress profiles and reattachment length. Although it was noted that the results where still not particularly accurate with a 14 percent under prediction of the reattachment length for an inclined

upper wall case. Full details of tests with this model, in the field of wind engineering, can be found on reference to Lakehal and Rodi (1997).

This model is again a simple isotropic eddy viscosity model with more attention paid to the sub-layer. Furthermore, wall functions are used to calculate the energy dissipation term so it could well be argued that this model is not truly integrating to the wall as the low Reynolds number models.

Finally the author has not tested these models any further due to their high computational overheads (detailed in chapter 6) and availability of previously published results.

5.4 Revisions to the Boussinesq Hypothesis – The Non-Linear *k*-*e* Model

An effective viscosity hypothesis relates the Reynolds stresses solely to the rates of strain of the fluid and to scalar quantities. As described in section 4.2.1 the first effective viscosity hypothesis was proposed by Boussinesq as early as 1877. This formula, which simply represents the action of the *u'w'* shear stress, has been used with considerable success by, among others Ng (1971) and Rodi (1972) for free shear flows. Nonetheless it has been observed that the Boussinesq hypothesis fails in a number of applications including boundary layers over curved surfaces. Bradshaw (1973, 1992) has stated that this failure is due to the form of the stress strain relation rather than the inapplicability of the eddy viscosity approach.

In order to account for flows in which more than one Reynolds stress is required to fully describe a given flow field the Boussinesq hypothesis is generalised to give the isotropic eddy viscosity assumption used in the majority of turbulence models (described in section 4.2.1). It has been shown in previous sections that this theory is invalid for flows in which $u'u' \neq v'v' \neq w'w'$. The first attempts to remove this deficiency in the eddy viscosity assumption were undertaken by Lumley (1970). Pope (1975) adopted a similar approach to Lumley in formulating a constitutive relation for the Reynolds stresses resulting in a finite tensor polynomial to form a revised general effective viscosity hypothesis.

In deriving a new relationship Lumley (1970) shows that the mean velocity field and boundary values of the fluctuating velocity are sufficient to determine the Reynolds stresses and assumes that, far from boundaries, the boundary conditions serve at most

to set the levels of the time and length scales. With this assumption it follows that in a homogeneous or near homogenous flow, where the rates of strain contain all the information about the velocity field, the Reynolds stresses are a function of the rates of strain and scaling parameters only (Pope 1975). Furthermore, these two scaling parameters are sufficient provided that all the macroscales of turbulence are proportional i.e. at high Reynolds numbers when the influence of laminar viscosity may be excluded. Therefore using these arguments, applying dimensional analysis and imposing invariance under coordinate transformation Pope (1975) suggested the following form consisting of up to a fifth order relationship:

$$a_{ij} = \frac{\overline{u_i' u_j'}}{k} - \frac{2}{3}\delta_{ij} = \sum_{l=1}^{10} G_{ij}{}^{l} T_{ij}^{l} \qquad (5.9)$$

where

$$T_{ij} = T_{ij}(S_{ij}, \Omega_{ij})$$
$$G_{ij} = G_{ij}\left[k, e, \text{ Invariants of } (S_{ij}, \Omega_{ij})\right]$$

Pope (1975) states that the non-linear eddy viscosity has the following advantages over the algebraic stress model, with which these models have often been incorrectly compared:

- The inter-relation between strain and stress is retained within the differential equation, thus increasing numerical stability

- The time consuming solution of the algebraic stress simultaneous equations is not needed

This new model of eddy viscosity is therefore shown by Pope (1975) to correct the following fundamental weaknesses of the Boussinesq stress-strain relationship:

- Inability to capture normal stress anisotropy
- Insufficient sensitivity to secondary strains
- Excessive generation of turbulence at impingement zones
- Violation of realisability at large ratios of strain

Unfortunately at the higher orders of expansion the model is restricted to two-dimensional flows as the three dimensional form is so intractable as to be of no value

(Pope 1975). Fortunately Speziale (1989), Suga (1996) and Craft et al (1996) have made revisions to the anisotropic eddy viscosity relationship to allow their application to a wide range of three dimensional turbulent flows. Craft et al (1996) details both quadratic and cubic expansions of the Boussinesq hypothesis as follows:

$$\begin{aligned}\rho\overline{u_i'u_j'} = &-\mu_t S_{ij} + \tfrac{2}{3}\rho\delta_{ij}k \\ &+ C_1\mu_t\frac{k}{\varepsilon}\left(S_{ik}S_{kj} - \tfrac{1}{3}S_{kl}S_{kl}\delta_{ij}\right) \\ &+ C_2\mu_t\frac{k}{\varepsilon}\left(\Omega_{ik}S_{kj} + \Omega_{jk}S_{ki}\right) \\ &+ C_3\mu_t\frac{k}{\varepsilon}\left(\Omega_{ik}\Omega_{jk} - \tfrac{1}{3}\Omega_{lk}\Omega_{lk}\delta_{ij}\right)\end{aligned} \tag{5.10}$$

where:

$$S_{ij} = \left(\frac{\partial\overline{u}_i}{\partial x_j} + \frac{\partial\overline{u}_j}{\partial x_i}\right) \tag{5.11}$$

$$\Omega_{ij} = \left(\frac{\partial\overline{u}_i}{\partial x_j} - \frac{\partial\overline{u}_j}{\partial x_i}\right) \tag{5.12}$$

The cubic expansion takes the following form:

$$\begin{aligned}\rho\overline{u_i'u_j'} = &-\mu_t S_{ij} + \tfrac{2}{3}\rho\delta_{ij}k \\ &+ C_1\mu_t\frac{k}{\varepsilon}\left(S_{ik}S_{kj} - \tfrac{1}{3}S_{kl}S_{kl}\delta_{ij}\right) \\ &+ C_2\mu_t\frac{k}{\varepsilon}\left(\Omega_{ik}S_{kj} + \Omega_{jk}S_{ki}\right) \\ &+ C_3\mu_t\frac{k}{\varepsilon}\left(\Omega_{ik}\Omega_{jk} - \tfrac{1}{3}\Omega_{lk}\Omega_{lk}\delta_{ij}\right) \\ &+ C_4\mu_t\frac{k^2}{\varepsilon^2}\left(S_{ki}\Omega_{lj} + S_{kj}\Omega_{li}\right)S_{kl} \\ &+ C_5\mu_t\frac{k^2}{\varepsilon^2}\left(\Omega_{il}\Omega_{lm} + S_{il}\Omega_{lm}\Omega_{mj} - \tfrac{2}{3}S_{lm}\Omega_{mn}\Omega_{nl}\delta_{ij}\right) \\ &+ C_6\mu_t\frac{k^2}{\varepsilon^2}S_{ij}S_{kl}S_{kl} \\ &+ C_7\mu_t\frac{k^2}{\varepsilon^2}S_{ij}\Omega_{kl}\Omega_{kl}\end{aligned} \tag{5.13}$$

The coefficients C_1 to C_7 have been derived from considering the prediction of the stresses from a wide range of turbulent flows. The first term on the right in Equation

5.13 is the standard approximation. It can be seen that the addition of up to a further seven terms makes the relationship a great deal more mathematically complex and detailed and constitute the additional terms which are quadratic and cubic in the mean velocity gradients (Wilcox 1994). Detailed tests by the authors mentioned have shown that the quadratic model showed significantly improved predictions for the reattachment length of the separated region behind the backward facing step, with results similar in accuracy to that obtained using the differential stress model. Furthermore, the non-linear quadratic model successfully predicted an eight vortex secondary flow in the non circular duct, an occurrence usually only predicted by second order closure models which are able to predict the individual Reynolds stresses. The quadratic models are designed for problems in which flow anisotropies are the distinguishing feature. The cubic model includes extra terms in the constitutive relation between Reynolds stresses and strain rates so it is reported to give better predictions in curved flows, for example, over curved surfaces including hills. Therefore, it could be argued that the quadratic model should be sufficient to describe the flow in a majority of wind engineering bluff body simulations.

The quadratic non-linear model proposed by Speziale (1987) is as follows:

$$-\overline{u_i' u_j'} = n_t\left[\frac{\partial \overline{u}_i}{\partial x_j} + \frac{\partial \overline{u}_j}{\partial x_i}\right] - \tfrac{2}{3}\delta_{ij}k + C_D l^2\left(D_{im}D_{mj} - \tfrac{1}{3}D_{mn}D_{mn}\delta_{ij}\right) - C_E l^2\left(\overline{D^{\circ}}_{ij} - \tfrac{1}{3}\overline{D^{\circ}}_{mm}\delta_{ij}\right) \qquad (5.14)$$

where

$$D_{ij} = \frac{1}{2}\left[\frac{\partial \overline{u}_i}{\partial x_j} + \frac{\partial \overline{u}_j}{\partial x_i}\right] \qquad (5.15)$$

and the Oldroyd derivative term ($\overline{D^{\circ}}_{ij}$) is as follows:

$$\overline{D^{\circ}}_{ij} = \frac{\partial \overline{D_{ij}}}{\partial t} + \overline{u}_m \frac{\partial}{\partial x_m}\overline{D_{ij}} - \frac{\partial \overline{u}_i}{\partial x_m}\overline{D_{mj}} - \frac{\partial \overline{u}_j}{\partial x_m}\overline{D_{mi}} \qquad (5.16)$$

$$l = 2C_m \frac{k^{3/2}}{\varepsilon} \qquad (5.17)$$

This model, again based on the work of Pope (1975), differs slightly from the quadratic model of Suga (1996) due to the appearance of Equation 5.16 which is an approximation derived from the revised relationship to a visco-elastic medium, see Speziale (1987) for further details. Lumley (1970) explains how there are striking similarities between the mean turbulent flow of a Newtonian fluid and the laminar flow of visco-elastic fluid. Visco-elastic fluids, often termed Rivlin-Ericksen fluids, are used in the description of dilute polymer solutions. According to Speziale (1987) these fluids can be similarly modelled by the non-linear generalisation of the Boussinesq hypothesis.

Due to the nature of the non-linear model, comparisons have been made with the second order closure, algebraic stress model. There is a similarity in both models in that the stresses are linked non-linearly to all strain components, but beyond this the two models are very different as the algebraic stress model is based on simplified transport terms for the full Reynolds stress equations.

In a similar manner to the k and e equations and the Reynolds stress transport equations detailed earlier, the non-linear models are rigorously derived from either the Navier-Stokes equations or the eddy viscosity Boussinesq hypothesis. The author is of the opinion that turbulence models of this kind, rather than turbulence models modified in an ad-hoc manner, are the most sensible way to improve the current modelling technology.

Reported deficiencies and errors with these models are particularly scarce due to the minimal testing undertaken in this field. Nevertheless it has been stated that the cubic non-linear model is the preferred expansion due to the fact that it can be applied to a greater range of flow fields, including curved surfaces (Craft et al 1996). As such the model constants used to close the equations can be calibrated from a much wider range of flows thus making the model more universally applicable than the quadratic model. In addition, it should be noted that the algebraic expressions for the Reynolds stresses are unable to model fluid transport effects, in contrast to the differential stress model (see section 4.2.7).

Consequently as these models have not yet been applied to three dimensional wind engineering flow fields the author has undertaken extensive testing and offered critical discussion of the findings in chapter 6.

5.5 Wall Reflection Terms – The Pressure Strain Relationship for the Differential Stress Model

5.5.1 Theory

Referring to the work of Uzkan and Reynolds (1967), Thomas and Hancock (1977) and Perot and Moin (1995) it is apparent that the effects of a solid wall on turbulence behaviour are very complex. Viscous effects in the near wall region damp the turbulence intensities, while wall blocking effects amplify tangential turbulence intensities. This is due to the fact that the fluid cannot penetrate the boundary and as such any fluid moving towards the wall must eventually turn and move parallel to the wall. In this way energy is transferred from the normal velocity to the two tangential velocity components increasing the turbulence intensity and anisotropy near the wall (Perot and Moin 1995). Consequently the distinctive features in this region immediately adjacent to a solid boundary are strong inhomogenity and excessive turbulence anisotropy. This is a non-trivial effect due to the solid boundary that is known as the pressure echo effect or wall reflection effect.

5.5.2 Modelling

In the differential stress model the pressure-strain term is important in explaining the correlation between the fluctuating pressure and strain. In non-wall bounded flows this term is used to derive the pressure-strain fluctuations due to interactions between adjacent eddies and eddies and the mean flow and to steer the turbulence towards isotropy. In wall bounded flows it is necessary to further predict the influence of the wall on the flow field. Thus a pressure-strain term is required that is applicable to all points in the flow from the wall region to an infinite distance from the wall. Adequate mathematical expressions to describe the behaviour of the wall pressure reflections and pressure strain interaction have proved particularly difficult to find. This is due to the significant complexity of the problem and the existence of unmeasurable terms in the pressure-strain term leading to highly empirical models. A great degree of cleverness and ingenuity is required to establish a rational closure approximation. The problems caused by the wall are further compounded by the use of isotropic dissipation models, in the Reynolds stress transport equation, which imply dissipation of energy by the small scale isotropic eddies. This is incorrect near the wall where the

eddies are small, i.e. no larger than the distance from the wall, but are highly anisotropic due to the effects of the solid boundary.

Early Reynolds stress models, such as Gibson and Launder (1978), have used isotropic or quasi-homogeneous assumptions in some important aspects of their formulation. Such formulations tended to increase the isotropisation process as the wall is approached thus leading to non-physical representations (Leschziner 1995). In order to perform the near wall integrations these traditional pressure-strain terms require the introduction of a variety of ad-hoc wall damping and wall refection terms that depend inversely on the distance from the wall as well as the unit normal to the wall. These damping functions essentially correct the erroneous behaviour of the basic models by adjusting the model solution to fit a particular data set. The isotropisation process, correctly predicted in non-wall bounded flows, is damped to allow the turbulence to become increasingly anisotropic due to the influence of a solid boundary. These case specific revisions are against the very nature of second moment closure models (differential stress models) which are said to be more universally applicable. Furthermore, the introduction of the damping terms makes the application of these models to flows in complex geometries very difficult, as the local wall distance is not uniquely defined. Consequently, at present, in order to use the DSM as a generic wind engineering model, applicable to all geometries and simulations, it is necessary to omit the wall reflection terms. The only known alternative, at present, to this is to use non-linear pressure-strain terms that asymptotically follow the correct distribution of stresses as the wall is approached. For example the SSG model (Speziale, Sarker and Gatski 1991) does not use a wall reflection term in the pressure-strain relationship, instead a number of the constants in the pressure strain term have been calibrated with homogeneous shear flow. Unfortunately although these models perform reasonably well in simple flow fields they show considerable errors when applied to wind engineering flow fields. For example;

> ‘The use of non-linear models, together with an inhomogenity correction to $\phi_{ij,2}$, is not satisfactory for handling flows impinging on a wall’ (Gatski et al 1996, p273).

> ‘This non-linear scheme has so far been tested only for flows parallel to the wall. Whether it will be satisfactory for flows impinging on a wall is open to doubt’ (Launder and Li 1993, p1005).

Furthermore Speziale (1994), in a review of the most recent state of the art second moment closure models with wall effects, stated that the move towards the non-linear models is not without problems even in generally simpler flows without impinging. It is apparent that at present there is no model that is generally applicable to a wide range of flow fields and disciplines, consequently many researchers have produced unworkable models that are overly complex and empirical.

An early example of a pressure-strain term with wall reflection effects, that has been tested in chapter 6, is given below. The pressure-strain term used consists of the sum of three parts as follows:

A return to isotropy term involving the fluctuating velocities only (Rotta 1972)

$$f_{ij,1} = -c_1 \frac{e}{k}\left(\overline{u_i u_j} - d_{ij} k\right) \tag{5.18}$$

A return to isotropy of the production term (the rate of production of the Reynolds stresses) (Naot et al 1970)

$$f_{ij,2} = -c_2\left(P_{ij} - \frac{2}{3} d_{ij} P\right) \tag{5.19}$$

The wall reflection terms to account for the effect of walls on the pressure-strain terms (Gibson and Launder 1978)

$$f_{st,w} = \left(c_1' \frac{e}{k}\left(\overline{u_n' d_{ij}} - \frac{3}{2} u_n u_i d_{ij} - \frac{3}{2} u_n u_j d_{ni}\right) + c_2'\left(f_{nn,2} d_{ij} - \frac{3}{2} f_{ni,2} d_{ni} - \frac{3}{2} f_{nj,2} d_{ni}\right)\right) f\left(\frac{L}{x_n e}\right)$$

(5.20)

where the index, *n*, indicates the direction normal to the wall. The function f takes the form:

$$f\left(\frac{L}{x_n e}\right) = C_w \frac{k^{1.5}}{x_n e} \tag{5.21}$$

where x_n is the normal distance from the wall. As these terms are a simplification of more complex relationships experimental constants are incorporated to simplify the equations.

The interested reader is referred to Bernard and Speziale (1992) for details of future proposals for improved pressure-strain terms.

In a similar manner to the two layer models described earlier, full and detailed wind engineering testing of a number of the wall reflection models, described above, has already been undertaken for a surface mounted cube in an atmospheric boundary layer, the interested reader is referred to Murakami et al (1993). Further details are given in chapter 6.

5.6 Direct Numerical Simulation (DNS)

This technique is the easiest to define but is the most computationally expensive. Direct numerical simulation solves the instantaneous Navier-Stokes equations for the full range of turbulent motions from the largest scales down to the dissipative scales. As such DNS does not involve turbulence modelling of any kind, the flow field is in fact discretised corresponding to the Kolmogorov microscale. This approach yields the complete spatial and temporal state of the turbulent flow. Full details of experiments conducted using DNS can be found in Le et al (1993).

The overwhelming problems with this technique are the massively high computing costs and memory requirements involved. An estimate of numerical grid and CPU requirements for predicting high Reynolds number flows is shown in Table 2.

Reynolds number	6600	20,000	100,000	10^6
Grid nodes	2×10^6	40×10^6	3×10^8	15×10^{12}
Time at 150 Mflops	37 hours	740hours	6.5years	3000years
Time at 1 Tflops	20secs	400secs	8.3hours	4000hours

Table 2: CPU requirements for DNS (Leschziner 1995)

An excellent example of the massive computational requirements is given by Speziale (1991) who states that a typical flow domain of 0.1m by 0.1m with a high Reynolds number turbulent flow would contain eddies down to 10 to 100μm in size. These very small eddies would naturally have very high frequencies of approximately 10kHz, thus requiring time steps of about 100μs. In order to directly capture the details of the smallest eddies it has been calculated that a computational finite volume mesh of 10^9 to 10^{12} points would be needed. The direct numerical simulation of such a turbulent flow at a Reynolds number of 500000 would require a computer 10 million times faster than a current generation supercomputer.

Due to the extremely high computational costs incurred, DNS is not able to calculate anything other than low Reynolds number flows in simple geometries. The simplest application of DNS requires access to a supercomputer. It is apparent that more practical applications of this technique await significant developments in computer technology. Nevertheless at present DNS has proved invaluable in supplying computed statistics that can be used to test proposed closure approximations in engineering models. DNS has been used at a fundamental level to obtain a greater understanding of turbulence structure and processes that are of value in developing turbulence theory that would be impossible to measure with traditional experimental techniques, for example the dissipation rate of turbulence (Lee et al 1990).

5.7 Large Eddy Simulation (LES)

This technique directly resolves the large eddies present in turbulent flows and models the smaller scale eddies. LES rests on the supposition that the most important turbulent transport processes arise from the large to medium scale eddies while smaller eddies are principally responsible for dissipation of the turbulent energy. Direct numerical simulation is used to resolve the eddies that are larger than the size of the finite volume cell, while a RANS or simpler, model is used to model the more universal nature of the small scale eddies that are smaller than the mesh size. Since Reynolds averaging is not applied to the basic equation used in LES the scale of the resolved eddies is much smaller than when using, for example, the k-ε model. The main task of this so called sub-grid scale model is to extract the appropriate amount of energy from the resolved flow field and dissipate it (Murakami et al 1987). As LES models the small scale turbulence a much coarser mesh, and larger time-steps, can be used than in direct numerical simulation in which eddies are resolved to the Kolmogorov microscale. Furthermore, as the size of the smallest eddies decreases

with increasing Reynolds number it is possible, for a given computing cost, to achieve simulation of much higher Reynolds number flows with LES than DNS.

The size of the grid cell used in large eddy simulation generally defines the level at which the smaller scale eddies are filtered and thus modelled. For this reason this technique is often referred to as space filtering.

5.7.1 Discussion.

This technique, vigorously pursued in Japan and the USA, has the advantage of producing time dependent flow information of generally very high quality and accuracy even in complex flow fields such as those found in wind engineering. It is widely felt that LES is a promising tool for the future:

> "LES has succeeded in reproducing the properties of a highly anisotropic flow field in wind engineering problems" (Murakami and Mochida, 1989a, p69)

Present difficulties in using LES mainly revolve around the constraints on available computer processing time and storage capacity which effectively hold back its use and advancement. This technique, although being more economical than DNS is still very resource intensive and as such is not yet used outside of the research community. Further difficulties are apparent in the use of the sub-grid scale model to dissipate the flow energy. Leschziner (1993) reports that the sub-grid scale eddies are not simply dissipative but can contribute significantly to turbulent mixing. Such processes as 'backscatter' can occur in which the small eddies combine with larger eddies and transfer energy to them.

A number of models are available to be used as sub-grid scale models ranging from simple Smagorinsky eddy viscosity models to full Reynolds stress closure models. Due to the promising results from this method it was considered important to further evaluate the necessary computational requirements of this technique, consequently further details and experimental testing are discussed in chapter 7.

5.7.2 Coherent Structure Capturing (CSC), or Very Large Eddy Simulation

Coherent structures are usually defined as the large turbulent structures observed in many shear flows. The accepted features of these structures are their large size and low frequencies such as the horseshoe vortex (see section 2.2.2) and the large vortices produced in the wake of a bluff body (Ferziger 1994). It has been found from experiments that these coherent structures account for a significant fraction of the turbulent kinetic energy and Reynolds stresses and fluxes in turbulent shear flows. Many flow fields, particularly those found in wind engineering, contain these large so called coherent structures that can in many ways define the flow field. If LES is applied to flow fields with a small number of these energetic coherent structures which are larger than the bulk of the motion that constitutes the turbulence it is possible to increase the size of the filter. This effectively increases the coarseness of the grid, retaining the large-scale coherent structure while omitting more of the small-scale turbulence. The theory being that the coherent structure is responsible for more of the turbulence behaviour thus further reducing the importance of the smaller scale eddies.

Ferziger (1993) gives an example of the reduced mesh size required to calculate the flow over a circular cylinder.

Technique	D.N.S	L.E.S	C.S.C
Grid points	10^{12}	10^{10} - 10^{8}	10^{6}

Table 3: CPU requirements for CSC (Ferziger 1993)

5.7.3 Discussion.

As the success of this method relies on the simulation of large, essentially coherent structures responsible for the large scale pressure field rather than eddies responsible for momentum and energy transport it is felt that CSC may be well suited to wind engineering applications (Ferziger 1993). As such this technique has moved the use of LES one step closer to mainstream application in the field of wind engineering.

Unfortunately, although CSC has low computational costs in comparison to DNS and standard LES, it is still a relatively computationally intensive procedure. Furthermore, the use of CSC in LES requires considerable expertise in constructing suitable grids

that can capture the correct detail. Further detail on this subject is given by Speziale (1998).

5.8 Summary

The literature search conducted thus far has very quickly highlighted the deficiencies in the most popular turbulence models, including the errors in the isotropic eddy viscosity concept and the possible numerical instabilities found when applying the DSM to complex wind engineering flow fields. Although full testing was required before definitive conclusions could be drawn, this information was very useful in giving direction to the project and demonstrating the requirements for improved turbulence models for computational wind engineering. It is apparent that a turbulence model, suitable for wind engineering applications, should be able to model anisotropic turbulence, as the DSM, but it should also be sufficiently numerically stable to allow its application to the vast majority of flow fields, as the standard k-e model. These early investigations suggested that a turbulence model is required that incorporates the best aspects of both these turbulence models, such as the non-linear k-e models detailed in section 5.4. The fact that these models may offer potential improvements and as yet have not been fully applied to the field of wind engineering made them an ideal subject for this thesis. It is also clear that the technique of very large eddy simulation is becoming of greater importance as computers become ever more powerful. Therefore the following chapters will address and discuss these points.

6 Results: A Comparison of Data Obtained from Both CFD Simulations and Full Scale Experimental Studies.

6.1 Introduction

Originally this project proceeded by testing the accuracy of the more popular turbulence models detailed in chapter 4, thus determining the validity of the information found in the literature search when the results were compared to full-scale rather than wind tunnel scale buildings. The outcome of these results suggested that the early considerations regarding the standard *k-e* and differential stress models were in fact correct. Further tests were then completed using a number of the models detailed in chapter 5.

The following chapter will therefore detail all of these tests together to enable direct comparison of the results obtained from a total of eight turbulence models. As far as the author is aware these tests are the first to detail comparative results of CFD and experimentally obtained data for a full-scale surface mounted cube. In addition, it is the first time the non-linear and RNG *k-e* models have had their predictive accuracy assessed when applied to wind engineering flow fields.

Overall results and conclusions will be given in both chapters 6 and 8 for all models tested in this project based on the following criteria, which the author considers to be the essential requirements for a suitable wind engineering turbulence model:

- overall accuracy
- stability and ease of use in complex flow fields.
- computational requirements and overheads.

Although the accuracy of the model is the prime consideration, the model applicability is also of paramount importance. An accurate turbulence model that cannot be applied to say 6 out of 10 flow simulations, due to poor numerical stability, is of little use to the computational wind engineer. Steady state simulations using modern computer facilities makes the issue of computational overheads only a relatively minor concern, nevertheless this point will be addressed as fast simulation times are preferred. Finally it is also preferable that the model has a general universality and so can be applied with equal success to other engineering disciplines and thus gains acceptance among the engineering community in general.

In order to assess the relative abilities of the turbulence models these tests included comparisons of 1:1 scale CFD and experimentally obtained data for a 6m surface mounted cube both normal and skewed at 45 ° to the incident wind. Further tests have included the Silsoe structures building at normal and transverse orientations and the Silsoe experimental wall, all of which are detailed later. Validation tests were carried out using the two dimensional backward facing step. Test variations included the use of different turbulence models, inlet velocities and convective differencing schemes in order to ascertain their effect on the accuracy of the flow field.

6.2 Full Scale Test Details

6.2.1 The 6m Cube

A 6m cube, located at the Silsoe Research Institute (SRI), was recently constructed to allow the comparison of full-scale rather than model scale wind tunnel data to CFD derived results. The cube is positioned so that the boundary layer is generated from a fetch consisting of short grass with an effective roughness length of 0.01m. Checks undertaken in previous years have shown that the effective roughness length of the fetch is constant due to regular cutting of the grass (Quinn 1999). The cube can be rotated through 360° and pitched on the horizontal axis by 5°. The cube surface consists of sheet metal cladding with a smooth plastic coating to afford protection and avoid changes of the surface roughness due to rust. A photograph of the cube can be seen in Figure 14.

A number of measurements were made of the pressures around the cube and the wind dynamic pressure at the roof height. The 16 pressure taps used were located along the centre line of the cube on the windward face, roof and leeward face. The information required to derive the pressure coefficients was obtained from an ultrasonic anemometer positioned 25m upstream of the building at roof height. The pressure tap locations were also used to obtain data when the cube was skewed at 45° to the incident wind. The tapping points were constructed of simple seven millimetre diameter holes (a size sufficient to prevent water blocking the tapping points) and the pressure signals were transmitted pneumatically, using a 6mm internal diameter plastic tube to transducers mounted centrally within the cube. Tube lengths of up to 10 metres were used in this system giving a frequency response of 3dB down to 8Hz (Hoxey et al 1999). The full recorded information consisted of simultaneous

measurements of all the pressures and the three components of wind at a sampling rate of 5hz, which were processed to give all the required experimental data including mean, fluctuating and spectral properties. A polynomial fit has been used to enable actual measurements of wind speed and direction to be manipulated to give a full quasi-steady prediction of surface pressure. These estimates are compared with actual measurements in the form of statistical moments, probability densities and power spectral densities. Mean pressure coefficients were derived from a recording period of ten minutes (Hoxey et al 1999).

6.2.2 The Silsoe Structures Building

The Silsoe structures building (SSB) (Robertson and Glass 1988) was constructed during 1986/87 to enable the measurement of full-scale wind loading and to aid the understanding of gaseous and particulate pollution dispersion from agricultural buildings. In order to further study the air flow characteristics around the building the SSB was constructed with optional eaves geometry of the traditional sharp eaves or curved eaves of 635mm radius. The 24m long by 12.9m span by 5.3m ridge height building with a 10° duo-pitch roof (see Figure 15) is located on a flat, exposed site adjacent to the 6m cube described earlier in this work (Hoxey et al 1995).

For this particular study there were a total of 32 pressure taps installed along the various measurement lines, sampling at a rate of 5Hz, to allow a detailed study of the pressures around the building with various incident wind angles. In a similar manner to the 6m cube tests, a three component ultrasonic anemometer was used to allow determination of the dynamic pressure upstream of the building at eaves height.

Records of one hour duration were made, and these were partitioned into 6 minute records for analysis. All the pressures were measured relative to static pressure sensed by a probe positioned upstream of the building where the influence of the pressure field associated with the building was small. The pressure transducers were automatically zeroed using a solenoid valve to equalise the pressure across the transducer. This was followed by a calibration, again activated by solenoid valves, where the wind dynamic pressure was applied to all transducers (Hoxey et al 1995). Richardson et al (1995) has stated that this procedure ensured a pressure measurement accuracy of better than +/- 1N/m^2.

All the experimental data was processed to give mean, rms, maximum and minimum values of surface pressures and similar statistics for the wind dynamic pressure, together with the mean and rms of the wind direction. Further details of the tests are given by Richardson et al (1995) and Hoxey et al (1995) and Robertson and Glass (1988).

6.2.3 The Silsoe Experimental Wall.

The Silsoe experimental wall and the various studies associated with it are described in detail by Robertson et al (1996, 1997). The information below is an extract from one of those papers used to inform the reader of the main technical details of the wall and the relevant testing procedures.

The experimental wall (shown in Figure 16) has a height of 2m and is 215mm thick (representing typical freestanding masonry walls). It was erected on a specially prepared concrete foundation but, for experimental convenience, was constructed not of bricks but of 2m high steel posts at 2m centres and square, hollow, timber panels which were located between pairs of posts. The panels were readily removable and relocatable, enabling the length of the wall to be changed from 2m (one panel) to 18m (nine panels) in 2m increments. At either end of the 18m long wall, a corner could be formed as required by introducing one or two wall panels to form a perpendicular run of wall of 2 or 4m in length. The wall was constructed on the flat and exposed site at Silsoe, near the Silsoe structures building and the 6m cube. One of the 13 panels contained 15 tappings on each face located at corresponding positions in three rows of five columns. All the pressure transducers, switching solenoids and power supplies were mounted inside the panel. An ultrasonic anemometer, static probe and directional pitot tube were mounted at a height of 2 metres on a reference mast positioned some 15 metres off one end of the wall. When the wind speed and direction complied with the prescribed settings, the data logger automatically recorded at 5Hz the outputs from the 30 pressure transducers, the load cell and the ultrasonic anemometer for one hour. The pressure transducers were automatically zeroed and calibrated at the start and end of each hour using the pitot and static probe pressures (Robertson et al 1996, 1997).

6.3 CFD Test Details - Accuracy Checks

6.3.1 Introduction

In any numerical simulation of fluid flow there are a number of checks that have to be made to assess the overall accuracy of the results obtained and to ensure that the CFD data is of a sufficiently high quality. The following work details all these important checks and wherever necessary explains any assumptions that have been made.

The CFX-Visualise package was used to obtain velocity, pressure and turbulent kinetic energy profiles for the cube, SSB and Silsoe experimental wall to be used in the following checks and comparisons. Linear interpolation between the nodal points with the CFX post processor meant that a minimum of 11 data points were recorded for each metre length of the domains for use in the various graphs in the following work. In order to obtain the pressure data the measurement lines were located approximately 10mm from the face of the various building shapes. To obtain velocity and turbulent kinetic energy profile data the measurement lines were located approximately 50mm from the respective faces. Further detail on the exact positions of the measurement lines used for each test case is given in sections 6.5.1, 6.5.5, 6.6 and 6.7. All vector and contour plots shown are located along either the vertical or horizontal centrelines of the cube, SSB and experimental wall.

Unless otherwise specified this section refers equally to all the models tested.

6.3.2 Use of Full-Scale Results for CFD Validation.

Although not strictly a numerical accuracy check, there are a number of accuracy issues that are very important to this project when using full-scale rather than wind tunnel scale building models. This sub-section will briefly highlight some of the more important aspects with regards to this project, for detailed information the interested reader is referred to Cook (1986a, 1986b).

For the full-scale observations, the most apparent advantage is that they do not suffer from any scale mismatch due to Reynolds number, wind shear and turbulence intensities or from blockage effects. On the other hand, they are costly and time consuming. It is, moreover, impossible to control the approach flow conditions, e.g.

the static and dynamic reference pressures, the thermal stratification etc., which will inevitably obscure details in the observed data (Holscher and Niemann 1998). In addition, it is stated that the error of measurements could possibly be larger for full-scale observations compared to well controlled wind tunnel tests, which should be borne in mind when using them for calibration, such as is the case for this project.

Nonetheless there are serious matters to be considered when undertaking scale simulations in a wind tunnel. One of the most important aspects, with regards to this project, are the effects of the differing Reynolds numbers involved in the areas of flow recirculation over the cube models. For the skewed cube case experimental evidence shows the existence of delta wing vortices over the roof. These are regions of flow involving very high re-circulatory velocities (Hoxey 1998). The scaling down of such regions of flow to wind tunnel models will result in very small vortices that will be influenced to a much larger degree by the effects of the fluid viscosity, thus in effect reducing the strength of the predicted vortex. These so called Reynolds number vortex effects may result in unrealistically small roof and wake recirculation zones, for both the normal and skewed cube cases, and thus errors in the prediction of pressures. Therefore the novel use of 1:1 scale CFD and experimental models should, in theory, eliminate this detrimental effect.

Referring to Davenport 1999:

> ‘In this paper we have stressed the importance of full-scale testing as a benchmark for both wind tunnel and CFD modelling. As Martin Jensen has reminded us, the lack of full-scale verification that has been tolerated is embarrassing. It is not characteristic of other technologies such as shipping, transportation or aeronautics.’ (Davenport 1999, p2)

Finally in this section, it is important to discuss the probable error in the mean pressure coefficient data, used in this thesis, for the full-scale cube, SSB and experimental wall tests. Hoxey (1999) and Quinn (1999) have stated that the predicted error for the individual RMS readings for a full-scale test with a ten minute sampling time were approximately ± 4 percent. Furthermore, by repeating the tests the individual reading error is reduced (ten minute sampling time error divided by the square root of the number of times the test is repeated). As these tests were repeated for ten samples the approximate error for the individual mean pressure readings was reduced to between ± 1 and 2 percent, although minor changes in the incident wind, between samples, will have an affect. This predicted error was used, as a ‘general rule

of thumb', for all the full-scale data used in this project. Nonetheless, it is clear that this error will also be dependent on the location of the pressure tap, with the above mentioned error in an area of steady flow. The error may marginally increase in areas of unsteady flow, such as in the wake (Hoxey 1999). Further discussion on the experimental errors in the full-scale tests is given later in this chapter.

6.3.3 CFD Solver

As previously explained all tests for this project made use of a commercially available code, CFX (CFX-International 1998). This route was taken as opposed to the development of a bespoke code for several reasons:

- CFX, like other commercial codes, has been validated for many test cases in a number of different application areas.

- The tools for geometry building, mesh definition and the presentation and analysis of the results are versatile and readily available.

- The code has many options for different methods and solution algorithms.

- Transfer of results and recommendations to end-users is easily accomplished as the code is available for many computer platforms and there is comprehensive documentation and training.

- Rapid development times for new model implementation.

Where necessary use was made of the ability to add user-defined FORTRAN subroutines to accomplish specific tasks and for more substantial alterations, including the addition of new turbulence models, the University of Nottingham had access to the source code for CFX4.2 (Wright and Easom 1999).

6.3.4 Geometry

Although the tests undertaken in these simulations compare the CFD and full-scale experimental data at an equal scale, it is nevertheless particularly important to specify the correct boundary conditions and domain dimensions for the CFD runs, as is the

case in actual wind tunnel experimental studies. Therefore the sides, lid and most importantly the inlet and outlet of the domain were positioned so as to minimise the interference with the flow field around the cube. The height and width of the domain was decided upon after discussions with Professor Baker (1997) and reference to Baetke et al (1990). Baetke et al (1990) states that the blockage ratio, defined as the ratio of the frontal area of the cube to the vertical cross sectional area of the computational domain, should be no greater than 3 percent. The blockage ratio for these tests ranged from approximately 1.5 to 3 percent. Furthermore, symmetry boundaries were specified to further reduce the effect of the sides and lid of the domain. The conditions at this boundary are:

1. no flow across the boundary
2. no scalar flux across the boundary.

The normal velocities are set to zero at the symmetry boundary and the values of all other properties just outside the solution domain are equated to the nearest node just inside the domain.

The position of the outlet boundary is another important consideration (see Figure 17). The outlet boundary for a flow simulation must be placed at a sufficient distance from the inlet and obstacle to the flow so that there are no flow gradients in the flow direction. The flow at outlet must be in a state of equilibrium otherwise the interior solution to the flow problem will be influenced and the accuracy of the solution will be compromised. For high accuracy solutions it is recommended that the flow solution be compared for a number of different outlet positions to test sensitivity (Versteeg and Malalasekera 1996).

The domain was meshed to allow a high degree of resolution of the flow with particular attention paid to areas of high flow gradients at the points of flow impingement and separation. Full details on the grid refinement tests are given in section 6.3.9.

The computational domain for the skewed cube, whose relative length and width are equal to $2 \times (6 \times \text{cosine } (45°))$, was constructed to adhere to the blockage ratio requirements previously discussed.

6.3.5 Atmospheric Boundary Layer Inlet Conditions.

As the main aspect of this project was to determine the accuracy of a number of turbulence models in wind engineering flows it was particularly important to remove any other differences between the experimental and numerical results. It is well known that in a numerical wind engineering simulation even minor changes to the inlet conditions can significantly modify the predicted flow field. It is of paramount importance that the conditions at the inlet of any CFD simulation match, as far as possible, those of the wind tunnel or full-scale study. In order to obtain CFD results that could be directly compared with mean experimental values the ground roughness length was set equal to 0.01m to represent the fetch at the SRI and the cube walls were given a roughness length equal to 0.005m. Fully developed equilibrium atmospheric boundary layer flow profiles including variables such as stream-wise velocity, turbulent kinetic energy and Reynolds stress were specified at the inlet. These profiles allowed for a sustainable equilibrium boundary layer when used in conjunction with the appropriate wall roughness lengths. Full use was made of user FORTRAN routines that allow the user to override the simple default settings in CFX.

6.3.5.1 Silsoe Research Institute: Boundary Layer Inlet Conditions for the *k-e* Turbulence Model

Richards and Hoxey (1993) and Richards (1989), detail the computational inlet conditions for the Silsoe fetch for the *k-e* turbulence model. The following work details the methods used in deriving the appropriate equations.

In modelling the atmospheric boundary layer there are a number of important rules to follow that have been defined by Jensen (1958) and Ludwig and Sundaram (1969). The classical approach, and the starting point, is to define a two-dimensional thermally neutral boundary layer in which Coriolis forces are ignored, with all flow variables in equilibrium. It is stated that in steady incompressible two dimensional flow modelling the existence of homogeneous flow has the following properties:

1. the vertical velocity is zero
2. the pressure is constant
3. the shear stress is constant.

i.e. $$(\mu_l + \mu_t)\frac{\partial u}{\partial z} = \tau_O = \rho u_*^2 \qquad (6.1)$$

Using these rules and assuming that the atmospheric boundary layer is in equilibrium with the ground, the researchers at the SRI used a suitable velocity profile at the inlet based on the Harris and Deaves (1981) model. This model states that the mean velocity profile in the lower part of the atmosphere may be adequately described by:

$$U(z) = \frac{u_*}{k}\left[\ln\left(\frac{z + z_0}{z_0}\right) + 5.75\frac{z}{d}\right] \tag{6.2}$$

$$u_* = \frac{k.U_{ref}}{\left(\ln\left(\frac{Z_{ref}}{z_0}\right)\right)} \tag{6.3}$$

(Richards 1989)

The corresponding derivation of the k and e profiles is obtained from Richards (1989).

In the equilibrium boundary layer it is assumed that the shear stress decreases parabolically with height, as follows:

$$t_{(z)} = ru_*^2\left[1 - \left(\frac{z}{d}\right)\right]^2 \tag{6.4}$$

As an equilibrium boundary layer is being modelled and there is no change of fetch the rate of generation of turbulent kinetic energy will ideally equal the rate of dissipation. This further implies that:

$$e_{(z)} = \text{generation of } k = \frac{t_{(z)}}{r}.\frac{\P u_{(z)}}{\P z} \tag{6.5}$$

So substituting Equations 6.2 and 6.4 into Equation 6.5 gives

$$e_{(z)} = u_*^2\left[1 - \frac{z}{d}\right]^2.\frac{u_*}{k(z + z_0)}\left(1 + \left(5.75\frac{(z + z_0)}{d}\right)\right) \tag{6.6}$$

Now turning the attention to the complementary profile equation for the turbulent kinetic energy k:

$$k = \frac{1}{2}\left(\overline{u'^2} + \overline{v'^2} + \overline{w'^2}\right) \tag{6.7}$$

The velocity fluctuations or normal Reynolds stresses in this equation may be derived by considering the turbulent viscosity as defined in the *k*-*e* model:

$$m_t = rC_m \frac{k^2}{e} \tag{6.8}$$

Referring back to chapter 4, because the turbulent viscosity greatly exceeds the laminar viscosity it follows that:

$$t_{(z)} = m_t \frac{\P u_{(z)}}{\P z} \tag{6.9}$$

and hence from Equations 6.3, 6.4, 6.7 and 6.8:

$$k = \frac{u_*^2\left(1 - \frac{z}{d}\right)^2}{\sqrt{C_m}} \tag{6.10}$$

In many cases the domain is considerably shallower than the layer thickness, or so called gradient height, which is typically at least a few hundred metres. In such circumstances it is reasonable to set the function of variation of shear stress across the layer equal to 1 (Richards and Hoxey 1993).

Equations 6.2, 6.6 and 6.10 are reduced accordingly as follows:

$$U_{(z)} = \frac{u_*}{k}\ln\left(\frac{z + z_0}{z_0}\right) \tag{6.11}$$

$$k = \frac{u_*^2}{\sqrt{C_m}} \tag{6.12}$$

$$e = \frac{u_*^3}{k\left(z + z_0\right)} \tag{6.13}$$

Equation 6.11 has been derived from the Deaves and Harris (1981) mean velocity profile model, as stated earlier. Further assumptions regarding the shear stress profiles, the eddy viscosity concept and equilibrium relationships between kinetic energy production and dissipation have resulted in Equations 6.12 and 6.13. Theoretically these equations should represent the boundary layer profiles of the atmospheric wind at the SRI. Richards and Hoxey (1993) have directly compared these profile equations with full-scale site data and found that there is an acceptable match. Modifications since 1993 have included the inclusion of acceptable decay profiles with height for both the k and e equations. Furthermore, these equations have been accepted by CFX International as suitable representations of the boundary layer and are supplied to users upon request (Sinai 1995).

6.3.5.2 Appropriate Inlet Conditions for the Differential Stress Turbulence Model

A further procedure was necessary to generate equilibrium profiles of variables for the differential stress model that could be entered into the cube flow field simulations as boundary layer inlet conditions. These tests used a short length of a computational domain with mass flow boundaries at inlet and outlet set as a single patch with zero mass flux. This method effectively recycles the outlet flow therefore replicating a very long wind tunnel or length of fetch. As it is not possible to set an inlet velocity using this method, the floor of the 'virtual' wind tunnel was made to move with a horizontal velocity. The moving floor ensured that the necessary shear in the flow was generated due to the specification of a ground roughness equal to 0.01m. Using this technique it was envisaged that the turbulent kinetic energy, Reynolds stresses and energy dissipation profiles would develop in the same way as if an inlet velocity had been specified, as these flow variables are invariant under coordinate transformation. These tests were also undertaken for the standard k-e model.

The boundary layer data generated was incorporated into the CFD simulations by fitting curves to the first 40m of the profiles and entering the equations into the appropriate user FORTRAN routine.

Validation of the numerical boundary layer generated was possible through comparisons to published work by Richards and Hoxey (1993) entitled 'Appropriate boundary condition for computational wind engineering models using the k-e

turbulence model'. This paper details equations that specify the velocity profile as well as a maximum value of turbulent kinetic energy and energy dissipation at ground level for the Silsoe fetch (see section 6.3.5.1). Figure 18, which shows velocity profiles for the differential stress and standard *k-e* models, with a reference velocity of 10m/s at 60m, shows that there is an exact match between the numerically derived velocity profiles from the SRI data and the DSM numerically derived profile. Substitution of the friction velocity into the turbulent kinetic energy equation derived by Richards and Hoxey (1993) shows that the differential stress model accurately predicts the maximum ground turbulent kinetic, at $0.00008 m^2/s^2$ for a simulation velocity of 0.1 m/s at 60m (as shown on Figure 19). It is explained by Sinai (1995), that in the absence of information on the shear stress profiles a constant, linear or more accurately a quadratic decay profile should be assumed. Analysis of the profile shown in Figure 19 shows that the quadratic profile assumptions are in fact closest to the decay profile generated by the computational simulations. Therefore using the available experimental boundary layer data it is apparent that the DSM predicts an accurate match to experimentally obtained mean data. In addition, previous investigations have been undertaken to obtain more detailed information on the boundary layer at the Silsoe Research Institute. To date a number of experiments have been conducted to provide full-scale fluctuating velocity data using both 20hz and 100hz anemometers (Hoxey and Richards 1992 and Richards and Hoxey 1999). Mean profile data from these results for the various Reynolds stresses have highlighted discrepancies that, for example, show the magnitude of the stresses increasing with height above ground. It appears from the spectral analysis that the anemometry equipment was unable to record the correct magnitude of the Reynolds stresses due to the smaller scale higher frequency fluctuations near the ground, particularly in low wind speeds (Quinn 1999). This is perhaps an unfortunate consequence of using full-scale comparative data. It has therefore proved difficult to use any of the more detailed experimental data thus far. Nonetheless it should also be emphasised that simulations with the DSM have used sustainable equilibrium boundary layer inlet conditions generated as explained. Any attempt to force any other inlet conditions would result in a rapid decay or change in the variable profiles as the computational fetch is traversed.

6.3.6 Variations on the Ground and Building Roughness Length

Discussions with Drs Hoxey (1999) and Robertson (1999) at the SRI suggest that the roughness length of the fetch at the Institute may vary, throughout the year, from

approximately 0.008 to 0.04m. It was also stated that variations between these limits have no noticeable effect on the recorded full-scale mean pressure distributions. The majority of CFD tests undertaken have used an average roughness height of 0.01m. It was therefore decided to undertake a small number of tests with modifications to the roughness height between the limits discussed. Figures 20 and 21 show the windward face and roof pressure distributions for the quadratic non-linear *k-e* model, firstly with the ground and inlet roughness length set to 0.04m and secondly with the ground roughness at 0.01m and the building roughness reduced to 0.001m. Interestingly it can be seen that for the computational tests the increase in the turbulence due to the higher roughness length has the effect of marginally increasing the front face stagnation pressure and increasing the roof front corner maximum negative pressure. This in turn causes a shorter recirculation zone that reattaches half way along the roof and a steeper pressure gradient recovery (these effects are discussed in full in the following chapters). These effects, whereby the flow and pressure fields are modified as the incident wind turbulence increases, are well documented, the interested reader is referred to Castro and Robbins (1977). The effects of changing the building roughness were negligible. Drs Hoxey (1999) and Robertson (1999) of the Silsoe Research Institute have confirmed that the cube, wall and SSB experiments were conducted during the winter months. Furthermore analysis of the incident wind, by members of the SRI, during these tests has further confirmed that the effective roughness length was equal to 0.01m.

6.3.7 Revision to Wall Functions for the High Reynolds Number Turbulence Models.

Analysis of the high Reynolds number wall functions used to model rough walls, and included in the CFX supplied user FORTRAN, showed a discrepancy upon comparison to the terms used in a number of other codes, including Star CD and Fluent (Hargreaves 1998).

The standard wall function used in CFX is as follows:

$$\frac{u_p}{u_*} = \frac{1}{k}\ln(Ey^+) \qquad (6.14)$$

where u_p is the velocity of the fluid at a point p near the wall, E is an empirical constant, k is the Von Karman constant, u_* is the friction velocity and is given by:

$$u_* = \sqrt{\frac{t_w}{r}} \tag{6.15}$$

where t_w is the wall shear stress.

When a rough wall is encountered with an average roughness height K_s, Equation 6.14 needs to be modified in the following manner:

$$\frac{u_p}{u_*} = \frac{1}{k}\ln(Ey^+) - \Delta B(K^+_s) \tag{6.16}$$

where ΔB is the amount by which the rough wall velocity profile changes and is a function of the dimensionless roughness, $K^+_s = rK_s u_* / m$. With some manipulation (section 14.6 of the FLUENT Users Manual Version 4.22 (1992)) this can be written as:

$$\frac{u_p}{u_*} = \frac{1}{k}\ln\left(\frac{Ey^+}{1+0.3K^+_s}\right) \tag{6.17}$$

with

$$E' = E/(1+0.3K^+_s) \tag{6.18}$$

It is explained by Versteeg and Malalasekera (1996) that the thickness of the laminar sub-layer will change depending on the effective Reynolds number at the near wall node. In a similar manner the log layer thickness changes depending on the flow velocity, Reynolds number and wall roughness along any given wall.

The standard CFX rough wall function incorrectly assumes a constant log layer value as detailed in Equation 6.14 and therefore does not account for the changes described by Versteeg and Malalasekera (1996). As a consequence it was necessary to amend the rough wall functions used in CFX to allow calculation of a dynamic log layer constant through the appropriate user FORTRAN routine and check a number of the simulations to assess if there are any differences in the results obtained. Figures 22 and 23 show comparisons of the computed windward face and roof pressure distributions predicted by the non-linear *k-e* model, for the 6m cube, with CCCT convective differencing. It is apparent from these results that there is a very small

difference between the use of the original and revised wall functions. This test was repeated for a number of other turbulence models and cube orientations, which all showed similar results. Nonetheless, all tests have used the revised wall functions described.

6.3.8 Assessment of the y^+ Values

As explained in section 4.3 a near wall flow is taken to be laminar if the non-dimensionalised wall distance y^+ is less than 11.22. When using high Reynolds number turbulence models it is very important to check that the finite volume mesh does not encroach into this region. If this is the case the turbulence model will attempt to solve a transport equation validated for the turbulent region of the flow in an area of purely laminar flow and consequently significant errors occur. As the simulations presented in this thesis required high levels of accuracy it was necessary to use a large number of nodes to grid the domain, therefore checks had to be undertaken to assess whether the y^+ values were satisfactory. CFX4.2 can provide the y^+ values for every node in the finite volume domain. As a consequence of these checks model domains and finite volume meshes were amended as necessary.

6.3.9 Grid Refinement tests

The level of grid refinement can have a significant effect on the accuracy of the flow pattern produced by the CFD simulation. In regions of separated recirculating flow, such as found on the windward edge of the roof on a surface mounted cube, it is possible to not resolve the change of direction of flow if a coarse grid is used. The absence of separation is due to the integration of the flow over a whole cell, which if only a small part of it is negative or reversed, will result in a net flow which remains in a stream wise direction.

All CFD simulations should therefore be able to adequately prove that a sufficiently fine mesh has been used. This is done by demonstrating that successive grid refinements do not change the flow field in any way. Therefore extensive grid independence checks were undertaken with both the cube and SSB for a number of model orientations as detailed below. Simpler tests were carried out for the experimental wall structure, which was found to be less sensitive to grid refinements. The grid independence tests were as follows:

1. a 300 percent increase in the number of grid points in the computational domain (total nodes approximately 550,000).

2. As part 1, plus a further 200 percent to 450 percent increase in the number of grid points around the cube only (i.e. increases from 20^3 to 90^3 grid points on the actual cube), depending on the cube orientation (total nodes 850,000 to 1.2million).

3. For the SSB three successive grid refinement tests were undertaken with, approximately, a 100 percent increase, per refinement, in finite volume nodes, using the most critical test case, the SSB with sharp eaves.

Test part 2 was necessary in order to confirm or otherwise that small scale flow effects, such as the delta wing vortex on the skewed model, had been adequately resolved. Obviously this is particularly important in order to accurately predict the pressure distributions and the cube flow field. Murakami (1990) further discusses the above mentioned points. All these tests used the RNG and non-linear *k-e* models and CCCT differencing.

Figures 24 and 25 show the RNG *k-e* model predicted windward face and roof pressure distributions for the normal cube test 1. It can be seen from this graph that there is a minimal change between the two grids used. These results were also found for other turbulence models including the non-linear and standard *k-e* models and for the skewed cube orientation.

Using only the normal cube, test number 2 showed revised pressure distributions for the roof of the cube only (see Figure 26). A negligible difference was found for the windward and leeward face of the cube. Further refinements made to the grid which involved increasing the number of points around the cube from 40^3 to 60^3 (see Figure 27) showed no further changes to the predicted pressures on the roof of the cube. As it was not possible to obtain sufficiently converged results for the DSM only the RNG and non-linear *k-e* models were run to the highest levels of grid refinement.

Figures 28 and 29 show the roof pressures distributions for grid refinement test 2 with the cube at 45° to the incident wind, for the non-linear *k-e* model. These tests used four different grids incorporating 150,000 to 1,250000 nodes. As a negligible difference was found for the windward and leeward face of the cube the main aim of

these tests was to attempt to adequately resolve the delta wing vortex. The grid refinements incorporated 20^3, 40^3, 60^3 and 90^3 grid points around the actual cube. The graphs show that as the number of grid points increased the simulations were able to more accurately predict the sharp negative peak at the front corner. Unfortunately it was not possible to obtain a grid independent solution for the flow at the very front corner of the skewed cube, due to computer hardware memory limits. This suggested that the vortices produced have a very high angular velocity and therefore are very small and difficult to resolve. Figure 30 highlights the predicted increase in strength of the delta wing vortex (middle section of the cube), with refinement of the grid. Due to the excessive run times of these simulations it was decided not to test the standard and MMK *k-e* models, which were found to produce poor results for relatively coarse meshes, as described later. Furthermore, it was not possible to obtain adequately converged solutions when using the differential stress model

Figure 31 shows grid refinement tests for the SSB, with sharp eaves at a normal orientation, for comparisons between 220,000 and 440,000 and 750,000 node model runs. In a similar manner to the earlier tests there was a negligible difference between the pressures for the front and leeward faces of the building. It can be seen that, for the windward roof, there is a negligible difference between the latter two grids consequently the majority of SSB simulations were undertaken with approximately 500,000 nodes. These results were initially surprising when considering the refinements needed for the 6m cube. Analysis of the results for the 6m cube showed that only the roof area produced changes with successive grid refinements. Therefore it appears that as the roof of the SSB is pitched the predicted velocity gradients on the roof of the SSB are less severe therefore reducing the level of grid resolution required. This is particularly so for the SSB with curved eaves where there is no flow separation.

Grid refinement tests for the experimental wall structure, from the original model with 550,000 nodes to approximately 1 million nodes, showed no change in the predicted mean pressure coefficients (see Figure 32).

6.3.10 Double Precision Checks

All the numerical simulations for this project were run using single precision numerical accuracy. The effect of rounding off the solutions over a number of iterations can be a source of error in the calculations. Therefore a small number of

tests were undertaken to assess any possible effects of running the simulations with single precision accuracy. These tests used the RNG *k-e* turbulence model and CCCT convective differencing and the results showed that there was no difference between the single precision and double numerical precision results. Residual convergence histories can be seen on Figures 33 and 34, for a 6m cube simulation.

6.3.11 6m Cube Model - Reynolds Number Effects, changes to the Inlet Velocity

A number of simulations were run using the non-linear *k-e* model and CCCT differencing with inlet velocities of 0.1 and 10 m/s, set at a reference height of 10 metres, in order to assess the effects of increasing the Reynolds number by a factor of 100.

Figure 35 shows the normalised roof pressure distribution for the two simulations with differing velocities. It is clear from this graph that the change in Reynolds number from approximately 600,000 to 60 million had relatively little effect. Referring to Figure 36, it can be seen that there is an increase in the roof vortex recirculation strength of approximately 6 percent.

The latter results are not a surprise as one would expect a larger roof recirculation vortex as the Reynolds number increases due to a reduction in the effects of the fluid viscosity, i.e. Reynolds number vortex effects (Hoxey 1998). Consequently although only minor changes to the model predictions are shown all tests were run at a standard wind speed of 10 m/s at cube height. This velocity compared with the full-scale experimental wind speed data collection range of between 6 and 10 m/s. The small differences in wind speed between the full-scale and CFD data should have a negligible effect on the comparisons.

6.3.12 6m Cube Model - Effects of the Differencing Scheme.

All the simulations undertaken used both the CCCT (section 3.5.5) and Hybrid (section 3.5.3) differencing schemes. These particular schemes were chosen as they represent the most popular stable high and low order accuracy differencing schemes. Attempts to use the QUICK scheme with the *k-e* model were unsuccessful, due to the over and undershoots which are common with this scheme because of its lack of the boundedness property (section 3.5.4). Tests using upwind differencing were not

considered as it is very similar to the hybrid scheme when used in high Reynolds number flows (see section 3.5.3).

Figures 37 and 38 show the simulation results for the pressure coefficient and turbulent kinetic energy values calculated on the roof of the cube for both CCCT and hybrid differencing. Figure 39 shows the roof recirculation velocity calculated for the two differencing schemes.

The effects of numerical viscosity were apparent with all model simulations with the first order accurate hybrid differencing scheme. The most notable effects were an increase in the windward face and roof front edge mean pressure coefficients brought about by a general increase in the effective fluid viscosity and therefore an increase in the turbulent kinetic energy levels. For the 6m cube normal to the incident wind, with both the RNG and non-linear *k-e* model simulations, the extra numerical viscosity resulted in a 5-7 percent reduction in the length of the roof vortex.

The hybrid scheme, utilising upwind differencing is showing the effects of false diffusion, apparent in multi-dimensional flows if the velocity vector is not parallel to one of the coordinate directions. This can be graphically demonstrated by the calculation of a scalar property in a domain where the flow is at an angle of 45° to the Cartesian grid. By setting the flow to be laminar and using symmetry boundary conditions there should be no turbulent and minimal viscous diffusion of the scalar. The effects of false diffusion can be clearly seen on Figure 40 causing the scalar to disperse with distance along the domain for the hybrid scheme. Figure 41 clearly shows the reduced diffusion predicted by the higher order CCCT differencing scheme. It is therefore recommended that all CFD simulations should incorporate higher order convection differencing to achieve the highest levels of accuracy.

6.3.13 Use of High Reynolds Turbulence Models

For the tests undertaken in this project it has only been possible to use turbulence models that use wall functions in the near wall region. There are errors in using the oversimplifications for the wall functions in wind engineering simulations as reported by Murakami (1990). Unfortunately due to the size of the computational domains and the significant inlet velocities and high Reynolds numbers (see section 6.3.4) it proved impossible to mesh the geometries to allow sufficient resolution of the viscous sub-layer for the low Reynolds models. Low Reynolds number turbulence models require

approximately 30 nodes in the viscous sub layer alone with the two layer models requiring between 15 and 20 nodes. Therefore it is conservatively estimated that 1.5 to 2 million nodes would be required for the 6m cube model with the larger SSB geometries requiring an even greater number. An indication of the increased computational overheads required by the use of these models is given by Lakehal and Rodi (1997). It is stated that experiments using the standard *k-e* model with wall functions took 15 minutes to complete while similar two layer and low Reynolds number model tests required 6 and 20 hours respectively. Furthermore, it is reported by Hanjalic et al (1998) that two layer and low Reynolds number models produced only slight improvements to the predicted flow field around a surface mounted cube. This indicates that wind engineering flows are dominated by convection and diffusion of the large scale vortices and eddies that form around the cube and less by the small scale structures in the flow.

Finally it has been reported that the use of low Reynolds number turbulence models may significantly reduce the numerical stability of the model. Menter and Grotjen (1999) state that this is due to the highly non-linear damping terms used on the transport equations. Nonetheless, low Reynolds number turbulence models have been used to provide comparative data for the large eddy simulation runs reported in chapter 7, which use a revised computational domain to aid resolution of the sub-layer.

6.3.14 Solution Convergence

All the tests undertaken were ran to achieve high levels of convergence. For the eddy viscosity based models the minimal residual reduction factors achieved (that is the ratio of the second to last residual error values) were 1×10^5. Meeting this criteria for the differential stress model proved more of a challenge, particularly so when using CCCT differencing, therefore for the DSM the minimal residual reduction factors achieved were 1×10^3 to 1×10^5. If there were difficulties in obtaining residual reduction factors of greater than 1×10^3 further checks were carried out, which included analysis of the flow field for flow symmetry, to ensure adequate solution convergence had been attained.

6.3.15 Calculation of Pressure Coefficients.

The standard method of detailing pressure distributions in wind engineering are wind induced dynamic pressure coefficients, C_p, where ambient static pressures cancel out, for full details see Cook (1986b). Referring to Patankar (1980):

> 'If the absolute value of pressure were used, then round off errors arise in calculating differences for pressure at each face of the control volume. It is therefore best to set $p = 0$ as a reference pressure at a suitable grid point and to calculate all other values of p as pressure relative to this reference value.' (Patankar 1980, p131)

Therefore the CFX derived pressures are in an appropriate form to allow correct calculation of the pressure coefficients which are calculated by dividing the CFD derived pressure by the dynamic pressure calculated at 6m, obtained from $\frac{1}{2} r V^2$.

Nonetheless there is in fact a small error associated with this assumption as used in the following work. There are extra contributions to the dynamic pressure that need to be accounted for due to the effects of the turbulent kinetic energy in the flow. If the free stream turbulent kinetic energy levels are relatively low, at the reference height, then the additional terms will be small and of little consequence. The following text, provided by Dr Hoxey (1999) of the SRI, derives this additional contribution for the CFD calculations.

$$q = \frac{1}{2} r u^2 \tag{6.19}$$

$$\bar{q} = \frac{1}{2} r \overline{u^2} \tag{6.20}$$

$$= \frac{1}{2} r \overline{(\bar{u} + u')^2} \tag{6.21}$$

$$= \frac{1}{2} r \overline{\left(\bar{u}^2 + 2\bar{u}u' + u'^2\right)} \tag{6.22}$$

$$= \frac{1}{2} r \bar{u}^2 + \overline{u'^2} \qquad \text{since } \overline{u'} = 0 \tag{6.23}$$

or $$q = \frac{1}{2} r\bar{u}^2 \left(1 + \frac{\overline{u'^2}}{\bar{u}^2}\right) \quad (6.24)$$

$$= \frac{1}{2} r\bar{u}^2 (1 + I^2) \quad (6.25)$$

where I = turbulence intensity and in a complete analysis should include *u'*, *v'* and *w'*. Therefore Equation 6.25 becomes:

$$\bar{q} = \frac{1}{2} r(\overline{u^2} + \overline{v^2} + \overline{w^2}) \quad (6.26)$$

hence $$I^2 = \frac{\overline{u'^2} + \overline{v'^2} + \overline{w'^2}}{\bar{u}^2} = \frac{2 \times TKE}{\bar{u}^2} \quad (6.27)$$

where *TKE* is the free stream turbulent kinetic energy at the reference height, which for the cube model is equal to 1.187m^2/s^2. Therefore the actual value of dynamic pressure at the reference height of 6m for the cube, due to the mean and turbulent contributions, is:

$$\bar{q} = \frac{1}{2} r \times (10)^2 \times (1 + \frac{2 \times 1.187}{(10)^2}) \quad (6.28)$$

$$= \frac{1}{2} r \times (10)^2 \times (1.024) \quad (6.29)$$

The effect of the turbulent kinetic energy in the flow will result in an increase of the dynamic pressure of approximately 2.4 percent. Calculations for the SSB and experimental wall structure provided a similar result. Therefore it is apparent that the additional effects of the turbulent kinetic energy in the CFD calculations for the derivation of dynamic pressure are relatively small. The effects for the full-scale experimental work are more profound with an increase in the dynamic pressure of approximately 8 percent (Hoxey 1999).

6.3.16 Accuracy test summary.

A summary of the accuracy test results is given in Table 4 below. This table shows the sensitivity of the models tested to the changes discussed above as a worst case percentage error. Therefore the values given represent the maximum worst case

change in the predictions at some location on the front or roof of the model. This method of assessing the accuracy of the turbulence model with remain consistent throughout chapter 6.

Test information.	***Percentage error.***	
	Windward face	***Roof***
Domain size	Negligible	Negligible
Revision to the wall functions	5	5
Ground Roughness 0.01 to 0.04m	15	15
Building Roughness 0.005 to 0.001m	Negligible	Negligible
y^+ checks	-----	-----
Grid refinement – cube – normal	Negligible	10-15
Grid refinement – cube – skewed	Negligible	Unknown
Grid refinement – experimental wall	Negligible	Negligible
Grid refinement – SSB	2	12
Double precision	Negligible	Negligible
Reynolds number effects	Pressure 0	Pressure 0 / velocity 6
Full-scale press. coeff. error (approx.)	$\pm$ 1-2	$\pm$ 1-2
Calc. of dynamic pressure coefficient.	2.4	2.4
Changes to the differencing scheme	Pressure 10	Pressure 12 / velocity 30

Table 4: Accuracy test summary.

6.4 Turbulence Model Validation – The 2-Dimensional Backward Facing Step

As this project required the testing of a number of new turbulence models, as detailed in chapter 5, it was important to prove that the models were correctly coded and that they were capable of providing acceptable or improved flow field predictions.

Since the 1980 AFOSR–HTTM Stanford conference on complex turbulent flows the two-dimensional backward facing step has been established as a standard method of validating turbulence model performance and accuracy. Therefore this provided the ideal test case for the new turbulence models.

Basora and Younis (1992) have previously compared standard *k-e* model results with wind tunnel based 2D back-step tests undertaken by Kim et al (1980). Therefore to effectively calibrate a 2D back-step model for use as a test case, it was necessary to match the standard *k-e* model results produced by CFX4.2 to those found by Basora and Younis (1992). It was then possible to test the revised turbulence models and directly compare their accuracy to the experimental data.

Although the above mentioned models required access to source code to allow the author to implement them into CFX4.2 it was in fact possible to implement the MMK *k-e* model through the use of the user defined FORTRAN routines. As such this model was programmed and tested by Dr Andrew Quinn, of the Silsoe Research Institute, at an early stage in this project and kindly passed on to allow full testing in the following chapters.

Table 5 shows the results.

Turbulence model	***Reattachment. length***
Std k-ε	5.4h
Non-linear quadratic (Speziale)	------
Non-linear quadratic (Craft et al 1996)	6.5h
Non-linear cubic (Craft et al 1996)	7.15h
D.S.M (no wall reflection)	6.5h
D.S.M (wall reflection terms)	------
Experimental (Kim et al 1980)	7.0h

Table 5: Reattachment lengths for backward facing step

(h = step height)

The Speziale (1987) quadratic non-linear turbulence model was tested for this case but could not provide converged solutions. It has been reported by Speziale and Ngo (1988) that there are general convergence problems due to high gradients returned by the second derivatives of velocity brought about by the use of the Oldroyd derivative term (see Equation 5.16). As such this model will not be tested further in this report.

Preliminary testing of the DSM with the Gibson and Launder (1978) wall reflection terms for the 2D back-step test case was unsuccessful. The addition of these terms as sources to the Reynolds stress transport equation resulted in extremely poor numerical stability and a resulting lack of convergence.

Comparisons between the standard *k-e* model and the quadratic non-linear *k-e* model, detailed by Craft et al (1996), show no measurable difference in solution times. The extra time required per iteration of the non-linear model was offset by an increase in the speed of convergence, as this model avoids the unrealisable values returned by the production of the turbulent kinetic energy term in the standard *k-e* model.

In terms of the accuracy of the models tested it can be seen that the standard *k-e* model predicts the worst results with an error of approximately 23 percent. This was

followed by the DSM and the quadratic and cubic non-linear *k-e* models with errors of 7 and 2 percent respectively. These initial results combined with extensive checks of the new code added to CFX effectively validate the revised models and gave an early indication of possible improvements in the predicted flow fields.

6.5 CFD and Full-Scale Test Results

6.5.1 Cube Normal to the Incident Wind - Introduction

All of these tests included the 6m cube at a normal orientation to the incident wind with the computational domain 'constructed', as detailed in Figure 42. Further representations of the computational domain and mesh can be seen in Figures 43 and 44 respectively.

A total of 8 turbulence models were tested as discussed in section 6.1. The Speziale (1987) version of the quadratic model and the Craft et al (1996) version of the cubic non-linear *k-e* model were omitted due to their inability to meet the convergence criteria adopted. Discussions with Dickens (1999) of Computational Dynamics suggests that on the basis of his experience, of incorporating these models into Star-CD, the numerical instabilities are simply a result of the numerous extra terms present in the cubic model. Further refinements may be possible to improve the overall stability of this model.

Both the two layer model and the DSM with wall reflection terms were omitted from these tests due to the fact that a number of wind engineering simulations have already been undertaken and reported on (detailed in chapter 5). Furthermore, as explained previously, the need to tailor the DSM with wall reflection terms to each individual test case immediately made it difficult to justify as a 'generic' turbulence model to be used by the wind engineering community.

All graphs and data presented are for cube centreline measurement positions unless otherwise stated, as shown in Figure 45.

Although it would have been preferable to directly compare mean turbulent kinetic energy and Reynolds stress profiles from the experiments undertaken at the SRI with CFD data this was, unfortunately, not possible. At present only the mean pressure

coefficients and recirculation vortex reattachment length data are available. Nonetheless, this information was sufficient to clearly distinguish which CFD models were the most accurate in wind engineering applications.

6.5.2 Roof / Wake Flow Field Patterns

Turbulence Model.	*Roof Reattachment.*	*Wake Reattachment.*
Standard k - epsilon.	No separation.	2.1H
M.M.K. k - epsilon.	No reattachment.	3.12H
RNG k - epsilon.	0.84H	2.5H
Non-lin. Quad., k-eps.	0.75H	2.2H
Differential stress.	No reattachment.	2.1H
Exp. ((Hoxey 1999)	0.5-0.6H	1.2-1.4H

Table 6: Reattachment lengths: cube normal to the incident wind.

(H = cube dimension)

Table 6 shows the CFD and experimentally obtained reattachment locations for the roof and wake recirculation vortices. The non-linear and RNG *k-e* models predicted the most accurate roof reattachment lengths with respective errors of between 25 to 50 percent and 40 to 68 percent. The standard *k-e* model predicted no separation in contrast to both the MMK *k-e* and differential stress models, which did not predict any reattachment of the roof vortex. For the wake recirculation the differential stress and standard *k-e* model simulated the most accurate vortex followed by the quadratic non-linear *k-e* model. Surprisingly the standard *k-e* model predicted a relatively accurate wake recirculation length and the MMK poorly calculated the wake flow field. The results for standard *k-e* models wake were also found by Hanjalic et al (1998). It should be noted that none of the models tested was able to accurately predict the length of the wake vortex. The comparative vortex strengths are shown on Figures 46 and 47. Figures 48 to 52 show the roof velocity vectors for the turbulence models tested.

6.5.3 Normal Cube Mean Pressure Distributions

Figure 53 shows the centreline windward face mean pressure coefficient distributions. It can be clearly seen that the standard *k-e* model over predicted the pressure distribution by approximately 25 to 30 percent at the flow stagnation point. The remaining four models all predicted relatively similar results within approximately 10 percent of the experimentally obtained values. The differential stress model calculated

the most accurate result with a pressure distribution marginally closer to the experimental value. It is also apparent from the results that the CFD predicted stagnation points are approximately 0.5m higher than that obtained by experiment.

Figure 54 shows the centreline pressure coefficient distributions for the roof of the cube. The differential stress and the non-linear quadratic model predicted similar pressure distributions and the most accurate suction peak pressures within 5 percent of the peak mean experimental values. The RNG and MMK *k-e* models slightly over and under predicted the peak pressure at the front edge of the cube respectively, although an accurate assessment was difficult due to the fact that the nearest experimental point was 0.4m from the edge of the cube. The standard *k-e* model over estimated the peak suction pressure by approximately 65 percent. It is apparent that none of the models tested could accurately predict the pressure distribution over the remainder of the roof with even the best CFD results calculating errors of 20 to 30 percent. Grid refinement tests for the RNG and non-linear *k-e* models resulted in an overall improvement of 5 to 10 percent for the roof pressure distribution.

It should be noted that there are a few inconsistent experimental points both on the side wall and most noticeably on the roof of the cube that cannot be fully explained. According to Hoxey et al (1999) these errors are most likely due to approach flow turbulence intensity variations. These possible errors are to be the subject of further investigations by the SRI (Hoxey et al 1999).

The CFD results presented thus far are not as good as might be hoped, although they do display the correct magnitude and trends in many cases.

The leeward pressure distributions can be seen on Figure 55. It was again apparent that none of the models tested could accurately predict the experimentally obtained distribution. The best results were obtained from the quadratic non-linear *k-e* model, although errors of approximately 30 to 35 percent were still apparent. The next most accurate model was the RNG *k-e* model. The DSM predicted the worst results with errors of up to 50 percent. It appears that the under predictions of negative pressure are a consequence of the over prediction of the wake recirculation and the corresponding lack of velocity deficit. These results confirm the need to accurately simulate the flow field around the bluff body. No improvement was found with grid refinement and there is some question over the middle experimental value obtained which appears to be out of sequence with the remaining values.

The side face and lateral roof pressure distribution can be seen on Figures 56 and 57 respectively. The experimental results for the side face showed a slow increase in negative pressure as the wind velocity increases with height. It can be seen that this trend was well reproduced by the MMK and RNG *k-e* models but not so well by the remaining models. The standard *k-e* model predicted the highest negative pressures for the first 3m height of the side face, possibly for the same reason that it failed to calculate flow recirculation over the roof of the cube, due to excessive prediction of turbulent kinetic energy as described below. Between 3 and 6m in height it is apparent that the non-linear model predicted the most accurate values with errors in the side and roof pressure prediction ranging from 20 to 30 percent and 30 to 40 percent respectively. Figure 57 further demonstrates the results shown by Figure 54, highlighting the inability of the models tested to accurately calculate the pressure distribution over the roof of the cube. The trend shown by the experiment represents the reduction in size and strength of the roof recirculation zone as the sides of the cube are approached and the mass of air flowing over the roof is reduced. It is clear that the experimental results are affected to a much larger extent by this three dimensional phenomenon, due to the significant difference between the centre and edge negative pressures. This perhaps suggests that the roof recirculation zone in the full-scale experiments contains a much stronger vortex than that predicted by CFD. This would further explain the slow reduction in negative pressure, for the experimental results, as the roof is traversed as shown on Figure number 54.

6.5.4 Turbulent Kinetic Energy Distributions.

Figures 58 and 59, show that at the front corner of the cube the standard *k-e* model predicted levels of turbulent kinetic energy that are several factors higher than those predicted by the differential stress model. The MMK *k-e* model predicted the lowest values of turbulent kinetic energy closely followed by the differential stress model. The non-linear and RNG *k-e* models calculated the next highest turbulent kinetic energy levels. In addition, Figure 59 shows that, both these models predicted a slight increase in turbulent kinetic energy in the region of the flow recirculation. Full kinetic energy contour plots for the range of models tested can be seen in Figures 60 to 64. The excessive stagnation and front corner turbulent kinetic energy predictions by the standard *k-e* model can be clearly seen, which are in contrast to the predictions by the other models. Full discussion of these results and their effects is given in section 6.9.

6.5.5 Pressure and Velocity Distributions – Cube orientated at 45°

The line positions shown (see Figure 65) indicate the locations used when recording data with the CFX-Visualise linegraph package. These cover the locations of the pressure taps for the full-scale experiments. All other experimental data is as described in the previous sections.

Figure 66 shows the CFD predicted strength of the lateral velocity over the roof of the cube. This graph therefore shows the relative strength of the delta wing vortices predicted. The differential stress model and the non-linear and RNG *k-e* models all predicted the highest velocities closely followed by the MMK *k-e* model. The standard *k-e* model, as would be expected, predicted the weakest vortices. Figure 67 shows a vector plot of the counter rotating vortices at the same measurement location used for the data shown on Figure 66, at the middle section of the cube.

Figure 68 shows the CFD and experimentally obtained pressure coefficient distribution for line number 1 (Figure 65). The differential stress model appears to calculate the most accurate values with the predicted pressure distribution within 15 percent of those obtained from experiment. The standard *k-e* model again appears to over predict the mean pressure at the stagnation point, although with a lower error than for the normal cube due to the reduced flow impingement. The remaining models all calculated similar front face pressures with an error of approximately 25 percent. In addition, all the CFD models simulated a flow stagnation point approximately 1.0 to 1.5m metres higher than that obtained from the full-scale experiment.

Figure 69 shows the roof pressure distributions for measurement line 2. The differential stress model predicted the highest suction pressure, perhaps as a consequence of calculating the strongest delta wing vortices. In this case the standard *k-e* model calculated the least negative pressures due to the prediction of very weak delta wing vortices. Successive refinements of the grid over the cube achieved a 15 percent increase in the peak pressure over the roof and improvements to the distribution of the pressures, see Figure 70. Unfortunately computational limitations did not allow calculation of a grid independent flow field for the roof. Nevertheless the overall predicted pressure distribution is relatively accurate for the turbulence models tested with an increase in accuracy of both the peak pressure and remaining profile upon successive grid refinements.

Referring to Figure 71, which shows the predicted pressure distributions for measurement line number 3, it can be seen that non-linear model calculated the most

accurate values with an error of approximately 40 percent. In addition, this model calculated a relatively accurate pressure distribution profile with a small increase at the centre of the cube. The DSM closely followed the non-linear model with the standard *k-e* model predicting the worst distribution with errors of up to 60 percent. None of the latter models correctly predicted the profile of mean pressure on the leeward face of the cube.

6.6 The Silsoe Structures Building (SSB)

6.6.1 Introduction

A number of different SSB geometries and orientations have been tested, for comparison to full-scale data, including the following:

1. SSB with sharp eaves normal to the flow

2. SSB with curved eaves at both normal and transverse orientations to the flow.

All the considerations detailed in the previous sections, relating to the obtaining of high quality CFD results, were fully applied to the SSB test case. Furthermore, considerations beyond those highlighted for the cube model were necessary due to the further complexity of this structure. Bickerton et al (1996) has reported that special care has to be taken to ensure that the method of domain construction and direction of the grid lines does not influence the flow field. This is particularly important in the region of the leeward roof where grid lines parallel to the roof may, for shallow angles, influence whether the flow remains attached or separated. Consequently tests were undertaken with different block structures that fully addressed these points and showed that for this case there was no noticeable effect to the roof flow field or pressures distribution calculated.

Due to the relatively poor results found from the application of the MMK *k-e* model to the 6m cube (section 6.6) it was decided not to test the model further.

Figure 72 details the SSB geometry and pressure measurement locations that extend along the position shown from the windward to the leeward face:

Full details of the experimental procedure, the Silsoe structures building (SSB) and further references are given in section 6.2.2.

6.6.2 Flow Field and Pressure Coefficient Distribution – SSB with Sharp Eaves at a Normal Orientation to the Incident Wind

For this orientation all CFD simulations, bar the DSM, were run with a reference velocity of 10 m/s at the ridge height. In order to obtain converged results with the DSM it was necessary to reduce the velocity to 1 m/s. Previous tests (see section 6.4.1) with the cube model and the SSB have shown a minimal difference in the normalised predicted flow field and pressure distributions for the differing velocities. This is due to the fact that both velocities involved sufficiently high Reynolds numbers.

Turbulence model	*Reattachment length*
RNG *k-e*	1.8m
Std *k-e*	No separation
Non-linear quadratic *k-e*	1.2m
DSM	2.0m
Experimental (Hoxey 1999)	1.0 – 1.5m

Table 7: Reattachment lengths for the front corner vortex: the SSB

Table 7 provides reattachment length detail for the roof vortex formed on the windward roof as a consequence of flow separation at the sharp front edge of the building. It can be seen that the non-linear model predicted the most accurate vortex length of all the models tested. It is also apparent that the differential stress model predicted flow reattachment in this case as a consequence of the pitched roof.

Figure 73 details the windward face pressure distribution at measurement line 3 (see Figure 72). It can be seen that all four CFD predictions follow the correct trend with the non-linear *k-e* model predicting the most accurate pressure distribution closely followed by the RNG model with respective worst case errors of approximately 20 and 35 percent. In this case the differential stress model shows the worst prediction with errors of over 70 percent. Referring to the discussion offered for the 6m cube, this is a rather surprising result, as it can be seen that the differential stress model predicts a much lower level of turbulent kinetic energy than the standard *k-e* model (see Figure 74). For this test case it appears that the non-linear and standard *k-e*

models predicted the correct flow stagnation point location with the RNG and differential stress models under predicting the height by approximately 0.5m.

Figure 75 shows the windward roof centreline pressure distribution at measurement line number 3. It can be seen that the differential stress and non-linear models predicted relatively accurate and similar maximum mean peak pressures at the front edge of the building, although it should be stated that the nearest experimental value was approximately 0.5 metres from the windward edge of the SSB. For the remaining profile of the pressure distribution it appears that the differential stress model predicted a marginally more accurate distribution with a shallower gradient as the pressure recovers. The RNG and standard *k-e* models calculated a relatively similar peak suction pressure, significantly higher than predicted by experiment, with the standard model predicting a much steeper pressure recovery. The high negative pressure predicted by these models was due to the excessive calculation of turbulent kinetic energy at the windward face and roof of the building (see Figures 74 and 76). The steep gradient of the pressure recovery calculated by the standard *k-e* model is due to the lack of a predicted separation zone at the front edge as simulated by the remaining models and present in the experimentally obtained data. For the overall pressure distributions the percentage error in the CFD calculations ranged from 20 to 40 percent. These results effectively mirror those produced for the 6m cube whereby the CFD models all calculated too rapid a pressure recovery along the roof. Figure 77 shows kinetic energy contours for the full SSB simulation, using the non-linear *k-e* model. The increased values of turbulent kinetic energy can clearly be seen at the roof recirculation point.

Figure 78 shows the leeward roof pressure distribution at measurement line number 3. It was apparent that the non-linear and standard *k-e* models showed very good agreement with the pressures obtained by experiment. The RNG *k-e* model showed an under prediction of the pressure of approximately 5 percent, with the differential stress model calculating the least accurate pressures, with an error of approximately 20 percent near the ridge of the building. The flow over the latter half of the windward roof and over the whole of the leeward roof remained attached perhaps explaining the improved accuracy of the results for the different turbulence models tested. Due to the minimal number of experimental pressure measurement points it was difficult to interpolate the results and ascertain whether the CFD derived peak pressures at the ridge of the building were accurate or not.

For the leeward face pressure distribution at measurement line number 3 (see Figure 79) it was interesting to find that the standard *k-e* model predicted the highest negative and most accurate pressure distribution. This was most likely due to the velocity deficit in the wake due to the excessive prediction of eddy viscosity in the simulation. This effect resulted in a relatively accurate wake vortex prediction for the 6m cube model. The differential stress and non-linear models predicted similar distributions with errors of around 15 percent. As noted earlier, the lack of experimental data in this region made an accurate assessment of the model performance particularly difficult.

6.6.3 Pressure Coefficient Distribution: The SSB with Curved Eaves at a Normal Orientation to the Incident Wind.

For this orientation all the models tested were ran with an inlet velocity of 10m/s at a reference height of 5.3m (ridge height).

Figure 80 details the windward face pressure distribution for the SSB, with curved eaves, at measurement line number 3. Interestingly this graph shows that CFD under predicted the pressures for all the turbulence models tested. This is in contrast to results discussed earlier for the SSB with sharp eaves where the CFD calculated pressures were all over predicted. The experimental values for the two cases are relatively similar with a slightly lower pressure coefficient distribution for the curved eaves case. This was most likely due to the smaller surface area presented at the front face due to the curved eaves. For both tests the DSM predicted the highest front face pressure distribution which, for this test, proved to be the most accurate with errors ranging from 5 to 25 percent. The non-linear model, which on the SSB with sharp eaves calculated the most accurate and lowest pressure distribution, in fact calculated the worst pressure distribution for this case with errors of approximately 35 percent for the majority of the front face. The RNG model predicted similar results to the non-linear model. All the models tested predicted the correct trends for the pressure distribution.

Figure 81 shows the windward face roof pressure distribution for measurement line number 3. It was apparent that the non-linear model predicted the most accurate distribution near the windward corner of the roof followed by the DSM. After approximately half way along the roof the standard *k-e* model predicted the best pressure distribution followed by the non-linear model with the least accurate

prediction by the DSM. For this case there is no prediction of a separation vortex due to the curved eaves, consequently the problems encountered by the standard *k-e* model for the 6m cube simulations are not apparent. Furthermore, it is again clear that CFD was able to provide far more accurate results for a test case where the flow remained attached, such as this case for the windward roof of the SSB with curved eaves.

Figure 82 shows the pressure distribution for the leeward roof at measurement line number 3. This graph shows that for the first metre along the measurement line the standard *k-e* model actually predicted the most accurate pressure distribution. This was perhaps a result of the standard *k-e* models relatively accurate prediction of the windward roof pressure distribution (latter half). This was combined with the prediction of a high level of turbulent kinetic energy, as shown on Figure 83, resulting in higher suction pressures at the ridge. The DSM was the next most accurate model along this section. Beyond the front section of the leeward roof the remaining turbulence models predicted very similar pressure distributions which accurately followed the experimental values with the standard *k-e* model over predicting the pressure distribution.

Figure 84 shows the leeward face pressure distributions. All the models tested followed the same pattern, as displayed for all the previous simulations, in under predicting the distributions. For this test the non-linear *k-e* model predicted the most accurate results followed by the RNG model with the standard *k-e* model and DSM predicting the least accurate distributions.

6.6.4 Pressure Coefficient Distribution – SSB Curved Eaves / Transverse Orientation

For this set of tests measurements were taken with the Silsoe structures building in a transverse orientation to the incident wind, as shown in Figure 72. Three measurement positions were chosen, as shown, to determine the pressure distributions along the building.

In this case it was found that the DSM would not produce results that met the convergence criteria. This problem continued after numerous attempts to improve the model by re-meshing the domain with lower geometric progression ratios, restarts from converged *k-e* model solutions, reductions in the inlet velocity and changes to

the solution parameters in the command language. Consequently these tests were completed using three *k-e* model variants, the standard, RNG and non-linear models.

Figures 85 and 86 show the CFD and experimentally obtained pressure distributions for measurement line number one on the side face and roof of the building respectively. Figure 85 shows that the non-linear and standard *k-e* model produced the most accurate pressure coefficients with errors ranging from 25 to 40 percent for the front face of the building. Interestingly the non-linear model showed a profile that was similar to that predicted for the side face of the 6m cube. Initially there is an increase in the negative pressure coefficient near the ground followed by a decrease after which all the models follow the same pattern. At present it is unclear why this particular profile is occurring. The general profiles calculated by the RNG and standard *k-e* models more accurately followed the trend shown by the experimental results.

Figure 86 shows that the non-linear model produced pressure coefficients within 10 percent of the experimentally obtained values. The RNG model is the next most accurate model with a consistent error of approximately 30 percent followed by the standard *k-e* model with modelling errors of up to 65 percent near the curved eaves. For this case the standard *k-e* model incorrectly predicted the profile along the roof of the SSB. This is quite possibly due to the failure of the model to calculate a recirculation vortex along the roof as detailed, for the non-linear *k-e* model simulation, in Figure 87. A recirculation zone occurs which is strongest at the ridge and non-existent at the edge of the roof. It appears that the standard *k-e* model predicted that the flow remains attached to the roof for the majority of the measurement line.

Figure 88 shows the side face pressure coefficient distributions for measurement line number 2 (Figure 72). This graph shows that the RNG *k-e* model predicted the most accurate results followed by the non-linear model and standard *k-e* model which over and under predicted the negative pressures, respectively. The roof pressure coefficients for measurement line number 2 are shown on Figure 89. This shows that the non-linear and RNG models calculated the most accurate peak pressures but failed to predict the correct gradient of the line as the pressure recovers along the roof. The standard *k-e* model predicted a much lower negative pressure distribution than the other models due to the early recovery of pressure along the roof caused by the lack of simulation of a roof recirculation zone, as previously detailed for the 6m cube tests.

Figures 90 and 91 show the side face and roof pressure coefficients for measurement line number 3 respectively. Both graphs show how all the models tested significantly over predicted the suction pressure distributions, with errors up to approximately 100 percent, on comparison to the experimentally obtained results. The general over prediction of pressures by CFD at measurement line number 3 may be due to an over prediction of the roof separation vortex as shown in Figure 87. It is possible, although by no means proven, that the vortex had reattached in the experiment leading to a faster pressure recovery than that predicted by the CFD tests. Overall, the transverse SSB test case has highlighted significant CFD modelling errors.

6.7 The Silsoe Experimental Wall Structure

6.7.1 Introduction

A schematic of the experimental wall, including information on measurement locations, is given in Figure 92.

Full details and further references for the experimental wall were given in section 6.2.3. In order to obtain high quality CFD data these tests were subject to the same accuracy checks as the 6m cube model and the SSB. All tests used 1:1 scale CFD models and the atmospheric boundary layer inlet conditions discussed in section 6.3.5. Due to the previous convergence problems found when using the differential stress model it was decided to compare the experimental wall data to CFD runs of the standard, RNG and non-linear *k-e* models only.

6.7.2 Pressure Coefficient Distribution: Experimental Wall Windward and Leeward Faces for a 0° (normal) Incident Wind.

Figures 93 and 94 show the CFD and experimentally obtained windward and leeward centre face pressure coefficient distributions for the experimental wall setup shown in Figures 16 and 92. For the windward face it can be seen that the non-linear and standard *k-e* models predicted relatively accurate pressure distributions at the centre section of the wall. The RNG *k-e* model over predicted the pressure coefficients at the centre of the wall with an approximate error of 20 percent. All the CFD models tested predicted a large pressure differential between the centre and edges of the wall, in contrast to the experimental data which showed relatively little change in the pressure

coefficients along the wall. The experimental results are therefore surprising considering that the flow is subjected to a greater obstruction at the centre than towards the edges, thus a higher stagnation pressure should be experienced at the wall centre. Referring to Figure 94 for the leeward face it can be seen that the standard *k-e* model calculated the most accurate results at the centre of the wall and least accurate at the edges with an error of approximately 80 percent. The non-linear model predicted the most accurate results overall with an average error of between 10 and 15 percent. The RNG *k-e* model calculated an error at the wall centre of approximately 40 percent with relatively accurate wall edge pressure predictions. This model appeared to more accurately follow the pattern shown by the experimental results although unfortunately it significantly over exaggerated the general trend towards a decrease in suction pressure at the wall centre.

6.7.3 Pressure Coefficient Distribution: Experimental Wall Windward and Leeward Faces for a 30° Incident Wind.

Figures 95 and 96 show the windward and leeward face mean pressure coefficient distributions for the experimental wall structure skewed at 30° to the incident wind. Referring to Figure 95 it can be seen that all the models tested over predicted the mean windward face pressure distribution with maximum errors of approximately 75 percent for the standard and RNG *k-e* models. The non-linear *k-e* model provided improved results with errors of up to 40 percent. The CFD calculated leeward face pressures were generally much closer to the values obtained from experiment with the RNG and non-linear *k-e* models both calculating accurate pressure distributions along the length of the wall. Unfortunately these models were unable to predict the maximum peak negative pressure at the leading edge of the wall. The standard *k-e* model predicted a peak negative pressure approximately 25 percent higher than that obtained from the experiment. Referring to Figures 97 and 98, it can be seen that the standard model calculated a higher level of turbulent kinetic energy in the wake region and at the leading edge of the wall, than the non-linear model. This had the effect of reducing the strength of the recirculation vortex on the leeward side of the leading edge of the wall (see Figures 99 and 100) resulting in a much higher peak negative pressure at this location. The reason for this was similar to that described for the 6m cube model tests (section 6.6.4)

6.7.4 Pressure Coefficient Distribution: Experimental Wall Windward and Leeward Faces for a 60° Incident Wind.

Figures 101 and 102 show the experimentally and computationally obtained windward and leeward face mean pressure coefficient distributions for the experimental wall structure skewed at 60° to the incident wind. These results showed a general reduction in the percentage error on comparison of CFD to experimentally obtained results. For the windward face, all the models tested provided similar results with a small improvement in the accuracy provided by the non-linear model. All the models tested provided accurate peak pressure predictions at the leading edge of the wall with the maximum errors at the far end of the wall where the CFD calculated pressure coefficients reduced too quickly. The results for the leeward face of the wall show accurate predictions for the maximum peak pressure, particularly so for the RNG and non-linear models, with CFD predicted errors in the remaining profile of approximately 20 percent. It is apparent that the flow only weakly separates on the leeward face thus returning high negative pressures at the leading edge, as demonstrated for the 6m cube results when using the standard *k-e* model. Referring to Figure 103 it is clear that this test case is less complicated than the former case as to a large extent the flow remained attached to the wall. This is highlighted by the fact that the results returned by the standard *k-e* model were, in this case, reasonably accurate. The reduced flow impingement on the leading edge and the consequent reduction in the turbulent kinetic energy produced allowed the standard *k-e* model to calculate a similar flow field to that predicted by the non-linear *k-e* model. This includes the small leeward face recirculation shown on Figure 103.

6.8 Turbulence model: Discussion

6.8.1 The Standard *k-e* Model

Referring to the experimental results obtained from the SRI it is clear that the standard *k-e* model cannot, in the majority of cases, adequately predict the flow fields and pressure distribution around a bluff body. Nonetheless, there were a few notable exceptions where the flow remained attached to the bluff body and flow impingement was not so severe and the standard model performed acceptably.

For the 6m cube model, the most severe errors were due to the inaccurate and excessive prediction of turbulent kinetic energy levels, particularly at the flow stagnation point. The results of which were to raise the maximum possible windward face stagnation pressure to a value greater than unity due to contributions from the three normal Reynolds stress turbulence components. In addition, the excessive values of turbulent kinetic energy predicted excessively mix and arrest the flow causing it to remain attached to the roof of the cube. This resulted in a poor flow field prediction and the sharp peak and large gradient of the negative pressure behind the upstream edge. It is also apparent that excessive levels of turbulent kinetic energy and thus eddy viscosity are generated for the majority of the flow field resulting in a surprisingly short wake recirculation. A similar result was found for the cube skewed at 45° to the incident wind with the excessive levels of turbulent kinetic energy reducing the strength of the delta wing vortices.

All of the models tested, including the standard *k-e* model, under predicted the leeward face pressure distribution for both the normal and skewed cube. The time averaged CFD simulations appear to predict an excessively high recirculation velocity in the wake. Therefore the velocity deficit produced in the wake by the full-scale cube was not matched by CFD and lower suction pressures were returned.

With regards to the results obtained from the SSB it appears that, on average, this model performed better than for the 6m cube test. This may be due to the fact that fewer demands are placed on the turbulence model when predicting the flow over a sloping rather than a flat roof. This is particularly the case when considering the SSB with curved eaves, where the flow remains attached over the entire building, with separation only occurring in the wake.

The standard *k-e* model performed relatively well for the Silsoe experimental wall structure, with the worst results returned for the case with maximum flow impingement, with the wall normal to the incident wind. As the wall was progressively skewed to the wind and the flow impingement and separation reduced the model provided increasingly accurate results that approached the accuracy of both the RNG and non-linear *k-e* models.

However, as was emphasised earlier, the standard *k-e* model fails mainly when modelling flows with significant impingement, due to the incorrect prediction of turbulent kinetic energy. The reason why the standard *k-e* model over predicts turbulent kinetic energy in such areas is due to the eddy viscosity model's inability to

deal with irrotational strain, which arises principally in impingement and reattachment zones. As eddy viscosity models have arisen from, and been calibrated by, reference flows which are strongly sheared they have great difficulty in dealing with flow fields which are dominated by extensive straining (Leschziner 1995). Hence eddy viscosity models which feature the turbulence energy transport equation tend to return excessive levels of energy and thus turbulent diffusion in the presence of strong compressive strain.

Therefore, to conclude, the errors brought about by the isotropic eddy viscosity assumptions and the resulting simplifications, particularly to the production term in the turbulent kinetic energy transport equation (detailed in full in sections 4.2.3.1 and 5.2.1) are primarily responsible for this model's poor performance.

6.8.2 The RNG *k-e* Model

Referring to the results obtained from the 6m cube tests, the RNG *k-e* model (detailed in section 4.2.6) appeared to produce relatively good results particularly when compared to the performance of the standard *k-e* model. It is the only widely available turbulence model that was able to predict flow separation and reattachment on the roof of the cube which in turn produced an improved roof pressure distribution. Generally this model predicted relatively accurate pressure distributions for all sides of the normal cube.

Similar improvements were found for the skewed cube, the SSB and the experimental wall cases with relatively accurate results returned. In fact the skewed cube case showed a significant increase in the predicted strength of the delta wing vortices, which is attributed to the reduced turbulent kinetic energy at the flow stagnation point.

There are several reasons for the RNG *k-e* models improvement over the results produced by the standard model. The RNG model is derived from renormalisation group analysis of the Navier-Stokes equations and incorporates revised model constants used to close the transport equations. In addition, the turbulence energy dissipation equation, which has long been considered a source of inaccuracy in both the *k-e* and differential stress model, has been revised. The *e* equation now includes a strain dependent term to aid the model in dealing with flows that experience large rates of deformation (see Equation 4.18). These two factors are very important in helping the model to deal with impinging flow fields and lead to reduced eddy

viscosity and turbulent kinetic energy production. It is stated by Orzag (1994) that the reduced value of Ce_2 compared with the equivalent standard *k-e* model coefficient has the beneficial consequence of decreasing both the rate of production of k and the rate of destruction of energy dissipation, leading to smaller eddy viscosities. The net effect of this is to increase the rate of energy dissipation that will in turn reduce the value of turbulent kinetic energy and eddy viscosity returned. Secondly, the strain dependent term in the modified e equation has the effect of modifying the rate of dissipation depending on whether the flow is subject to isotropic or strongly anisotropic turbulence. In areas of high straining, i.e. high turbulence anisotropy at flow impingement areas, the value of h becomes very large and the variable C_{RNG} may become negative. This will increase the production of energy dissipation in the dissipation equation leading to further reductions in the predicted eddy viscosities. Conversely in areas of low straining the value of h and consequently C_{RNG} becomes small, thus the equation for energy dissipation will tend towards returning results similar to the standard model equation. Therefore the net effect of these terms is to amend the errors apparent in the standard model in areas of high straining such as flow impingement as a consequence of the eddy viscosity concept.

Nonetheless, it should be noted that the RNG model predicted a less accurate wake recirculation than the standard *k-e* model. As the standard *k-e* model generally calculates high levels of eddy viscosity for the flow field it in turn calculates a smaller wake recirculation. The extra terms in the RNG model reduce the levels of eddy viscosity returned with the resulting error in the calculation of the wake vortex. This is compounded by the fact that the RNG model lacks the ability to predict anisotropic turbulence and underestimated the value of $v'v'$ in the wake region, which in turn leads to an underestimation of the momentum diffusion in the lateral direction (Murakami 1993). This is in fact an important result, as it demonstrates the effect of adding 'ad-hoc' terms to the turbulence transport equation whereby the accuracy of the flow predictions is increased in some areas and reduced in others. Furthermore, it should be noted that the additions to the RNG *k-e* model equations are not rigorously derived from the Navier-Stokes equations and are not bounded. Consequently it has been reported that in certain flow fields that experience very high levels of fluid strain, the additions can destabilise the model equations resulting in convergence difficulties and poor accuracy (Tehrani 1999).

6.8.3 The MMK *k-e* Model

With reference to the 6m cube test, the general aim of the MMK *k-e* model was to reduce the production of turbulent kinetic energy at the front face of the cube (see section 5.2). In this respect it achieved its aims, perhaps too well as the model appeared to calculate a roof flow field similar to that produced with a uniform incident wind (see Figure 5). The turbulent kinetic energy produced at the front edge now appeared to be too small and there is no flow reattachment on the roof whatsoever. It is also clear that the large roof recirculation had the effect of producing a wake recirculation that extended from the base of the cube to the top of the roof vortex. The net effect of this, combined with the low levels of turbulence and thus eddy viscosity, produced a wake recirculation for a cube of larger dimensions than that found by experiment. This highlights the importance of accurately predicting the correct flow field at all points over the cube. Nevertheless an improvement over the standard *k-e* model can be seen for the cube windward face and roof pressure coefficients.

Further tests were undertaken with the MMK model in an attempt to force the correct roof flow field. These tests involved making changes to the ratio of vorticity over shear, reducing the ratio set by Tsuchiya et al (1996) from 1 to 0.7 and 0.5. The general idea was to increase the turbulence production value before the MMK model was used and thus influence the roof vortex. These tests did not result in any improvements.

The results for the skewed cube model showed a marginal improvement in the pressure coefficient prediction around the cube and the strength of the delta wing vortices over the standard *k-e* model predictions. Overall it appears that although in some areas this model produced improved results over the standard *k-e* model, it also produced significantly poorer results in others areas. This again leads to the general conclusion that the use of ‘ad-hoc’ modifications is unsatisfactory in wind engineering simulations.

6.8.4 The Quadratic Non-Linear *k-e* Model.

The results presented previously show that for a number of cases the quadratic non-linear *k-e* model appeared to outperform the DSM both in terms of mean pressure distributions and predicted vortex dimensions. The fact that the more complex DSM

did not necessarily perform any better than the simpler models is also stated by Mentor and Grotjen (1999). It was also clear that improved predictions have been obtained with the anisotropic non-linear model over the isotropic eddy viscosity models such as the RNG and standard *k-e* models for the majority of simulations undertaken in this study.

Referring to the 6m cube test, it has been reported by Murakami et al (1996) that the DSM fails to predict reattachment of the roof vortex due to an underestimation of the *u'w'* shear stress at the front corner of the cube. Although absolute values are not available from the SRI experiments, Figures 104 and 105 show that the non-linear model predicted markedly higher values of the shear stress at the front corner, thus resulting in a more accurate vortex prediction. The reattachment of the roof vortex resulted in a marginally more accurate roof pressure distribution.

Figures 106 to 108 demonstrate the abilities of the non-linear model to predict anisotropic stresses and correctly shows the dominant stress over the roof to be the streamwise Reynolds stress. The results for the non-linear model should be contrasted with those produced by the standard *k-e* model shown in Figures 109 to 111. Although the standard *k-e* model calculates anisotropy in the normal stresses it is clear that the simple isotropic eddy viscosity model is incapable of accurately predicting the stresses. Figure 109, which highlights the streamwise normal stresses, shows a massive over prediction at the stagnation point and front corner of the cube. This is also the case for the lateral stress component, shown in Figure 110. Figure 111 seems to show reasonably low levels of the vertical normal stress component.

Murakami et al (1996) states that the DSM accurately predicts the distribution and anisotropy of the Reynolds stresses over the roof of a surface mounted cube and errors in both the eddy viscosity model and algebraic stress model are not reproduced. Figures 112 and 113 show that there is a very similar distribution of stresses along the roof for both the DSM and non-linear models. Furthermore, the non-linear model correctly predicted turbulence anisotropy and higher levels of the lateral *v'v'* Reynolds stress in the wake region, see Figures 107 and 114. However, it should be noted that the model incorrectly predicted the streamwise Reynolds stress to be the smallest in magnitude in the wake region. Nonetheless the results further validate the non-linear model and highlight its improved accuracy over the ASM and eddy viscosity models.

The prediction of the roof vortex size with the isotropic eddy viscosity models is usually related to the levels of turbulent kinetic energy produced at the front face stagnation point. Consequently it was interesting to note that although the non-linear model predicted a lower level of kinetic energy than the RNG model it still predicted a shorter more accurate roof vortex. This was most likely due to the increased lateral diffusion predicted by the model, due to its anisotropic turbulence modelling abilities, and the increased levels of shear stress returned as discussed above. The same arguments also apply to the wake region. Improvements over the standard *k-e* were also apparent for both the velocity and pressure distributions obtained from the skewed cube, although it should be noted that no improvement is apparent over the RNG model for this case.

The results from the Silsoe experimental wall and SSB experiments further demonstrated the non-linear model capabilities, although it should be mentioned that the latter results were generally poor for all the models tested for a number of the measurement locations.

Non-linear *k-e* models have been developed in an attempt to incorporate the effects of anisotropic turbulence and thus to try to obtain a width of applicability approaching that of the differential stress model. The advantage of using non-linear expansions of the Boussinesq hypotheses to develop improved turbulence models is that it should produce universal improvements. This is in contrast to ad-hoc improvements, such as the MMK model that may improve predictions only for a particular application of the model. To a much lesser extent, the wake results obtained from the RNG model have further highlighted this. The overproduction of turbulent kinetic energy, as explained in the *k-e* model results, is not an issue with this model, which uses the full turbulent kinetic energy production term. Furthermore, non-linear models require much less computational effort, due to their improved stability characteristics, as demonstrated in this work.

6.8.5 The Differential Stress Model.

The DSM, which solves an extra transport equation for each of the Reynolds stresses, is a fully anisotropic turbulence model. Each of the transport equations for the Reynolds stresses incorporates terms to deal with curvature related strain, adverse and favourable pressure gradients and other flow effects. Consequently when taking account of the greater modelling abilities of this more complex model it was rather

surprising to find that it does not predict a very accurate roof flow field for the 6m cube. The initial conclusion is that this error must be attributed to the lack of wall reflection terms in the pressure-strain model. However, Murakami et al (1993) has previously undertaken testing of a total of 6 differential stress models which incorporated different pressure-strain models for the flow over a surface mounted cube in an atmospheric boundary layer. Although a scale model was used, this simulation used the same general test case and flow field as the tests undertaken in this work. Therefore the physics and general effect of the extra terms will be identical. The results showed that there was no improvement in the prediction of the roof vortex. It is apparent from this that although these terms are important for certain flow fields, they are perhaps of relatively small importance for wind engineering flow fields that are dominated by the convection and diffusion of large scale eddies and coherent structures in the flow, as discussed in section 5.3.

Referring to the SSB simulations the DSM appeared to perform in a similar manner to the normal cube tests with similar accuracy to the RNG k-e model. Furthermore, the significant instabilities and convergence difficulties experienced when using the DSM with the 6m cube model, were further compounded with the SSB geometry. The general instability of this model resulted in the failure to successfully apply the DSM to any transverse SSB cases. Therefore these tests highlighted the inability of the DSM to provide converged results for a marginally more complex geometry than the previous test case and thus its failure to meet one of the most important criteria for a suitable wind engineering turbulence model. It could well be argued that the RNG model calculated a comparatively accurate pressure and flow field distribution at a far lower computational cost. Nevertheless the DSM provided encouraging improvements for the skewed cube case, which has traditionally been the cause of major errors with eddy viscosity models.

6.8.6 Results summary

The overall summary of the results of the testing, based on the criteria stated in the introduction (section 6.1) are given in Table 8.

Turbulence model	***Accuracy***	***Stability***	***Comp. overheads***
Standard k-e	Low	Medium-high	Low (1.2)
RNG k-e	Medium-high	High	Low (1)
MMK k-e	Medium	Medium	Low (1.2)
Quad non-linear k-e (Speziale 1987)	-------	--------	---------
Quad non-linear k-e (Craft et al 1996)	High	High	Low (1)
Cubic non-linear k-e (Craft et al 1996) *	High	Very low	Low (1)
DSM	Medium-high	Low	High (3)

Table 8: Results summary (* limited data available)

Note the assessments given are relative to the other turbulence models tested. The numbers given in the computational overheads column refer to the comparative run times (in days) for the different turbulence models, using the same model test case, when ran on a Digital Dec-Alpha Unix workstation.

Overall the accuracy of all the models tested in these wind engineering flow fields was disappointing. This was particularly the case for some of the measurement points on the SSB, which returned CFD prediction errors as high as 100 percent.

7. Large Eddy Simulation (LES).

7.1 Introduction

The subject of large eddy simulation is at present too important a technique not to investigate although, unfortunately, it is too large a subject to investigate fully as part of this thesis. The application of LES to computational wind engineering is worthy of several theses and therefore the aim of this chapter is to undertake a limited number of LES tests and to inform the interested reader of future work that should be pursued in this field.

The aim of this analysis was mainly as a preliminary study to both assess the difficulties in applying this technique to wind engineering and the minimum hardware requirements necessary. Interesting transient details omitted from the steady state simulations, undertaken in chapter 6, will be presented. The overall conclusions gained have been based on the validity of this model as a wind engineering technique in terms of its accuracy and applicability. The results of the LES work have also been compared to a number of steady state models simulations, including the low Reynolds number k-e and k-w and the high Reynolds number quadratic non-linear k-e models. All of these simulations have used the same model geometries with periodic inlet and outlet conditions to provide basic comparative data.

The following sections that detail the theory behind large eddy simulations are based on the work of Jacobsen (1997). The methods used to implement and test the LES technique, using CFX4.2, are based on the work of Jacobsen (1997) and Ciofalo and Collins (1989).

7.2 Theory: Filtering the Navier-Stokes Equations

With large eddy simulations it is essential to define those quantities that are to be computed precisely. A velocity field is required that contains only the large scale components of the total field. This is best achieved by filtering the large or resolved scale field (Leonard 1974). As such, in large eddy simulation, any physical quantity f is decomposed into two parts:

$$f = \bar{f} + f'' \qquad (7.1)$$

Here $\bar{f}$ is the resolvable scale component and f'' is the sub-grid-scale (SGS) component. Assuming that f'' is the filtered velocity, $\overline{u}_i$, then it is defined with a filter function $G(x,x')$ as follows:

$$\overline{u_i}(x) = \int G(x,x')u_i(x')dx' \tag{7.2}$$

The filter kernel $G(x,x')$ is a localised function and may include a Gaussian, box or cutoff filter. Every filter has a length scale associated with it that dictates which eddies are large and are directly resolved and which are small and therefore modelled.

Imposing the filter on the continuity and Navier-Stokes equations produces the following filtered equations:

$$\frac{\partial \overline{u}_i}{\partial x} = 0 \tag{7.3}$$

$$\frac{\partial \overline{u}_i}{\partial t} + \frac{\partial \overline{u_i u_j}}{\partial x_j} = -\frac{1}{r}.\frac{\partial \overline{P}}{\partial x_i} + \frac{m}{r}.\frac{\partial^2 \overline{u}_i}{\partial x_j \partial x_j} \tag{7.4}$$

where the over-bar means a space filtered quantity.

In order to define the large scale velocity field that is separated out from the sub grid scale components a Reynolds averaging type procedure is carried out:

$$u_i = \overline{u}_i + u'_i \tag{7.5}$$

As was described in section 3.2, the main difficulties are due to the non-linear convection terms in the Navier-Stokes equations.

Putting Equation 7.5 into the non-linear terms and expanding gives:

$$\begin{aligned} \overline{u_j u_i} &= \overline{(\overline{u}_j + u'_j)(\overline{u}_i + u'_i)} \\ &= \overline{\overline{u}_i \overline{u}_j} + \overline{\overline{u}_i u'_j} + \overline{u'_i \overline{u}_j} + \overline{u'_i u'_j} \\ &\quad (1) \quad (2) \quad (3) \quad (4) \end{aligned} \tag{7.6}$$

In general it must be noted that $\overline{u'_k u'_l} \neq 0$. In contrast to the time averaged approach all the four terms must now be considered. Terms 2 to 4 contain small scale, non-

resolvable components u'_i, which must be modelled. Term 1 is defined entirely in terms of the grid-resolved quantities by introducing the SGS stresses (Jacobsen 1997):

$$t_{ij} = \overline{u_i u_j} - \overline{u}_i \overline{u}_j \tag{7.7}$$

inserting this into Equation 7.6 means that the convective term in the filtered Navier-Stokes equation, Equation 7.4, will only depend on the resolved quantities (Jacobsen 1997).

7.3 Sub-Grid Scale Stresses

The sub-grid scale stresses can be expressed as the sum of three terms as follows:

$$t_{ij} = L_{ij} + C_{ij} + R_{ij} \tag{7.8}$$

where

$$L_{ij} = \overline{\overline{u}_i \overline{u}_j} - \overline{u}_i \overline{u}_j \tag{7.9}$$

$$C_{ij} = \overline{\overline{u}_i u'_j} + \overline{u'_i \overline{u}_j} \tag{7.10}$$

$$R_{ij} = \overline{u'_i u'_j} \tag{7.11}$$

L_{ij} are referred to as Leonard stresses, C_{ij} are the cross terms and R_{ij} are the SGS Reynolds stresses.

These stresses are modelled in the following manner:

> 'Leonard (1974) has shown that the Leonard stress term removes significant energy from the resolved scales. They can be computed explicitly but it has been shown that they are of the same order as the truncation error when a finite-difference scheme of order higher than two has been applied and thus they are implicitly represented (Wilcox 1994). The remaining stresses have been modelled in different ways. Their properties are assumed to be identical with those arising in the Reynolds time-averaging approach. For the sub-grid scale turbulence the eddy viscosity model assumes that the sub-grid scale

stress is proportional to the modulus of the strain rate tensor of the filtered large-scale flow' (Jacobsen 1997 p 48).

Therefore the SGS eddy viscosity is modelled using the same analogy as that proposed by Boussinesq and detailed in chapter 4:

$$t_{ij} = 2\nu_{sgs}\bar{S}_{ij} = \nu_{sgs}\left|\frac{\partial \bar{u}_i}{\partial x_j} + \frac{\partial \bar{u}_j}{\partial x_i}\right| \tag{7.12}$$

In a similar manner to the eddy viscosity models described in chapter 4 an extra term is added to this equation to model the effect of the SGS turbulence kinetic energy and normal stresses

$$t_{ij} = 2\nu_{sgs}\bar{S}_{ij} - \frac{2}{3}\rho k\delta_{ij} \tag{7.13}$$

This sub-grid scale stress model effectively models the sub-grid viscosity. It plays a role in LES similar to the role played by the Reynolds stresses in the RANS models but the physics that it models are different. The SGS energy is a much smaller part of the total flow than the RANS turbulent energy and thus model accuracy may be less crucial in LES than RANS computations.

7.3.1 The Smagorinsky Model

This model, proposed by Smagorinsky in 1963, is based on an equilibrium hypothesis: that the production of SGS energy is approximately in equilibrium with the viscous dissipation of the SGS energy. This gives:

$$-t_{ij}S_{ij} = \varepsilon \tag{7.14}$$

It can be shown that the sub-grid scale eddy viscosity ν_{sgs} then relates to the strain rate tensor of the resolved velocity field $\bar{S}_{ij}$ (Piomelli 1994).

$$\nu_{sgs} = (C_s\Delta)^2|S| = (C_s\Delta)^2\left[2\bar{S}_{ij}\bar{S}_{ij}\right]^{1/2} \tag{7.15}$$

The model constant C_s can be varied between 0.1 and 0.2 and affects the sub-grid viscosity and therefore the rate of energy drainage from large to dissipative scales.

Since an eddy dissipation formulation for the sub-grid scale stresses is used it is thereby assumed that the sub-grid turbulence is isotropic. As the smaller scales of turbulence are more likely to be isotropic due to the damping effects of viscosity, this can be considered to be a valid assumption. Therefore the filter width can be found for a Cartesian grid to be (Jacobsen 1997):

$$\Delta = (\Delta_x \Delta_y \Delta_z)^{1/3} \tag{7.16}$$

These simulations used an anisotropic grid distribution to reduce the overall number of finite volume nodes required in the simulations. There have been a number of investigators who have attempted to account for the effect of an anisotropic grid on the filter width and Smagorinsky model, but it has been reported that these modifications only showed small deviations from the standard isotropic grid method (Scotti and Meneaveau 1993).

The standard Smagorinsky model is so simple and well designed that it has been applied to many flow fields and has attained great success. However the standard model has several shortcomings:

1. the model is overly dissipative
2. the Smagorinsky constant C_s must be optimised for each flow field
3. no ‘natural’ account is taken of the effects of walls
4. no account is made of the effects of negative SGS viscosities or the apparent transfer of energy from the small to large scale eddies, known as backscatter (see section 5.7).

The second shortcoming represents the most serious problem in wind engineering flow fields. The rate of transfer from the large eddies to the small dissipative eddies varies according to both the spatial and temporal point in the flow field as a consequence of the many different flow types encountered. Consequently dynamic SGS models have been devised that calculate values of the model constant dependant on the spatial and temporal conditions in the flow field. For full details see Germano et al (1991).

7.4 Numerical Methods – The Time Dependant Terms

The CFX user has a choice of either a fully implicit backward differencing scheme or a time centered Crank-Nicolson treatment that is second order accurate in time.

A particular advantage of using the Crank-Nicolson scheme is apparent when the Courant-Friedrichs-Lewy or CFL criterion is adhered to obtain a stable solution. The CFL criterion states that:

$$N_{CFL} = \frac{u.\Delta t}{\Delta x} < 1.0 \qquad (7.17)$$

If the implicit Crank-Nicolson method is used the CFL can then be exceeded by factors as large as 5 (Wilcox 1994) thus allowing for larger time-steps for the same model simulation. Trials undertaken by the author have generally agreed with the findings of Choi and Moin (1994) in that too large a time step will effectively damp the turbulent fluctuations leading to a laminar solution. Further details of the schemes highlighted can be found in Patankar (1980) and the CFX version 4.2 user manual (CFX-International 1998).

7.5 Model Validation and Analysis Details

The standard Smagorinsky LES model has been incorporated into CFX through the appropriate user FORTRAN routines and has been validated through previous tests undertaken by Ciofalo et al (1989) and Jacobsen (1997) as part of their respective Ph.D. theses. This model has been chosen due to its simplicity and ease of implementation into CFX4.2. The use of an anisotropic grid and the method of generating the inlet conditions, discussed below, have been validated through comparisons with the work of Scotti and Meneaveau (1993) and Thomas and Williams (1992), respectively. All the simulations undertaken were run to single precision numerical accuracy to speed up the analysis times and reduce the random access memory requirements.

The following section details the relevant calculations required to undertake the large eddy simulations and any assumptions made.

7.5.1 Domain Size

For the tests undertaken in this project a number of different geometries were used as follows:

1. 1:30 scale, cube model, normal orientation, fine mesh with approximately 1 million nodes and Van Driest wall damping (see section 7.5.5)

2. 1:30 scale, cube model, normal orientation, a mesh with approximately 180,000 nodes, no Van Driest wall damping

3. 1:30 scale, SSB model, sharp eaves, normal orientation, fine mesh with approximately 1 million nodes and Van Driest wall damping.

Due to time constraints it was not possible to undertake further grid refinements.

Strictly speaking the use of the standard Smagorinsky SGS model requires near wall damping to reduce the increased levels of eddy viscosity returned in the near wall region (see section 7.5.5). The necessity for wall damping depends to a large extent on the type of flow that is being simulated. Wind engineering flows are mainly concerned with the effects of the large scale structures in the flow so the errors in the Smagorinsky model in the near wall region are perhaps not a major concern. Nevertheless it was felt necessary to use a geometry that correctly modelled the near wall region by placing at least one grid point in the laminar sub-layer. Therefore a number of different tests were set up, as detailed above, to test this hypothesis.

Using the 6m model and the geometry dimensions shown in Figure 115 it was not possible to mesh the domain for a 6m cube, which was approximately 84m by 42m by 18m, to allow for near wall damping functions without the use of an unacceptably high number of grid points or a very large geometric progression of the grid. The 1/30 scaling of the model reduced the domain size to 2.8m by 1.4m by 0.6m, and as the sub-layer thickness is the same for a given flow Reynolds number and wall roughness, it was therefore the same for both these models. It was now possible to economically mesh this domain for test numbers 1 and 3.

7.5.2 Inlet conditions

Further problems were apparent due to the fact that no transient boundary layer data was available from the SRI for use as inlet conditions in these simulations. This was further compounded by the fact that the rough wall functions used in the turbulent steady state simulations were not available when the laminar flow settings were used in CFX4.2. Due to time constraints on this work it was considered appropriate to generate transient inlet boundary conditions using periodic inlet and outlet boundaries to recycle the flow and use a non-slip, smooth wall condition for the domain floor.

The initial conditions for the mean velocity profiles at each cell were set to obey the power law expressed as:

$$\overline{u} = Z^{0.25} \tag{7.18}$$

The initial velocity fluctuations for the *u* and *v* components were generated by means of random numbers. The turbulence intensities were set to 15 percent and the initial velocity fluctuation for *w* was set to satisfy the continuity equation (Murakami et al 1987). After many cycles the initial velocity fluctuations were effectively overwritten as the turbulence in the flow evolves. These initial conditions effectively speed up the process of generating turbulence rather than starting the simulation from a laminar flow.

Validation of the method of generating the inlet conditions is available on reference to Thomas and Williams (1992) and Castro and Robins (1977). It is suggested that turbulence levels induced by the cube above the background turbulence extend to approximately 6 times the stream-wise cube dimension (Castro and Robins 1977). Therefore provided the computational domain is longer than say 8 times the cube dimension it is possible to generate the inflow by recycling the outflow (Thomas and Williams 1992). The inflow parameters are therefore not set a priori but are determined by the simulation and the turbulent boundary layer is generated as a consequence of the non-slip floor wall condition set, as opposed to the turbulence generated by the cube. A pressure drop across the domain was specified in order to maintain the flow through the ‘computational wind tunnel’. General guidance on how to estimate the resulting wind velocities is given by Ciofalo (1989). Using this work and, to an extent, some ‘trial and error testing’ the velocity and Reynolds number for these simulations measured at eaves height was approximately equal to 1.7 m/s and 28,000, respectively.

7.5.3 Determination of Time-Step

The appropriate time step was determined using the simple CFL criterion discussed earlier (section 7.4) with the worst case combination of streamwise velocity and smallest cell size for the various test cases. Consequently a number of different time steps were chosen, depending on the model geometry used, ranging from approximately 0.01 to 0.0001 seconds

7.5.4 Large Eddy Turnover Time

The simulations have to be run for a period that ensures that the turbulent structures have fully developed before any averaging can be performed (Jacobsen 1997). This period is a multiple of the large eddy turnover time (LETOT) which refers to the time it will take for the large eddies in the simulation to do one revolution.

For this case the largest eddies in the flow are of approximately the size of the building, consequently the time for one LETOT is as follows for test case number 1:

$$\text{LETOT} = \text{Building dimension, (H)} / \text{velocity at roof height} \qquad (7.19)$$

Therefore one LETOT = 0.2/1.7 = 0.12 seconds.

It was necessary to run the simulations for a time that ensured that sustained and statistically stationary turbulence levels were generated beyond the initial conditions set. This required approximately 20 to 30 LETOTS prior to the averaging of the results (2.35 to 3.52 seconds).

7.5.5 Wall Conditions

As was briefly highlighted in section 7.5.1, obtaining satisfactory wall conditions when undertaking large eddy simulations is a major problem when using the Smagorinsky SGS model. It has been discovered that the conventional Smagorinsky model returns increased values of sub-grid scale viscosity in the near wall region. This is in contrast to the fact that viscous effects give way to laminar flow below y^+ values of approximately 11.22. Consequently an ad-hoc method is required when using this sub-grid model to force it into agreement with experimental results. A

recipe that has been found to be successful is Van Driest damping that has long been used to reduce the near wall viscosity in RANS models. The Van Driest damping factor, which is normally used, is as follows (Driest 1956):

$$d = 1 - \exp\left(-\frac{y^+}{A^+}\right) \tag{7.20}$$

where d is the damping factor used to modify the SGS eddy viscosity returned and A^+ is a constant equal to 25.

The wall distance in wall units is found from:

$$y^+ = y.\frac{u_t}{n} \tag{7.21}$$

where

$$u_t = \sqrt{t_{wall}/r} \text{ is the wall friction velocity.} \tag{7.22}$$

In addition,

> 'It should be noted that the expression for the wall friction velocity is strictly only valid for a channel flow without recirculation zones including separation and re-attachment points. This is due to the fact that t_{wall} and the wall friction velocities vanish at reattachment points. Nevertheless this method is implemented in the absence of a more advanced solution to the problem' (Jacobsen 1997, p55).

The wall shear stress is found from the dynamic viscosity multiplied by the gradient of the main streamwise velocity parallel to the wall:

$$t_{wall} = m\frac{\partial \overline{u}}{\partial y} \tag{7.23}$$

A similar procedure was used as with the steady state RANS models (described in section 6.3.8) to test that a satisfactory number of grid nodes were in the laminar sub-layer. Although this modification is difficult to justify in the context of LES it does produce the desired results and has been successfully applied to many engineering flow problems.

7.5.6 Calculation of Velocity Statistics

In order to directly compare the large eddy simulation data with the mean data provided by the steady state, low Reynolds number turbulence models it was necessary to time average the velocity statistics. This involved calling a user FORTRAN routine at each time step that calculated the mean velocities and root mean square fluctuating velocities as follows:

$$\bar{u} = \frac{\sum_{tstart}^{t} u_n}{t - t_{start}} \tag{7.24}$$

$$\overline{u'^2} = \sqrt{\frac{\sum_{tstart}^{t} (u_n - \bar{u})^2}{t - t_{start}}} \tag{7.25}$$

The time averaging process started after a designated number of time steps, t_{start}, to allow the solution to develop and generally the longer the time averaging process the more accurate the calculated mean and RMS values became (Jacobsen 1997). Using the information found from Equations 7.24 and 7.25 it was also possible to calculate transient and time averaged Reynolds stress data.

7.6 Results

7.6.1 Introduction

It is intended that the analysis of the results will focus primarily on the flow fields produced by the different models used and a discussion will be given on any difficulties found during these simulations. The discussion initially focuses on the tests undertaken to assess whether the LES simulations are performing correctly. This is followed by analysis and comparison of the steady state results from the low Reynolds number and the quadratic non-linear *k-e* models and the LES data.

7.6.2 Steady State Simulation and LES Results

Various checks were made using the LES models to test whether a suitable level of turbulence had been generated and that the LES algorithms incorporated into CFX were performing correctly.

It is stated that the turbulent flow over a surface mounted bluff body in an atmospheric boundary layer is only quasi-periodic or even completely non-periodic (Shah and Ferziger 1997). This can be seen upon reference to experiments undertaken with a square cylinder, refer to Frank and Mauch (1993) for further details.

Following the method used by Shah and Ferziger (1997) a ‘probe’ was positioned at the side wall of the cube model to return fluctuating velocity data, for a single node, for each time step of the simulation. Figure 116 shows the time series of the fluctuating velocity returned. The change in direction of the flow, highlighted by the time series, is graphically demonstrated by Figures 117 to 120 that show snapshots of the flow generated by the coarse model at 2-second intervals. The flow appears to change direction as the stagnation point at the front face of the cube switches from either the left or right of the centre of the front face, which results in the flow either separating at the side or remaining attached.

The Fourier transform of the time series signal (see Figure 121) showed no peak in the spectrum. This matches the results found by Shah and Ferziger (1997) who state that this is typical of turbulent flows where repeatable structures are found but they are not identical in size or strength and do not occur periodically. As LES is unable to adequately resolve the small scale eddies responsible for dissipation the decay in the energy of the flow with increasing frequency (see Figure 121) represents the effects of the SGS model and near wall damping terms. As such any assessment of this region of the spectrum is particularly difficult.

Referring to Figures 122 to 124, that show snap-shots in time of the flow for various planes for both the SSB and cube models, it is apparent that the flow appears very different from the steady state simulations tested and is in fact highly turbulent and transient. Unfortunately these fine grid simulations only had limited success due to the need to finely mesh the near wall region of the flow and the use periodic boundaries for the inlet and outlet. The result of these constraints meant that it was necessary to geometrically progress the grid to the outlet to allow for a model that had at least a computationally workable finite volume mesh. This technique led to a

situation where the turbulence generated in the flow was effectively damped by a finite volume mesh that became progressively coarser as the outlet was approached. Both the LES cube and SSB model simulations returned time averaged flow fields that appeared to show a reduced level of turbulence in the flow on comparison to the steady state models, i.e. no flow reattachment on the roof of the cube. Unfortunately continued run time for these simulations showed no further increase in turbulence levels. This is demonstrated in Figure 124, which shows the transient flow field for the entire SSB domain.

As a consequence of this and in the knowledge that, reportedly, wind engineering simulations are less sensitive to the near wall treatment (Hanjalic et al 1998), a number of coarse model simulations were undertaken without Van Driest wall damping that allowed for a more uniform grid. Figures 125 and 126 show the level of turbulence generated in the flow, for this coarser model, which, on comparison to Figure 124 for the SSB, appears to be better sustained when convected downstream. Figures 127 and 128 show the time averaged velocity and pressure contours around the cube.

Using the information gained from the various checks undertaken it was possible to obtain suitable time averaged LES data to compare to the steady state turbulence model results.

Referring to Figure 127 which highlights the roof and wake recirculation zones for the LES simulations and Figures 129, 130 and 131, which show the recirculation zone data for the time averaged turbulence model runs, the following results were found:

Turbulence model.	***Roof reattachment.***	***Wake reattachment.***
Non-linear k-epsilon.	0.67H	2.3H
Low Re. No. models.	No separation	2.2H
LES	approx. 0.6H	1.8H

Table 9: Reattachment lengths, cube normal to the incident wind.

(H = cube dimension)

Interestingly with this simulation it appears that a similar flow field was being produced, by the non-linear *k-e* model, to that modelled in chapter 6 for the 6m cube. The flow field results from the low Reynolds model simulations, which were identical for both the *k-e* and *k-w* models, show no improvement on the results found for the standard *k-e* model tested in chapter 6.

Although the large eddy simulation perhaps required a longer averaging time, the results were sufficient to determine some important flow data. The time averaged coarse LES model returned a similar roof flow field to that predicted by the non-linear *k-e* model and a wake reattachment length of approximately 1.8 times the cube length. Although only tentative conclusions can be drawn from the data presented in this section of the thesis, it should be stated that inaccuracies in the calculation of the wake flow field, which resulted in over prediction of the reattachment point, were one of the consistent and unresolved problems of the simulations undertaken in chapter 6. The early results from the large eddy simulations were therefore generally encouraging.

7.6.3 Discussion and Recommendations for Future Work

The scope of the LES work undertaken in this section is just the starting point of a full investigation into LES and wind engineering. The work undertaken has given the author an insight into actual LES work beyond simply researching published material on this subject and has tentatively highlighted possible improvements in predictive accuracy.

This initial approach has conclusively shown the requirement for future work in this field. Firstly in order to compare the SRI cube results to any LES data it is necessary to obtain transient boundary layer data from the field experiments and convert this into data to be used at the inlet for the CFD simulations. Secondly a non-trivial amount of work needs to be undertaken to supply suitable wall functions that will sustain the inlet boundary conditions and match the roughness of the fetch at the SRI. The author is of the opinion that these problems alone could well be the basis of a further thesis in their own right. Thirdly SGS models need to be incorporated that rely less heavily on the ad-hoc damping of the near wall eddy viscosities returned, perhaps utilising the dynamic SGS model of Germano (1991). Fourthly, and perhaps most importantly, is the issue of the necessary computational power and data storage facilities. Even the limited simulations undertaken as part of this project required the use of some expensive computer hardware (multi-processor Sun Unix workstations) that turned out to be barely adequate for this project with run times of up to 6 months for a number of the LES models. More detailed studies may require more substantial hardware or parallel processing facilities. This alone implies that LES will not be routinely used in the near future.

Finally this section has clarified that, at least for the next 5 years, most CFD simulations will be undertaken using the techniques utilised in chapter 6. Not only does LES require major computer hardware it also requires significant operator skills. LES appears to be a much more difficult, less ‘black box’, approach to modelling fluid flow with a much greater scope for error. Significant operator skills and a good knowledge of fluid mechanics are required.

8. Conclusions and Recommendations for Future Work.

8.1 Introduction

This project has seen the first exhaustive test of all the available non-linear *k-e* models and the RNG *k-e* model in wind engineering simulations with validation data supplied from full-scale rather than model scale experiments.

In this chapter a number of conclusions are drawn from the work undertaken and to aid clarity they will be presented in list form.

8.2 Conclusions

Primary

- Development work on a commercial CFD code has seen the successful implementation and testing of state of the art methods of modelling turbulence and fluid flow. Extensive tests undertaken on the non-linear *k-e* turbulence models have shown that they produce, on average, the most accurate pressure and flow field predictions of all the models tested in wind engineering applications. In addition the Craft et al (1996) quadratic model is numerically stable and has solution times equal to that of the standard *k-e* model. Overall, in terms of predictive accuracy, the RANS turbulence models are ranked as follows:

    1. The cubic and quadratic non-linear *k-e* models
    2. The RNG *k-e* model / DSM
    3. The MMK *k-e* model / standard *k-e* model.

- These investigations suggest that a suitable turbulence model for wind engineering should be able to model the anisotropy of turbulent flow, such as the Reynolds stress model, whilst maintaining the ease of use and computational stability of the two equation models. This is necessary, firstly to account for the fact that wind engineering flows are inherently anisotropic and secondly to aid correct calculation of the turbulent kinetic energy production term, which has been shown to be the main reason why the isotropic eddy viscosity models fail. The requirement for ease of use and computational stability has been highlighted by

the numerical stiffness problems associated with the DSM. It appears that, at least for the next five years, RANS techniques, such as the non-linear models, offer the most promising computational models in wind engineering.

- It should be stated that none of the RANS models provided accurate results for the whole range of test cases, with errors sometimes exceeding 100 percent. This suggests the eventual need to reduce the importance of the turbulence model and the necessity to resolve more of the flow field directly, i.e. large eddy simulation. Unfortunately, as was highlighted in chapter 7, large eddy simulation currently requires significant computer facilities. In the author's opinion this will hold back the widespread use of such a technique for between five to ten years after which time this method will most likely be the dominant CFD technique used.

Secondary

- A number of points regarding the use of the more popular turbulence models and various methods of refining the models have been discovered as follows:

    1. The inadequacies of the standard *k-e* model in wind engineering flows has been extensively shown and discussed. The problems are rooted in the isotropic eddy viscosity concept and the linear Boussinesq hypothesis which not only result in an inadequate description of turbulence but also major errors in the turbulence model transport equations.

    2. The methods referred to in this thesis as making 'ad-hoc' modifications to turbulence models, such as the MMK *k-e* model, are generally unsatisfactory. Although this technique was found to improve the results in some areas of the flow it had the opposite effect in other areas. Care should be exercised when using such models to ensure that results are checked over a wide range of flow fields. This method is generally unsound and modifications should be rigorously derived from either the Navier-Stokes equations or Boussinesq hypothesis.

    3. The strongly coupled Reynolds stress partial differential equations result in finite difference equations that are highly numerically unstable. Particular problems are apparent when the differential stress model is used in conjunction with higher order differencing schemes. These problems were

so severe as to negate its use for a number of simulations in this project. Use of the differential stress model in complex flow fields requires skill and expertise to coax a fully converged solution. In addition this model requires greater overheads in terms of time and computational power. Nonetheless, it is the author's opinion that the DSM is, in theory, a rational and sound model which may, following some major improvements, become a useful wind engineering turbulence model in the future. Further development work on this model should concentrate on improving the stability characteristics and accurately pinpointing the errors in this model.

- Further supplementary points regarding the turbulence model developments are as follows:

    1. At present the Speziale (1987) quadratic and Craft et al (1996) cubic non-linear *k-e* models appear to require further development work to improve their numerical stability in wind engineering applications. Simple tests have highlighted the greater accuracy and potential of the cubic non-linear model.

    2. Particular errors were apparent in modelling the flow over more 'complex' structures such as the SSB and the 6m cube skewed to the incident wind. The problems associated with CFD and turbulence modelling in correctly predicting the delta wing vortices and lobes of high negative pressure still persist, although it is possible that difficulties in flow resolution at these areas may be partially to blame.

    3. The problems associated with the wall reflection terms in the pressure-strain model appear to have no solution for the foreseeable future. At present the use of such terms makes the DSM unusable in a generic sense and as such of no use to the wind engineering community as a whole. This is a non-trivial issue that is at present holding back the development and use of a complete DSM.

Further points regarding the CFD testing in general are as follows:

- The experimental data supplied by the SRI for full-scale structures has enabled both novel and high quality analysis of the accuracy of state of the art CFD turbulence models when applied to wind engineering studies.

- The first full application of the differential stress model to simulating the flows around the experimental structures at the SRI has been completed. In addition, full mean Reynolds stress inlet profiles, for a range of velocities, have been generated that represent the atmospheric boundary layer at the SRI site.

- This work has clearly shown the need to undertake a significant number of tests to determine the accuracy of a CFD simulation. In particular the importance of undertaking the following has been demonstrated:

    1. successive grid refinements to prove a grid independent solution.

    2. the importance of accurately specifying the inlet conditions for any CFD wind engineering problem

    3. that all CFD simulations should incorporate higher order differencing schemes such as CCCT or QUICK to minimise the effects of false diffusion

    4. and when solving flows that involve complex flow fields and geometries the use of algebraic multi-grid methods may be beneficial.

8.3 Recommendations for Future Work.

- The full potential of the non-linear *k-e* models should be realised by development work on the cubic variant to improve its stability in wind engineering flows. The author believes this will be the most rewarding path to take rather than concentrating on finding the highly elusive universal wall reflection term, for the differential stress model, that is not dependent on the wall normal distance. The DSM presently has a number of other problems, as described, which should take precedence.

- Full SRI transient inlet conditions and suitable wall functions need to be developed to enable a complete assessment of the ability of LES to model fluid flow for the full-scale structures tested at the SRI. Analysis and 'back-engineering' of presently available frequency spectra obtained from the full-scale

cube, SSB and experimental wall studies may provide a possible solution to this problem.

- More detailed experimental work is required to further validate the inlet conditions for the differential stress turbulence model.

Nomenclature

A^+ = a constant equal to 25.

ABL = Atmospheric Boundary Layer

C_{e1}, C_{e2}, C_{1RNG}, C_m = constants in the turbulence transport equations

C_{ij} = convection term of $\overline{u_i' u_j'}$

C_s = model constant

CFD = Computational Fluid Dynamics

CWE = Computational Wind Engineering

DSM = Differential Stress Model

d = Van Driest damping factor

D_{ij} = diffusion term of $\overline{u_i' u_j'}$

e_{ij} = the rate of deformation tensor

F = body force per unit volume.

F_{ij} = stress production of $\overline{u_i' u_j'}$ by action of rotational or body forces

k = turbulent kinetic energy, $k = \frac{1}{2}\left(u_i' u_i'\right)$

l = length scale

LES = Large Eddy Simulation.

LETOT = Large Eddy Turn Over Time

N_{CFL} = the Courant-Friedrichs-Lewy or CFL number

$\overline{P}$ = mean pressure

P_k = production of turbulent kinetic energy

P_{ij} = the production term in the algebraic stress model

RANS = Reynolds Averaged Navier-Stokes

s = shear

SGS = Sub-Grid Scale

S_{ij} = strain rate tensor, $S_{ij} = \left(\frac{\partial \overline{u}_i}{\partial x_j} + \frac{\partial \overline{u}_j}{\partial x_i} \right)$

$S_{(n)}$ = spectrum function.

SSB = Silsoe Structures Building

t = present time step

t_{start} = time step at start of averaging process

$\overline{u}$ = mean veloc ity.

u' = random fluctuatin g component of velocity.

u_* = friction velocity

u^+ = velocity scale (non-dimensional)

u_i = the filtered resolvable scale velocity field, and

u'_i =	the sub-grid scale (SGS) components.
$\overline{u_i' u_j'}$ =	Reynolds stresses
U_{ref} =	reference velocity
$U(z)$ =	the mean velocity at height z
x_i =	the co-ordinate direction (subscript indicates the coordinate direction, *x, y* and *z* for *i, j* and *k)*
y^+ =	the distance from the wall in non-dimensional wall units
y =	the distance from a point in the fluid to the nearest wall
z =	vertical height
z_0 =	ground roughness length
Z_{ref} =	reference height

d =	gradient height
d_{ij} =	Kronecker delta
Δ =	the filter width.
Δ_t =	time step size or duration.
Δ_x =	grid spacing.
e =	dissipation rate of *k*
e_{ij} =	dissipation term of $\overline{u_i' u_j'}$
f_{ij} =	pressure-strain correlation term
k =	Von Karman's constant
m_l =	laminar viscosity
m =	dynamic viscosity.
m_t =	eddy viscosity
n =	the laminar kinematic viscosity.
n_{sgs} =	the sub-grid viscosity
r =	fluid density
$\sigma_k, \sigma_\varepsilon$ =	turbulent Prandtl number, for *k and e,* for the *k-e* turbulence model
t =	shear stress
t_{ij} =	the turbulent stresses tensor
t_O =	surface shear stress
W =	vorticity (equal to twice the instantaneous rate of spin of a fluid element, determined by lateral velocity gradients.)

References.

Abbott, M. B. and Basco, D. R. (1989). *'Computational Fluid Dynamics - An introduction for Engineers.'*, Longman Scientific, Singapore.

Abou-Arab, T. W. and Serag-Eldin, M. A. (1992). *'Turbulence modelling and simulation of atmospheric boundary layers.'*, Transactions of the ASME, Vol. 114, No.40, March 1992.

Anderson, J. D. (1995). *'Computational Fluid Dynamics - The basics with applications.'*, Mac Graw - Hill Inc. , New York, USA.

Baetke, F., Werner, H. and Wengle, H. (1990). *'Numerical simulation of turbulent flow over surface mounted obstacles with sharp edges and corners.'*, Journal of Wind Engineering and Industrial Aerodynamics, Vol. 35, pp. 129-147, Elsevier, Amsterdam, Netherlands.

Baker, C. J. (1996). Wind Engineering course notes, Master of Research Degree, The University of Nottingham , Nottingham, UK.

Baker, C. J. (1997). Private Communication, The University Of Nottingham, Nottingham, UK.

Basora, B. and Younis, B. A. (1992). *'Progress in the prediction of turbulent wind loading on buildings.'*, Journal of Wind Engineering and Industrial Aerodynamics, Vol. 41-44, pp. 2863-2874, Elsevier, Amsterdam, Netherlands.

Bernard, P. S. and Speziale, C. G. (1992). *'Bounded energy states in homogeneous turbulent shear flow - An alternative view.'*, Journal of Fluid Engineering, Vol.114, pp. 29, March 1992.

Bickerton, J. E., Graysmith, J. L., Howell, J. P. and Haynes, T., (1996) *'The CFD investigation of flow separation over a simple vehicle model.'*, ISATA, Florence, Italy.

Boussinesq, T. V. (1877). *Mem. Pre. Acad. Sci.*, 3rd Edn., Paris XXIII, p. 46.

Bradshaw, P. (1973). *'Effects of streamline curvature on turbulent flow.'*, AGARDograph no. 169.

Bradshaw, P. (1992) *'Turbulence: The chief outstanding difficulty of our subject.'*, 5th Symposium on Numerical and Physical Aspects of Aerodynamic Flows, January 1992, California State Univ., USA.

BS6399 part 2. (1997), *'Code of Practice for Wind Loads.'*, HMSO, London, England

Castro, I. P. and Robins, A. G. (1977). *'The flow around a surface mounted cube in a uniform and turbulent shear flow.'*, Journal of Fluid Mechanics, Vol. 79, part 2, pp. 307-335.

CFX - International (1998). *'CFX Version 4.2: User Manual.'*, Harwell Laboratory, Oxfordshire, OX11 0RA, UK: CFX - International.

Choi, H. and Moin, P. (1994). *'Effects of the computational time step on numerical solutions of turbulent flow.'*, Journal of Computational Physics, Vol. 113, part 1, pp. 1-4.

Ciofalo, M. (1988). *'Algorithms and auxiliary routines for FLOW3D release 2.'*, Ph.D. Thesis, City University, London, TRERC Res. Memo No. TF/03/88/01.

Ciofalo, M. (1996). *'Large eddy simulations of turbulent flow with heat transfer in simple and complex geometries using Harwell-Flow3D.'*, Applied Mathematical Modelling, Vol. 20, pp. 262-271.

Ciofalo, M. and Collins. M. W. (1989). *'Large eddy simulations of turbulent flow in plane and rib-roughened channels.'*, Proceedings of the 6th International Conference: Numerical Methods in Laminar and Turbulent Flows, Swansea, UK, July 1989.

Clarke, D. S. and Wilkes, N. S. (1989). *'The calculation of turbulent flows in complex geometries using the differential stress model.'*, AERE - R 13428, Technical Report, CFDS, Harwell, Oxford, England.

Coakley, T. J. (1993). *'Turbulence modelling for the compressible Navier-Stokes Equations.'*, AIAA paper, Vol. 83, p. 1693.

Cook, N. J. (1986a). *'The designers guide to wind loading on building structures: part 1.'*, Butterworths , London, England.

Cook, N. J. (1986b). *'The designers guide to wind loading on building structures part 2.'*, Butterworths, London, England.

CP3 Chapter V Part II. (1972). *'Code of basic data for the design of buildings.'*, HMSO, London, England.

Craft, T. J. and Launder, B. E. (1992). *'New wall reflection model applied to the turbulent impinging jet.'*, AIAA Journal, Vol. 30, p. 2970.

Craft, T. J., Graham, A. and Launder, B. E (1993b). *'Impinging jet studies for turbulence model assessments Part 2: An examination of the performance of 4 turbulence models.'*, International. Journal of Heat and Mass Transfer, Vol. 36 p. 2685.

Craft, T. J, Launder, and Suga, K. (1993a). *'Extending the applicability of the eddy viscosity model through the use of deformation invarients and non linear elements.'*, Proceedings of the 5th International Symposium on Refined flow Modelling and, Turbulence Measurements, p. 125, Paris, France.

Craft, T. J., Launder, B. E. and Suga, K. (1996). *'Development and application of a cubic eddy-viscosity model of turbulence.'*, International Journal of Heat and Fluid Flow, Vol. 17, pp. 108-115.

Davenport, A.G. (1999). *'The Missing Links'*, The 10th ICWE, Copenhagen, June 1999.

Deaves, D. M. and Harris, R. I. (1978). *'A mathematical model of the structure of strong winds.'* CIRIA Report 76. London, Construction Industry Research and Information Association.

Deissler, T. (1989). *'On the nature of Navier-Stokes turbulence.'*, NASA, TM 109183.

Delaunay, D., Lakehal, D. and Pierrot, D. (1995). *'Numerical approach for wind load prediction on buildings and structures.'*, Journal of Wind Engineering and Industrial Aerodynamics, Vol. 57, pp. 307-321, Elsevier, Amsterdam, Netherlands .

Dickens, M. (1999). Private Communication, Computational Dynamics, Shepherds Bush, London, UK

Driest, E. R. v. (1956). *On turbulent flow near a wall.'*, Journal of the Aeronautical Sciences, pp. 1007-1011.

Durbin, P. A. (1993) *'A Reynolds stress model for near wall turbulence.'*, Journal of Fluid Mechanics, Vol. 249 pp. 465-499, 1993.

Durbin, P. A. and Speziale, C. G. (1991). *'Local anisotropy in strained turbulent flow at high Reynolds numbers.'*, Journal of Fluids Engineering, Vol. 113, p. 707.

Eaton, K.J. and Newbury, C.W. (1972) *'Wind Loading Handbook.'*, BRE Report, HMSO, London, England.

Ferziger, J. (1993) *'Simulation of complex turbulent flows: Recent advances and prospects in wind engineering.'*, Journal of Wind Engineering and Industrial Aerodynamics, Vol. 46 –47, pp. 195-212, Elsevier, Amsterdam, Netherlands.

Ferziger, J. (1994). Lecture notes of ICASE/LaRC Short course on Turbulence Modelling and Prediction, March 1994 in Gatskim, T. B., Hussaini, M. Y. and Lumley, J. L, (1996). *'Simulation and Modeling of Turbulent Flows'*, Oxford University Press, Oxford, UK.

FLUENT Users Manual Version 4.22 (1992), Fluent Europe Ltd, Sheffield, UK.

Frank, W. and Mauch, H. (1993) *'Large-eddy simulation of the flow around building models.'*, Journal of Wind Engineering and Industrial Aerodynamics, Vol. 46-47 pp. 213-218, Elsevier, Amsterdam, Netherlands.

Fu, S., Launder, B. and Leschziner, M. (1993) *'Modeling strongly swirling recirculating jet flow with Reynolds Stress transport closures.'*, Proceedings of the 5th International Symposium on Refined Flow Modeling and Turbulence Measurements.

Gaskell, P. H. and Lau, A. K. C. (1988). *'Curvature Compensated Convective Transport: Smart, A new boundness preserving transport algorithm.'*, International Journal for Numerical Methods in Fluids, Vol. 8, pp. 617-641, John Wiley and Sons Ltd., Chichester, UK.

Gatski, T. B., Hussaini, M. Y. and Lumley, J. L. (1996). *'Simulation and modelling of turbulent flows.'*, Oxford University Press, Oxford, UK.

Germano, M., Piomelli, P., Moin, P. and Cabot, W. H. (1991). *'A dynamic sub-grid scale eddy viscosity model.'*, Physics of Fluids A3, Vol. 7, pp. 1769-1765.

Gibson, M. M. and Launder, B. E. (1978). *'Ground effects on pressure fluctuations in the atmospheric boundary layer.'*, Journal of Fluid Mechanics, Vol. 86 pt. 3, pp. 491-511, 1978.

Gleick, J. (1988). *'Chaos: making a new science.'*, Penguin books, New York.

Goldberg, V. (1987). *'Separated flow predictions using a new turbulence model.'*, Rockwell International Science Centre, California, USA.

Gottlieb, D. and Orszag, S. A. (1977). *'Numerical analysis of spectral methods: Theory and Application.'*, SIAM, Philadelphia.

Haggkuist, K., Suensson, U. and Taesler, R. (1989). *'Numerical simulation of pressure fields around buildings.'*, Building and Environment, Vol. 24 No. 1 pp. 65-72.

Hanjalic, K. (1994). *'Advanced turbulence closure models.'*, International Journal of Heat and Fluid flow, Vol. 15, p. 178.

Hanjalic, K., Obi, S. and Hadzic, I. (1998). *'Wall-jets and flows over wall mounted cubical obstacles.'*, 6th ERCROFTAC/IAHR/COST Workshop on Refined Flow Modelling, ERCROFTAC Bulletin, No. 36, pp. 38-49, March 1998.

Hargreaves, D. M. (1998). Private Communication, The University Of Nottingham, Nottingham, UK.

Harris, R.I. and Deaves, D.M. (1981). *'The structure of strong winds. Wind engineering in the eighties.'*, Proceedings of the CIRIA Conference, London, Construction Industry Research and Information Association, Paper 4.

Hinze, J.O. (1975). *'Turbulence.'*, Mcgraw Hill.

Hirsch, C. (1990). *'Numerical Computation of Internal and External Flows, Vol. 1'*, p. 493, John Wiley and Sons, Chichester, UK.

Holscher, N. and Niemann, H. J. (1998). *'Towards quality assurance for wind tunnel tests: A comparative testing program of the Windtechnologische Gesellschaft.'*, Journal of Wind Engineering and Industrial Aerodynamics, Vol. 74-76, pp. 599-608, Elsevier, Amsterdam, Netherlands.

Hoxey, R.P (1997, 1998, 1999). Private communications, The Silsoe Research Institute, Silsoe, Bedfordshire, UK.

Hoxey, R.P. and Richards, P.J. (1992) *'Spectral characteristics of the atmospheric boundary layer near the ground.'*, Paper presented to the 1st UK Wind Engineering Society Conference, Cambridge, UK.

Hoxey, R.P., Short, L. and Richards, P.J. (1999). '*Quasi-steady theory developed with experimental verification.'*, Proceedings of the 10th ICWE, Copenhagen 1999, Vol. 3, pp. 1679-1692.

Hoxey, R.P., Richards, R. P., Richardson, G. M., Robertson, A. P. and Short, J. L. (1995) *'The Silsoe Structures Building - The completed experiment part 2.'*, 9th International Conference on Wind Engineering 1995, New Delhi, India.

Huxye, P. G. and Leschziner, M. A. (1985). *'Stabilisation of recirculating flow computations performed with 2nd moment closure and 3rd order discretization.'*, Proceedings of the 5th Symposium on Turbulent Shear Flow, pp. 20.7-21.2, Cornell University.

Iacovides, H. and Launder, B. E. (1987). *`The numerical simulation of flow and heat transfer in tubes in orthagonal mode rotation.'*, Proceedings of the 6th International Symposium on Turbulent Shear Flows, 1987, Toulouse, France.

Jacobsen, C. B. (1997) *'Large Eddy Simulation of confined swirling flow: mumerical part.'*, Ph.D. Thesis submitted to Aalborg University, Institute of Energy Technology.

Jensen, M. (1958). *'The model law for phenomena in natural wind.'*, Ingenioren (International Edition), Vol. 2, No. 4.

Jones, I. P. (1999). Private Communication, CFX - International, Harwell, Oxfordshire, UK.

Kawai, H. (1990). *'A discrete vortex analysis of flow around a vibrating cylinder with a splitter plate.',* Journal of Wind Engineering and Industrial Aerodynamics, Vol. 35, pp. 259-273.

Kawamoto, S. (1996) *'Improved turbulence models for estimation of wind loading.',* Report for the Nippon Sheet Glass Co., Chiba, Japan.

Kawamoto, S. Kawabata, S. and Tanahashi, T. (1993) *'Numerical analysis of wind around buildings using a high speed GSMAC – FEM.',* Journal of Wind Engineering and Industrial Aerodynamics, Vol. 46-47, pp. 115-120.

Kim, J., Kline, S. J. and Johnston, J. P. (1980). *'Investigation of a reattaching turbulent flow over a backward facing step.',* Transactions of the ASME, Vol. 102, September 1980.

Kolmogorov, A. N. (1941). de l'Academic des Sci. de 1'URSS 30:301.

Lakehal, D. and Rodi, W. (1997). *'Calculation of flow past a surface mounted cube with two layer turbulence models.',* Journal of Wind Engineering and Industrial Aerodynamics, Vol. 67-68, pp. 65-78.

Lau, A. K. C. (1987). *'Mathematical modeling of non-reacting and reacting recirculatory flows.',* Ph.D. Thesis - Dept. of Mechanical Engineering, The University of Leeds, Leeds, UK.

Launder, B. E. (1972). *'Lectures in mathematical models of turbulence.',* Academic Press , London, UK.

Launder, B. E. (1994). Lecture notes of ICASE/LaRC Short course on Turbulence Modelling and Prediction, March 1994 in Gatski, T. B., Hussaini, M. Y. and Lumley, J. L. (1996). *'Simulation and modelling of turbulent flows.',* Oxford University Press, Oxford, UK.

Launder, B. E. and Leschziner, M. A. (1987). *'Modelling strongly swirling recirculatory jet flow with Reynolds stress transport closure.'*, Proceedings of the 6th Symposium on Turbulent Shear Flow, pp. 17.61- 17.6.6, Toulouse, France.

Launder, B.E. and Li, S.P. (1993). '*On the elimination of wall topography parameters from second moment closure.*', Physics of Fluids, Vol. 6 pt.2, pp. 999-1006, 1994, USA.

Launder, B. E., Reece, G. J. and Rodi, W. (1975) *'Progress in the development of a Reynolds Stress turbulence model.'*, Journal of Fluid Mechanics, Vol.68, pt.3, pp. 537-566.

Launder, B. E. and Spalding, D. B. (1974). *'The numerical computation of turbulent flows.'*, Computational Methods in Applied Mechanics and Engineering, Vol. 3, pp. 269-289.

Launder, B. E. and Tselepidakis, D. P. (1991). *`Directions in second moment modelling of near wall turbulence.`*, AIAA Paper, Vol. 91, p. 219, Reno, Nevada, USA.

Le, H. Moin, P. and Kim, J. (1993). *'Direct numerical simulation of turbulent flow over a backward facing step.'*, Ninth Symposium on Turbulent Shear Flows.

Lee, M. J., Kim, J. and Moin, P. (1990). *'Structure of turbulence at high shear rates.'*, Journal of Fluid Mechanics, Vol. 216, pp. 561-583.

Leonard, A. (1974). *'Energy cascade in large eddy simulations of turbulent fluid flows.'*, Advances in Geophysics, Vol. 18A, pp. 237-248.

Leonard, A. (1985). *'Computation of 3D incompressible flows with vortex elements.'*, Annual Review of Fluid Mechanics, Vol.17, pp. 523-529.

Leonard, B. P. (1979). *'A stable and accurate convective modelling procedure based on quadratic upstream interpolation.'*, Computational Methods in Applied Mechanics and Engineering, Vol. 23, pp. 293-312.

Leschziner, M. A. (1990) *'Modelling engineering flows with Reynolds stress turbulence closure.'*, Journal of Wind Engineering and Industrial Aerodynamics, Vol. 35, pp. 21-47, Elsevier, Amsterdam, Netherlands.

Leschziner, M.A. (1993). *'Computational modelling of complex turbulent flow, expectations, reality and prospects.'*, Journal of Wind Engineering and Industrial Aerodynamics, Vol. 46-47, pp. 37-51, Elsevier, Amsterdam, Netherlands.

Leschziner, M. A. (1995). *'Modelling turbulence in physically complex flows.'*, Industrial Hydraulics and Multiphase flows - Hydro 2000, Thomas Telford, London, UK.

Libby, P. A. (1996). *'An introduction to turbulence.'*, Taylor and Francis, London, UK.

Livesey, F. M. and Mikkelsen, A. C. (1995). *'Evaluation of the use of the numerical k-e model Kameleon II for predicting wind pressures on building surfaces.'*, Journal of Wind Engineering and Industrial Aerodynamics, Vol. 57, pp. 375-389, Elsevier, Amsterdam, Netherlands.

Ludwig, G. R. and Sundaram, T. R. (1969) *'On the laboratory simulation of small scale atmospheric turbulence.'*, CAL report, 1969.

Lumley, J. (1970). *'Towards a turbulent constitutive relation.'*, Journal of Fluid Mechanics, Vol. 41, p. 413.

Lumley, J., Zhu, J. and Shih, T. (1995). *'A new Reynolds Stress algebraic equation model.'*, Computational Methods in Applied Mechanics and Engineering, Vol.125 pp. 287-302.

Mac Comb, W. D. (1990). *'The physics of fluid turbulence.'*, Oxford Science Publishers, Clarendon Press, Oxford, UK.

Malalasekera, W. and Versteeg, H. K. (1995). *'An introduction to computational fluid mechanics.'*, Longman Scientific and Technical, Essex, UK.

Malecki, P. Cousteix, J. and Houdeville, R. (1993). *'3D boundary layer calculations with a two layer turbulence model.'*, Proceedings of the 5th International Symposium on Refined Flow Modeling and Turbulence Measurements.

Mathews, E. H. (1987). *'Prediction of the wind generated pressure distribution around buildings.'*, Journal of Wind Engineering and Industrial Aerodynamics, Vol. 25, pp. 219-228.

Melbourne, W. H. (1995). *'Turbulence and the leading edge phenomena.'*, Dept. of Mechanical Engineering, Monash University, Clayton, Victoria, Australia.

Menter, R. F. (1992). *'Influence of freestream values on k-w turbulence model predictions.'*, AIAA Journal, Vol. 30, No. 6, pp. 1657-1659.

Menter, R. F. and Grotjans, H. (1999). *'Application of advanced turbulence models to complex industrial flows.'*, AEA Technology GmbH, Straudenfeldweg, 12 D-83624 Otterfing, Germany.

Murakami, S. (1990). *'Computational wind engineering.'*, Journal of Wind Engineering and Industrial Aerodynamics, Vol 35, pp. 4-6, Elsevier, Amsterdam, Netherlands.

Murakami, S. (1993). *'Comparison of various turbulence models applied to a bluff body.'*, Journal of Wind Engineering and Industrial Aerodynamics, Vol. 46-47, pp. 21-36, Elsevier, Amsterdam, Netherlands.

Murakami, S. (1997). *'Overview of turbulence models applied in CWE.'*, Institute of Industrial Science, University of Tokyo, Japan.

Murakami, S., Kato, S. and Kondo, Y. (1990) *'Examining the k-e EVM by means of ASM for a 3D horizontal buoyant jet in enclosed space.'*, Engineering Turbulence Modelling and Experiments, pp. 205-214, Elsevier Science Publishing.

Murakami, S. and Mochida, A. (1988). *'3D numerical simulation of air flow around a cubic model by means of the k-e model.'*, Journal of Wind Engineering and Industrial Aerodynamics, Vol. 31, pp. 283-303, Elsevier, Amsterdam, Netherlands.

Murakami, S. and Mochida, A. (1989a). *'Applications of CFD to bluff body aerodynamics - state of the art volume.'*, Journal of Wind Engineering and Industrial Aerodynamics 1989, Elsevier, Amsterdam, Netherlands.

Murakami, S. and Mochida, A. (1989b). *'3D numerical simulation of turbulent flow around buildings using the k-e turbulence model.'*, Building and Environment, Vol. 24, No.1, pp. 51-64.

Murakami, S. and Mochida, A. (1999) *'Past, present and future of CWE: The view from 1999.'*, The 10th ICWE, Copenhagen, Denmark, 1999.

Murakami, S., Mochida, A. and Hayashi, Y. (1990). *'Examining the k-e model by means of a wind tunnel test and LES of the turbulence structure around a cube.'*, Journal of Wind Engineering and Industrial Aerodynamics, Vol. 35, pp. 87-100, Elsevier, Amsterdam, Netherlands.

Murakami, S. Mochida, A. and Hayasi, Y. (1991) *'Scrutinizing the k-e EVM and ASM by means of LES and wind tunnel for flow fields around a cube.'*, 8th symposium on Turbulent Shear Flows, 1991, pp. 17.1-17.2, Technical University of Munich, Germany, Elsevier Science Publishers.

Murakami, S., Mochida, A. and Hibi, K. (1987). *'3D numerical simulation of air flow around a cubic model by means of LES.'*, Journal of Wind Engineering and Industrial Aerodynamics, Vol. 25, pp. 291-305, Elsevier, Amsterdam, Netherlands.

Murakami, S., Mochida, A., Hayashi, Y. and Sakamoto, S. (1992) *'Numerical study on velocity pressure field and wind forces for bluff bodies by k-e, ASM, and LES.'*, Journal of Wind Engineering and Industrial Aerodynamics, Vol. 41-44 pp. 2841-2852, Elsevier, Amsterdam, Netherlands.

Murakami, S., Mochida, A. and Ooka, R. (1993) *'Numerical simulation of flow fields over a surface-mounted cube with various second-moment closure models.'* Ninth Symposium on Turbulent Shear Flows, Kyoto, Japan, 1993.

Murakami, S., Mochida, A., Ooka, R., Shinsuke, K. and Iizuka, S. (1996). *'Numerical prediction of flow around a building with various turbulence models: Comparison of k-e EVM, ASM, DSM and LES with wind tunnel tests.'*, Transactions of the ASHRAE Symposia, 1996, Vol. 1, pp. 741-753.

Nakamura, Y. and Ozone, S. (1987) *'The effects of turbulence on separated and reattaching flow.'*, Journal of Fluid Mechanics, Vol. 178, pp. 477-490.

Naot, D., Shavit, A. and Wolfstein, M. (1970) *'Interactions between components of the turbulent velocity correlation tensor.'*, Israel Journal of Technology, Vol. 8, p. 259.

Ng, K. H. (1971).'*Predictions of turbulent boundary-layer developments using a two-equation model of turbulence.'*, Ph.D Thesis, University of London, UK.

Orzag, S. A. (1994). Lecture notes of ICASE/LaRC Short course on Turbulence Modelling and Prediction, March 1994, in Gatski, T. B., Hussaini, M.Y. and Lumley, J.L. (1996). *'Simulation and modelling of turbulent flows.'*, Oxford University Press, Oxford, UK.

Parameswaran, S., Kiris, I., Sun, R. and Gleason, M. (1993) *'Flow structure around a 3D bluff body in ground proximity: a computational study.'*, Journal of Wind Engineering and Industrial Aerodynamics, Vol. 46-47, pp. 791-800, Elsevier, Amsterdam, Netherlands .

Patankar, S. V. (1980) *'Numerical heat transfer and fluid flow.'*, Hemisphere - McGraw Hill, New York, USA.

Patankar, S. V. and Spalding, D. B. (1972). *'A calculation procedure for heat, mass and momentum transfer in three dimensional parabolic flows.'*, International Journal of Heat Mass Transfer, Vol. 15, p. 1787.

Patel, V. C., Rodi, W. and Scheuerer, G. (1985). *`Turbulence models for near wall and low Reynolds number flows: A review.'*, AIAA Journal, Vol. 23 pp. 1308-1319.

Patel, V. C. and Satiropouls, F. (1995) *'Turbulence anisotropy and near wall modelling in predicting 3D shear flows.'*, AIAA Journal, Vol. 33, No.3.

Paterson, D. A. and Apelt, C. J. (1989). '*Simulation of wind flow around 3D buildings.'* Building and Environment, Vol. 24, No.1 pp. 39-50.

Perot, B. and Moin, P. (1995). *'Shear free turbulent boundary layers Part 1, Physical insights into near wall turbulence.'*, Journal of Fluid Mechanics, Vol. 295 pp. 199-227.

Piomelli, U. (1994). *'Large eddy simulation of turbulent flows.'*, Technical Report 767, TAM Report.

Pollard, A. and Martin, R. (1993). *'A comparative study of 11 models of turbulence.'*, Proceedings of the 5th International Symposium on Refined Flow Modelling and Turbulence Measurements.

Pope, S. B. (1975). *'A more general effective-viscosity hypothesis.'*, Journal of Fluid Mechanics, Vol. 72, pt. 2, pp.331-340.

Qasim, A., Parameswaran, S. and Maxwell, T. (1992) *'Computational predictions of flow over a 2D building.'*, Journal of Wind Engineering and Industrial Aerodynamics, Vol. 41-44, pp. 2839-2840, Elsevier, Amsterdam, Netherlands.

Quinn, A. (1997, 1999). Private Communications, The Silsoe Research Institute, Silsoe, Bedfordshire, UK.

Reynolds, A. J. (1974). *'Turbulent flow in engineering.'*, J. Wiley and Sons, London, UK.

Reynolds, W. C. (1987). *'Fundamentals of turbulence for turbulence modelling and simulation.'* , Lecture notes for the Von Karman Institute AGARD, Lecture Series No. 86, pp. 1-66, New York, USA.

Rhie, C. M. and Chow, W. L. (1983). *'Numerical study of turbulent flow past an aerofoil with trailing edge separation.'*, AIAA Journal, Vol. 21, No. 11, pp. 1525-1532.

Richards, P. J. (1989) *'Computational modelling of wind flows around low rise buildings using Phoenix.'*, Report for the ARFC Institute of Engineering Research Wrest Park, Silsoe Research Institute, Bedfordshire, UK.

Richards, P. J. and Hoxey, R. P. (1992) *'Computational and wind tunnel modelling of mean wind loads on the Silsoe Structures building.'*, Journal of Wind Engineering and

Industrial Aerodynamics, Vol. 41-44, pp. 1641-1652, Elsevier Publishers, Amsterdam, Netherlands .

Richards, P. J. and Hoxey, R. P. (1993) *'Appropriate boundary conditions for computational wind engineering models using the k-e turbulence model.'*, Journal of Wind Engineering and Industrial Aerodynamics, Vol. 46-47, pp. 145-153, Elsevier Publishers, Amsterdam, Netherlands .

Richards, P. J. and Hoxey, R. P. (1999). *'Spectral models of the atmospheric surface layer.'*, Paper submitted to the 10th ICWE, Copenhagen, June 1999.

Richardson, G. M, Hoxey, R. P, Robertson, A. P. and Short, J. L. (1995) *'The Silsoe Structures Building - The completed experiment part 1.'*, 9th International conference on Wind Engineering 1995, New Delhi, India.

Richardson, G. M. and Surrey, D. (1992). *'The Silsoe Building: a comparison of pressure coefficients and spectra at model and full-scale.'*, Journal of Wind Engineering and Industrial Aerodynamics, Vol. 44, pp. 1055-1064.

Richards, P. J. and Wanigaratne, B. S. (1993). *'A comparison of computer and wind tunnel modelling of turbulence around the Silsoe Structures Building.'*, Journal of Wind Engineering and Industrial Aerodynamics, Vol. 46-47, pp. 439-447, Elsevier, Amsterdam, Netherlands.

Robertson, A. P. (1999). Private Communication, The Silsoe Research Institute, Silsoe, Bedfordshire, UK.

Robertson, A. P. and Glass, A. G. (1988). *'The Silsoe Structures Building – its design, instrumentation and research facilities.'*, Divisonal Note DN 1482, AFRC Institute of Engineering Research, Silsoe, UK, p. 1-59.

Robertson, A. P., Hoxey, R. P., Short, J. L., Ferguson, W. A., (1997). *'Full-scale measurements and computational predictions of wind loads on free standing walls.'*, Journal of Wind Engineering and Industrial Aerodynamics, Vol. 67-68, pp. 639-646.

Robertson, A. P., Hoxey, R. P., Short, J. L., Ferguson, W. A. and Osmond, S. (1996) *'Full-scale testing to determine the wind loads on free standing walls.'*, Journal of Wind Engineering and Industrial Aerodynamics, Vol. 60, pp. 123-137.

Rodi, W. (1972) *'The prediction of free turbulent boundary layers by use of a two equation model of turbulence.'*, Ph.D. Thesis, University of London, UK.

Rodi, W. (1990) *'Experience with two-layer models combining the k-e model with a one equation model near the wall.'*, American Institute of Aeronautics and Astronautics paper, Vol. 91, p. 216.

Rodi, W. (1993) *'On the simulation of turbulent flow past bluff bodies.'*, Journal of Wind Engineering and Industrial Aerodynamics, Vol. 46-47, pp. 3-19, Elsevier, Amsterdam, Netherlands .

Rotta, J. C. (1972) *'Turbulente Stromungen.'*, B.G. Teubner, Stuttgart.

Scotti, A. and Meneaveau, C. (1993). *'Generalised Smagorinsky model for anisotropic grids.'*, Physics of Fluids, Vol. 9, pp. 2306-2308.

Shah, K.B. and Ferziger, J. H. (1997). *'A fluid mechanicians view of wind engineering. LES of flow past a cubic obstacle.'*, Journal of Wind Engineering and Industrial Aerodynamics Vol. 67 and 68, pp. 211-227.

Shaw, C. T. (1989). *'Using computational fluid dynamics.'*, Prentice Hall, New York, USA.

Shih, T. H. and Lumley, J. L. (1985) *'Modeling of pressure correlation terms in the Reynolds stress and scalar flux equations.'*, Cornell University Technical Report FDA.

Shih, T. H. and Lumley, J. L. (1993) *'A critical comparison of second order closure with direct numerical simulation of homogeneous turbulent shear flow.'*, AIAA Journal Vol.31, No.4, April 1993.

Sinai, Y. L. (1995) *'A simple model of upstream boundary conditions in CFD simulations within the ABL.'*, AEA Technology. Report, Oxfordshire, UK.

Smagorinsky, J. S. (1963). *'General circulation experiments with primitive equations, Part 1; Basic experiments'*, Monthly Weather Review, Vol. 91, pp. 99-164.

Smith, G. D. (1978) *'Numerical solution of partial differential equations - The finite difference method.'*, Clarendon Press, Oxford, UK.

So, R.M.C., Lai, Y.G. and Zhang, H.S. (1994) *'Second order near wall turbulence closure : A Review.'*, Arizona State University, Arizona, USA.

Spalding, D. B. (1972). *'A novel finite difference formula for differential equations involving both 1st and second order derivatives.'*, International Journal of Numerical Methods in Engineering, Vol. 4 p. 551.

Speziale, C. G. (1987). *'On nonlinear k-J and k-e models of turbulence.'*, Journal of Fluid Mechanics, Vol.178, pp. 459-475.

Speziale, C. G. (1991) *'Analytical methods for the derivation of Reynolds stress closures in turbulence.'*, Annual Review of Fluid Mechanics, Vol. 23, pp.107-157.

Speziale, C. G. (1994). Lecture notes of ICASE/LaRC Short course on Turbulence Modeling and Prediction, March 1994, in Gatski, T. B., Hussaini, M. Y. and Lumley, J. L. (1996). '*Simulation and modelling of turbulent flows.'*, Oxford University Press, Oxford, UK.

Speziale, C. G. (1998). *'Turbulence modelling for time dependent RANS and VLES: A review.'*, AIAA Journal, Vol. 36, No.2, Feb 1998

Speziale, C. G. and Abid, R. (1995). '*Near wall integration of Reynolds stress turbulence closure with near wall damping.'*, AIAA Journal, Vol. 33, No.10.

Speziale, C. G., Abid, R. and Anderson, E. C. (1990). *'A critical evaluation of 2 equation models for the near wall turbulence.'*, AIAA Paper, Vol. 90, p. 1481.

Speziale, C. G., Abid, R. and Durbin, P. A. S. (1994) '*On realisability of the Reynolds Stress turbulence closures.*', Journal of Science and Computing, Vol. 9, pp. 369-403.

Speziale, C. G. and Bernard, P. S. (1992). *'The energy decay in self preserving isotropic turbulence revisited.'*, Journal of Fluid Mechanics, Vol. 241, pp. 645- 667.

Speziale, C. G. and Ngo, T. (1988). *'Numerical solution of turbulent flow past a backward facing step using a nonlinear k-e model'*, International Journal of Engineering Science, Vol. 26, No.10, pp. 1099-1112.

Speziale, C. G., Sarker, S. and Gatski, T. (1991). *'Modelling the pressure strain correlation of turbulence: an invariant dynamical systems approach.'*, Journal of Fluid Mechanics, Vol. 227, pp. 1245-272.

Stewart, I. (1989). *'Does God play dice, the mathematics of Chaos.'*, Blackwell, Oxford, UK.

Stone, H.L. (1968). *'Iterative solution of implicit approximations of multi-dimensional partial differential equations'*, SIAM Journal of Numerical Analysis, Vol. 5, part 3, pp530-558.

Suga, K. (1996). *'Development and application of a non-linear eddy viscosity model sensitized to stress and strain invariants.*' Ph.D. Thesis, Department of Mechanical Engineering, UMIST TDF/95/11.

Summers, D. M., Hanson, T. and Wilson, C. B. (1986). *'Validation of a computer simulation of wind over a building model.'*, Building and Environment, Vol. 21, pp97-111.

Taylor, G. I. (1938). Proceedings of the Royal Society. A164:476

Taylor, G. I. (1921). Proceedings of the London Mathematical Society.

Tehrani, A (1999), Private communication, Rolls Royce Nuclear Power, Wolverhampton, UK.

Tennekes, H. and Lumley, J. L. (1972). *'A first course in turbulence.'*, The MIT Press, Cambridge, UK.

Teubner, B. G. (1996). Second International Symposium on Computational Wind Engineering, Program and Abstracts, 1996, Colorado State University, USA.

Thomas, N. H. and Hancock, P. E. (1977). *'Grid turbulence near a moving wall.'*, Journal of Fluid Mechanics, Vol. 82, pp. 481 – 496.

Thomas, T. G. and Williams, J. J. R. (1992) *'Development of a parallel code to simulate skewed flow over a bluff body.'*, Department of Engineering, Queen Mary and Westfield College, London, UK.

Tsuchiya, M., Mochida, A., Ishida, Y., Murakami, S. and Konda, K. (1996). *'Development of a new k-e model for flow and pressure field around a bluff body.'*, Second International Symposium on Computational Wind Engineering 1996.

Uzkan, T. and Reynolds, W. C. (1967). *'A shear free turbulent boundary layer.'*, Journal of Fluid Mechanics, Vol.28, pp. 803-821.

Versteeg, H. K. and Malalasekera, W. (1996). *'An introduction to computational fluid dynamics - The finite volume method.'*, Longman Scientific and Technical, London, UK.

Webster, R. (1998). *'Efficient algebraic multi-grid solvers with elementary restriction and prolongation'*, International Journal of Numerical Methods in Fluids, Vol. 28, part 2, pp.317-336, 1998.

Wilcox, D. C. (1994). *'Turbulence modelling for CFD.'*, DCW Industries Inc., Canada

Wilcox, D.C. and Rubinesin, M.W. (1980). *'Progress in turbulence modelling for complex flow fields including effects of compressibility.'*, NASA TP - 15.7.

Wilkes, N. G. (1999). Private Communication, CFX-International, Harwell, Oxfordshire, UK.

Windstorm – Loss Dimensions of a Natural Hazard (1990). Munich Reinsurance Company, Munchener Ruckversicherungs-Gesellschaft, Koniginstrafe 107 D-8000 Munchen 40 Federal Republic of Germany.

Wright, N. G. (1997, 1998, 1999). Private Communications, The University of Nottingham, Nottingham, UK.

Wright, N.G., Easom, G.J. and Hoxey, R. (1997). *'Improved computational models for wind engineering.'*, Report for the School of Civil Engineering, The University of Nottingham, England, UK.

Wright, N.G., Easom, G.J. and Hoxey, R. (1998). *'Improved computational models for wind engineering.'*, Proceedings of the 4th UK Conference on Wind Engineering, Bristol University, Bristol, England.

Wright, N.G. and Easom, G.J. (1997). *'Improved computational models for wind engineering.'*, Proceeding of the 10th International Conference on Wind Engineering, Copenhagen, Denmark.

Wright, N.G. and Easom, G.J. (1999). *'Comparison of several computational turbulence models with full-scale measurements of the flow around a building.'*, Paper accepted for publication in the Journal of Wind and Structures.

Wright, N.G. and Easom, G.J. (1999). *'Improved computational models for wind engineering.'*, Paper accepted for publication in the Journal of Wind and Structures.

Wyngaard, J. C. (1976). *'The atmospheric boundary layer modelling and measurement.'*, Springer Verlag.

Yakhot, V. and Orszag, S. A. (1986). *'Renormalisation Group analysis of turbulence: Basic theory.'*, Journal of Science and Computing, Vol. 1, pp. 3 –51.

Yakhot, V., Orsag, S. A., Thamgam, S., Gatski, T. B. and Speziale, C. G. (1992). *'Development of turbulence models for shear flows by a double expansion technique.'*, Physics of Fluids A, Vol. 4, pp. 1510-1520.

Young, A. D. (1989). *'Boundary layers.'*, BSP Professional Books, Blackwell Scientific Publications Ltd., Oxford, UK.

Zannetti, P. (1990). *'Air pollution modelling: Theories, computational methods and available software.'*, Computational Mechanics Publications, Von Nostrand, Reinhold, New York, USA.

Zhang, Y. Q., Huber, A. H., Arya, S. and Snyder, W. H (1993). '*Numerical simulation to determine the effects of incident wind shear and turbulence level on the flow around a building.'* , Journal of Wind Engineering and Industrial Aerodynamics, Vol. 46-47, pp. 129-134, Elsevier, Amsterdam, Netherlands .

Zhang, H. L. Z. and Ko, N. W. M. (1996). *'Numerical analysis of incompressible flow over smooth and grooved circular cylinders.'*, Computers and Fluids, Vol. 25, No.3 , pp. 263-281.

Zienkiewicz, O.C. and Taylor, R.L. (1989) *'The finite element method, 4th edition Vol. 1 basic formulation and linear problems.'*, McGraw Hill, New York, USA.

Appendix A – Figures and Illustrations.

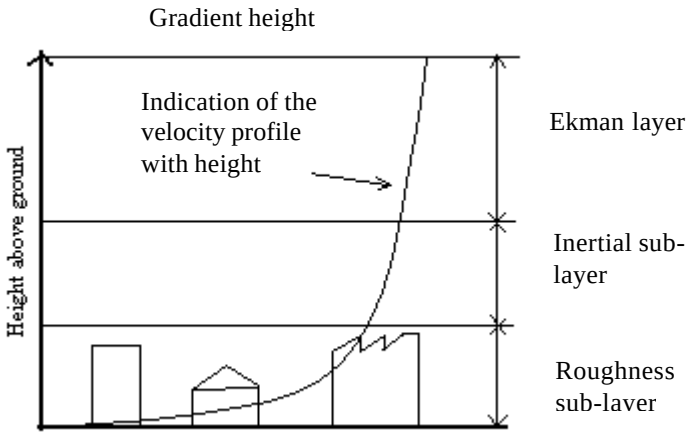

Figure 1: Details of the atmospheric boundary layer.

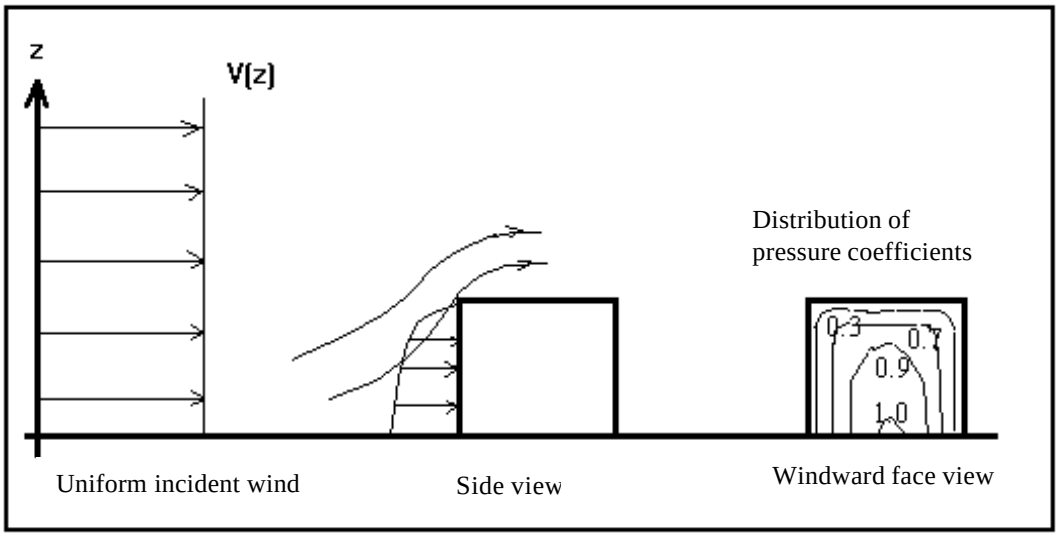

Figure 2: The effect of uniform wind profile on a surface mounted cube (Based on Cook 1986a)

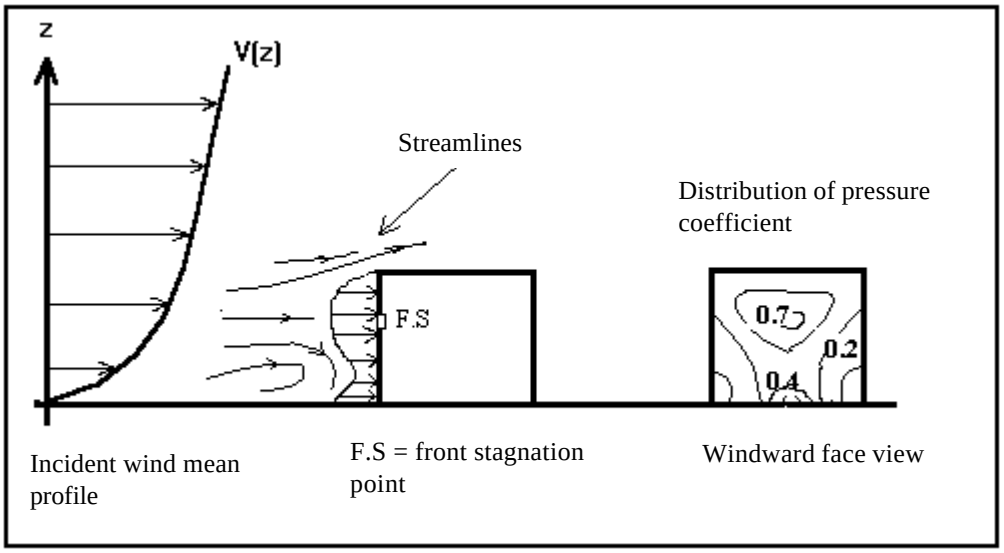

Figure 3: The effect of a boundary layer mean wind profile on a surface mounted cube (Based on Cook 1986a)

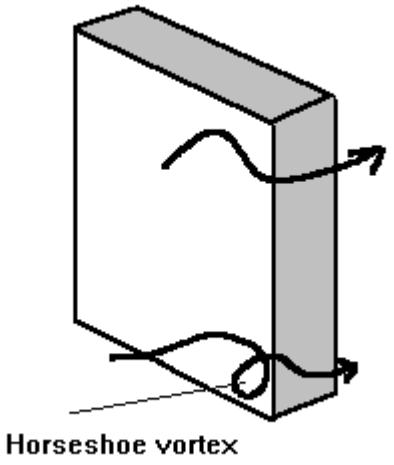

Figure 4: The flow at the side walls (Based on Cook 1986a)

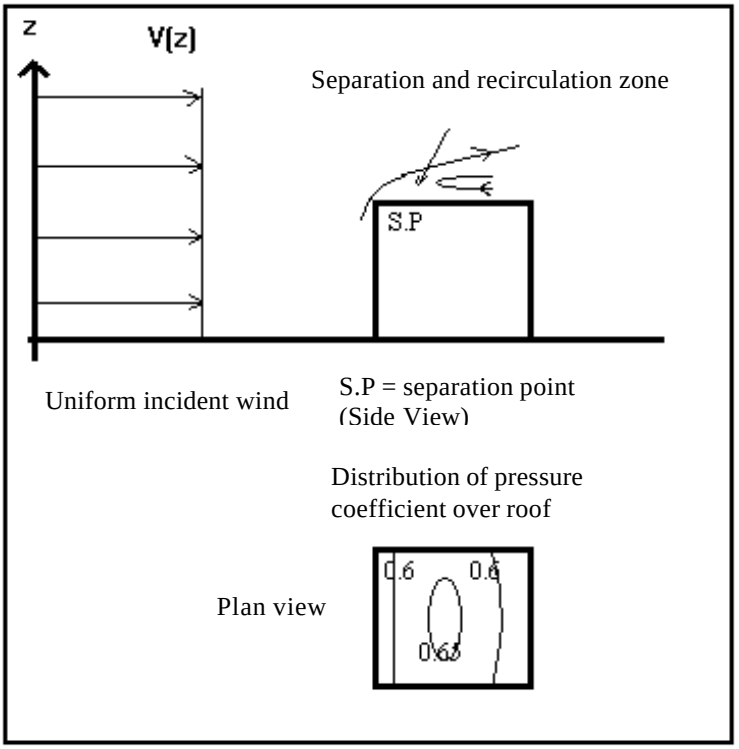

Figure 5: The flow over the roof of a surface mounted cube with uniform incident wind. (Based on Cook 1986a)

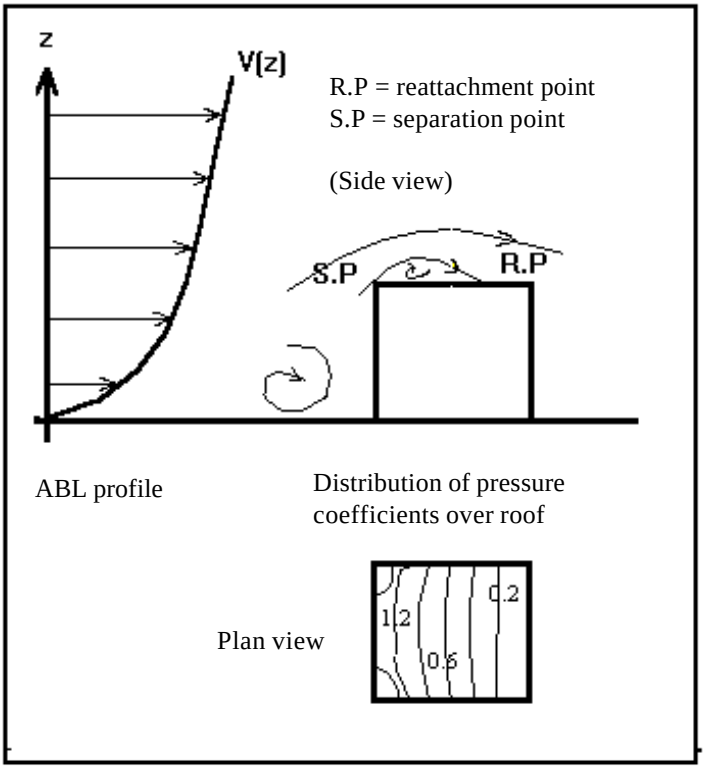

Figure 6: The flow over the roof of a cube with ABL incident wind (Based on Cook 1986a)

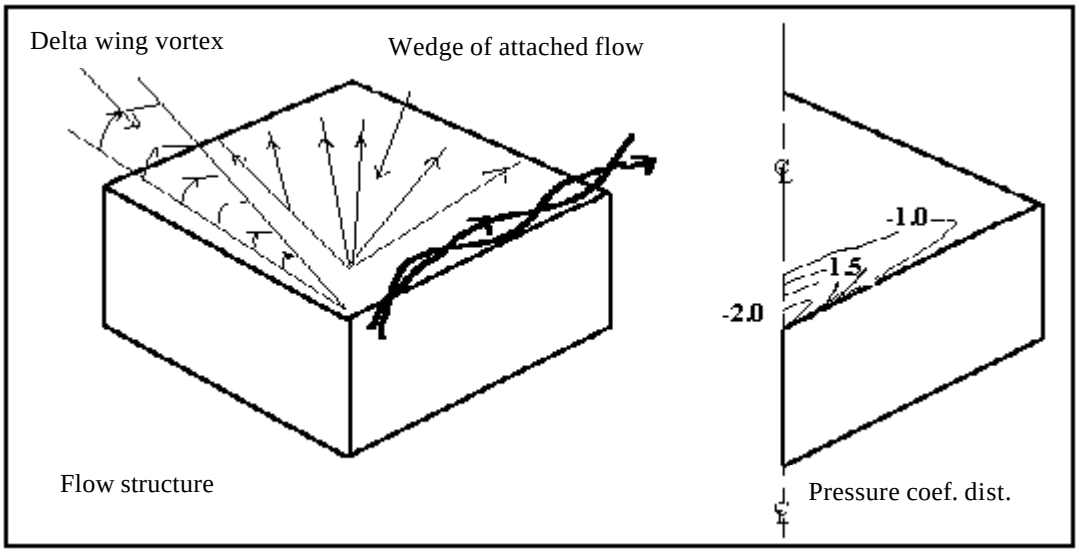

Figure 7: Cube skewed at 45 degrees to the ABL incident wind. (Based on Cook 1986a)

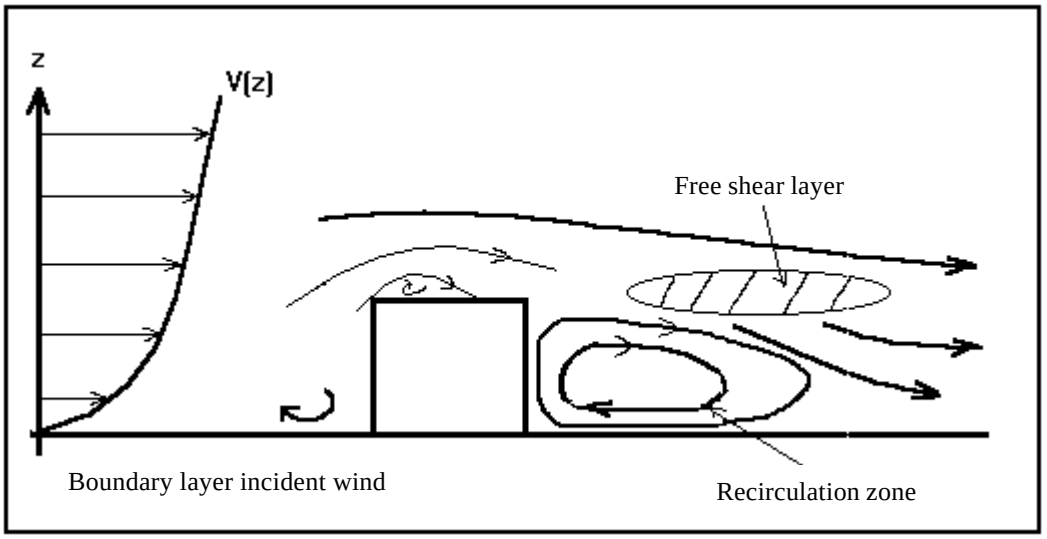

Figure 8: Flow in the wake (side view, Based on Murakami 1990)

Convention:

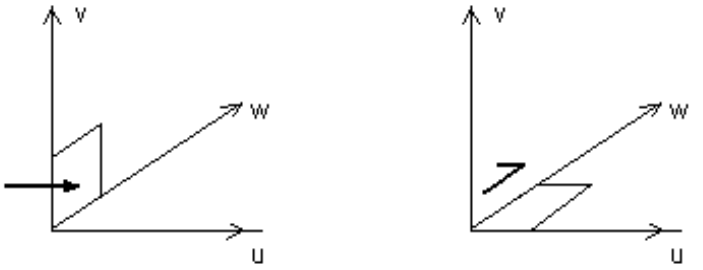

Normal stress = $-\rho\overline{u'u'}$ (Normal stress on plane *vw* in direction of u)

Shear stress = $-\rho\overline{v'w'}$ (Plane *wu*, force in positive w direction)

Figure 9: Reynolds Stresses: convention.

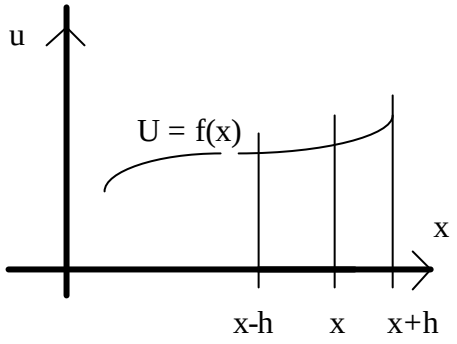

Figure 10: Finite differences. (Shaw 1989)

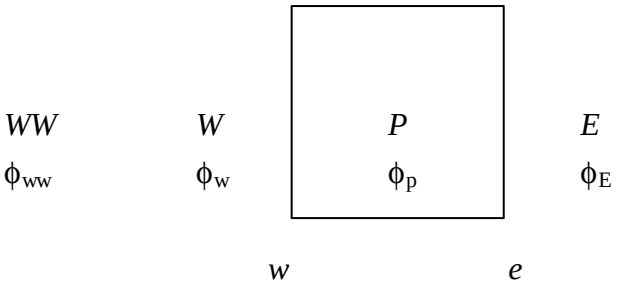

Figure 11: Control volume notation.

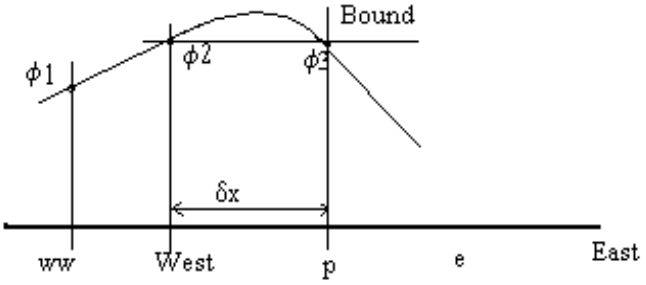

Figure 12: Overshoots using the QUICK method

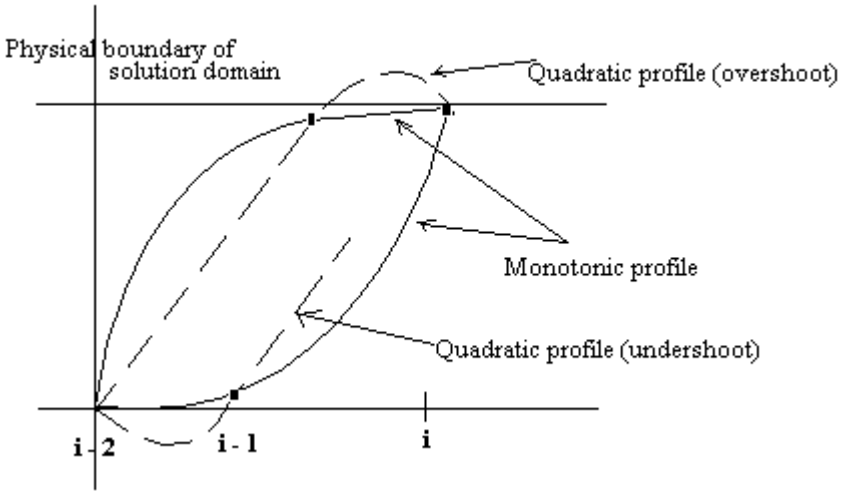

Figure 13: A comparison of CCCT and QUICK interpolation profiles. (Gaskell and Lau 1988)

Figure 14: The 6m cube (site photograph).

Figure 15: The Silsoe Structures Building (site photograph).

Figure 16: The Silsoe Experimental Wall (site photograph).

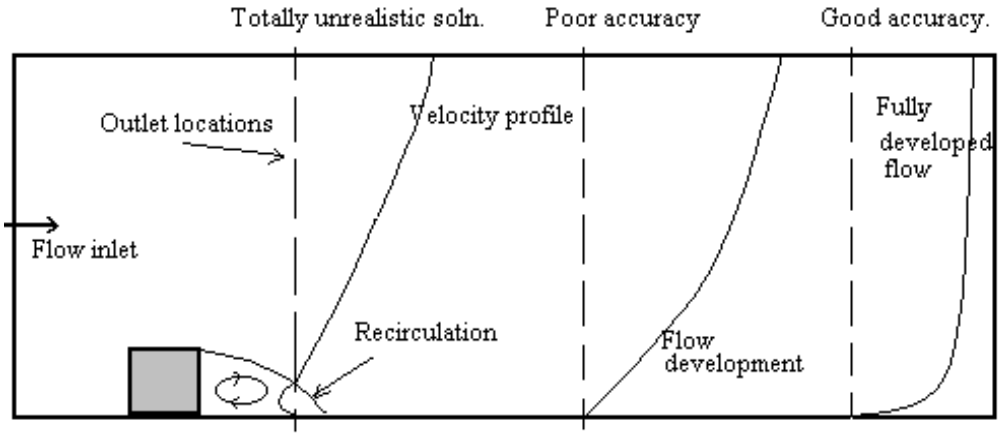

Figure 17: Positioning of the outlet boundary (Based on Versteeg and Malalasekera 1996)

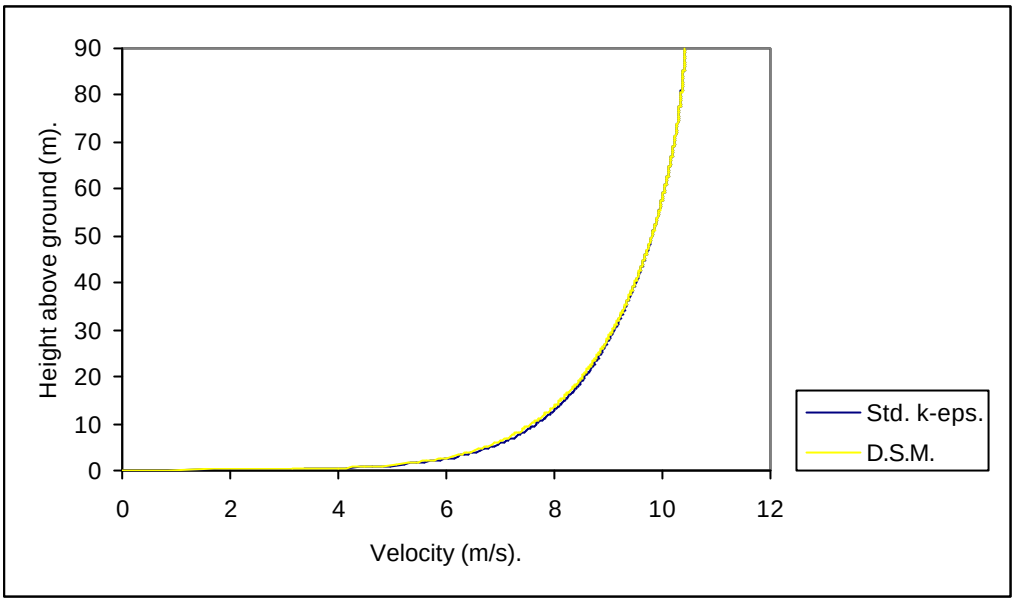

Figure 18: Comparison of boundary layer profiles for the DSM and standard *k-e* models. (Inlet velocity = 10m/s at 60m).

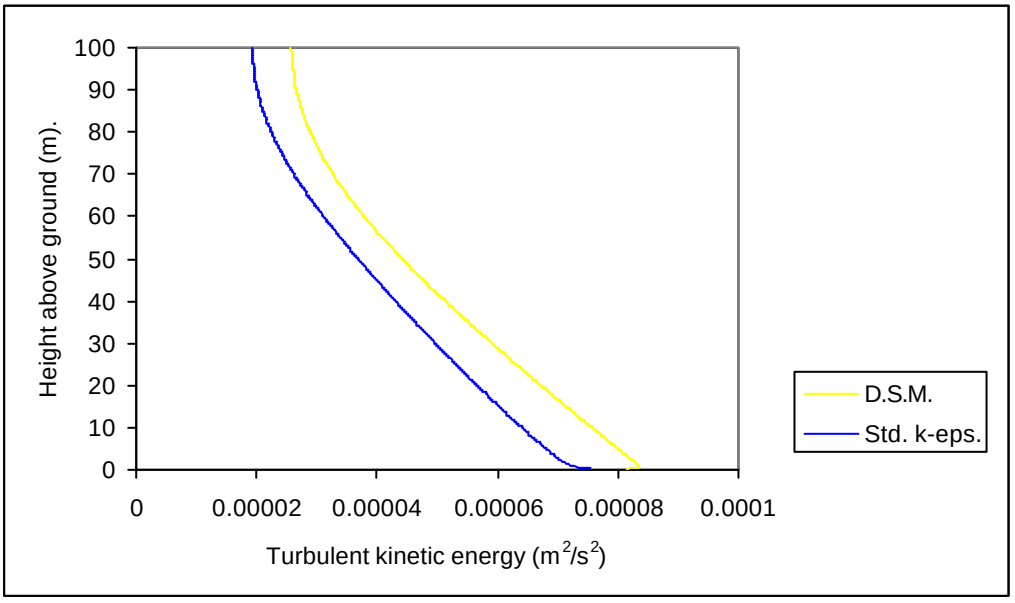

Figure 19: Comparison of turbulent kinetic energy, boundary layer profiles for the DSM and standard *k-e* models. (Inlet velocity = 0.1m/s at 60m).

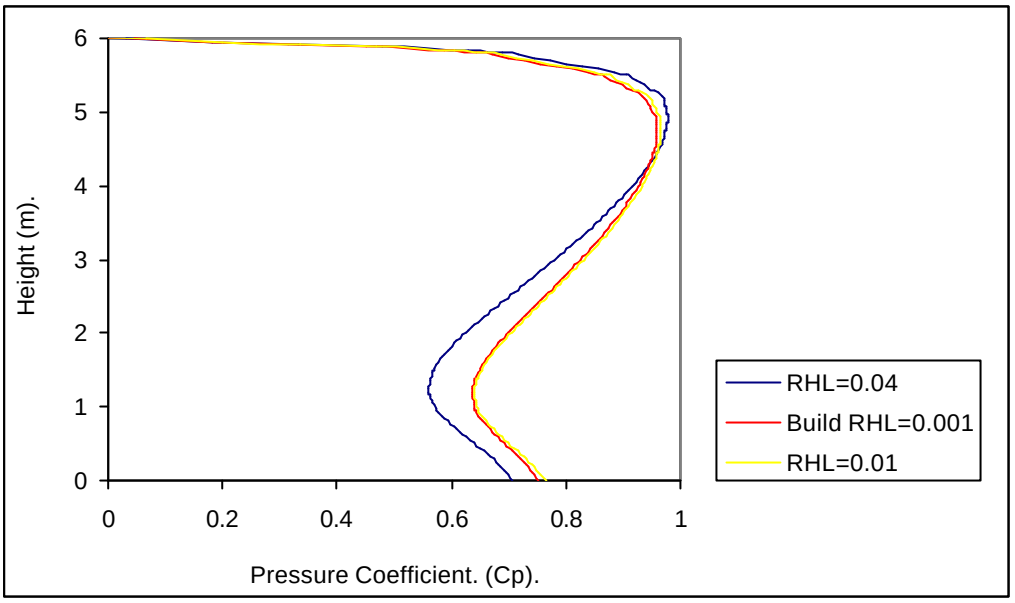

Figure 20: 6m cube, normal orientation, comparison of windward face pressure distributions for different boundary layer roughness heights and building roughness.

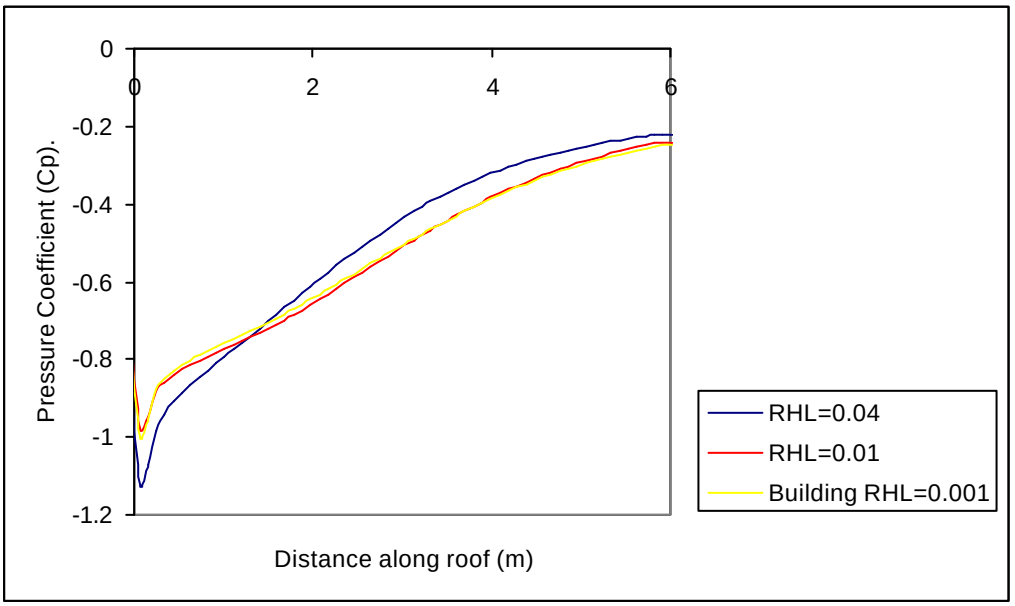

Figure 21: 6m cube, normal orientation, comparison of roof pressure distributions for different boundary layer roughness heights and building roughness.

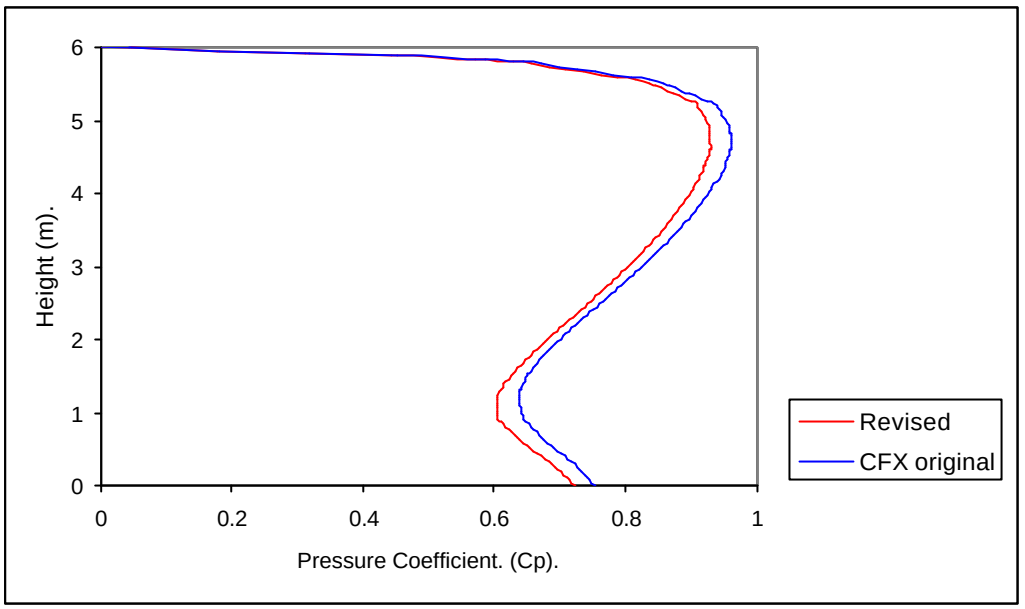

Figure 22: 6m cube, normal orientation, comparison of windward face pressure distributions for the CFX original and revised wall functions.

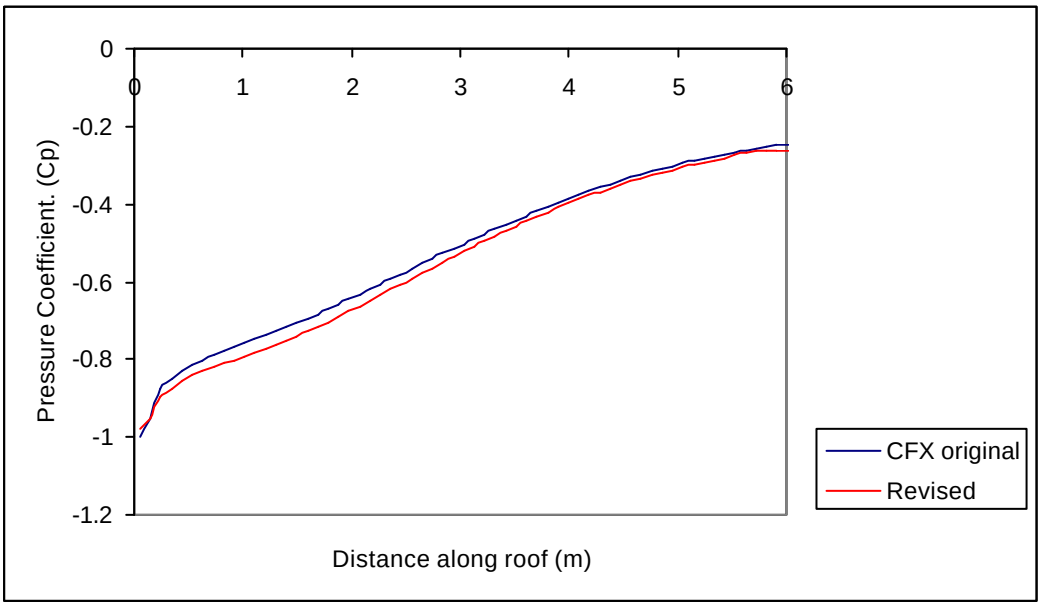

Figure 23: 6m cube, normal orientation, comparison of roof pressure distributions for the CFX original and revised wall functions.

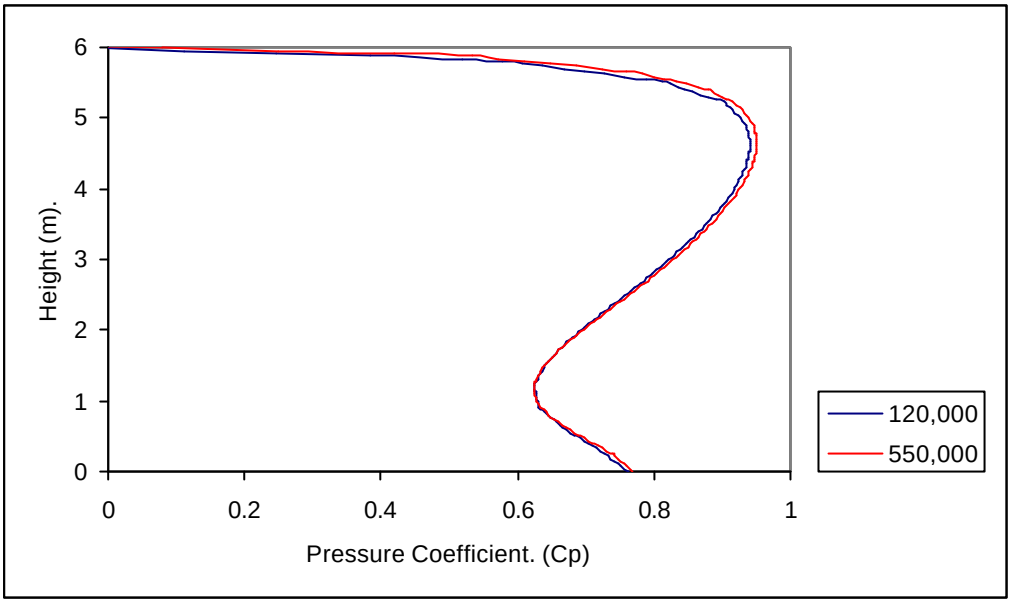

Figure 24: 6m cube, normal orientation, comparisons of windward face pressure distributions for the grid refinement test number 1.

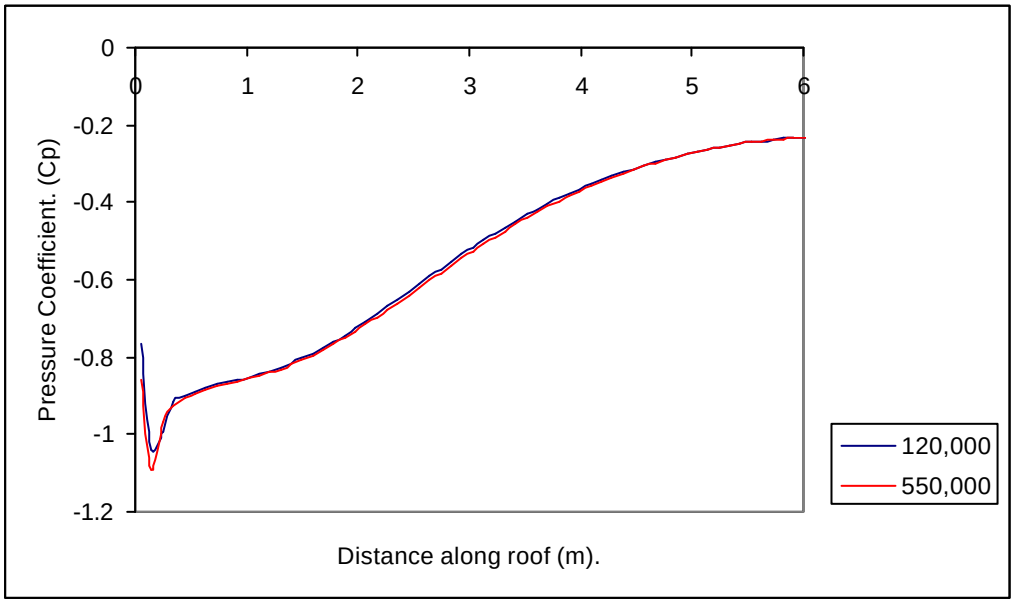

Figure 25: 6m cube, normal orientation, comparisons of roof pressure distributions for the grid refinement test number 1.

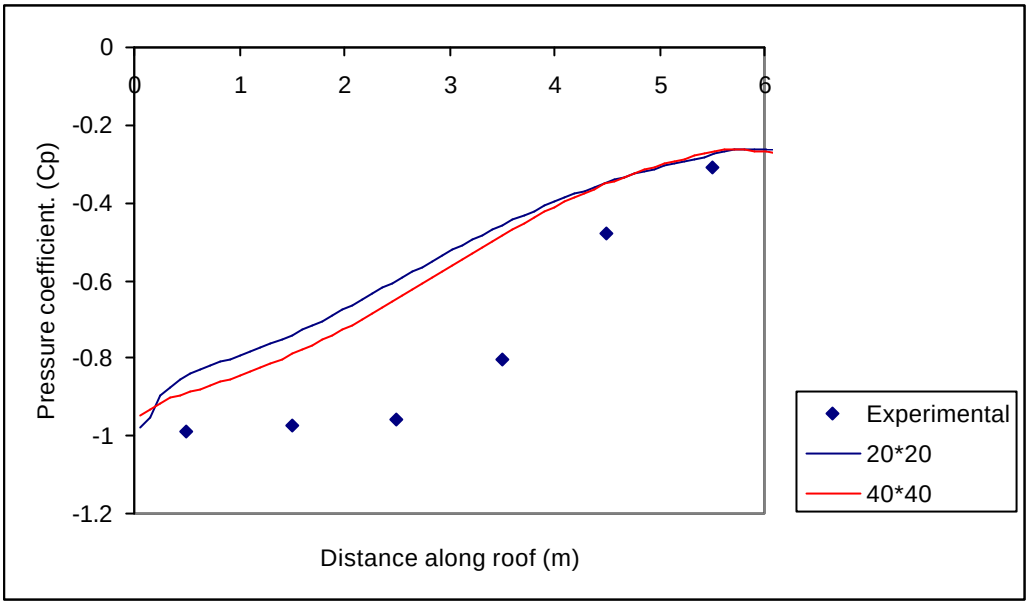

Figure 26: 6m cube, normal orientation, comparison of roof pressure distributions for the grid refinement test number 2 (Note: the key values refer to number of nodes around cube).

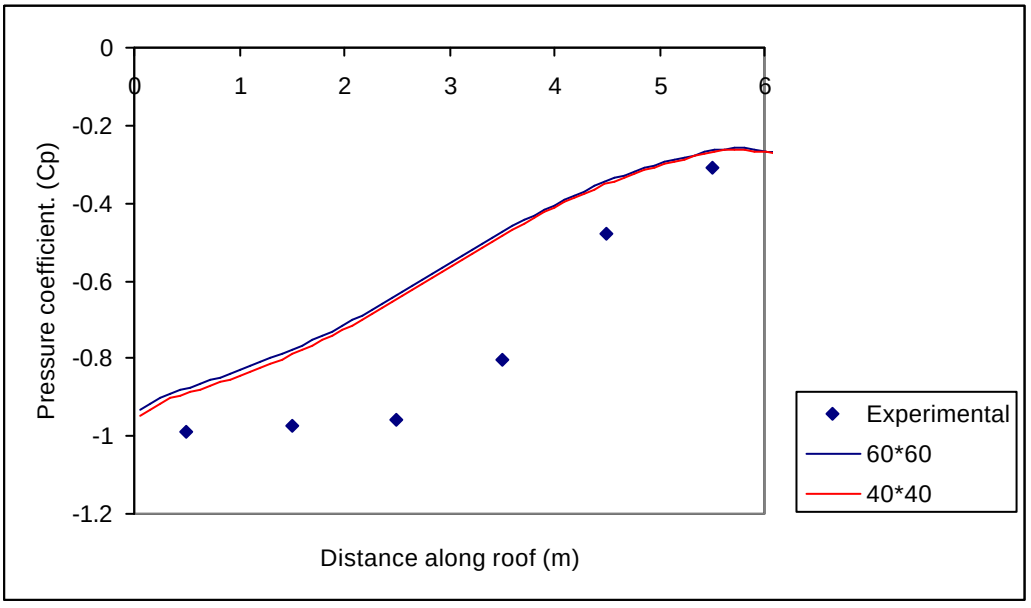

Figure 27: 6m cube, normal orientation, comparison of roof pressure distributions for the grid refinement test number 2 (Note: the key values refer to number of nodes around cube).

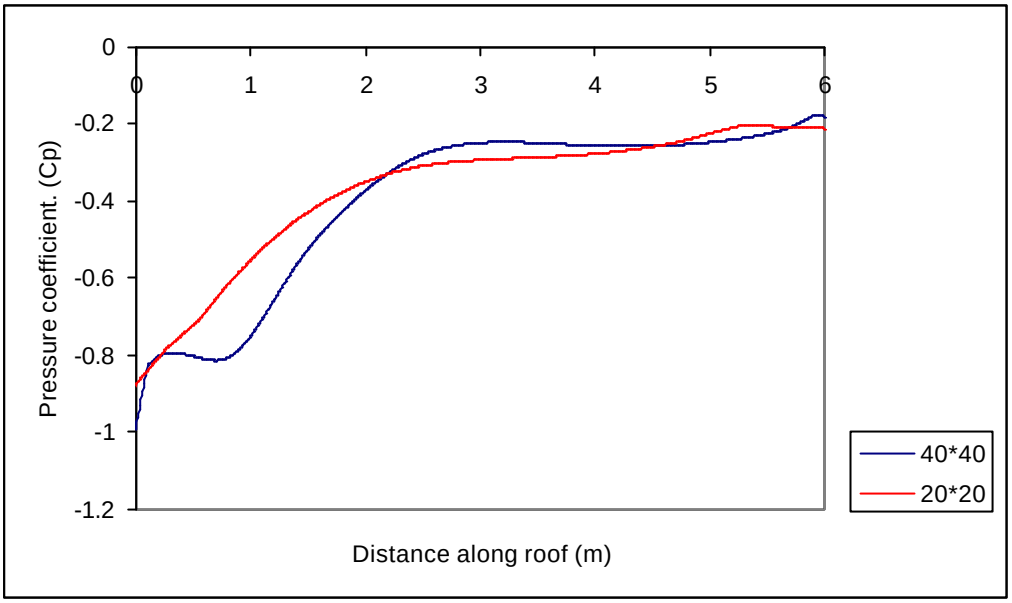

Figure 28: 6m cube, skewed orientation, comparison of roof pressure distributions for the grid refinement tests (Note: the key values refer to number of nodes around cube).

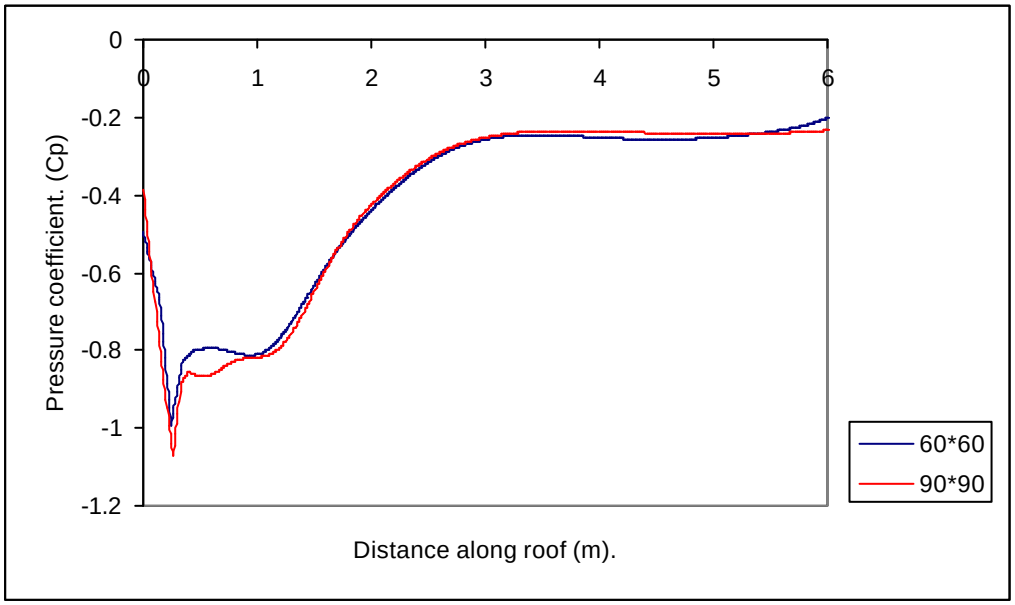

Figure 29: 6m cube, skewed orientation, comparison of roof pressure distributions for the grid refinement tests (Note: the key values refer to number of nodes around cube).

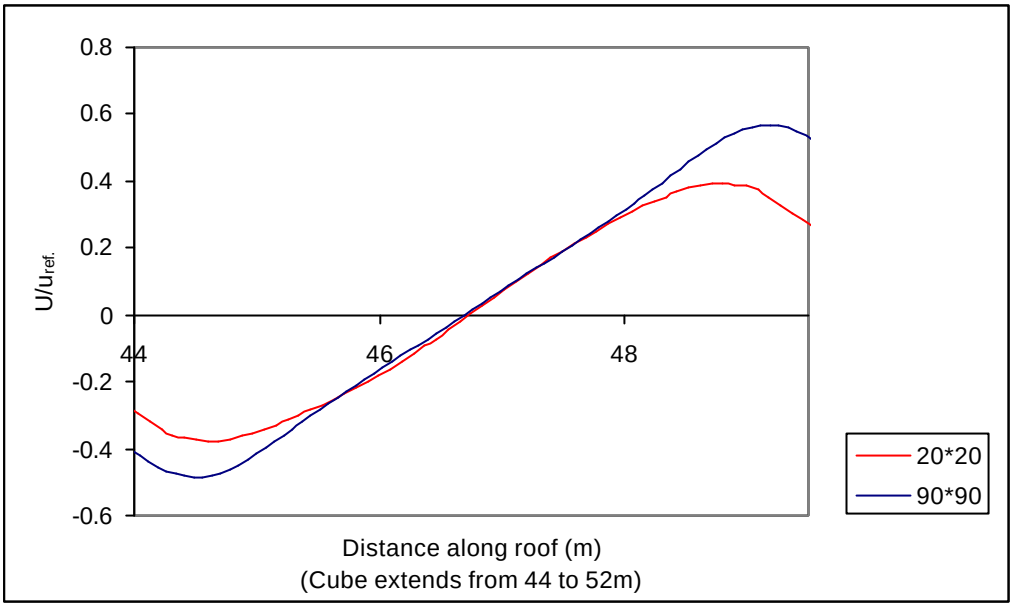

Figure 30: 6m cube, skewed orientation, comparison of the roof lateral velocity component, at the centre of the cube (y coordinate plane), for the grid refinement tests (Note: the key values refer to number of nodes around the cube).

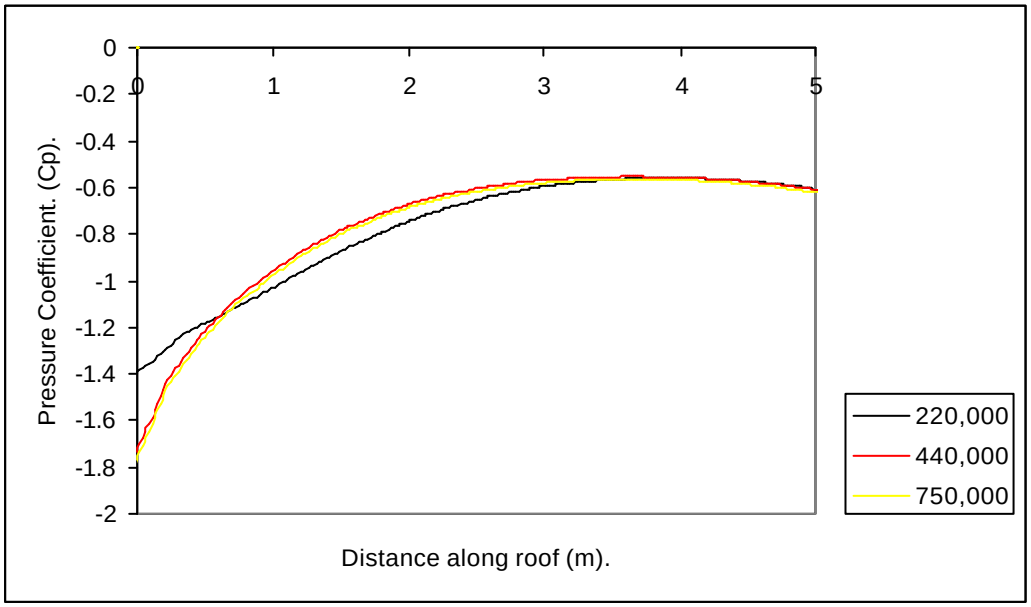

Figure 31: SSB, sharp eaves, windward roof pressure distribution, grid refinement test (Note: the key values refer to the total number of nodes in domain).

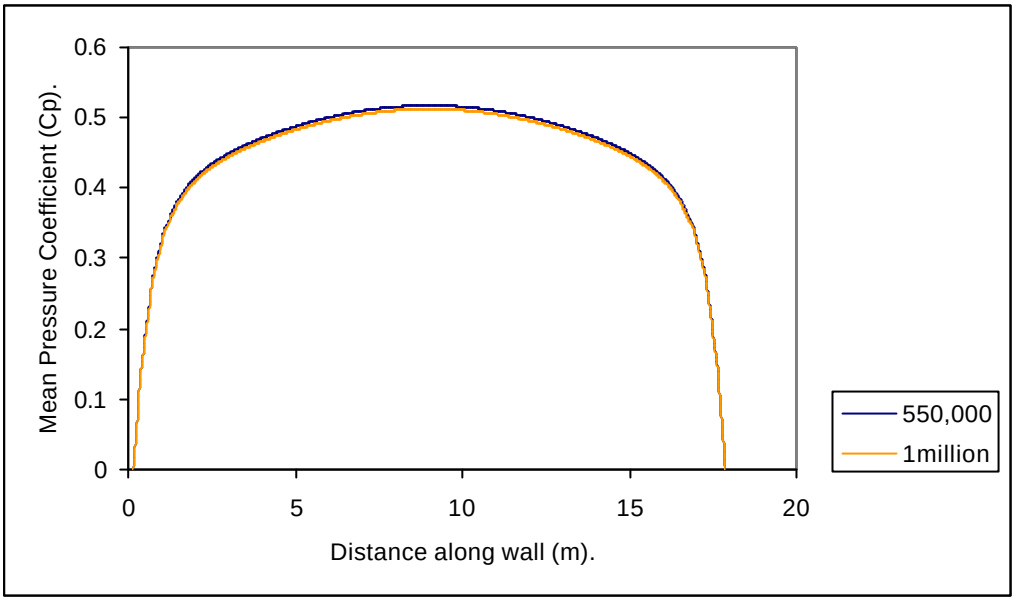

Figure 32: Silsoe experimental wall, windward face pressure distribution, grid refinement test (Note: the key values refer to the total number of nodes in domain).

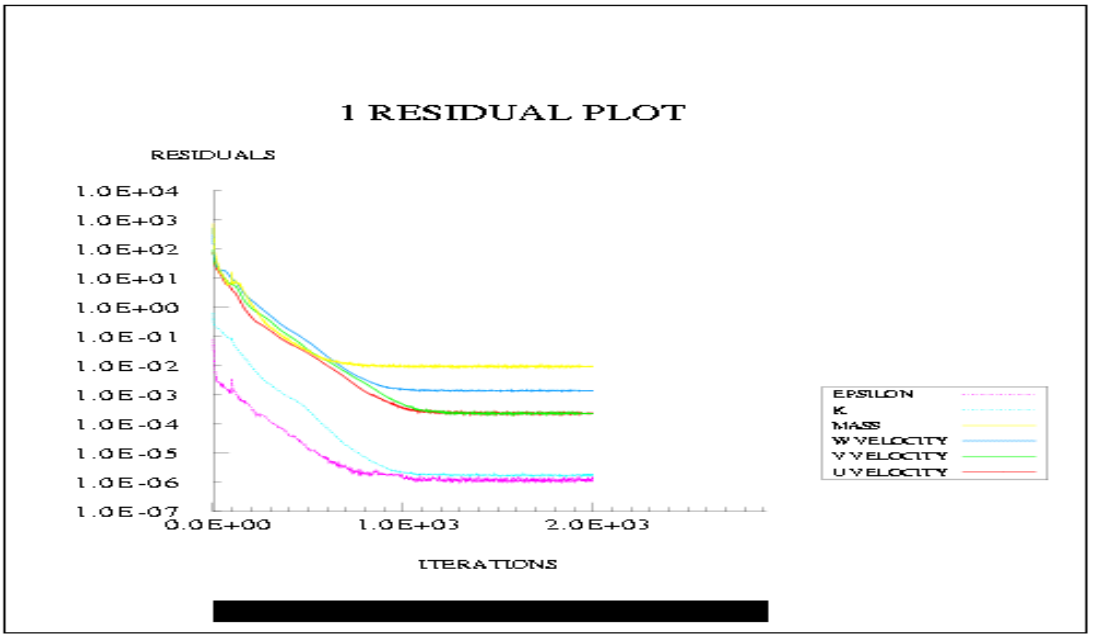

Figure 33: Convergence history, residual plot to show solution convergence for a single numerical precision run.

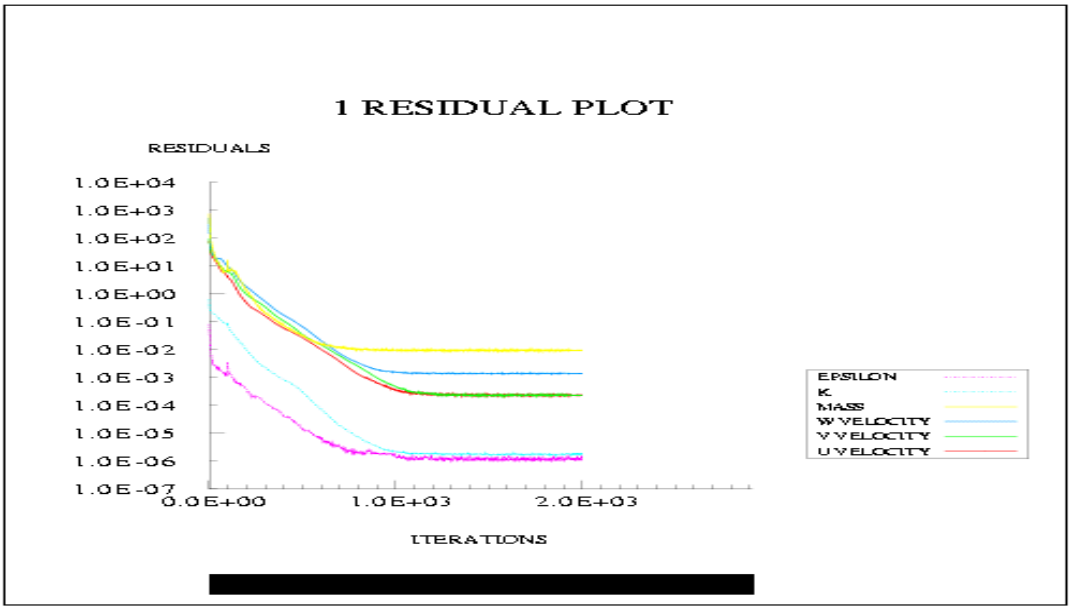

Figure 34: Convergence history, residual plot to show solution convergence for a double numerical precision run.

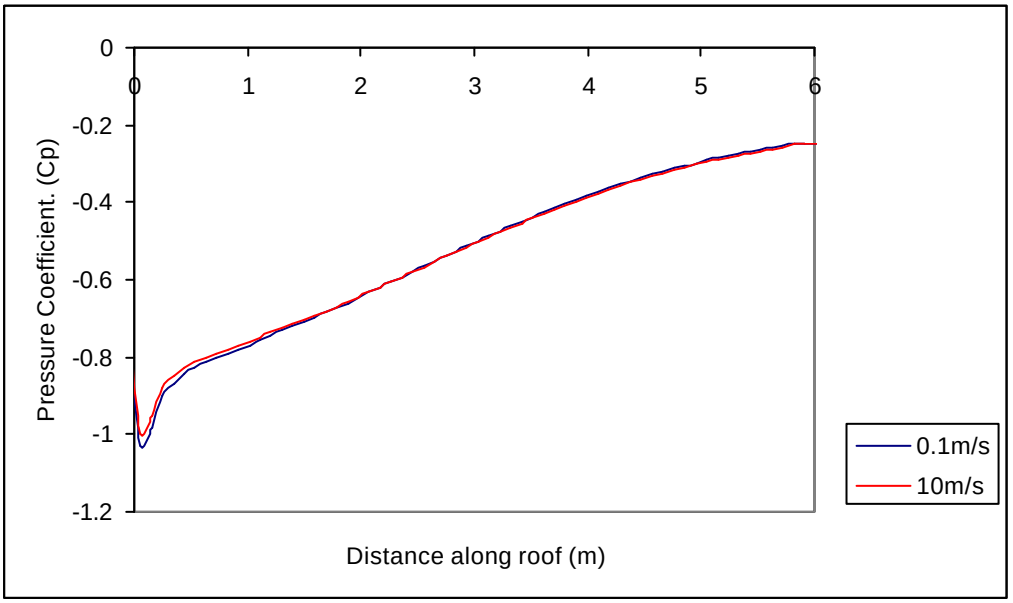

Figure 35: 6m cube, normal orientation, roof pressure distribution, Reynolds number test.

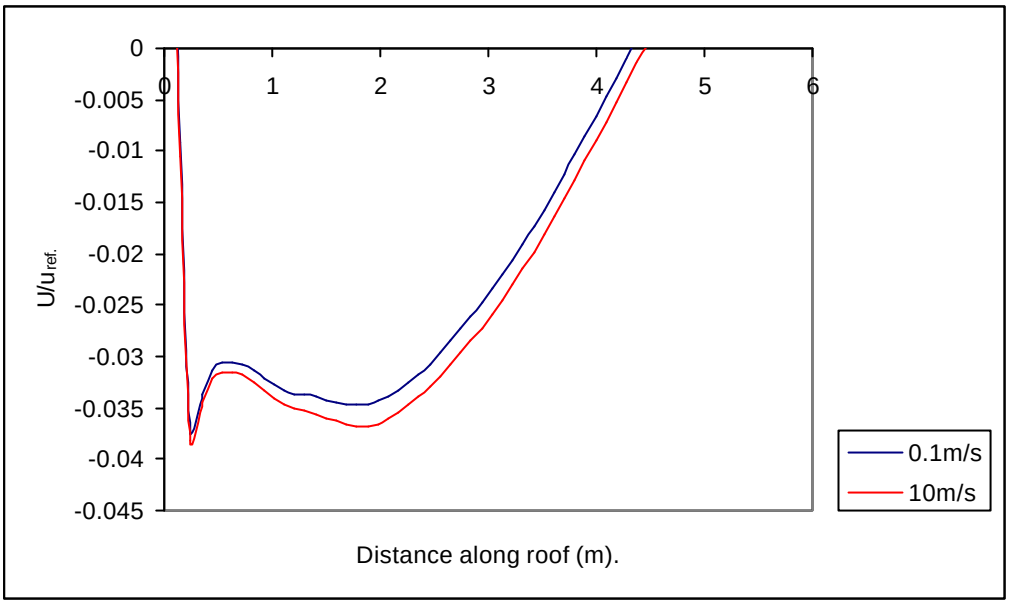

Figure 36: 6m cube, normal orientation, roof vortex strength, Reynolds number test.

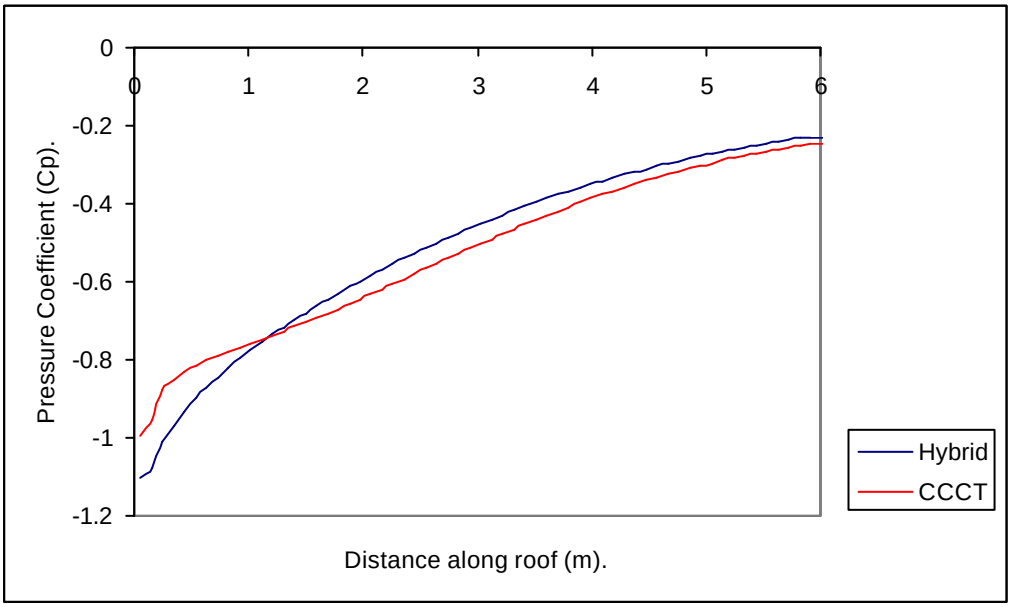

Figure 37: 6m cube, normal orientation, roof pressure distribution, comparison of differencing schemes.

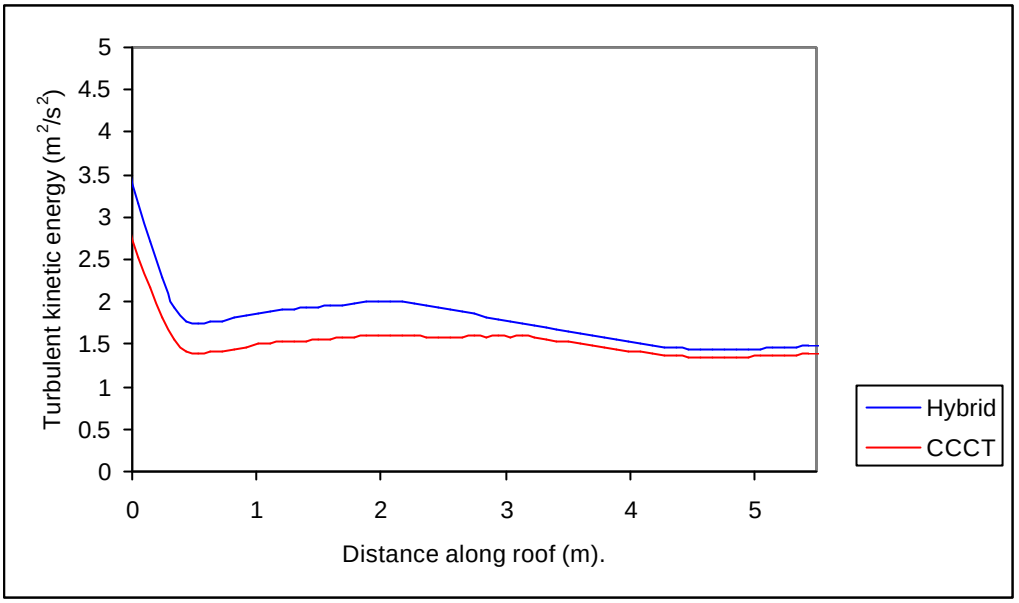

Figure 38: 6m cube, normal orientation, roof turbulent kinetic energy distribution, comparison of differencing schemes.

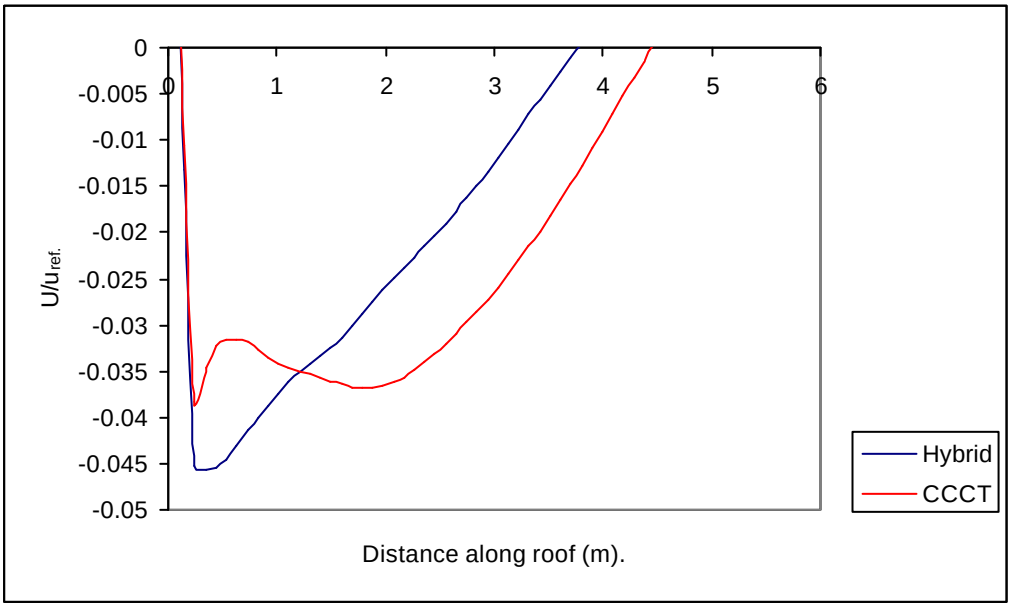

Figure 39: 6m cube, normal orientation, roof vortex strength, comparison of differencing schemes.

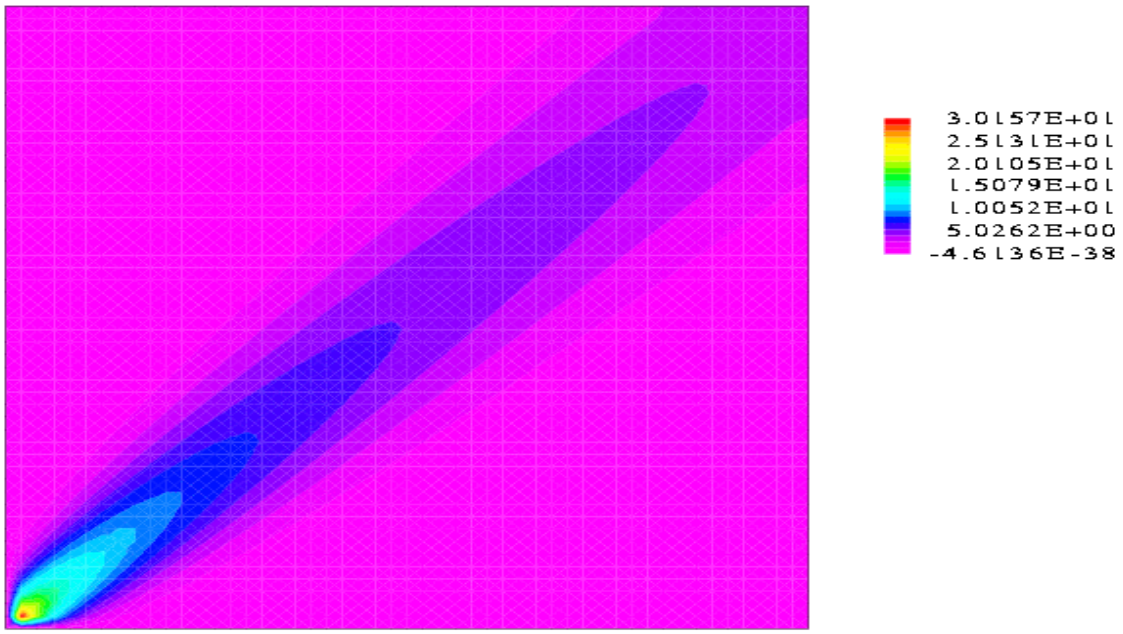

Figure 40: False diffusion with the hybrid differencing scheme.

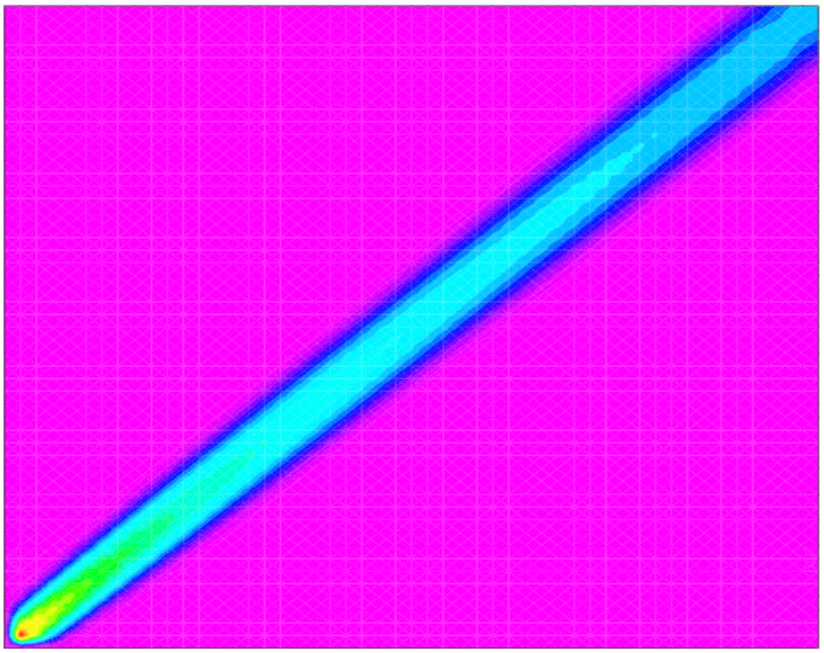

Figure 41: False diffusion with the CCCT differencing scheme

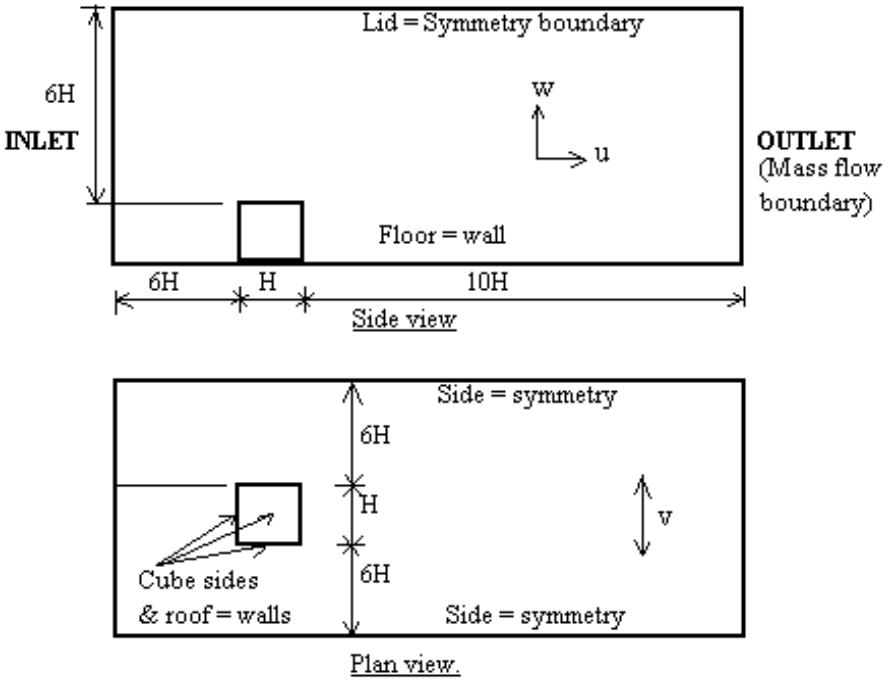

Figure 42: The computational domain for the 6m cube model.

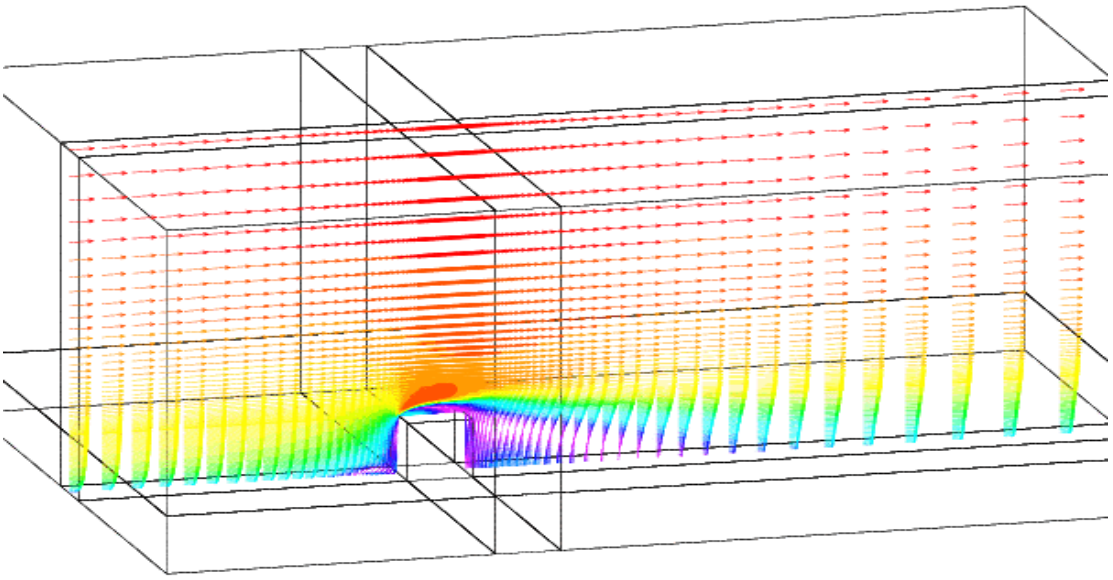

Figure 43: The CFD domain for the 6m cube simulations.

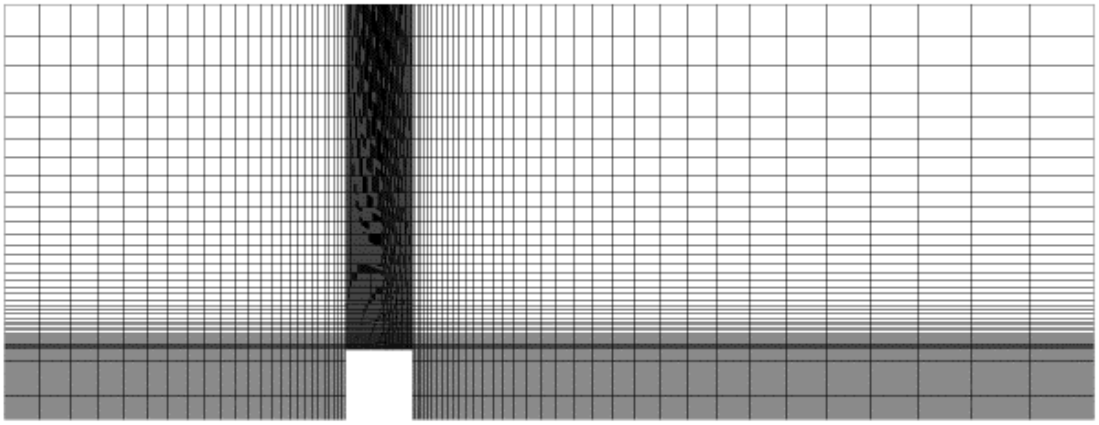

Figure 44: Example of the CFD mesh for the grid refined simulations.

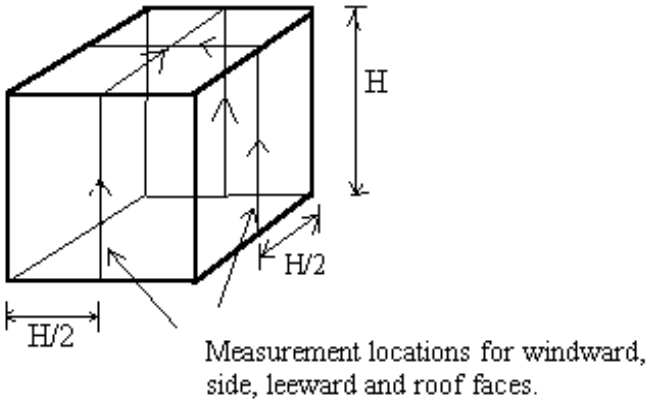

Figure 45: Normal cube measurement location

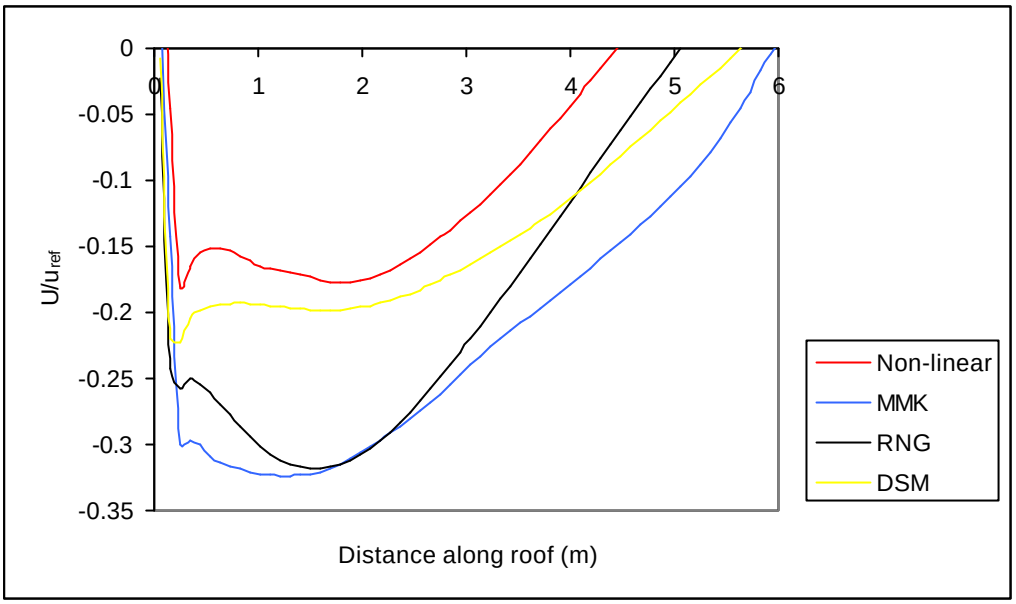

Figure 46: 6m cube, normal orientation, comparison of roof vortex strength and reattachment point.

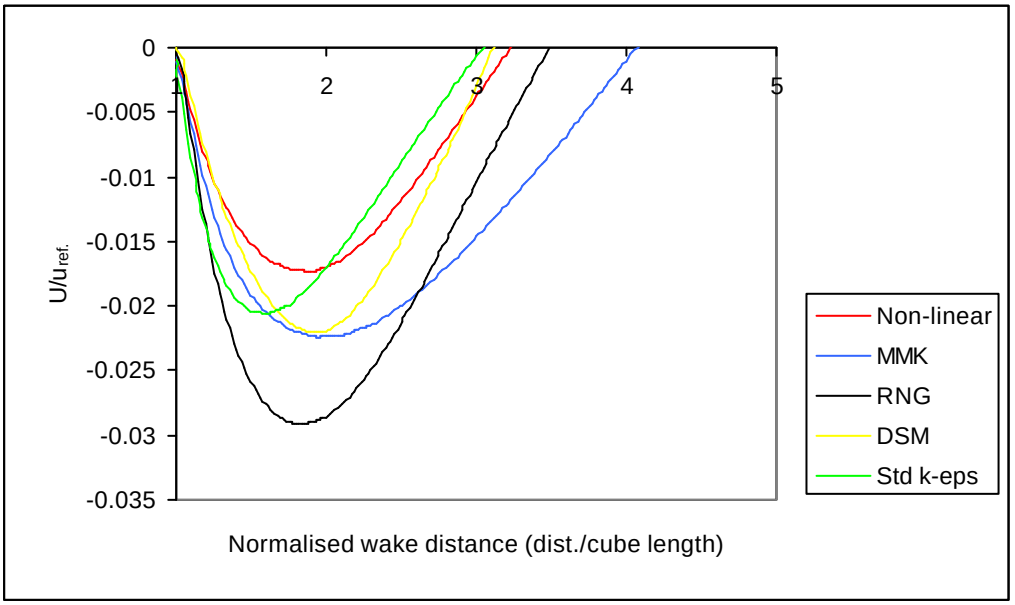

Figure 47: 6m cube, normal orientation, comparison of wake vortex strength and reattachment point.

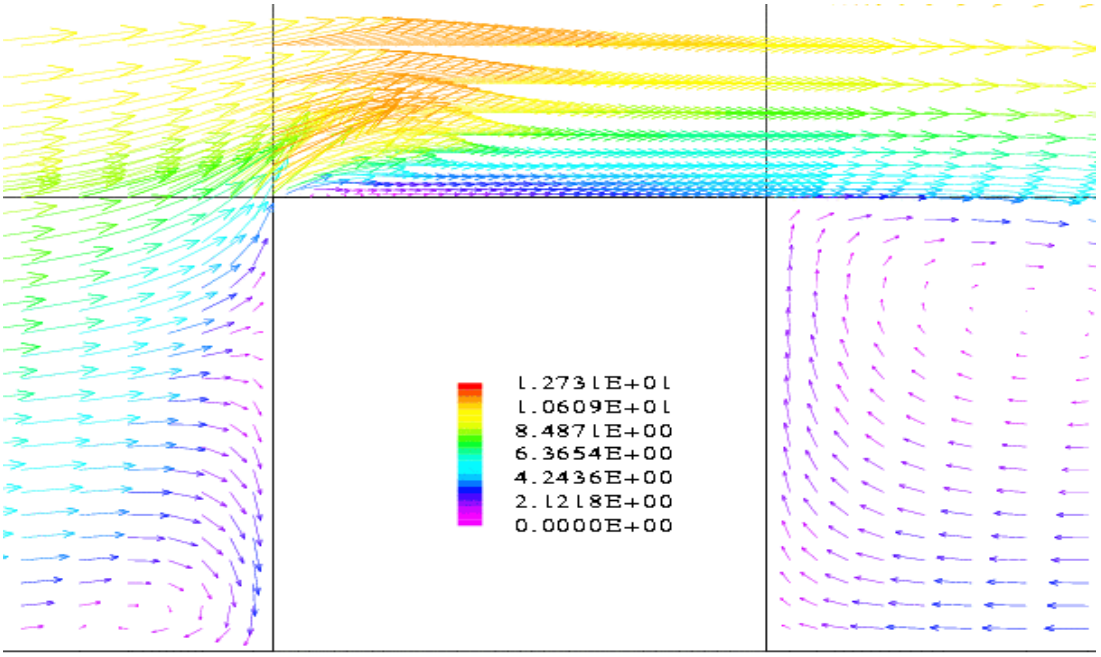

Figure 48: Velocity vectors showing the roof flow field for the 6m cube, standard *k-e* model.

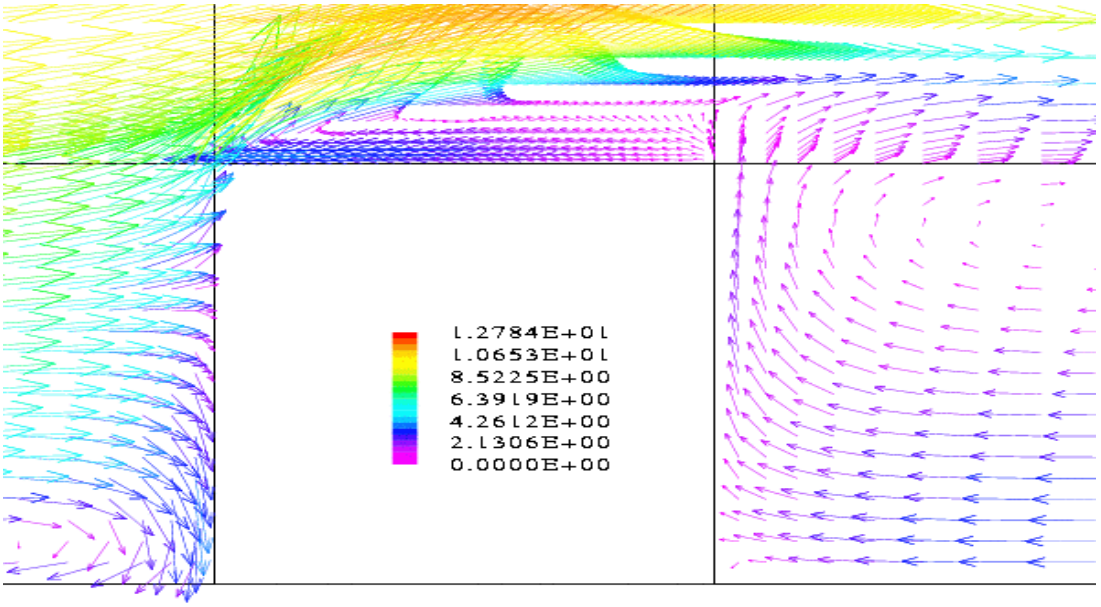

Figure 49: Velocity vectors, the MMK *k-e* model.

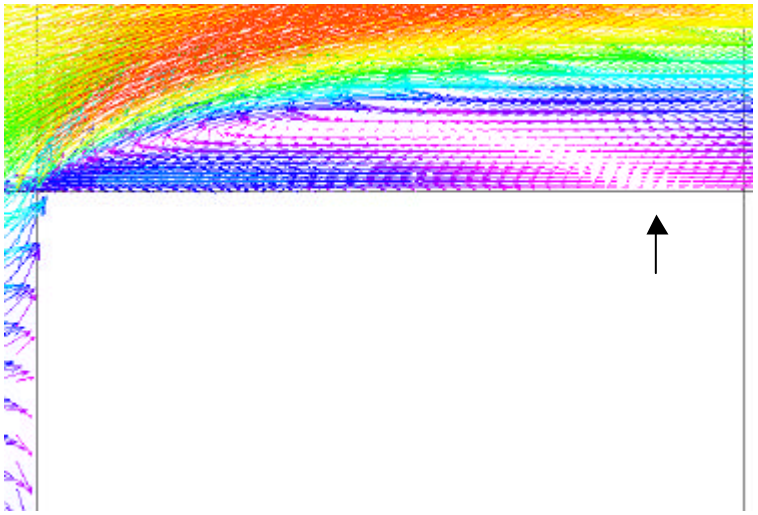

Figure 50: Velocity vectors, the RNG *k-e* model (arrows shows reattachment location)

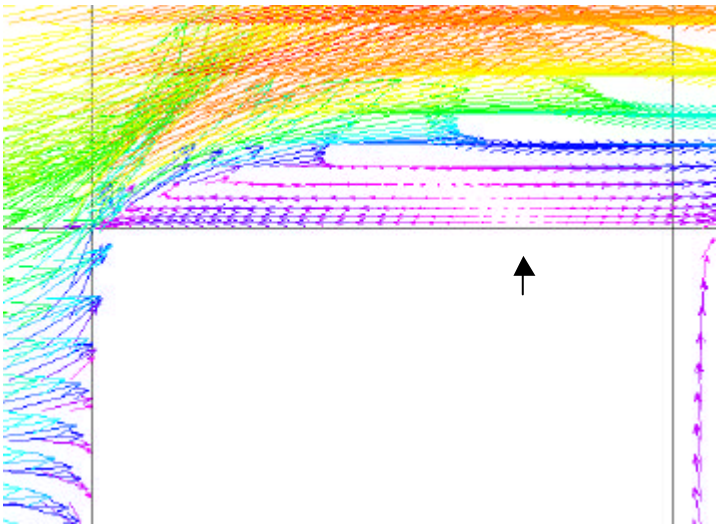

Figure 51: Velocity vectors, the non-linear *k-e* model (arrows shows reattachment location)

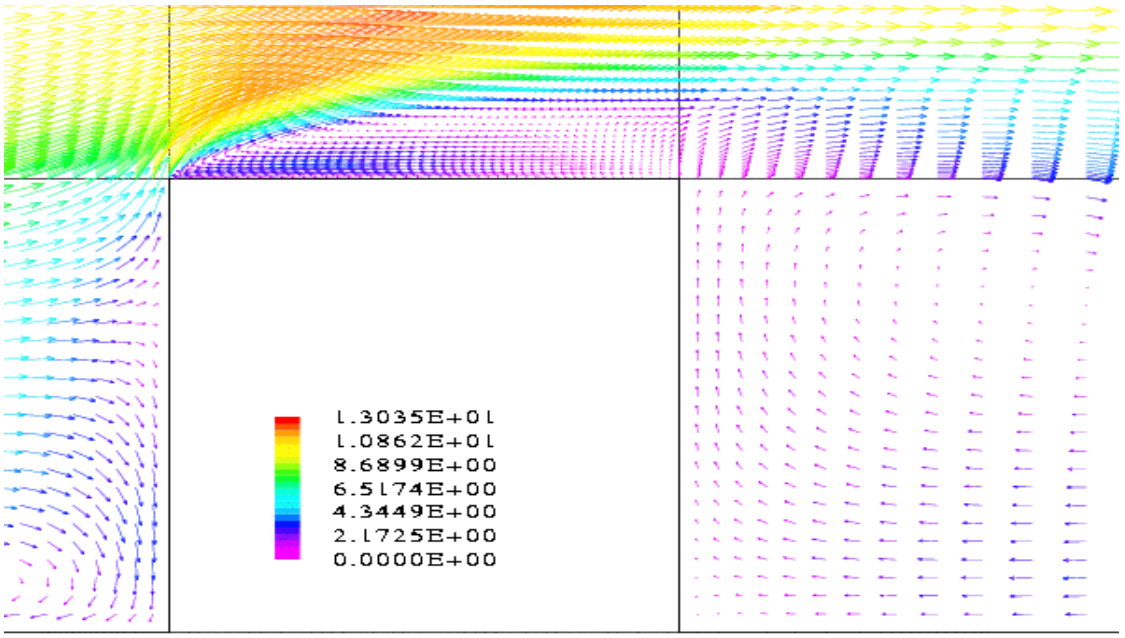

Figure 52: Velocity vectors, the differential stress model

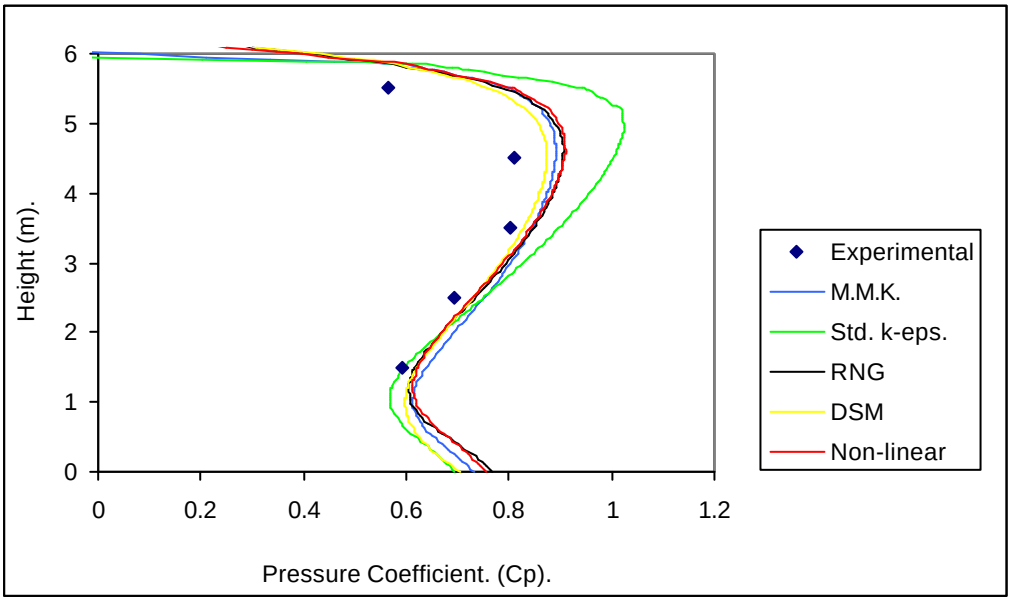

Figure 53. 6m cube, normal orientation, windward face pressure distribution.

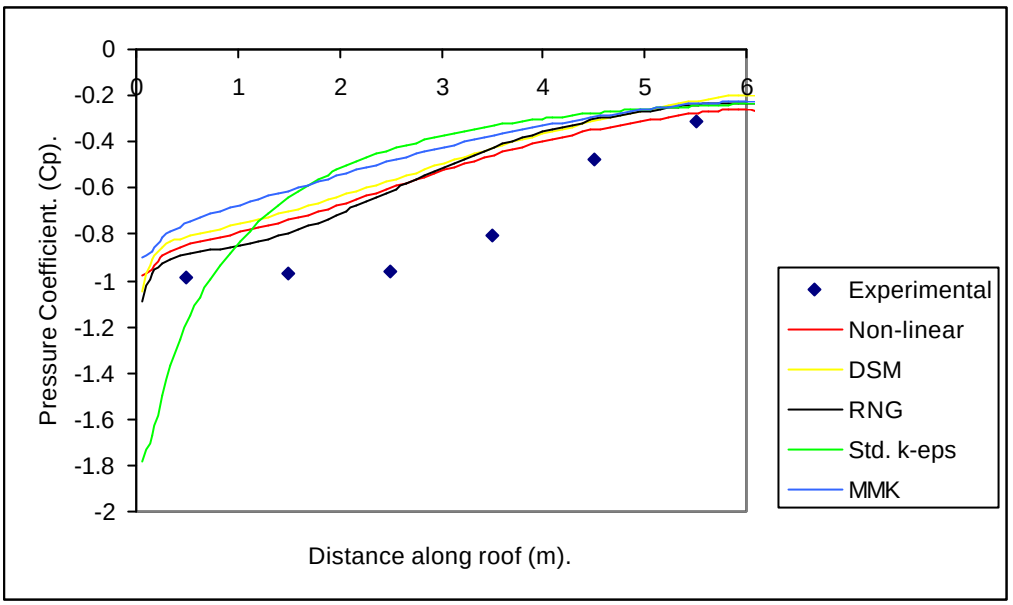

Figure 54: 6m cube, normal orientation, roof pressure distribution.

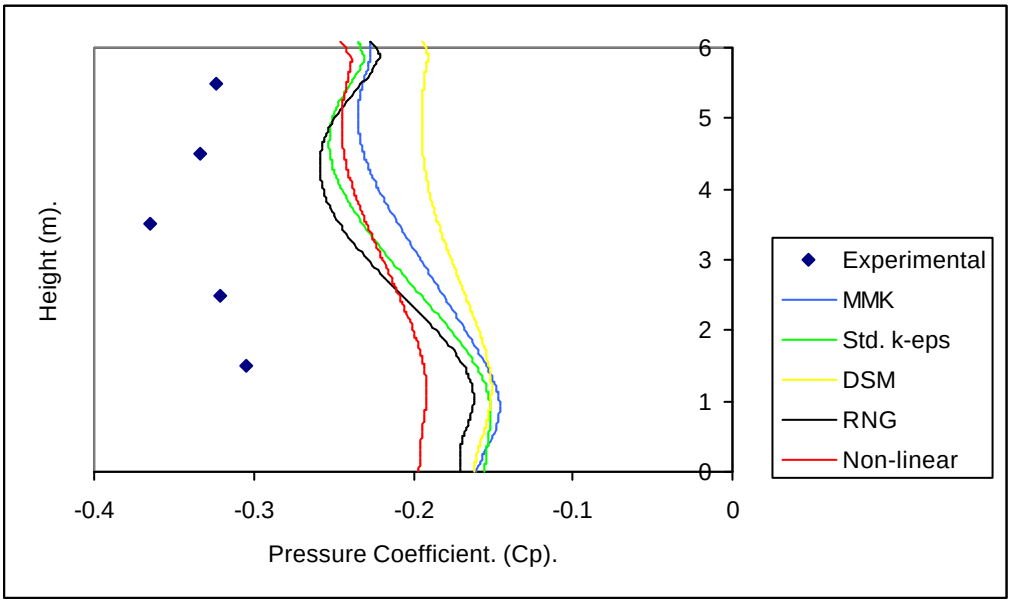

Figure 55: 6m cube, normal orientation, leeward face pressure distribution.

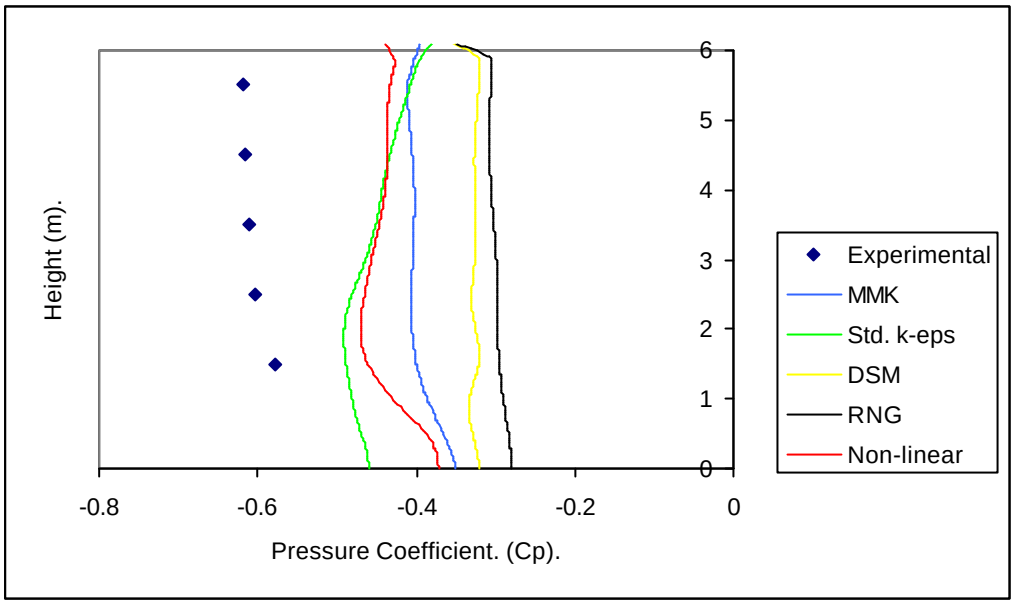

Figure 56: 6m cube, normal orientation, side face pressure distribution.

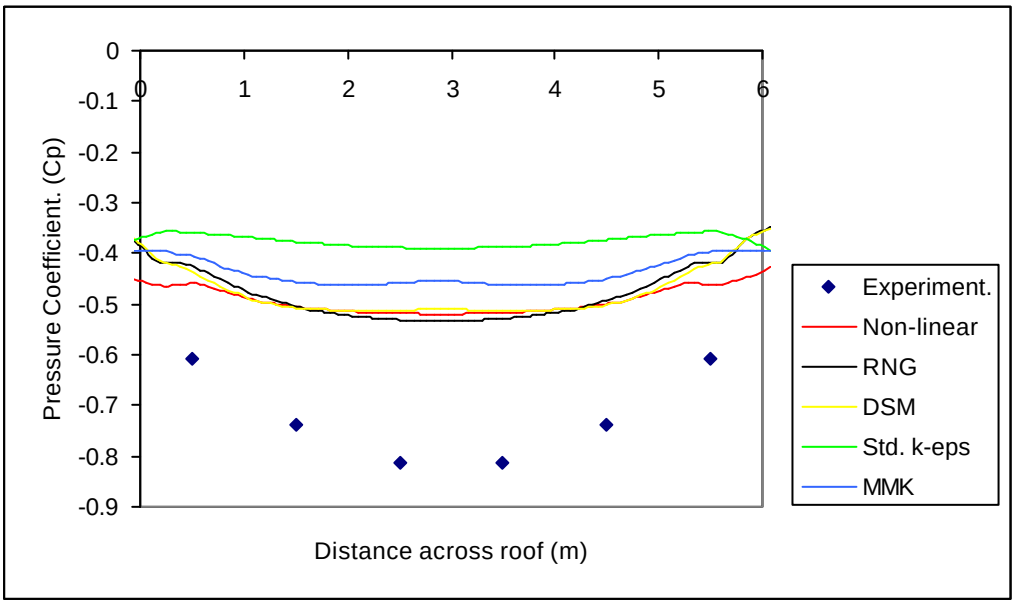

Figure 57: 6m cube, normal orientation, lateral roof pressure distribution.

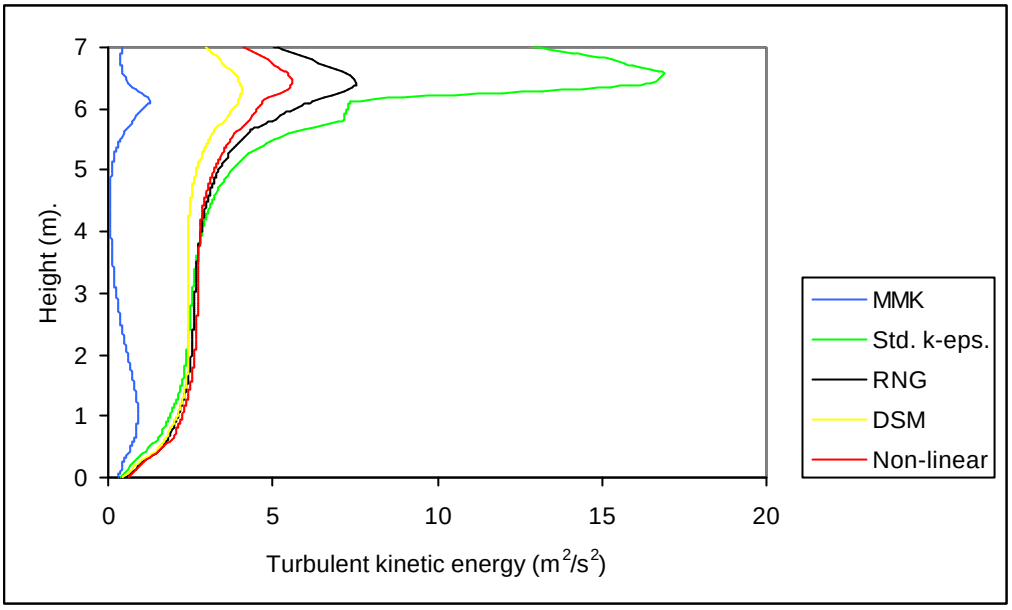

Figure 58: 6m cube, normal orientation, windward face turbulent kinetic energy distribution.

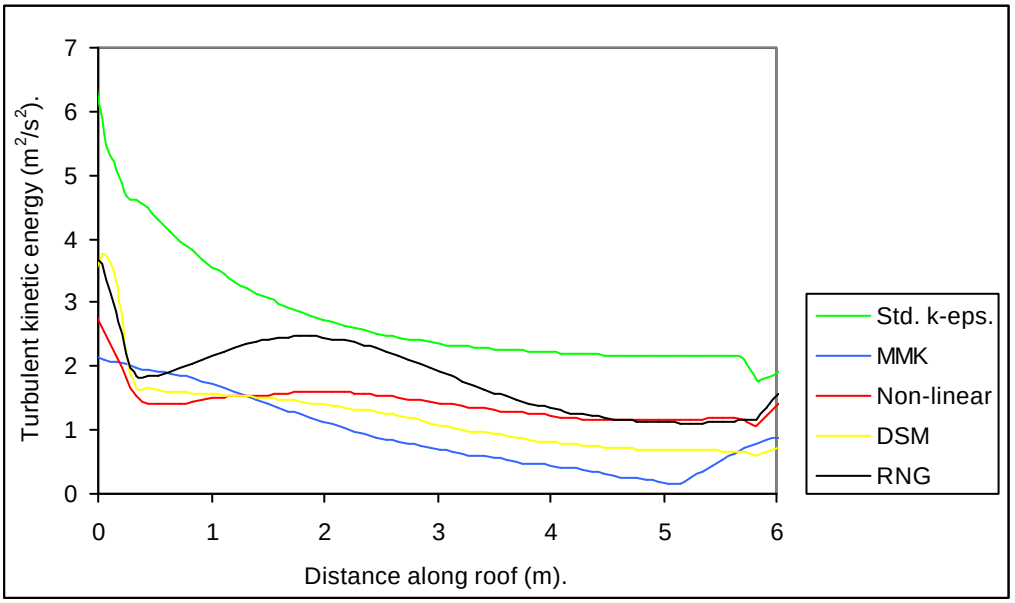

Figure 59: 6m cube, normal orientation, roof turbulent kinetic energy distribution

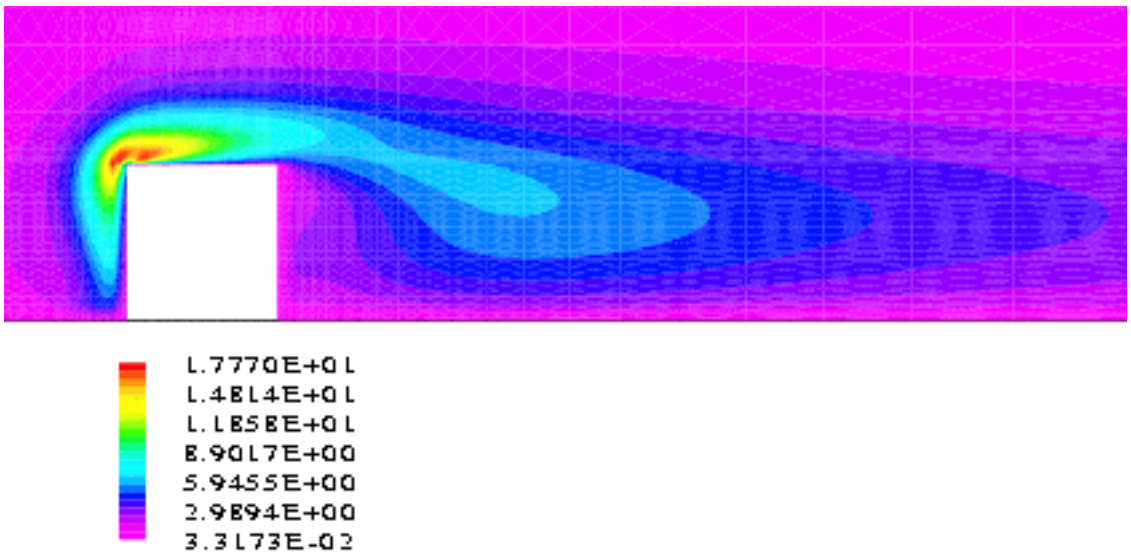

Figure 60: 6m cube, normal orientation, centreline turbulent kinetic energy contours for the standard *k-e* model.

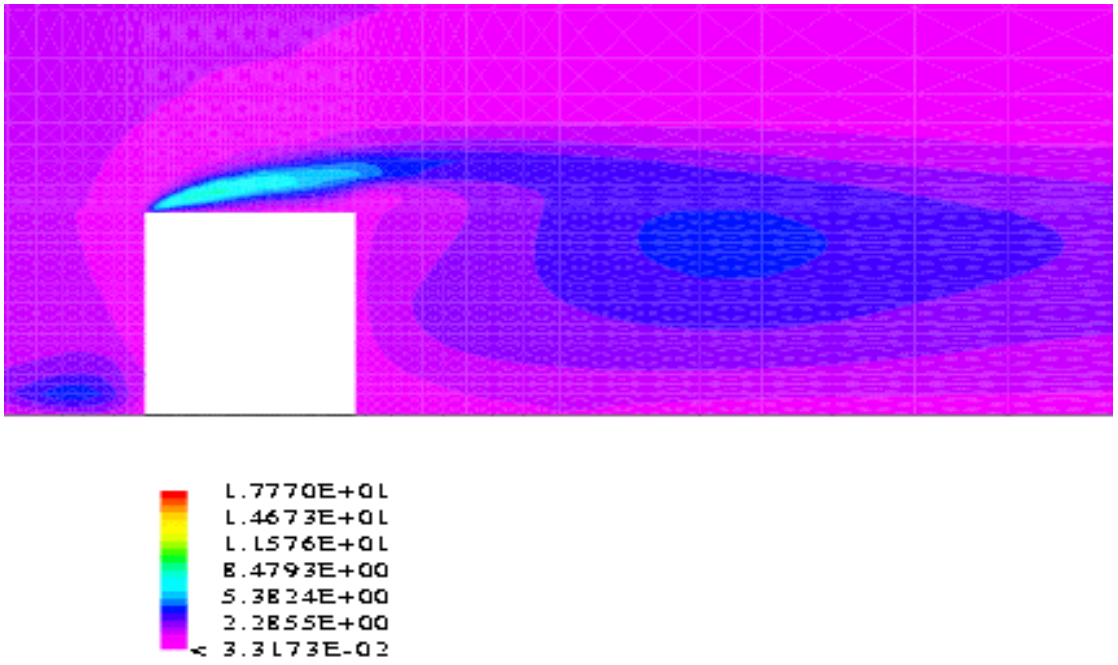

Figure 61: 6m cube, normal orientation, centreline turbulent kinetic energy contours for the MMK *k-e* model.

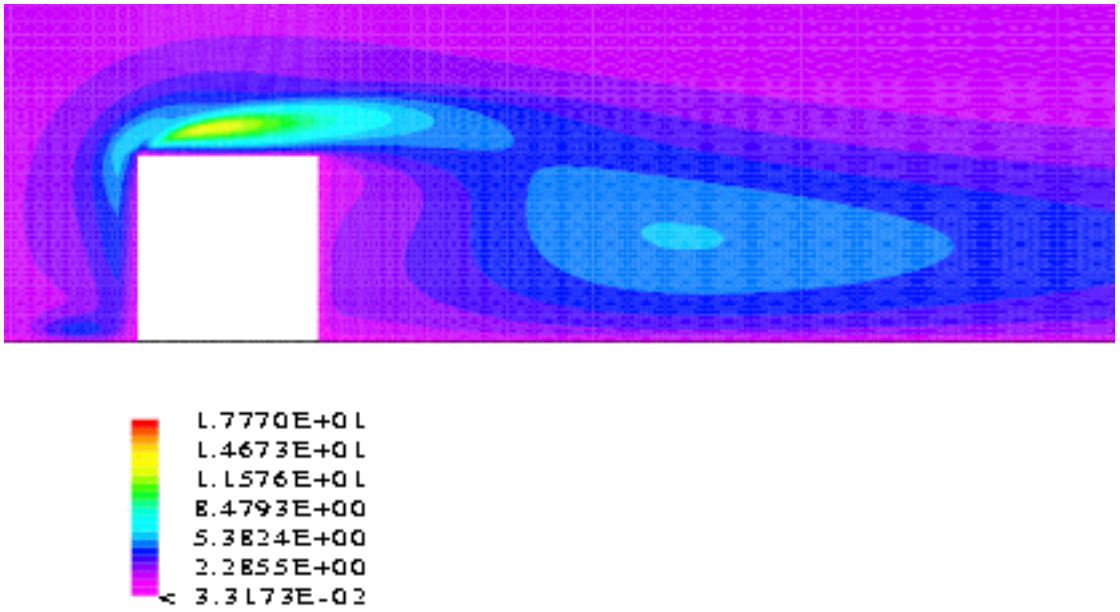

Figure 62: 6m cube, normal orientation, centreline turbulent kinetic energy contours for the RNG *k-e* model.

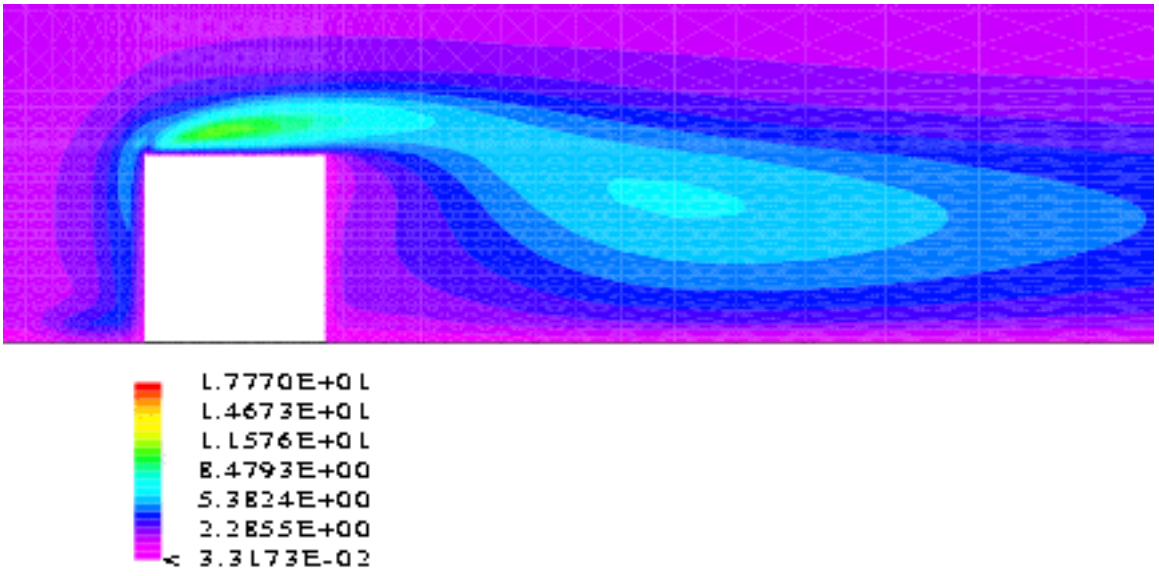

Figure 63: 6m cube, normal orientation, centreline turbulent kinetic energy contours for the non-linear *k-e* model.

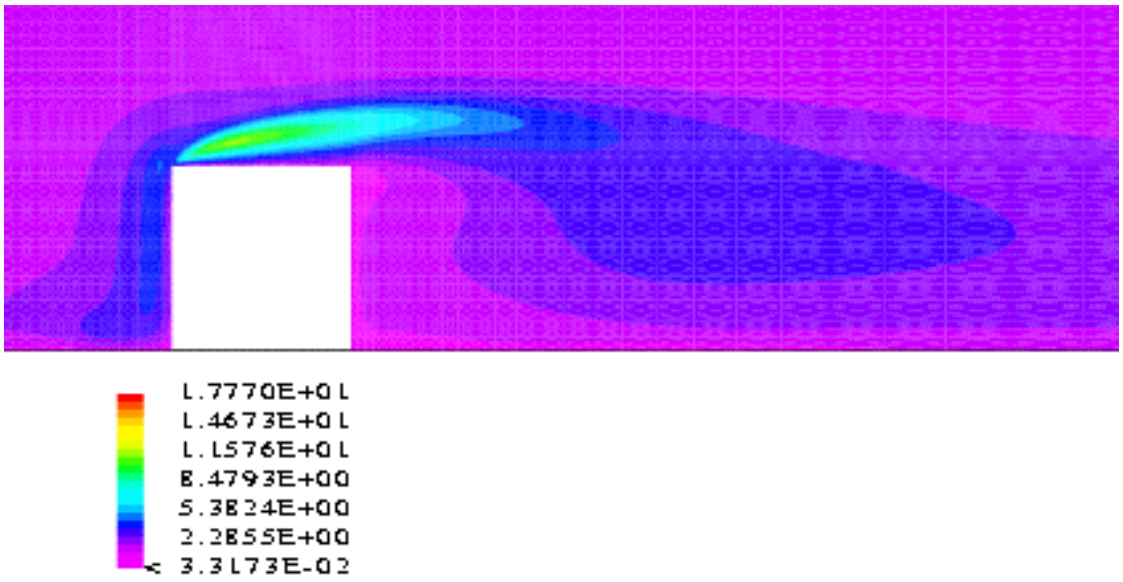

Figure 64: 6m cube, normal orientation, centreline turbulent kinetic energy contours for the differential stress model.

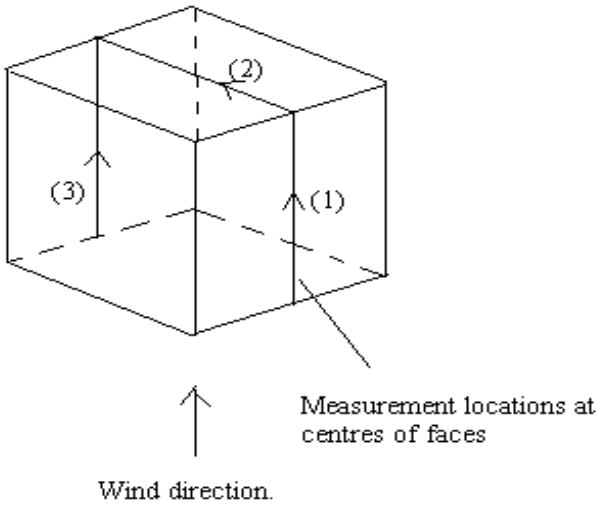

Figure 65: Skewed cube measurement locations

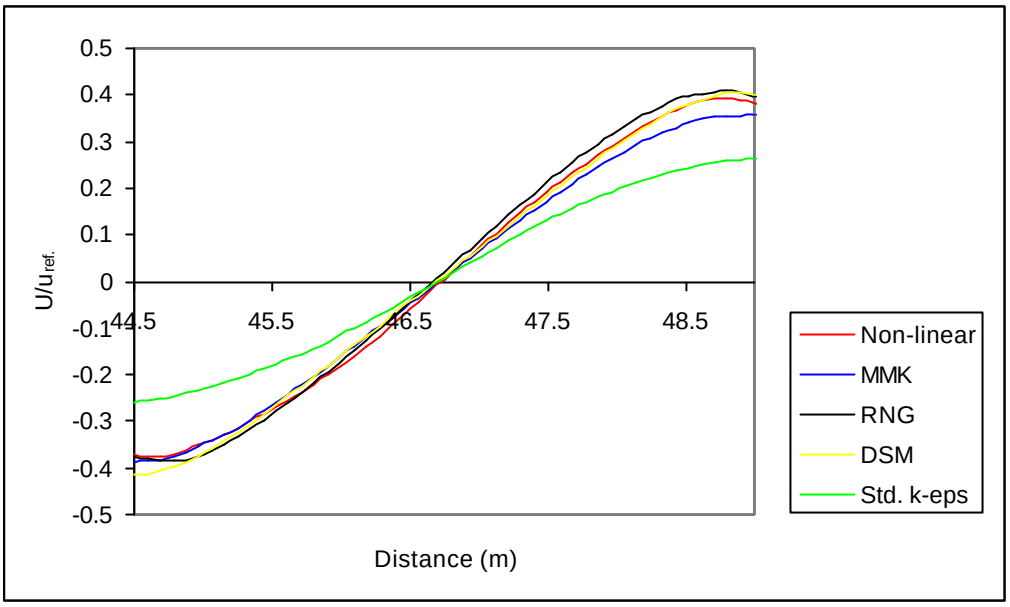

Figure 66: 6m cube, skewed orientation, comparison of roof lateral velocity component measured across the centre of the cube (y coordinate plane).

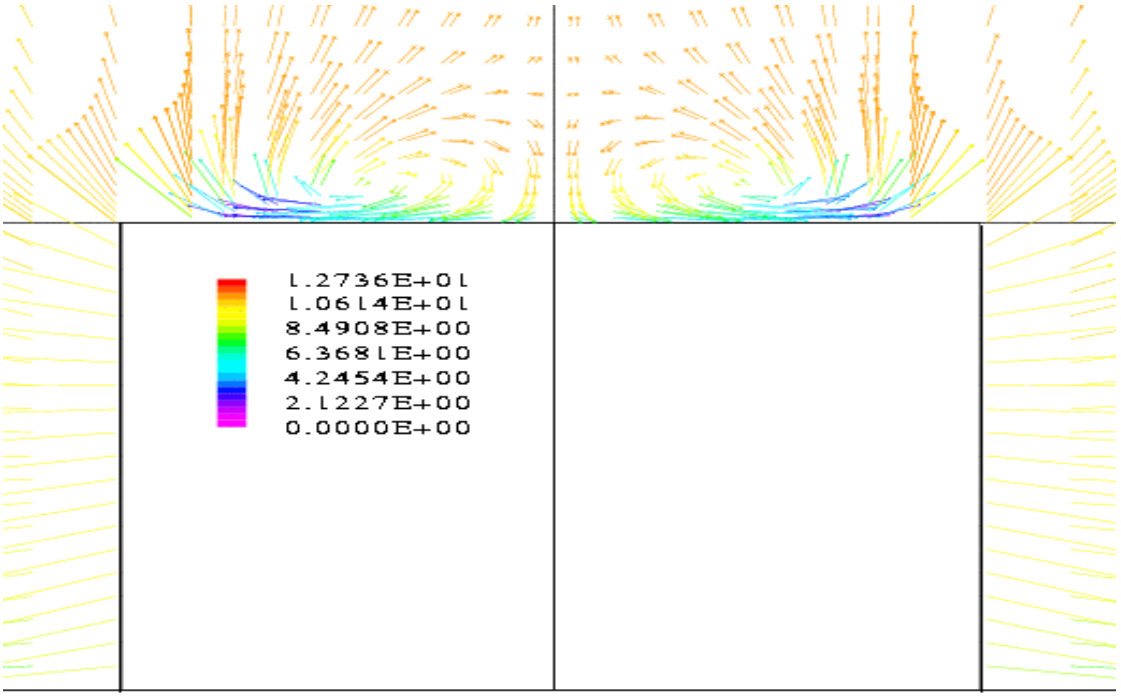

Figure 67: Skewed cube velocity vectors showing the delta wing vortices at the centre of the cube, using the non-linear *k-e* model

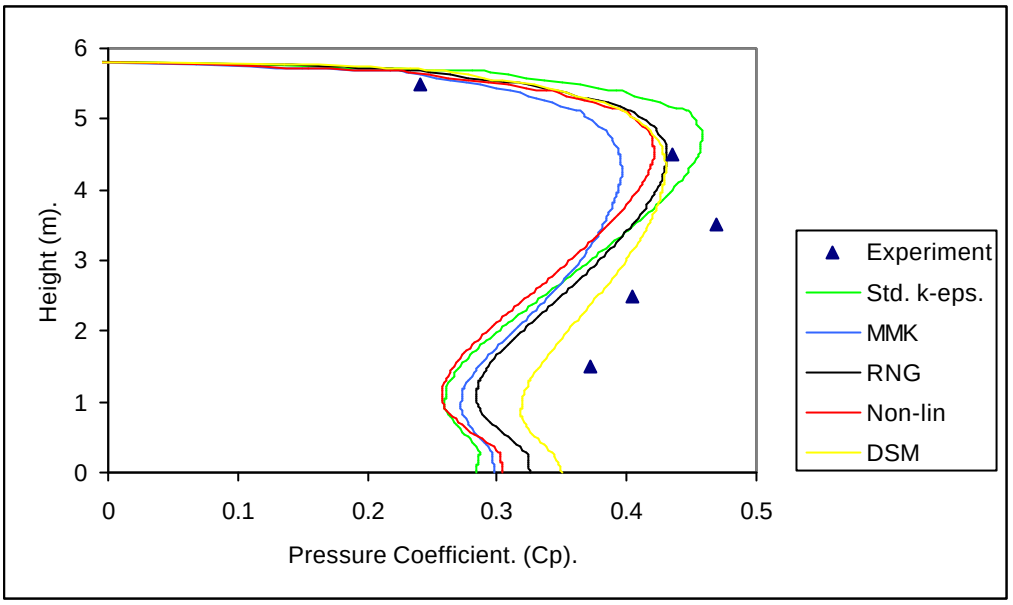

Figure 68: 6m cube, skewed orientation, comparison of windward face pressure coefficients (measurement line 1).

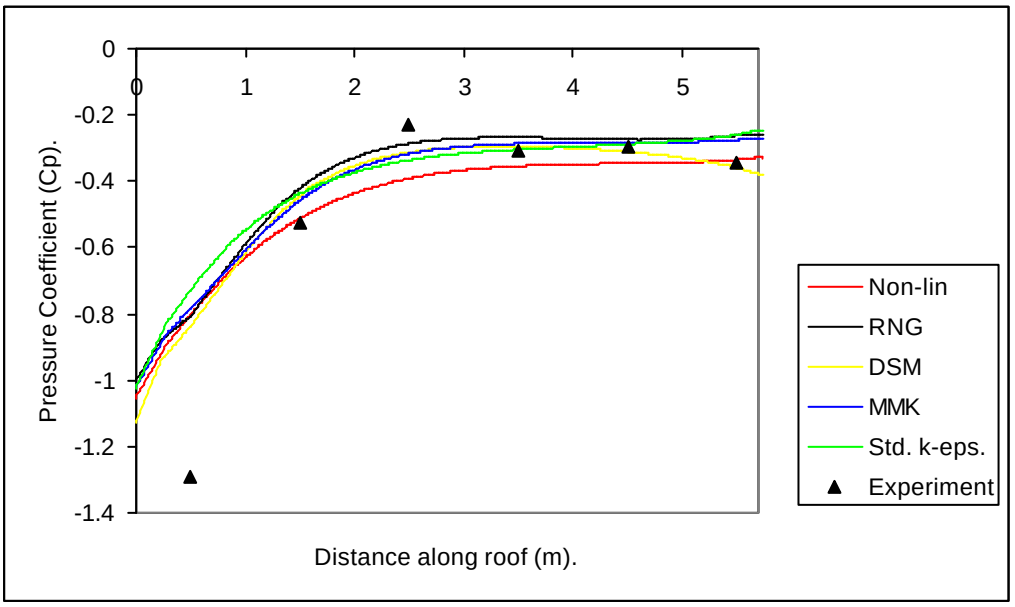

Figure 69: 6m cube, skewed orientation, comparison of roof pressure coefficients (measurement line 2).

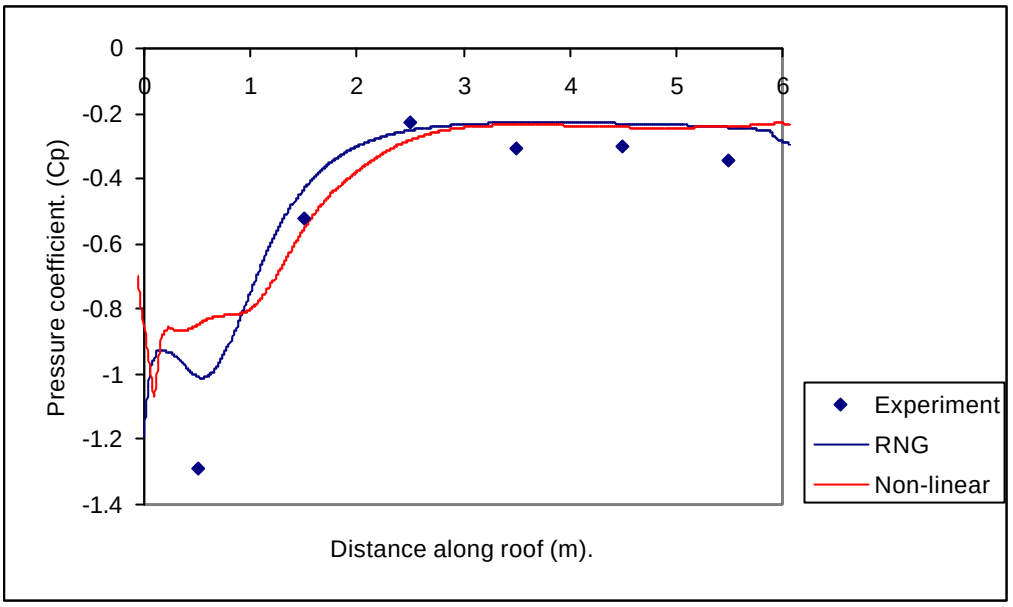

Figure 70: 6m cube, skewed orientation, comparison of roof pressure coefficients, grid refined results.

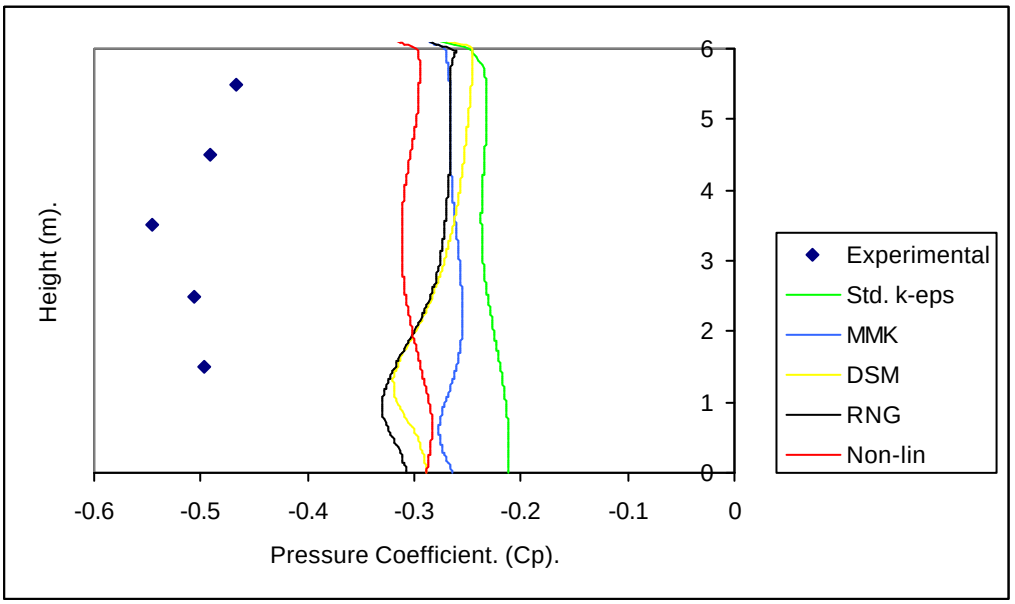

Figure 71: 6m cube, skewed orientation, comparison of leeward face pressure coefficients (measurement line 3).

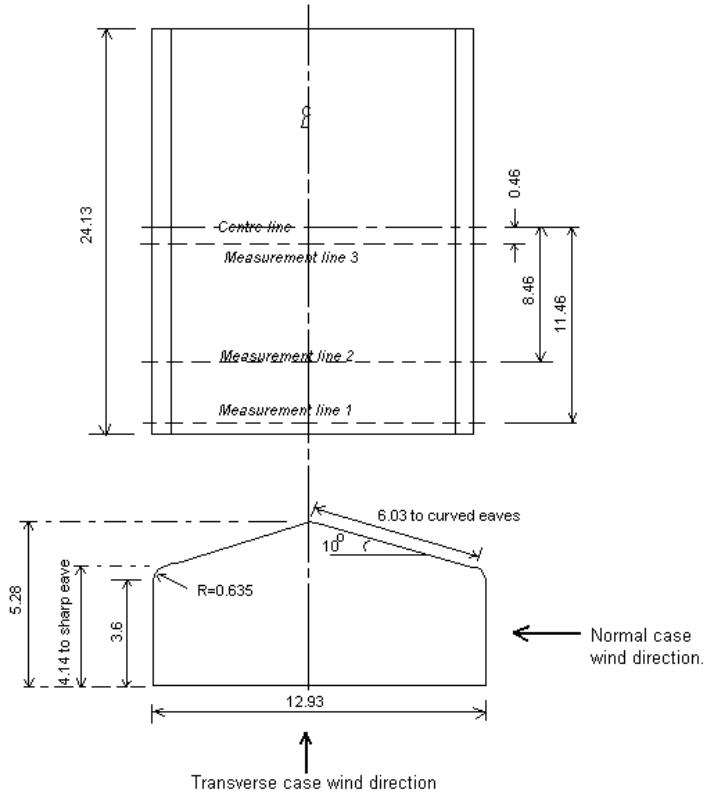

Figure 72: Schematic of the SSB / measurement line locations (all dimensions in m)

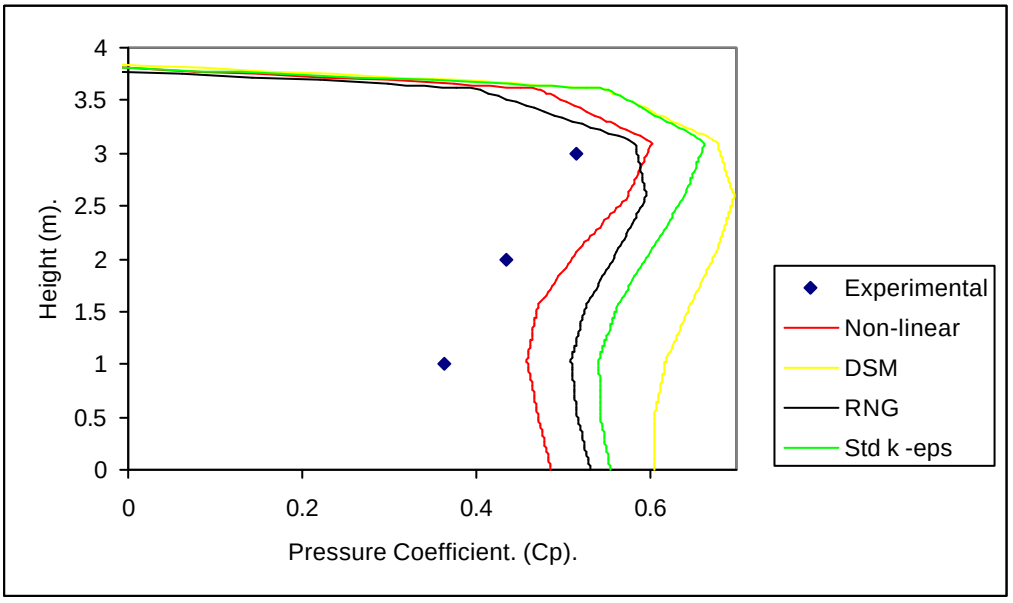

Figure 73: SSB, sharp eaves, normal orientation, windward face pressure (measurement line 3).

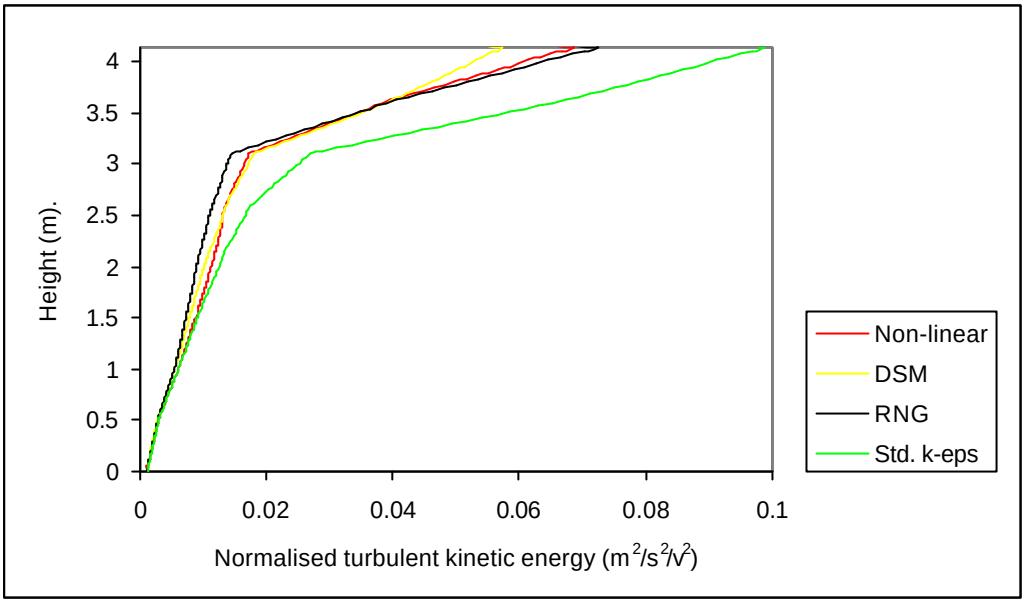

Figure 74: SSB, sharp eaves, normal orientation, windward face turbulent kinetic energy (measurement line 3).

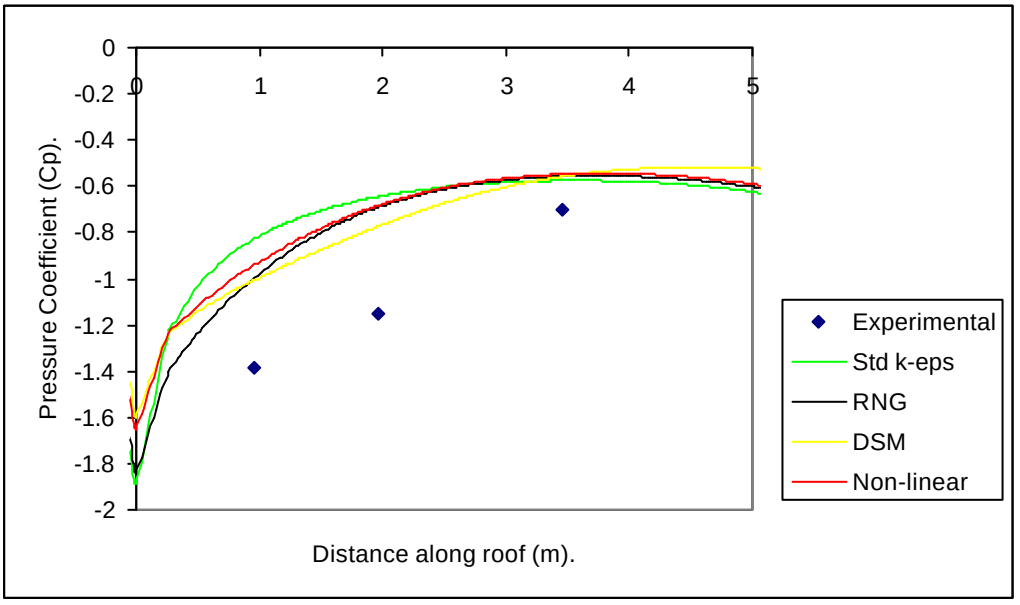

Figure 75: SSB, sharp eaves, normal orientation, windward roof pressure (measurement line 3).

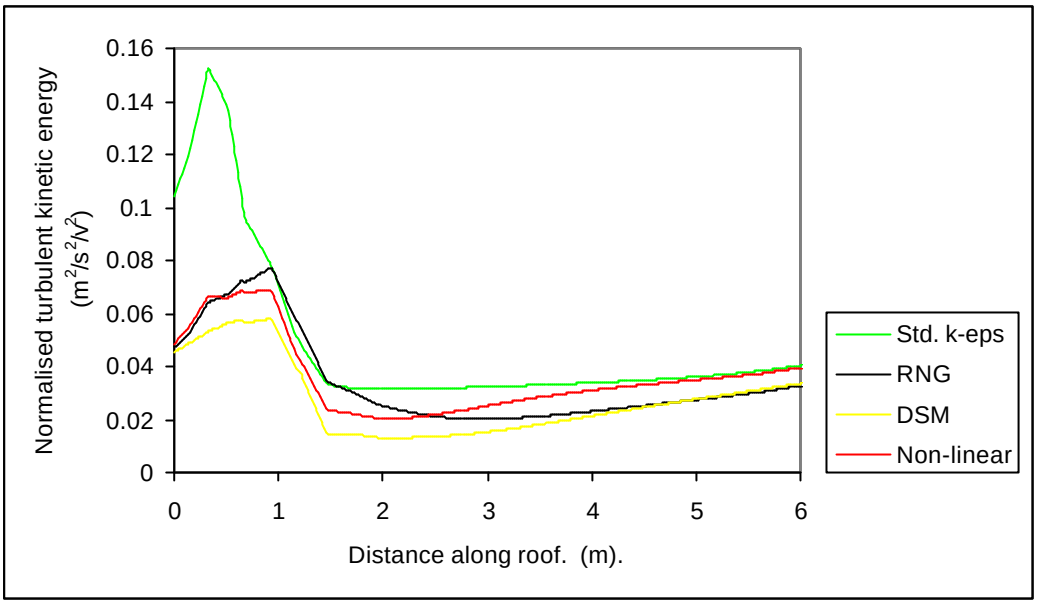

Figure 76: SSB, sharp eaves, normal orientation, windward roof turbulent kinetic energy (measurement line 3).

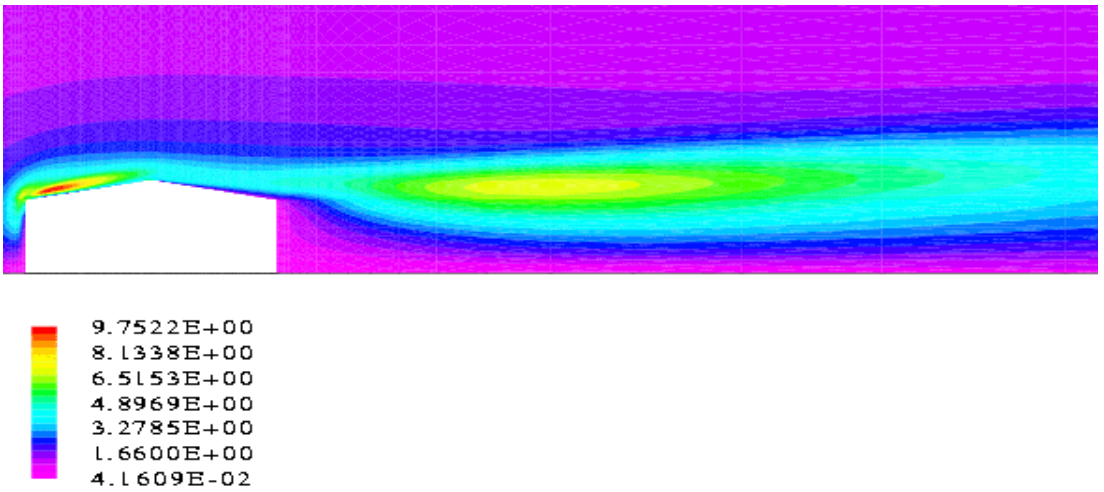

Figure 77: SSB, shape eaves, normal orientation, centreline turbulent kinetic energy contour plot for the non-linear *k-e* model.

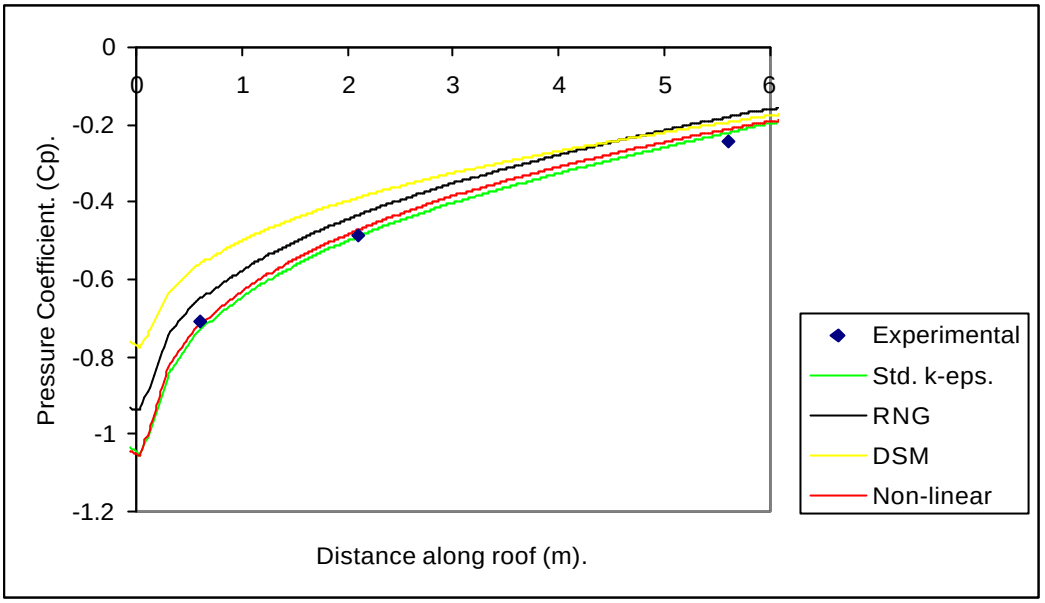

Figure 78: SSB, sharp eaves, normal orientation, leeward roof pressure distribution (measurement line 3).

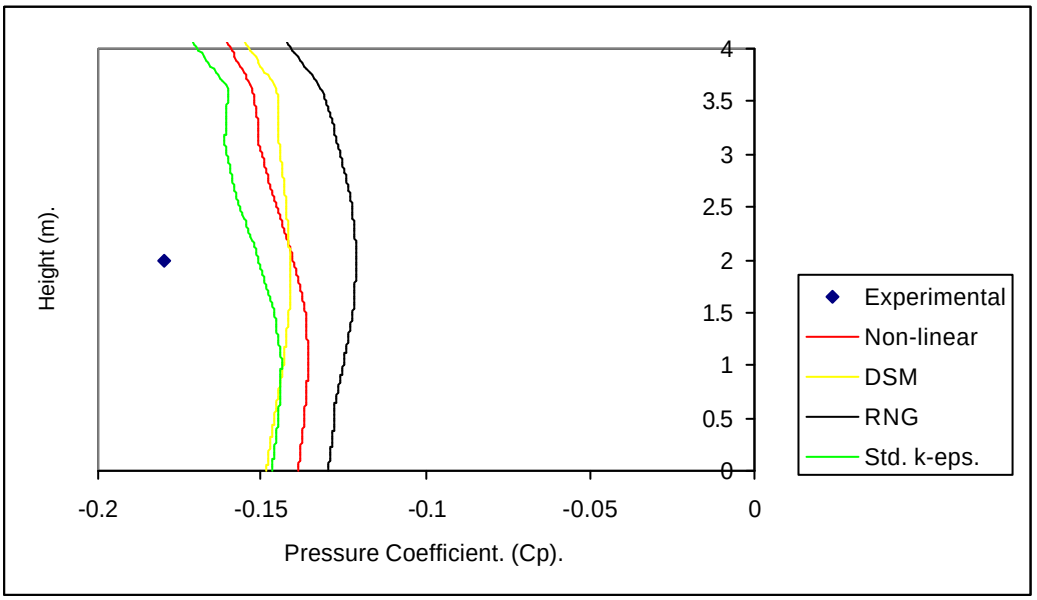

Figure 79: SSB, sharp eaves, normal orientation, leeward face pressure distribution (measurement line 3).

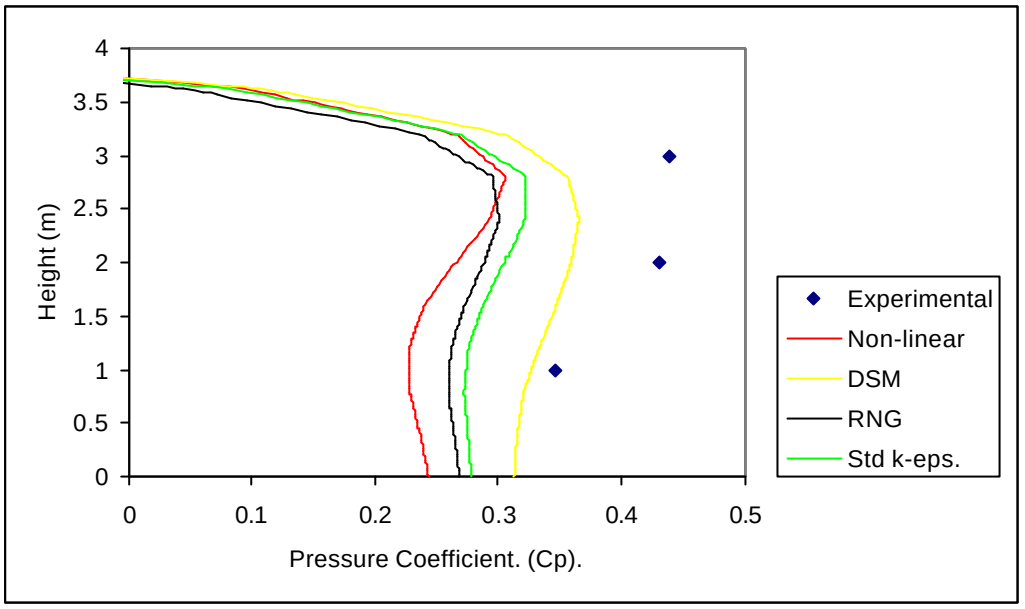

Figure 80: SSB, curved eaves, normal orientation, windward face pressure distribution (measurement line 3).

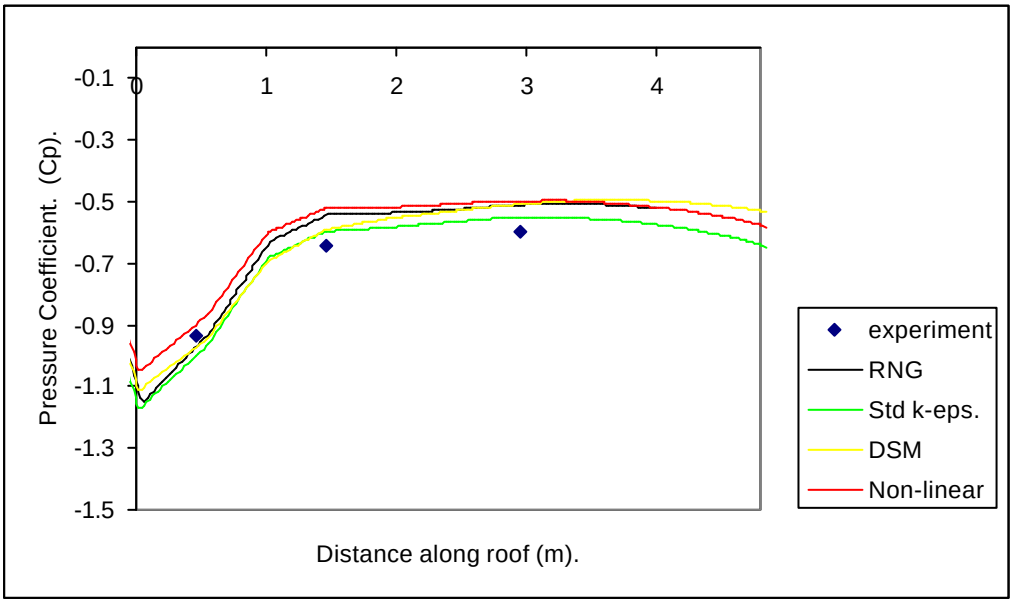

Figure 81: SSB, curved eaves, normal orientation, windward roof pressure distribution (measurement line 3).

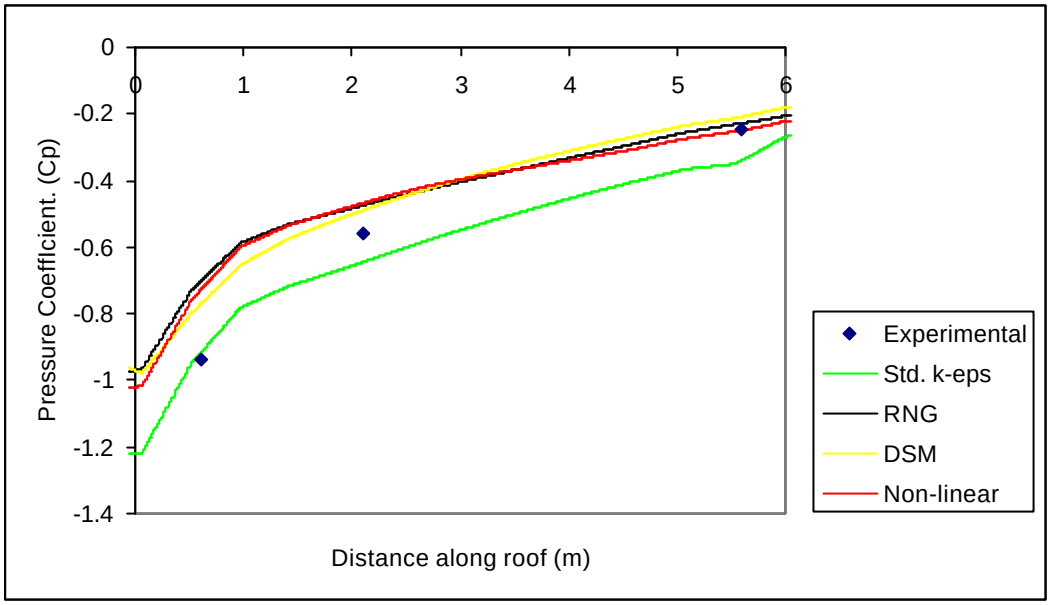

Figure 82: SSB, curved eaves, normal orientation, leeward roof pressure distribution (measurement line 3).

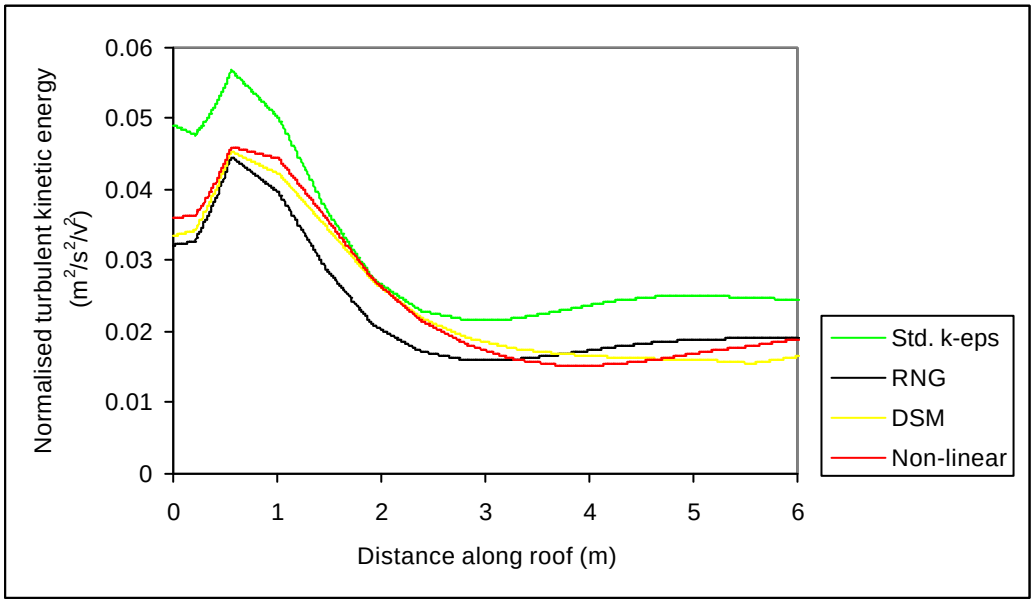

Figure 83: SSB, curved eaves, normal orientation, leeward roof turbulent kinetic energy distribution (measurement line 3).

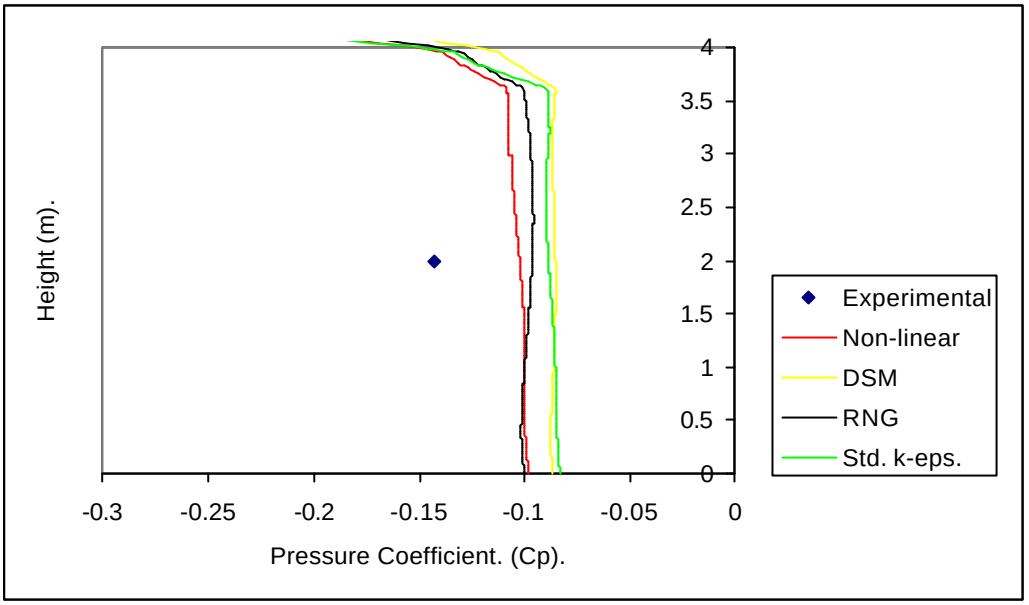

Figure 84: SSB, curved eaves, normal orientation, leeward face pressure distribution (measurement line 3).

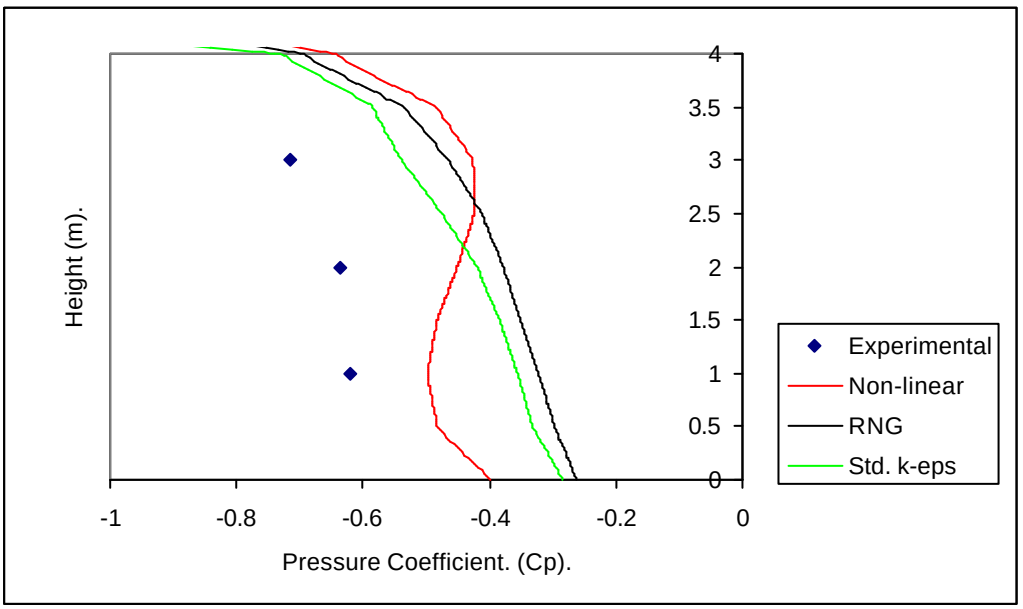

Figure 85: SSB, curved eaves, transverse orientation, side face pressure distribution (measurement line 1).

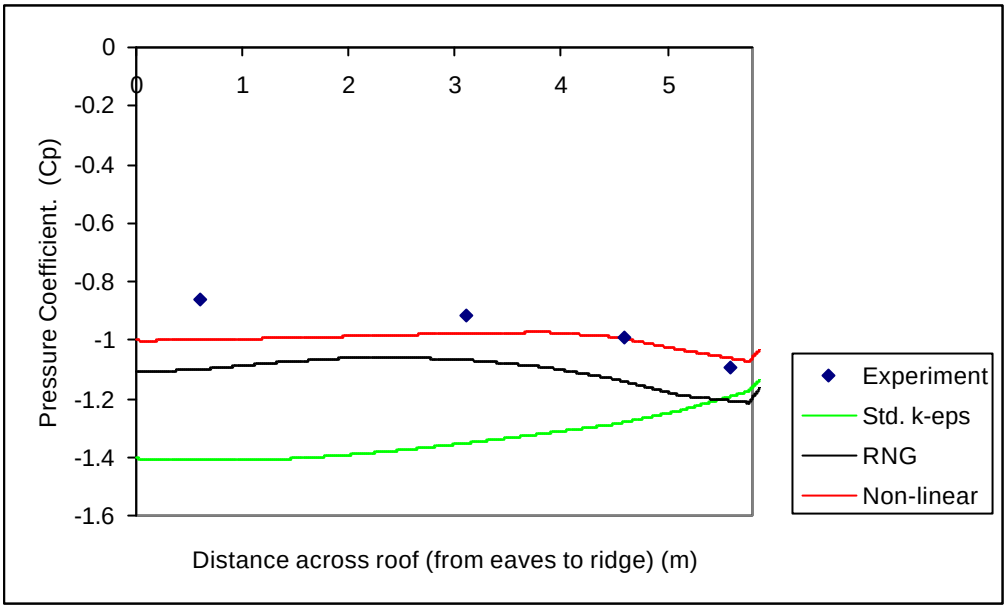

Figure 86: SSB, curved eaves, transverse orientation, roof pressure distribution (measurement line 1).

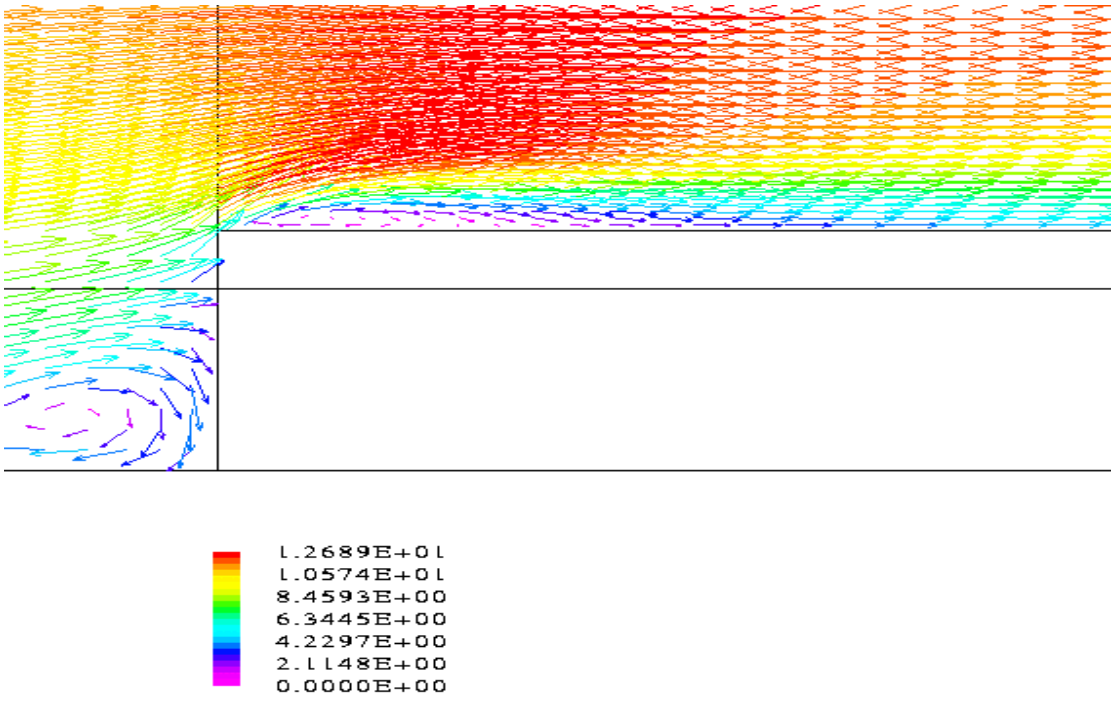

Figure 87: SSB, curved eaves, transverse orientation, centreline velocity vector plot for the non-linear *k-e* model.

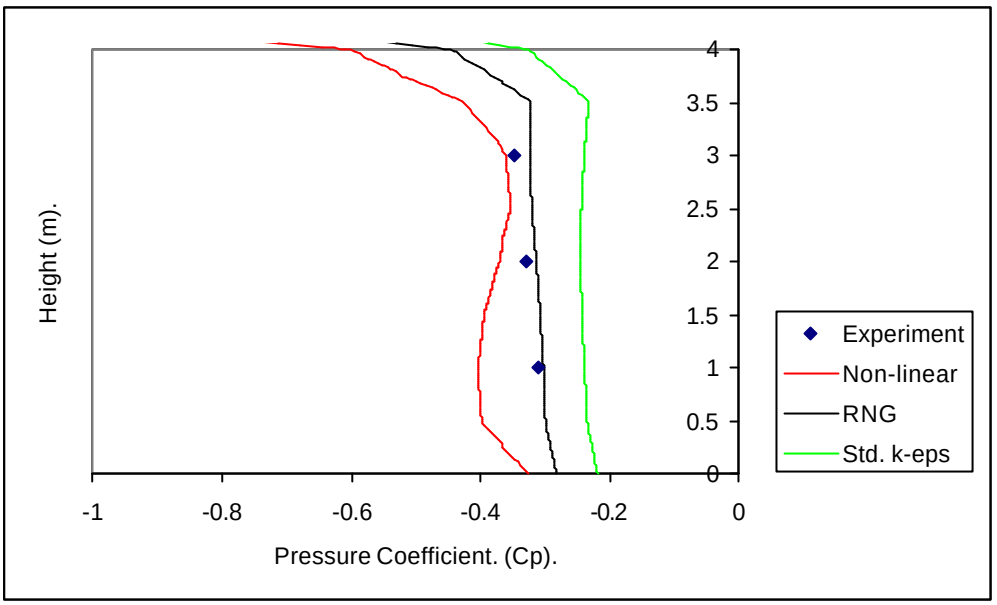

Figure 88: SSB, curved eaves, transverse orientation, side face pressure distribution (measurement line 2).

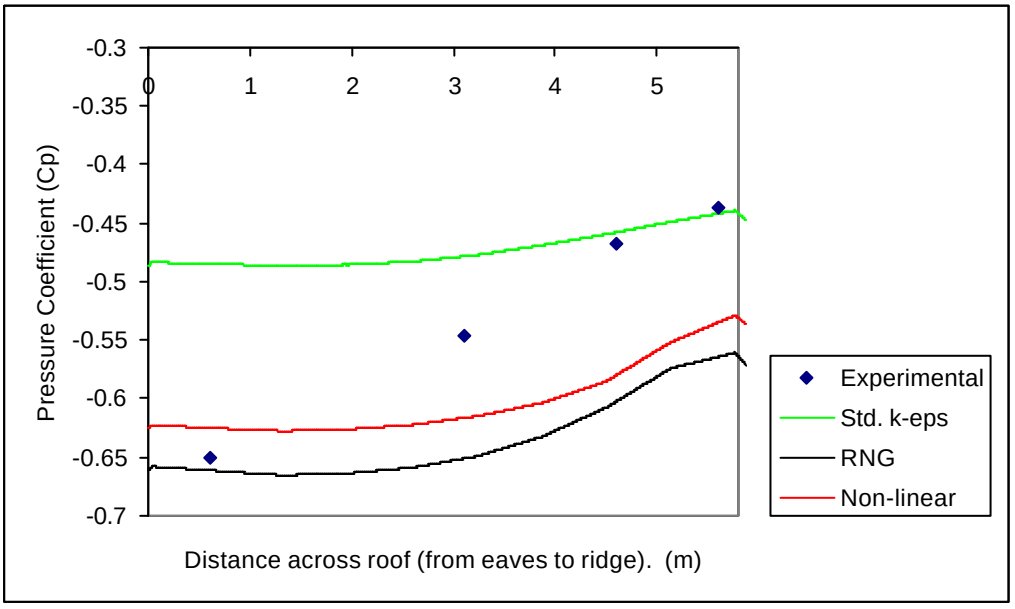

Figure 89: SSB, curved eaves, transverse orientation, roof pressure distribution (measurement line 2).

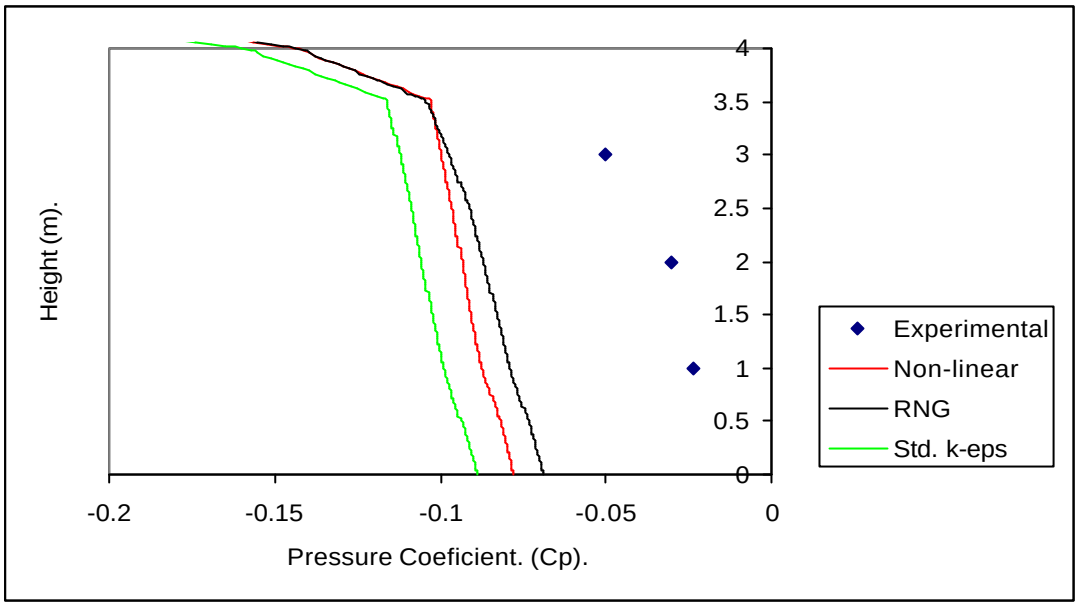

Figure 90: SSB, curved eaves, transverse orientation, side face pressure distribution (measurement line 3).

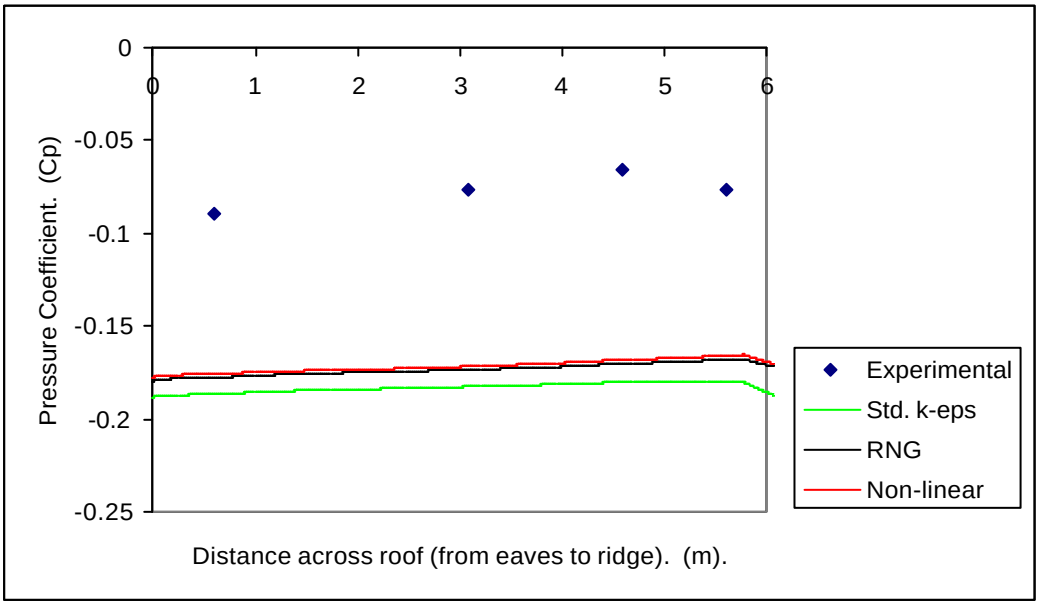

Figure 91: SSB, curved eaves, transverse orientation, roof pressure distribution (measurement line 3).

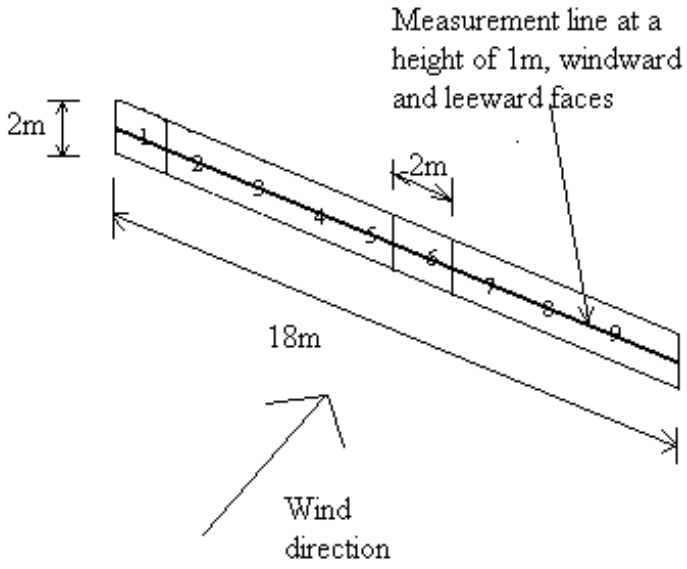

Figure 92: Schematic of the modular panel layout of the experimental wall (0° incident wind)

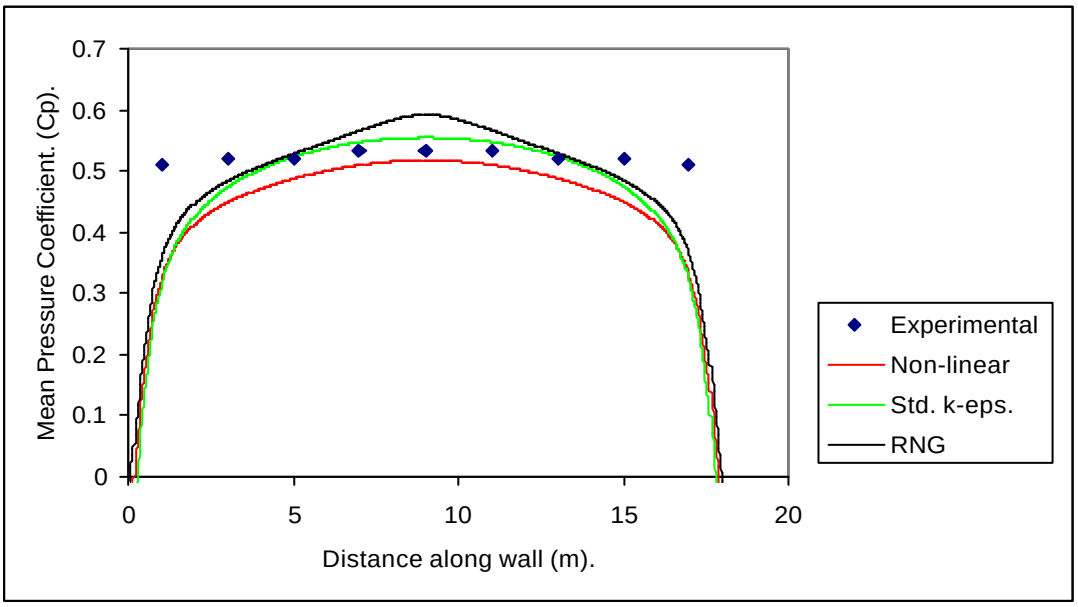

Figure 93: Silsoe experimental wall, windward face pressure distribution (0° case).

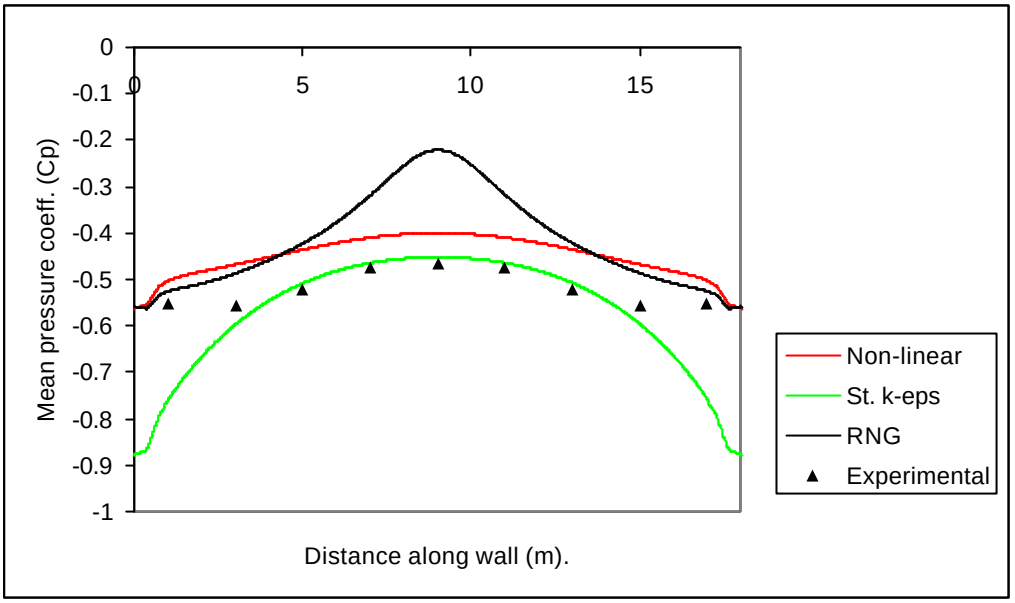

Figure 94: Silsoe experimental wall, leeward face pressure distribution (0° case).

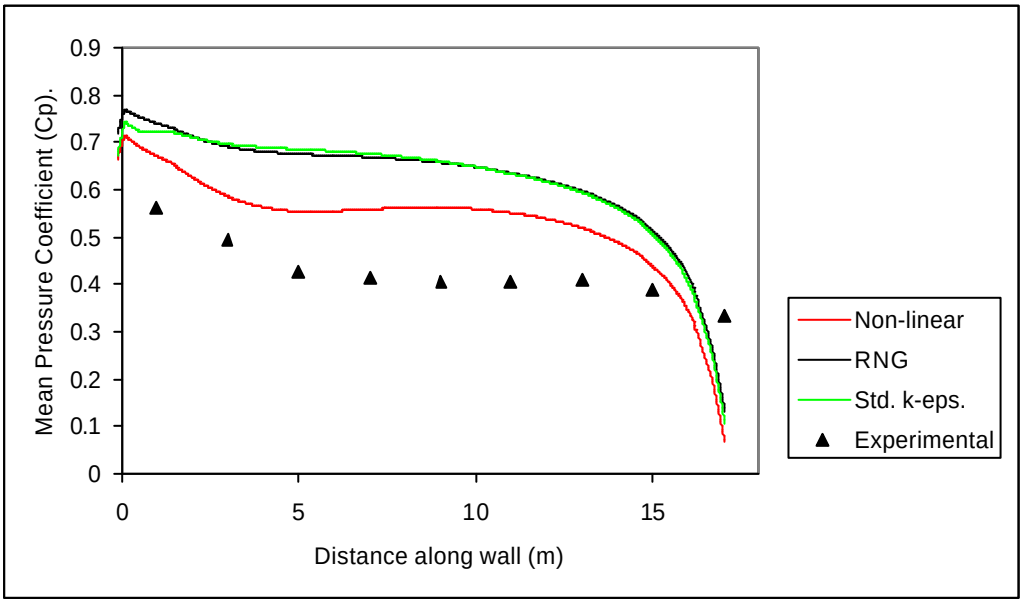

Figure 95: Silsoe experimental wall, windward face pressure distributions (30° case).

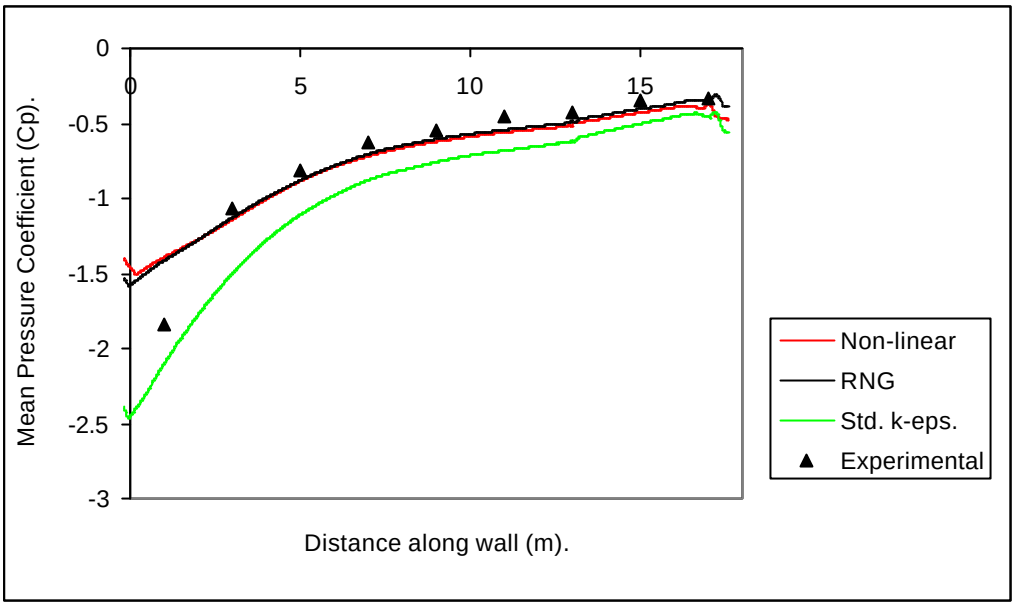

Figure 96: Silsoe experimental wall, leeward face pressure distributions (30° case).

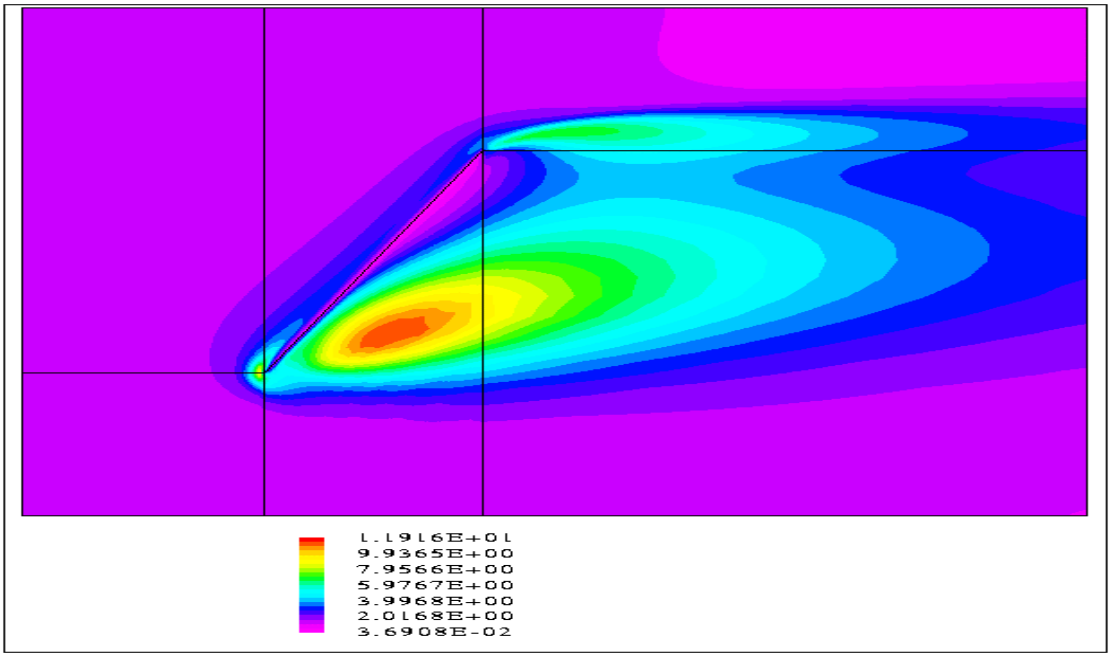

Figure 97: Turbulent kinetic energy contours for the experimental wall, the standard *k-e* model (30° case). (Note: wall may appear to be at an incorrect angle due to page sizing requirements).

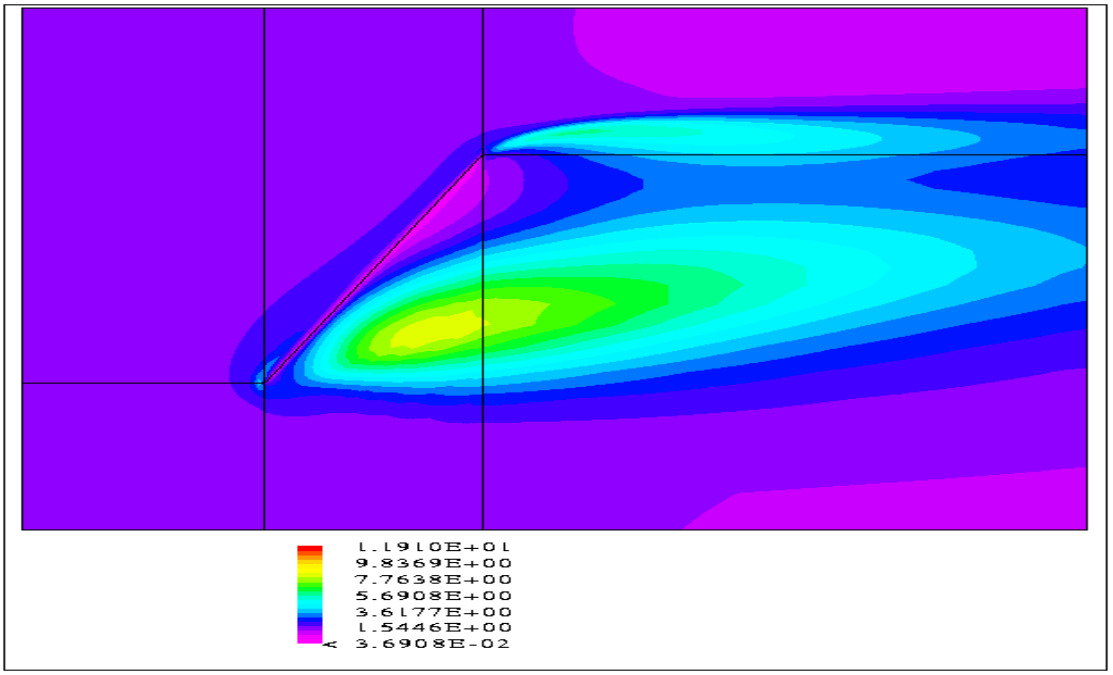

Figure 98: Turbulent kinetic energy contours for the experimental wall, the non-linear *k-e* model (30° case). (Note: wall may appear to be at an incorrect angle due to page sizing requirements).

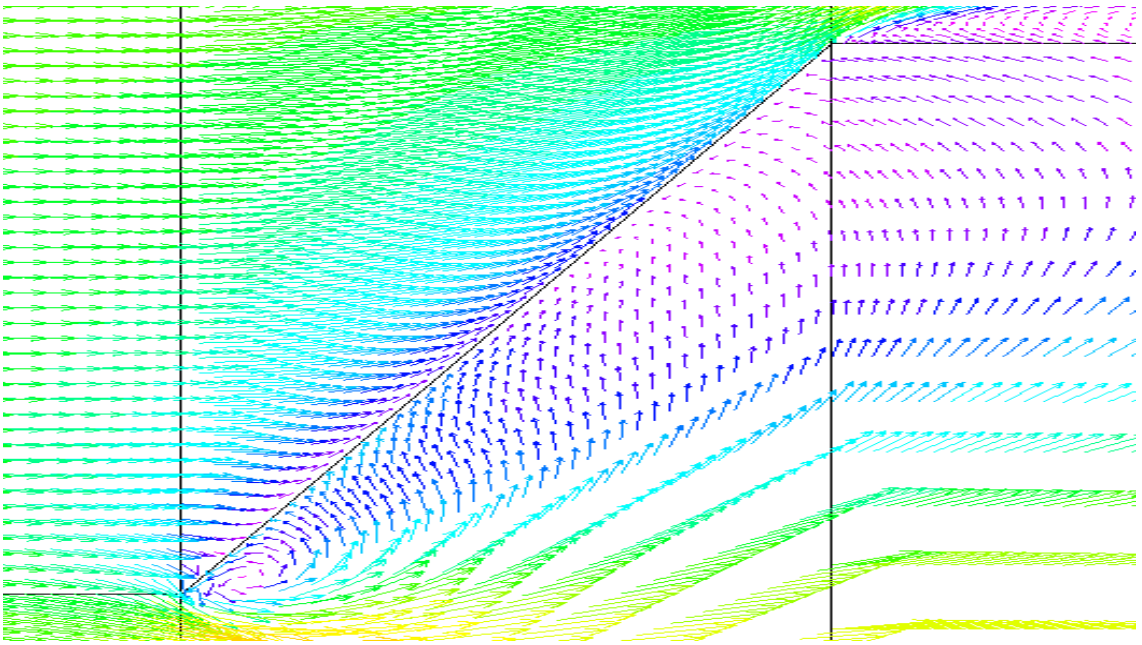

Figure 99: Velocity vectors for the experimental wall using the standard *k-e* model (30° case). (Note: wall may appear to be at an incorrect angle due to page sizing requirements).

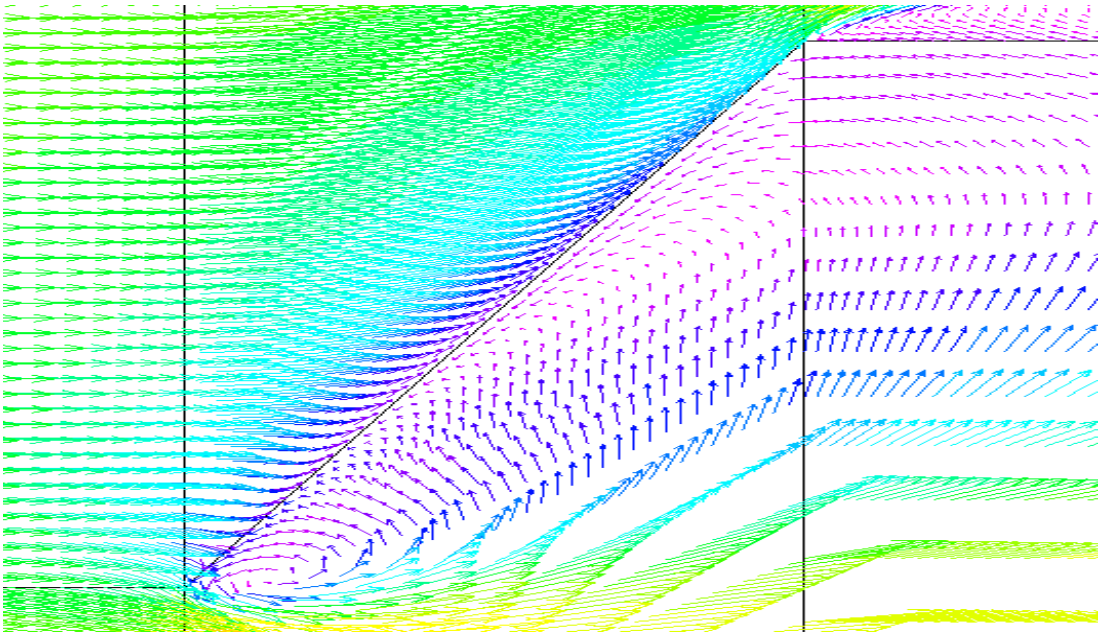

Figure 100: Velocity vectors for the experimental wall using the non-linear *k-e* model (30° case). (Note: wall may appear to be at an incorrect angle due to page sizing requirements).

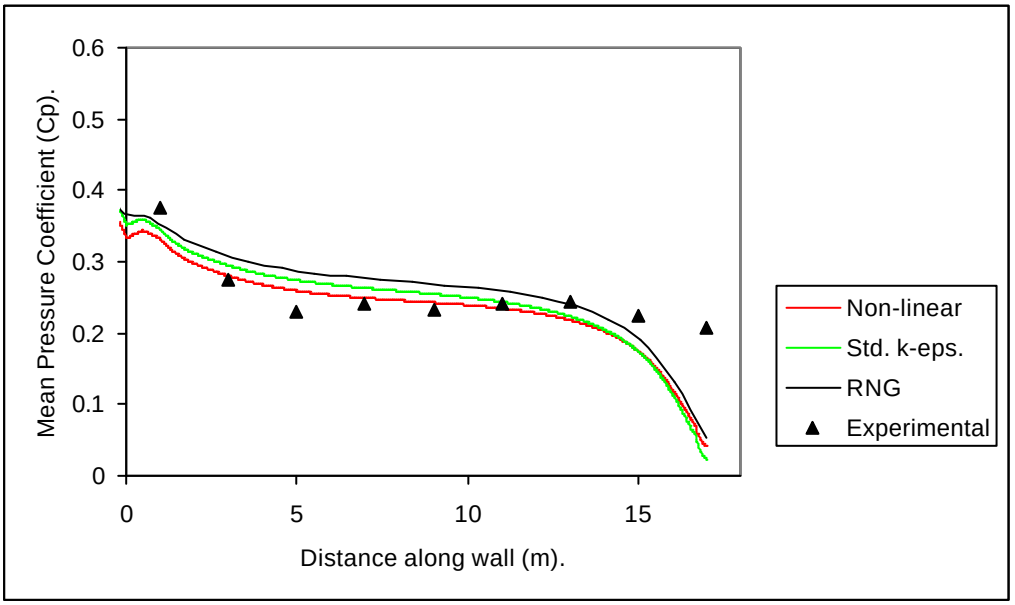

Figure 101: Silsoe experimental wall, windward face pressure distributions (60° case).

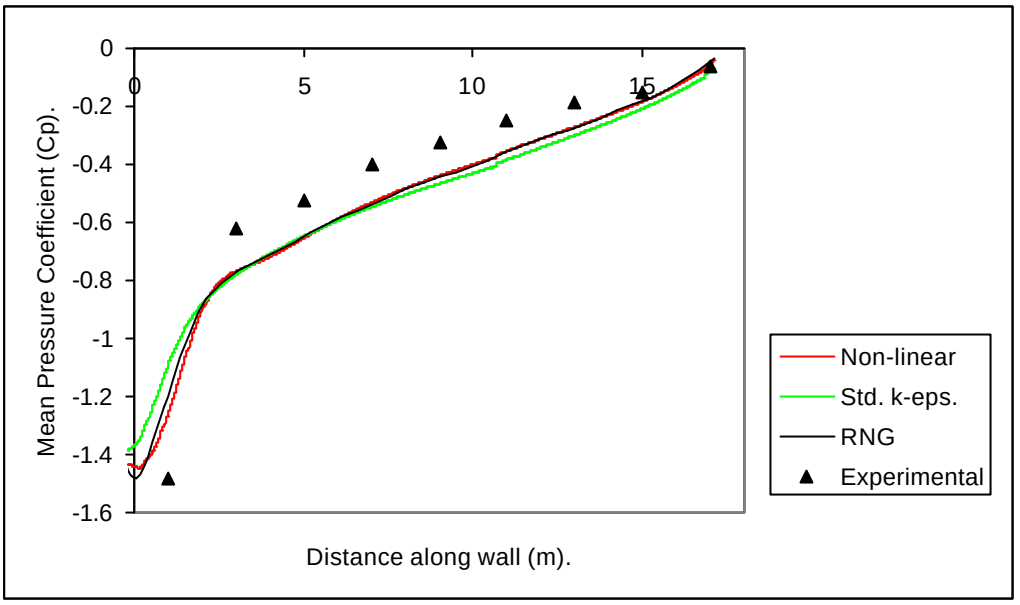

Figure 102: Silsoe experimental wall, leeward face pressure distributions (60° case).

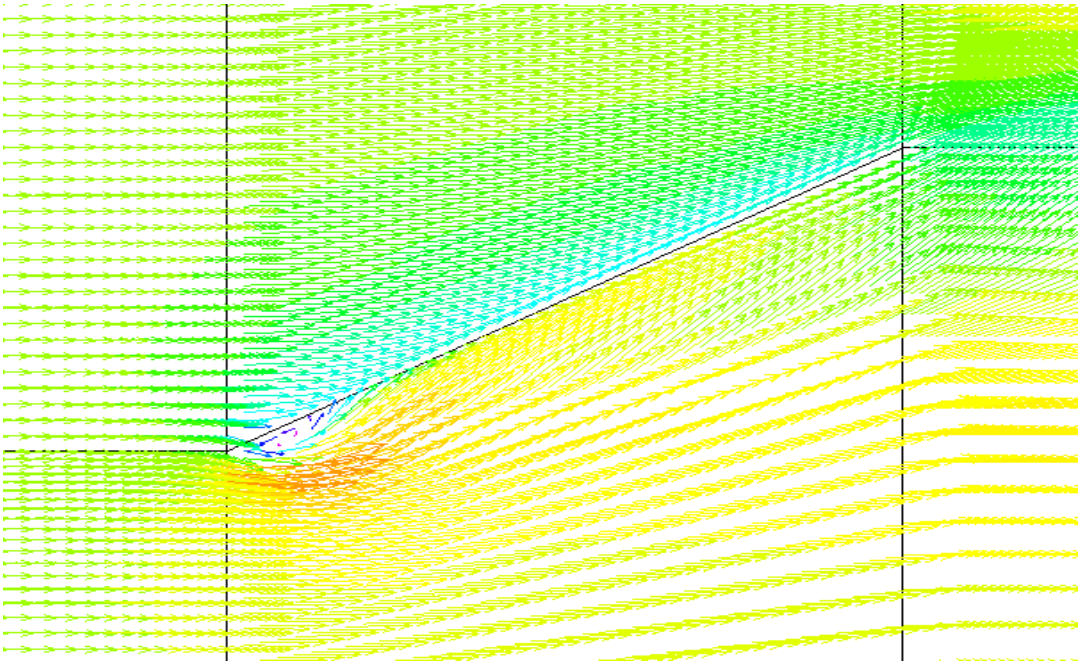

Figure 103: Velocity vectors for the experimental wall using the non-linear *k-e* model (60° case). (Note: wall may appear to be at an incorrect angle due to page sizing requirements).

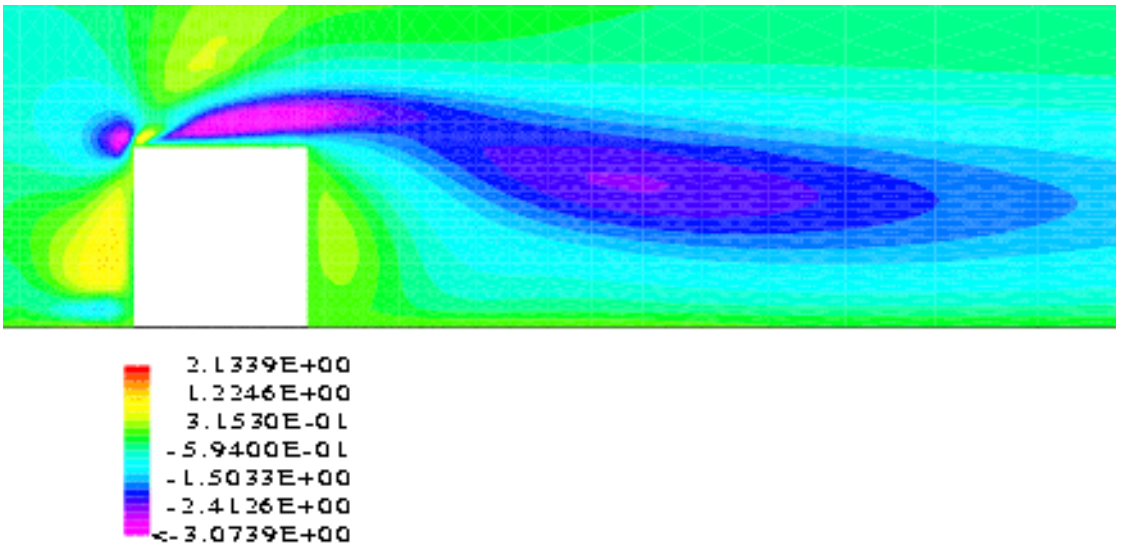

Figure 104: 6m cube, centreline *u'w'* shear stress contour plot for the non-linear *k-e* model.

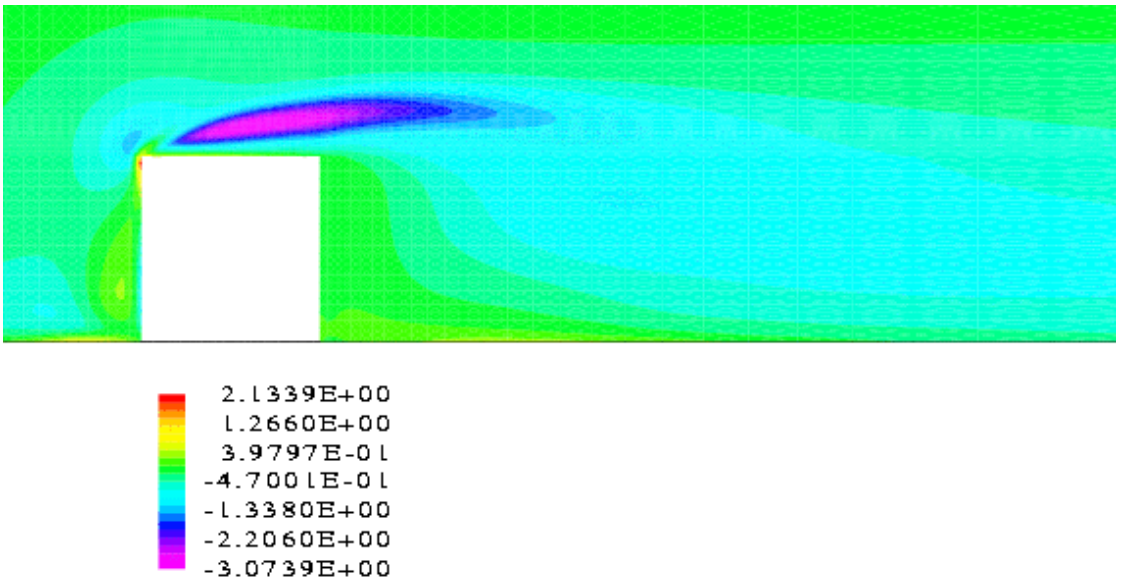

Figure 105: 6m cube, centreline *u'w'* shear stress contour plot for the differential stress model..

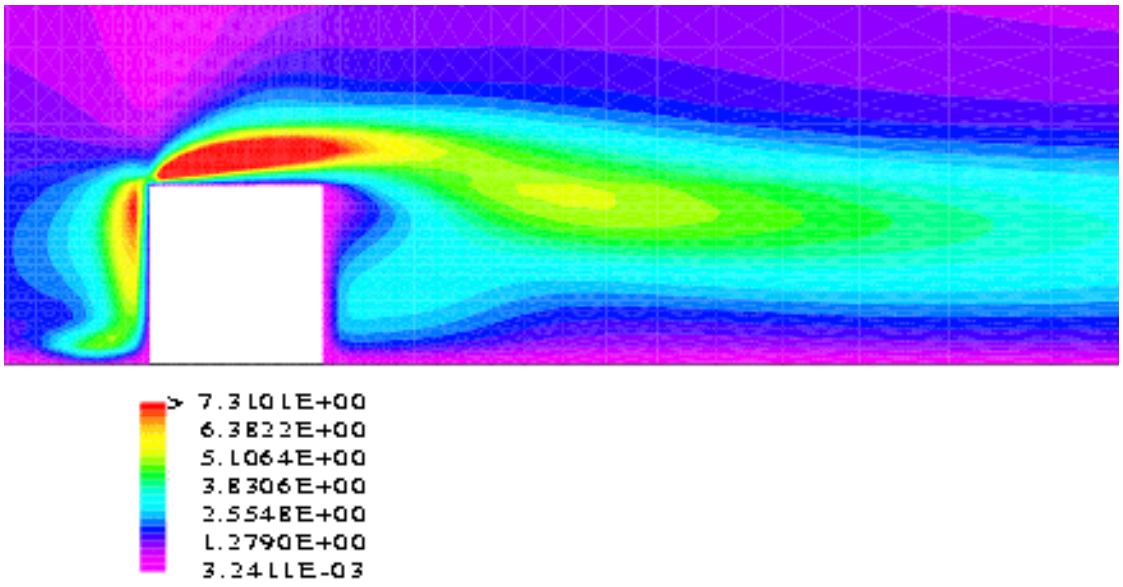

Figure 106: 6m cube, centreline *u'u'* stream-wise normal stress plot for the non-linear *k-e* model.

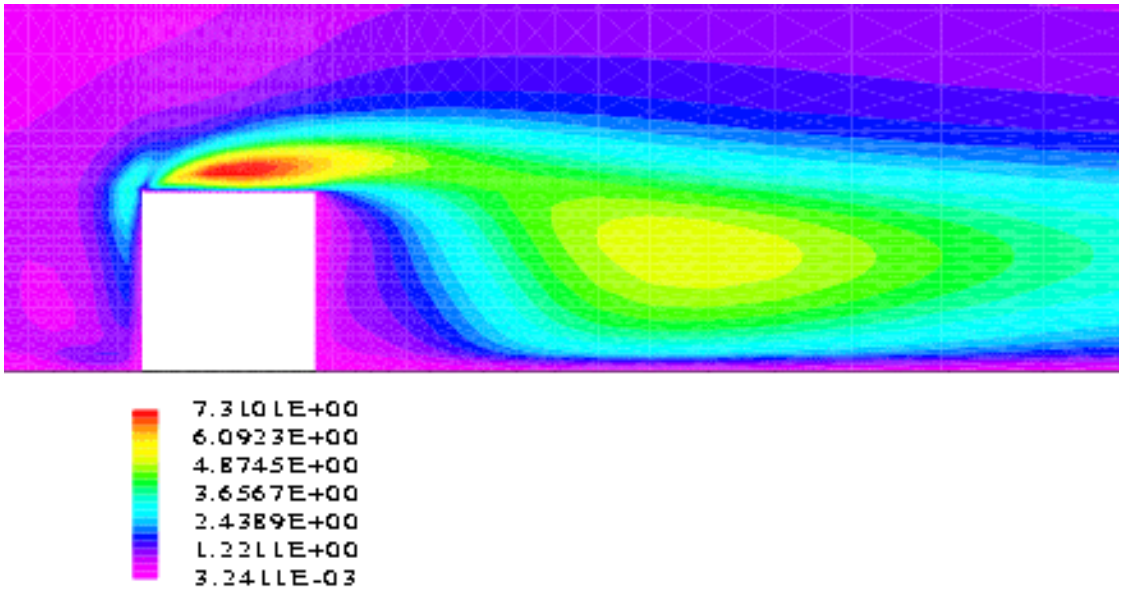

Figure 107: 6m cube, centreline *v'v'* lateral normal stress plot for the non-linear *k-e* model.

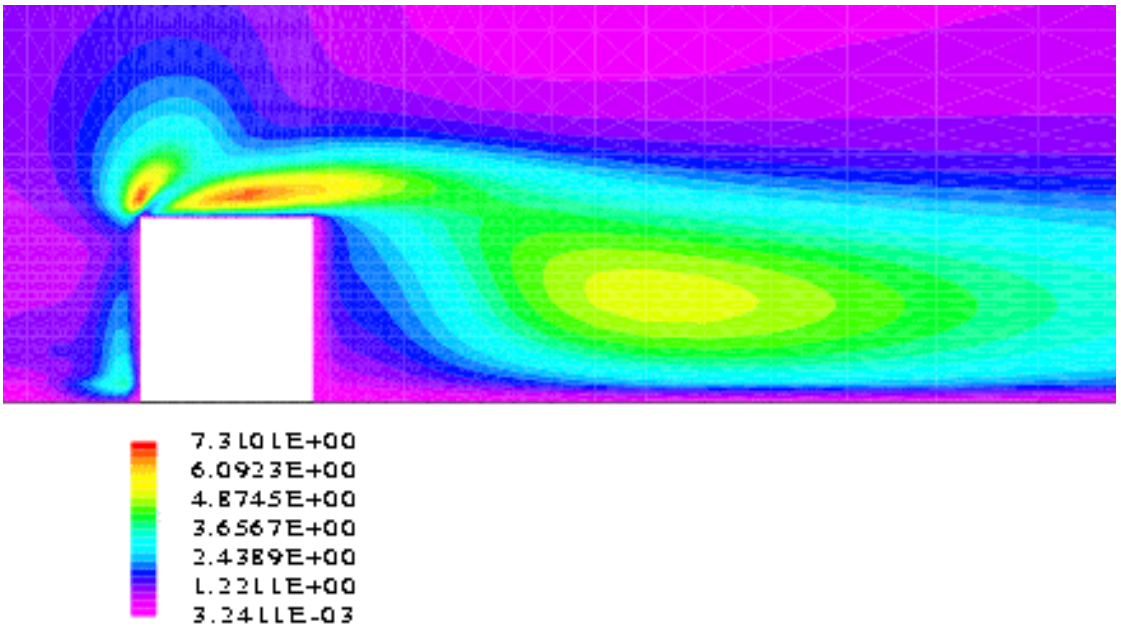

Figure 108: 6m cube, centreline *w'w'* vertical normal stress plot for the non-linear *k-e* model.

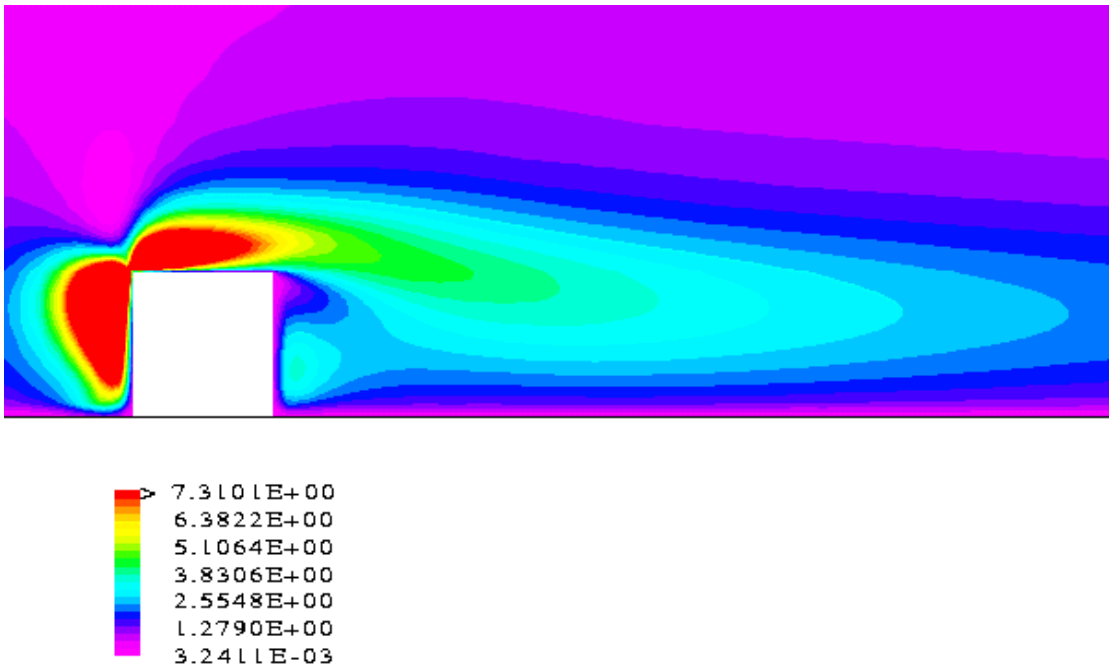

Figure 109: 6m cube, centreline *u'u'* stream-wise normal stress plot for the linear (standard) *k-e* model.

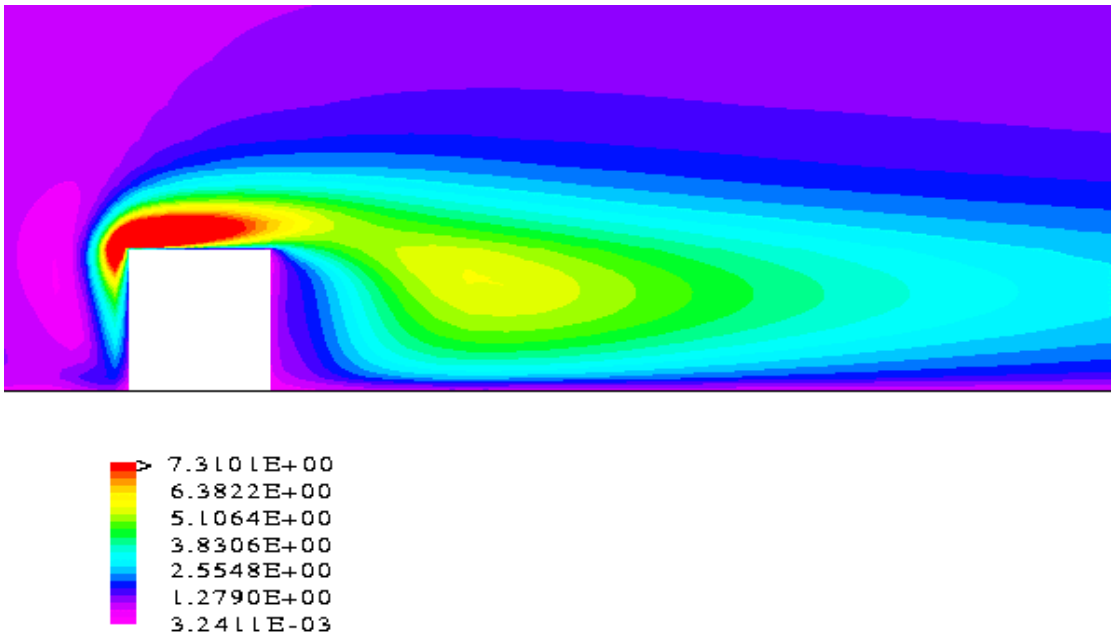

Figure 110: 6m cube, centreline *v'v'* stream-wise normal stress plot for the linear (standard) *k-e* model.

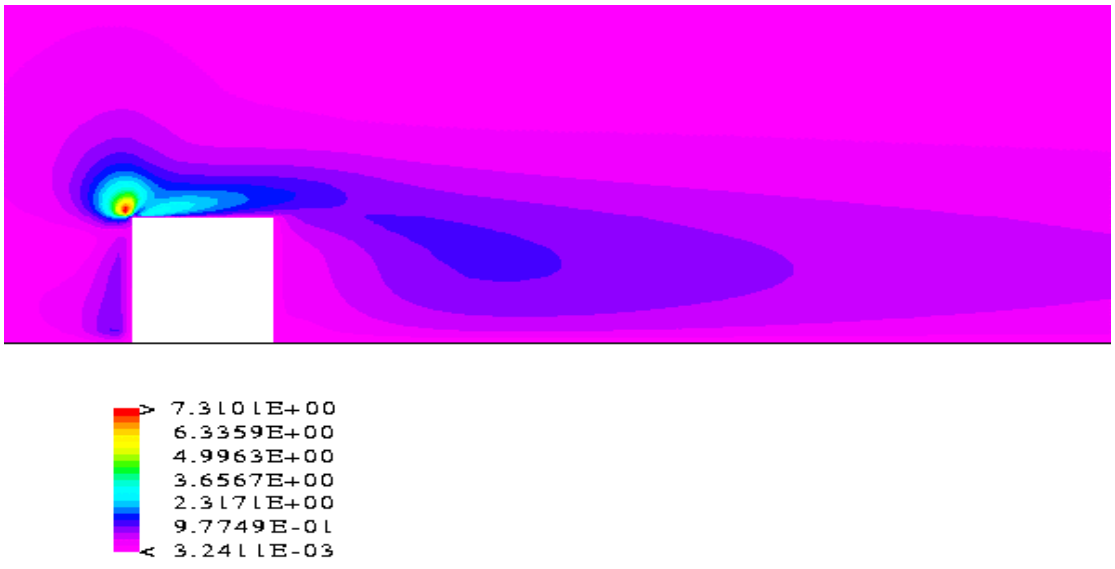

Figure 111: 6m cube, centreline *w'w'* stream-wise normal stress plot for the linear (standard) *k-e* model.

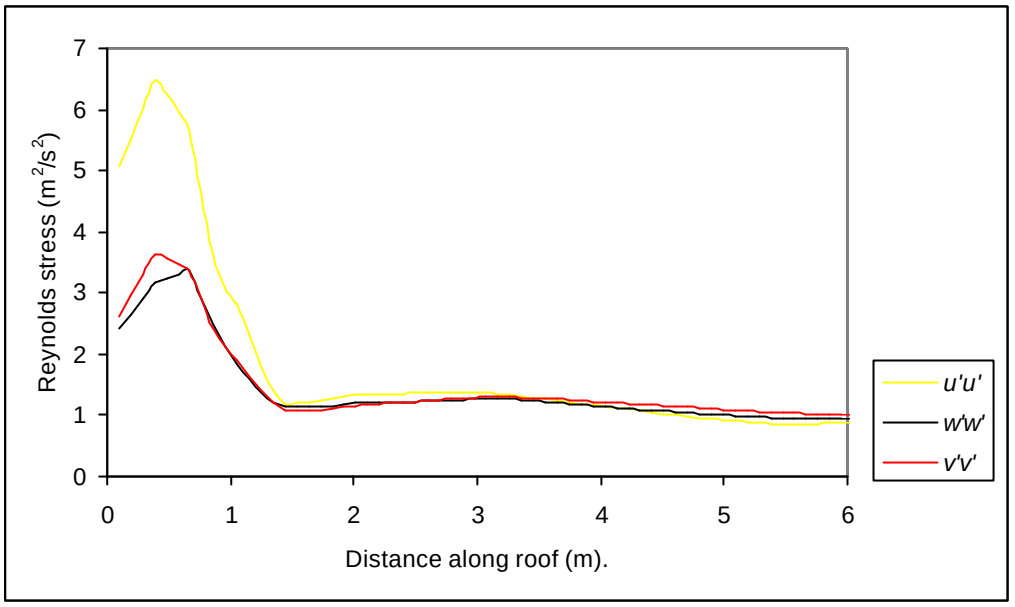

Figure 112: Normal Reynolds stress distribution for the roof (centre) of the 6m cube calculated using the non-linear *k-e* model.

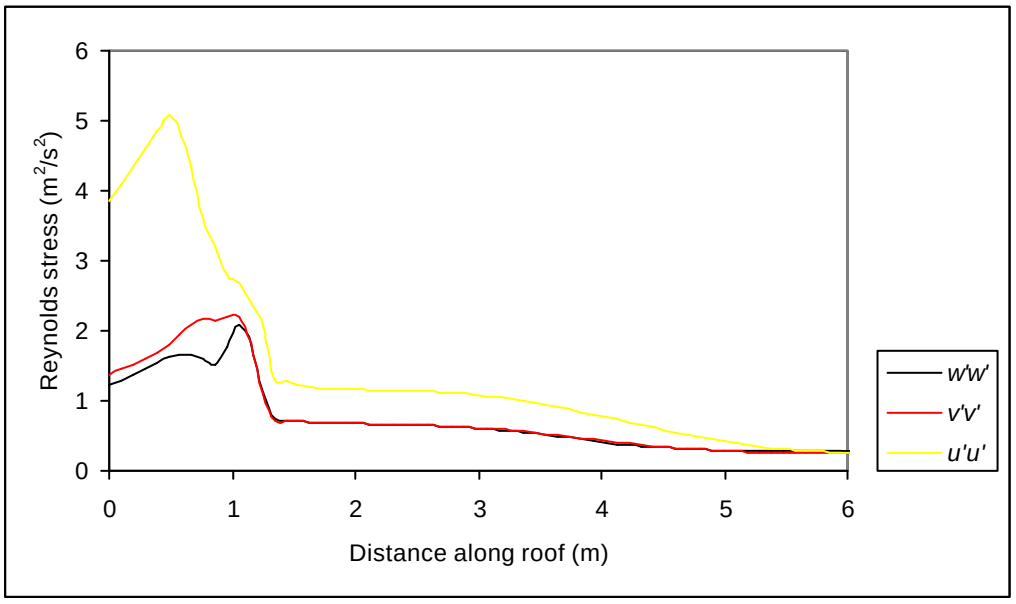

Figure 113: Normal Reynolds stress distribution for the roof (centre) of the 6m cube calculated using the differential stress model.

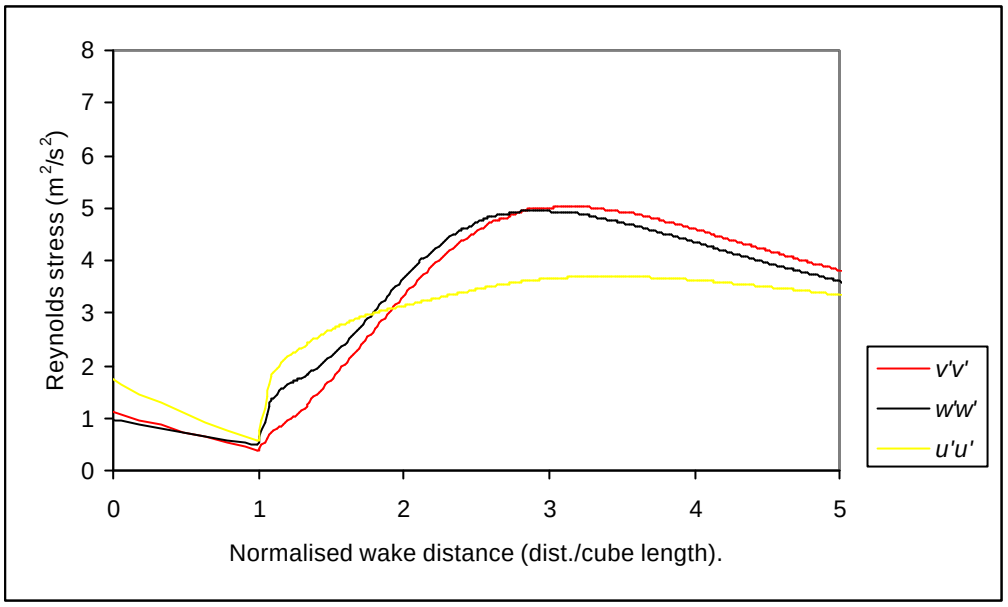

Figure 114: Normal Reynolds stress distribution for the wake of the 6m cube calculated using the non-linear *k-e* model

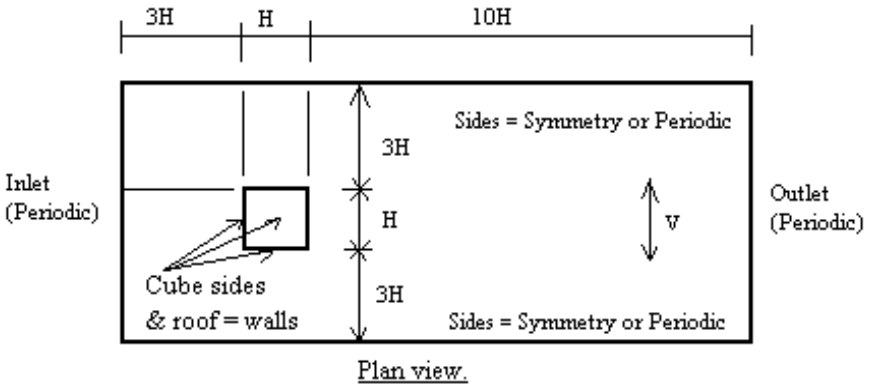

Figure 115: The computational domain for the LES simulations

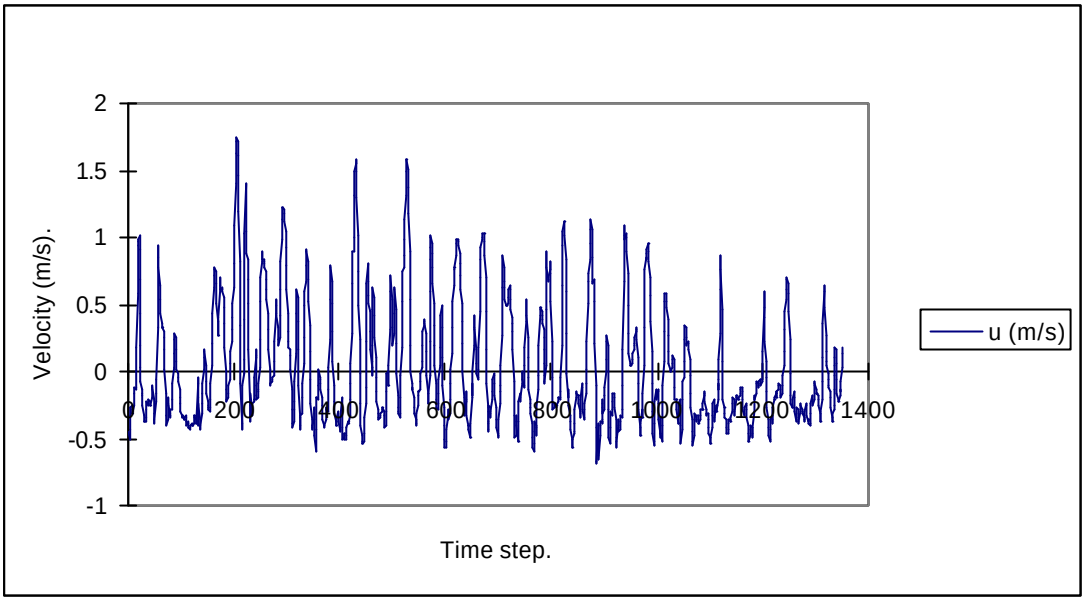

Figure 116: LES, time series of fluctuating velocity for the 1/30 scale cube model.

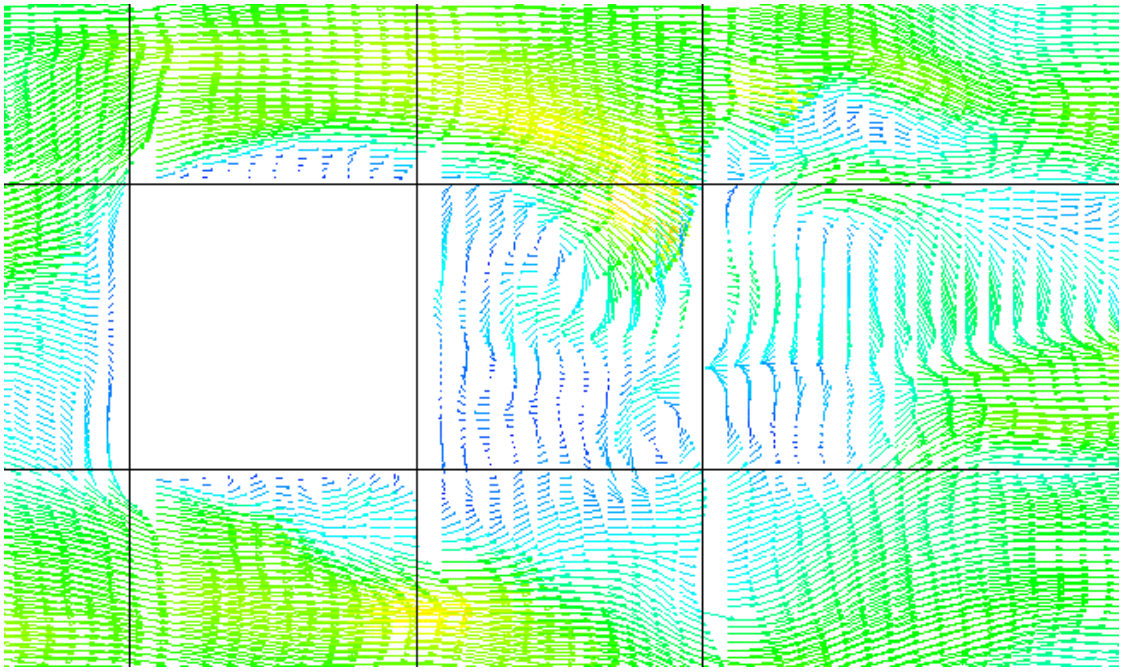

Figure 117: LES transient velocity vector plot number 1, 1/30 scale cube model, coarse grid (plan view).

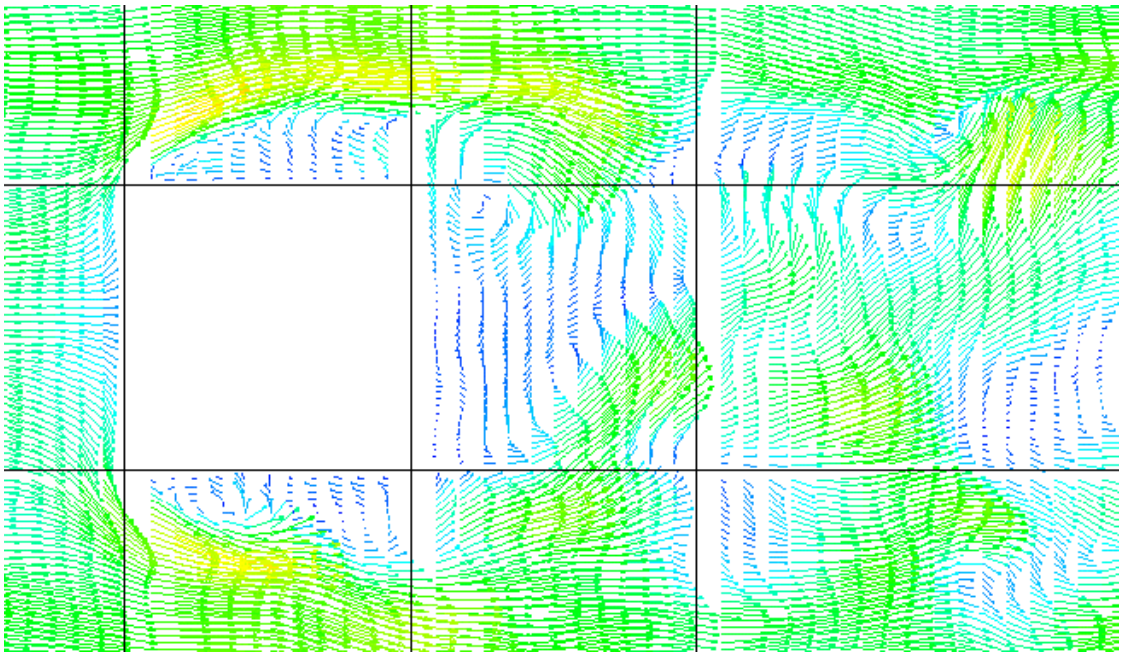

Figure 118: LES transient plot number 2.

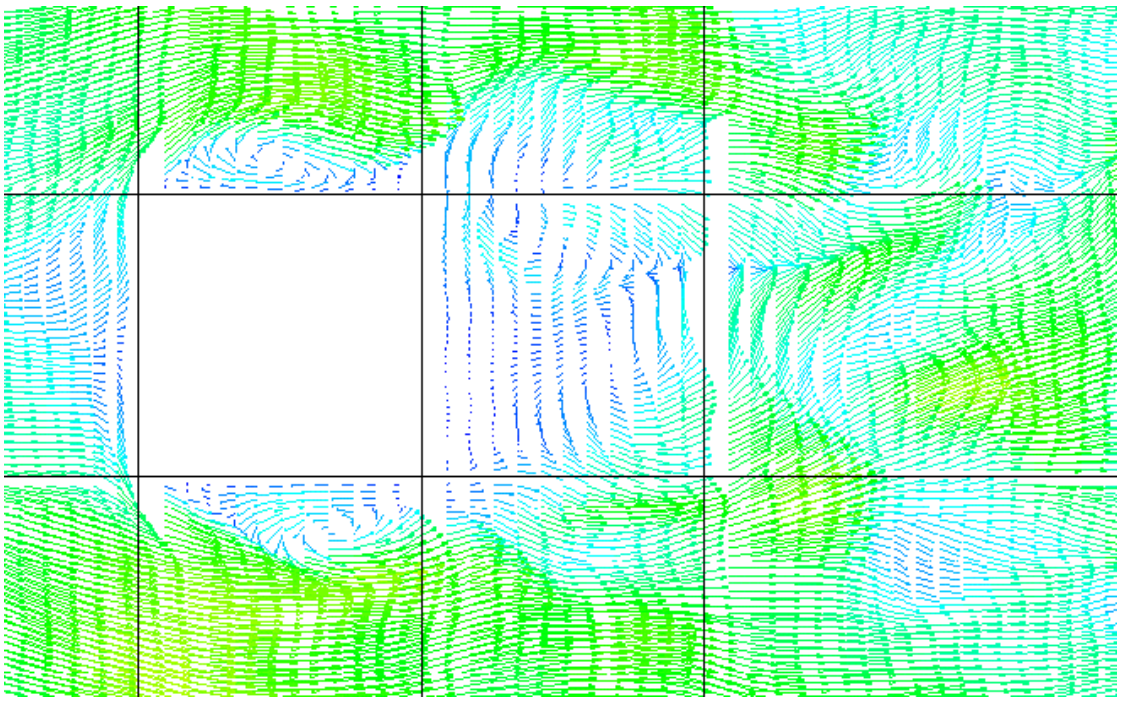

Figure 119: LES transient plot number 3.

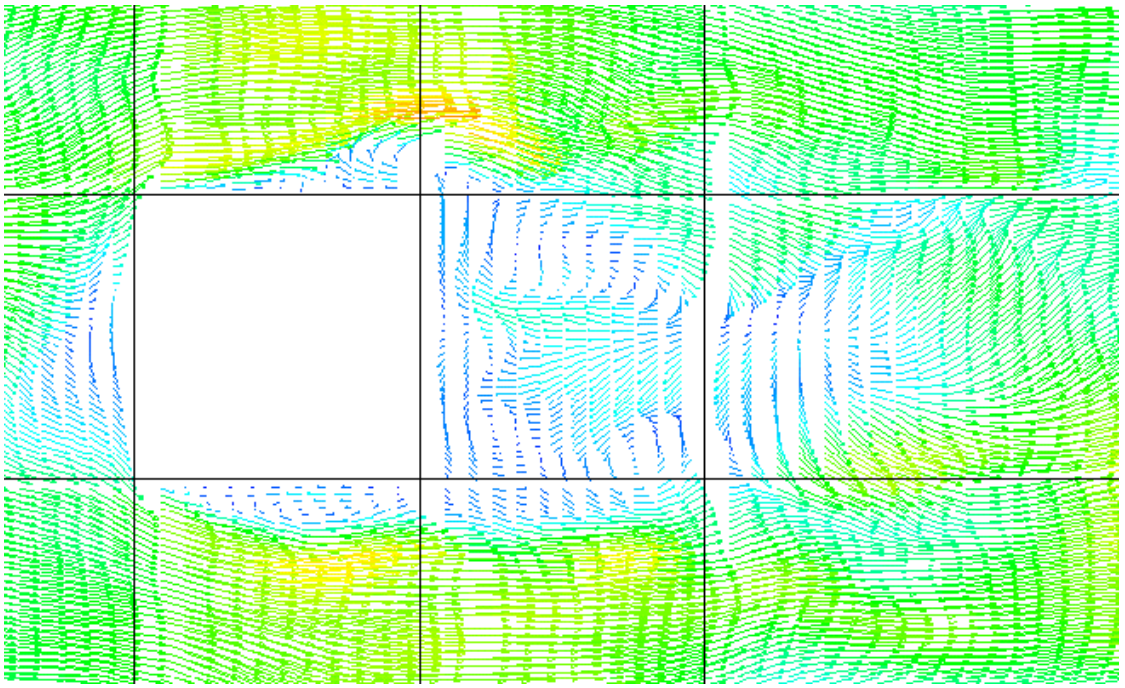

Figure 120: LES transient plot number 4.

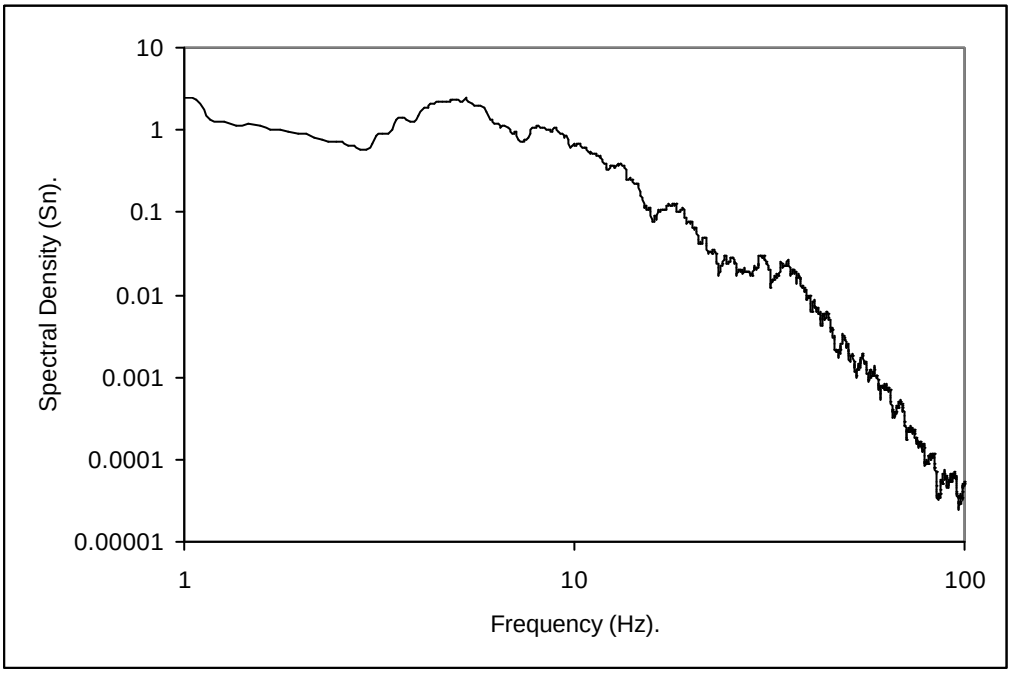

Figure 121: LES, Frequency Spectra for the 1/30 scale cube model.

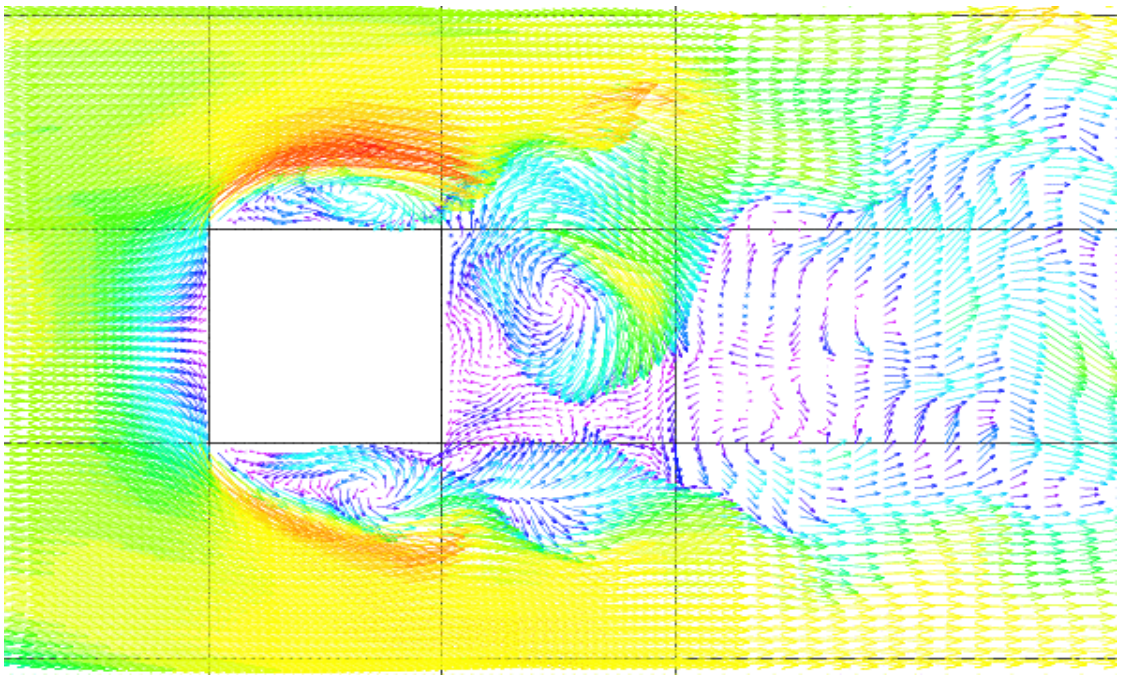

Figure 122: LES transient flow, velocity vector plot, fine resolution grid, 1/30 scale cube model (plan view).

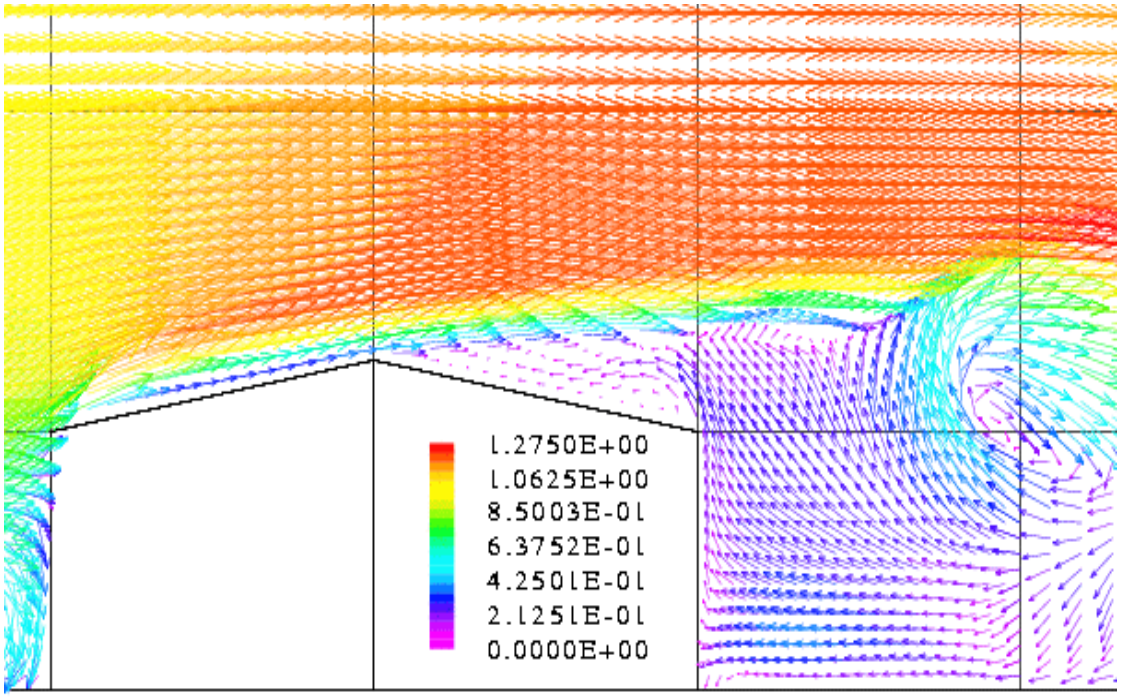

Figure 123: LES transient flow, velocity vector plot, 1/30 scale SSB model (side view).

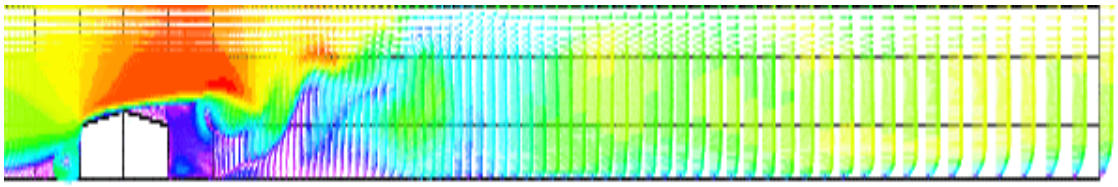

Figure 124: LES transient flow, velocity vector plot, 1/30 scale SSB model, full domain (side view).

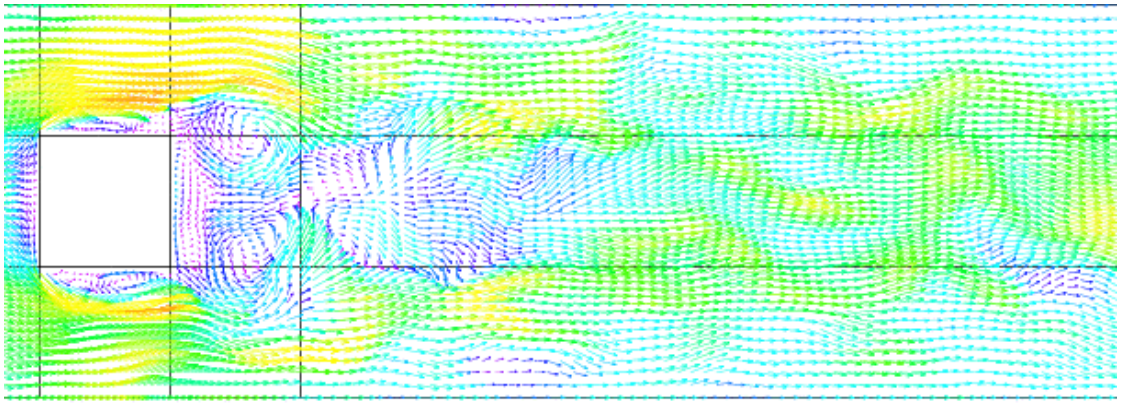

Figure 125: LES transient flow, velocity vector plot, 1/30 scale cube model, coarse grid, domain and flow field (plan view).

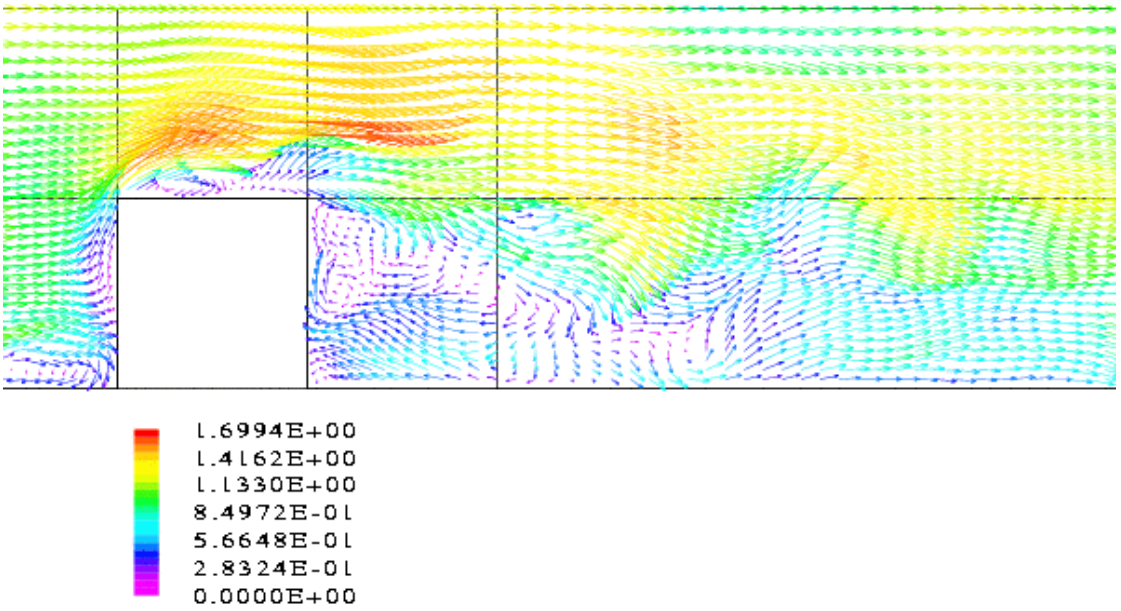

Figure 126: LES transient flow, velocity vector plot, coarse grid (side view).

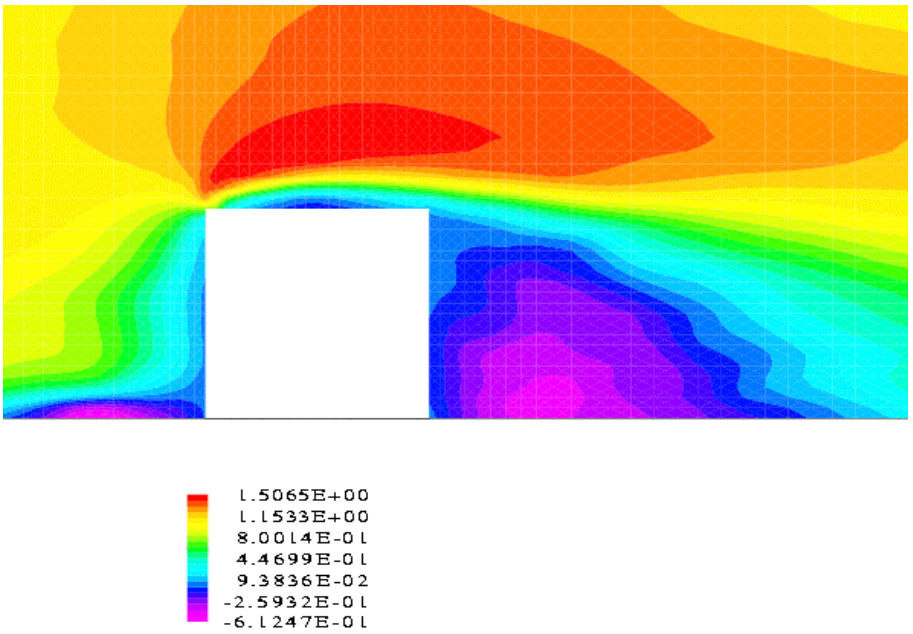

Figure 127: LES, time averaged velocity contour plot, 1/30 scale cube model, coarse grid (side view).

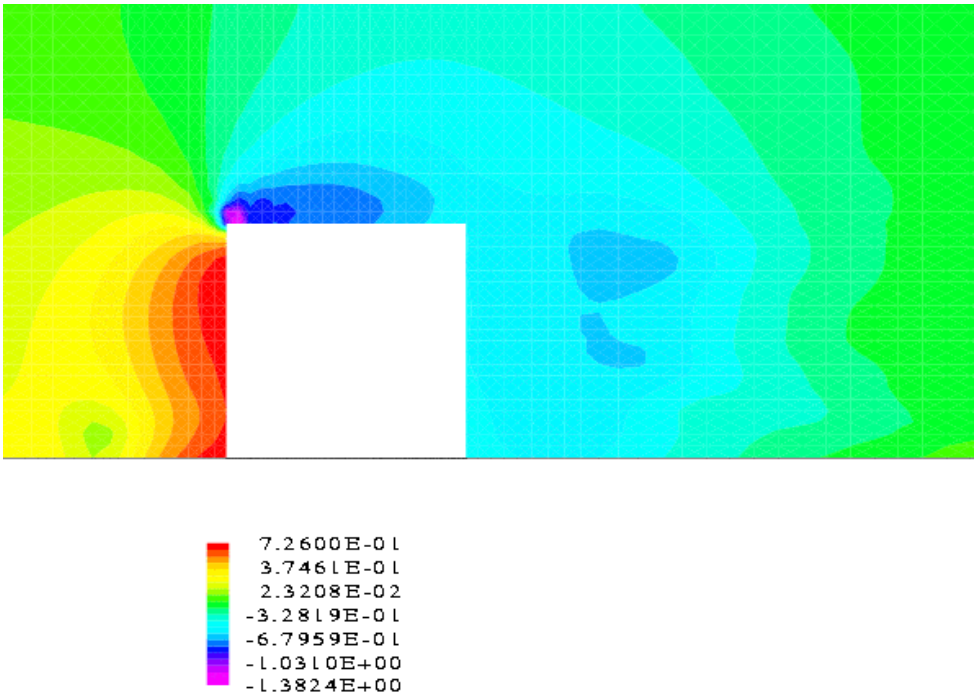

Figure 128: LES, time averaged pressure contour plot, 1/30 scale cube model, coarse grid (side view).

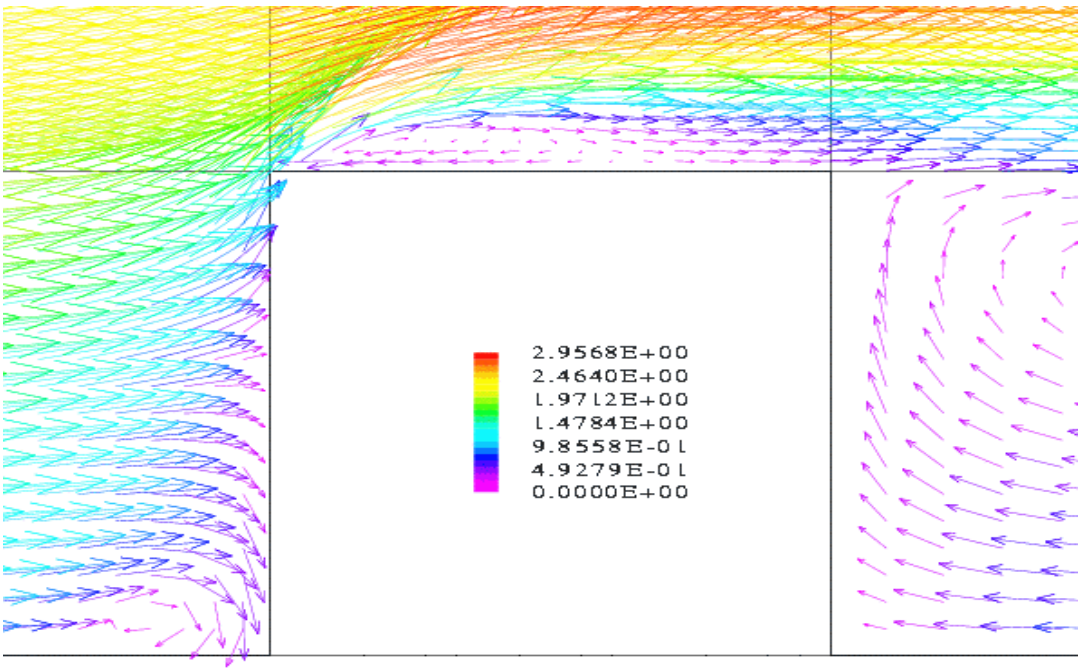

Figure 129: Roof velocity vectors for the LES comparisons predicted using the (steady state) non-linear *k-e* model.

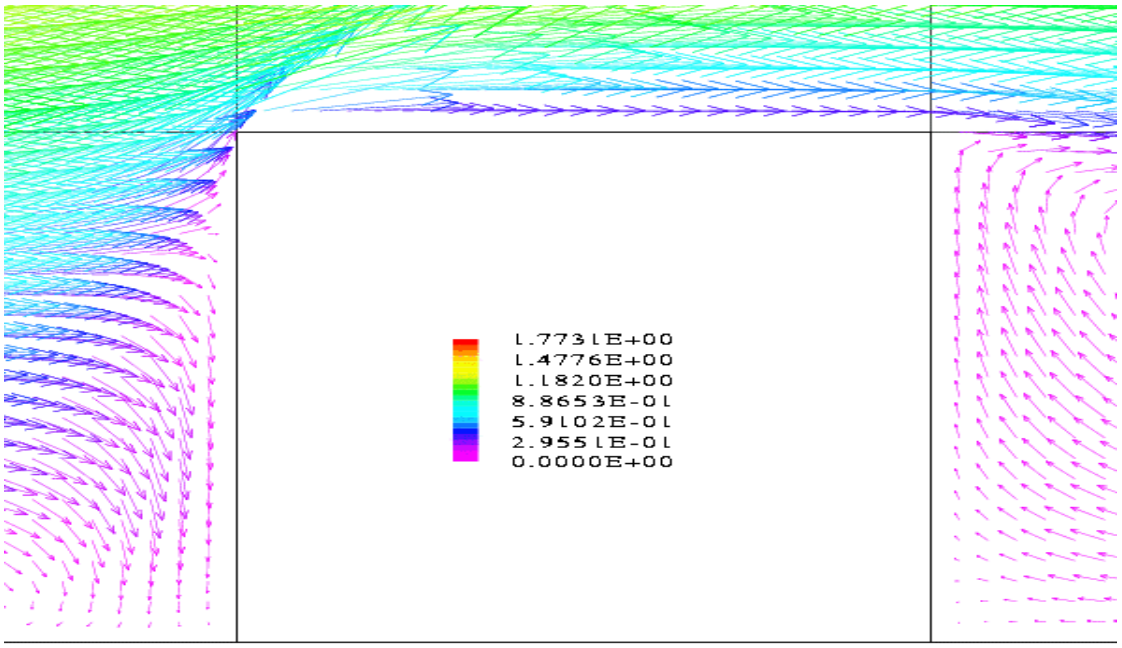

Figure 130: Roof velocity vectors for the LES comparisons predicted using the (steady state) low Reynolds number *k-e* model. (Note: The same roof flow field was found using the low Reynolds number *k-w* model.)

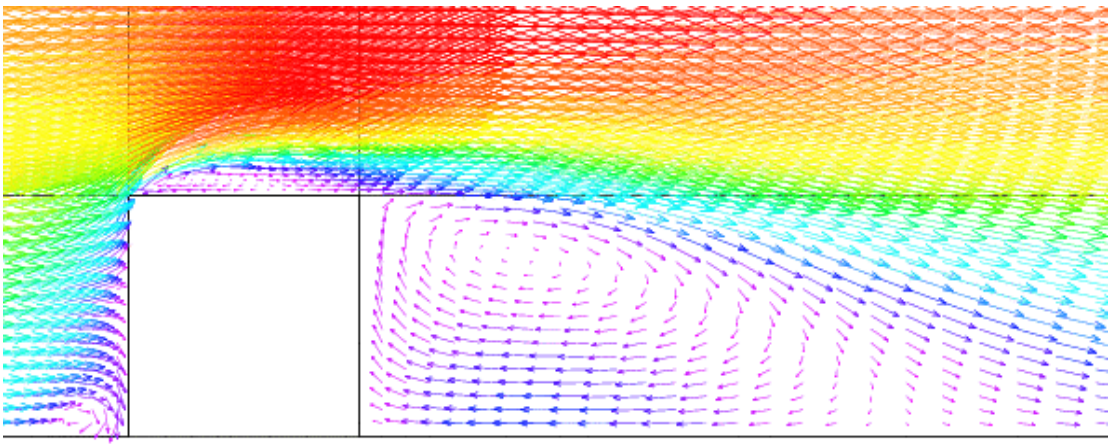

Figure 131: Wake and roof velocity vectors for the LES comparisons predicted using the (steady state) non-linear *k-e* model.